

ÉCOLE NATIONALE DES
PONTS
ET CHAUSSÉES

 POLYTECHNIQUE INSTITUT
IP PARIS

 cea

 inria

THÈSE DE DOCTORAT
de l'École nationale des ponts et chaussées
en partenariat avec le CEA

**Hybrid high-order methods for the numerical
simulation of elasto-acoustic wave propagation**

**Méthodes hybrides d'ordre élevé pour la simulation
numérique de la propagation d'ondes élasto-acoustiques**

École doctorale N°532, Mathématiques et Sciences et Technologies de l'Information et de la Communication (MSTIC)

Thèse préparée au Centre d'Enseignement et de Recherche en Mathématiques et Calcul Scientifique (CERMICS) de l'École nationale des ponts et chaussées, au CEA DAM et au sein de l'équipe-projet SERENA (INRIA)

PhD in Applied Mathematics

Romain Mottier

Composition du jury:

Pr. Paola Antonietti	<i>Politecnico di Milano</i>	Rapportrice
Pr. Hélène Barucq	<i>Inria Pau</i>	Examinateuse
Dr. Susanne Claus	<i>Onera Palaiseau</i>	Examinateuse
Pr. Alexandre Ern	<i>ENPC, IP Paris & Inria Paris</i>	Directeur de thèse
Dr. Laurent Guillot	<i>CEA, DAM, DIF</i>	Encadrant industriel
Dr. Sébastien Imperiale	<i>Inria Paris Saclay</i>	Examinateur
Pr. Christoph Lehrenfeld	<i>University of Göttingen</i>	Rapporteur

Résumé - Abstract

Résumé

L'objectif de cette thèse est de développer des méthodes d'approximation pour la simulation de la propagation d'ondes élasto-acoustiques. La discréétisation spatiale de ces équations repose sur des méthodes hybrides d'ordre élevé (HHO), qui présentent plusieurs propriétés favorables telles que l'utilisation de maillages généraux, une efficacité computationnelle et une grande précision. Une estimation d'erreur en norme d'énergie dans le cas semi-discret en espace est obtenue. La discréétisation en temps s'appuie sur des schémas de Runge–Kutta. Une attention particulière est portée à la stabilité des schémas explicites, et l'efficacité des approches implicites comme explicites. Des résultats numériques sont présentés allant jusqu'à une application géophysique impliquant une géométrie complexe et de fortes hétérogénéités. Un deuxième aspect important exploré dans cette thèse concerne l'utilisation de maillages dits "unfitted" pour des problèmes elliptiques comportant des interfaces courbes. Ces maillages ne suivent pas les interfaces physiques, ce qui conduit à des cellules pouvant être coupées par celles-ci. Cette approche permet de simplifier la phase de conception du maillage. Une méthode basée sur une extension polynomiale est introduite et analysée afin de traiter les mauvaises coupes. Cette approche est moins intrusive que celle, plus classique, basée sur une agglomération des cellules mal coupées.

Mot-clés : *Méthodes hybrides d'ordre élevé, Propagation d'ondes, Couplage élasto-acoustique, Discréétisation temporelle, Maillages unfitted, Extension polynomiale.*

Abstract

The objective of this Thesis is to develop approximation methods for the simulation of elasto-acoustic wave propagation. The spatial discretization of these equations relies on Hybrid High-Order (HHO) methods, which offer several advantageous properties, such as the ability to handle general meshes, computational efficiency, and high accuracy. An energy-norm error estimate is derived in the space semi-discrete setting. The time discretization is based on Runge–Kutta schemes. Particular attention is given to the stability of explicit schemes and to the efficiency of both explicit and implicit approaches. Numerical results are presented, including a geophysical application involving a complex geometry and strong heterogeneities. A second important aspect explored in this Thesis concerns the use of so-called *unfitted* meshes for elliptic problems with curved interfaces. These meshes do not conform to the physical interfaces, leading to mesh cells that may be intersected by them. This approach simplifies the mesh design. A method based on polynomial extension is introduced and analyzed in order to handle ill-cut cells. This approach is less intrusive than the more classical one based on the agglomeration of ill-cut cells.

Keywords : *Hybrid high-order methods, Wave propagation, Elasto-acoustic coupling, Time discretization, Unfitted meshes, Polynomial extension.*

Table of contents

I	Introduction	7
I.1	Contexte physique et objectifs de la thèse	7
I.2	Méthodes numériques pour la propagation d'ondes	9
I.3	Introduction aux méthodes Hybrid High-Order (HHO)	16
I.4	Introduction aux méthodes unfitted	23
I.5	Plan du manuscrit et contributions	31
II	HHO methods for elasto-acoustic wave propagation in the time domain	33
II.1	Introduction	34
II.2	Model problem	36
II.3	HHO space semi-discretization	39
II.4	Error analysis	43
II.5	Algebraic realization of the semi-discrete problem	52
II.6	Numerical results	53
II.7	Conclusion	66
III	Wave propagation in geophysical media using HHO on general meshes	67
III.1	Introduction	68
III.2	Model problem	71
III.3	HHO space semi-discretization	73
III.4	Fully discrete schemes	80
III.5	Numerical results	83
III.6	Conclusion	97
IV	Unfitted HHO methods stabilized by polynomial extension	99
IV.1	Introduction	100
IV.2	Model problem	101
IV.3	Unfitted HHO methods	103
IV.4	Stability, consistency, and error estimate	112
IV.5	Numerical results	118
IV.6	Proofs	125
V	Conclusion and perspectives	129
V.1	Summary	129
V.2	Perspectives	130
	Bibliography	143

Introduction

This chapter summarizes in French the main topics covered in this Thesis. Specific introductions in English can be found at the beginning of each of the following chapters.

Dans ce chapitre, nous exposons dans un premier temps le contexte, les enjeux et les objectifs de cette thèse. Après la présentation d'un état de l'art des méthodes numériques appliquées à la propagation des ondes mécaniques linéaires, nous proposons une introduction aux méthodes hybrides d'ordre élevé (*Hybrid High-Order* en anglais). Puis, nous nous intéressons à une variante de cette méthode pour la résolution d'un problème elliptique en présence d'une interface matérielle, pour lequel il n'y a pas de correspondance entre le maillage et l'interface. On parle alors de méthode unfitted (ou encore cut). Enfin, nous donnons le plan du manuscrit avec les principales contributions.

Contents

I.1 Contexte physique et objectifs de la thèse	7
I.2 Méthodes numériques pour la propagation d'ondes	9
I.2.1 Problème modèle	9
I.2.2 État de l'art des méthodes numériques	11
I.3 Introduction aux méthodes Hybrid High-Order (HHO)	16
I.3.1 Discrétisation d'un problème elliptique avec HHO	16
I.3.2 Liens avec les autres méthodes hybrides discontinues	20
I.4 Introduction aux méthodes unfitted	23
I.4.1 État de l'art des méthodes unfitted	24
I.4.2 Présentation de la méthode unfitted HHO	25
I.5 Plan du manuscrit et contributions	31

I.1 Contexte physique et objectifs de la thèse

Les ondes mécaniques sont des perturbations se propageant dans un milieu matériel. Elles peuvent être de nature scalaire, comme c'est le cas dans les fluides (on parle alors d'ondes acoustiques), ou vectorielle lorsqu'elles traversent un solide (on parle alors d'ondes élastiques). L'étude de leur propagation trouve de nombreuses applications en sciences et en ingénierie. Par exemple, la connaissance des propriétés mécaniques des tissus biologiques permet d'obtenir une imagerie fonctionnelle du vivant [136] en exploitant les ondes élastiques (*e.g.* en élastographie pour la détection et le suivi des tumeurs, voir Figure I.1 à gauche et [124]). Les ondes mécaniques sont également utilisées dans le contrôle non destructif des matériaux [104], le sondage du sous-sol [51] ou encore la bioacoustique pour l'étude des modes de communication animale [74].

Dans cette thèse, nous nous intéresserons à la propagation des ondes mécaniques en contexte géophysique [103]. Dans ce contexte, les ondes (élastiques dans la Terre solide, acoustiques dans l'atmosphère et les océans) traversent des milieux d'intérêt, sont sensibles à la présence d'interfaces matérielles et sont caractérisées par un spectre fréquentiel large. De nombreux instruments déployés dans divers environnements enregistrent les signaux associés à ces ondes. Leur analyse permet d'imager la structure interne de la Terre [83], d'analyser la structure de l'atmosphère et sa variabilité [10], de détecter des événements naturels ou anthropiques et caractériser leur source (séismes, explosions chimiques ou nucléaires, accidents industriels), ou de contribuer à la surveillance des aléas naturels [90] (voir Figure I.1 à droite pour un exemple). Tous ces phénomènes impliquent des milieux hétérogènes et de nature variée (solide, fluide), des structures complexes, des effets de couplage et de guidage d'ondes, ainsi qu'une large gamme de fréquences.

Ces objectifs d'analyse, de surveillance et de détection reposent ainsi fortement sur notre capacité à comprendre l'évolution d'un champ d'ondes élasto-acoustiques lors de sa propagation. Or, les solutions exactes ou semi-analytiques ne sont disponibles que pour les configurations géométriques les plus simples [3], et les approches asymptotiques reposent souvent sur des hypothèses susceptibles de ne pas être respectées dans des configurations réalistes. Il est donc indispensable de recourir à des méthodes numériques pour simuler la propagation d'ondes dans des milieux réalistes, caractérisés par des géométries complexes, des hétérogénéités multi-échelles, et des interfaces fluide-solide.

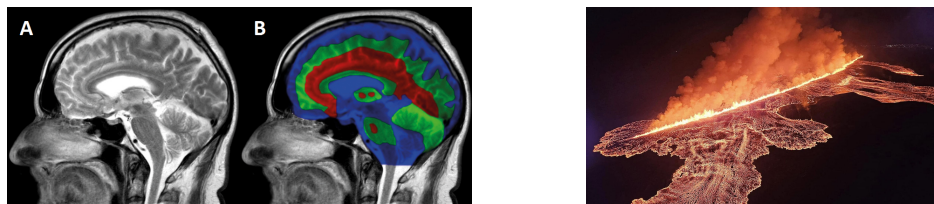


Fig. I.1: **Gauche:** Carte de rigidité cérébrale par IRM : A - IRM classique, B - élastographie par IRM avec rigidité croissante du bleu au rouge [24]. **Droite:** Éruption d'un volcan près de Grindavík, sur la péninsule de Reykjanes (@AFP - Police d'État islandaise).

Les enjeux liés à la surveillance sismique trouvent un écho particulier dans les activités stratégiques menées par la Direction des Applications Militaires (DAM) du Commissariat à l'Énergie Atomique et aux énergies alternatives (CEA), où j'ai réalisé ma thèse. En effet, dans le cadre de la lutte contre la prolifération nucléaire et le terrorisme, la DAM contribue activement à des programmes internationaux de vérification (Traité d'Interdiction Complète des Essais nucléaires, TICE). Cette implication s'appuie notamment sur le suivi et l'interprétation des événements sismiques à l'échelle mondiale. L'efficacité des diagnostics fournis par la DAM, repose en grande partie sur la capacité à simuler avec précision la propagation d'ondes élasto-acoustiques dans des milieux complexes. Ces applications stratégiques confirment ainsi la nécessité de disposer de méthodes numériques robustes et précises pour répondre à des objectifs à la fois scientifiques, technologiques et géopolitiques.

I.2 Méthodes numériques pour la propagation d'ondes

Les défis évoqués ci-dessus motivent le développement de méthodes numériques avancées grâce auxquelles on peut simuler sans biais la propagation d'ondes élasto-acoustiques. Ces méthodes doivent être suffisamment précises et flexibles pour prendre en compte des géométries complexes, intégrer des (fortes) hétérogénéités et représenter correctement les différents phénomènes de transmission et réflexion au niveau des interfaces. Elles doivent en particulier posséder de bonnes propriétés de dispersion et de dissipation numériques afin de garantir des simulations fiables. De nombreuses méthodes numériques ont été développées avec cet objectif.

Dans cette section, nous rappelons dans un premier temps les équations décrivant la propagation d'ondes acoustiques et élastiques, ainsi que leur couplage. Puis, nous présentons un état de l'art des méthodes numériques dédiées à leur résolution (dans le domaine temporel), en mettant en lumière leurs avantages et leurs limites.

I.2.1 Problème modèle

Une police en gras (resp. en caractère double barre) est désormais utilisée pour désigner les vecteurs (resp. les tenseurs), ainsi que les champs vectoriels (resp. tensoriels) et les espaces composés de tels champs. Les notations usuelles concernant les espaces de Lebesgue et de Sobolev sont adoptées. Pour un poids κ borné et strictement positif, on définit le produit scalaire L^2 pondéré par $(u, v)_{L^2(\kappa; \Omega)} := \int_{\Omega} \kappa u v \, d\Omega$ pour tout $u, v \in L^2(\Omega)$ et la norme associée $\|u\|_{L^2(\kappa; \Omega)} := \|\kappa^{\frac{1}{2}} u\|_{L^2(\Omega)}$.

Soit $J := (0, T_f)$ l'intervalle de temps de simulation, où $T_f > 0$ est le temps final de simulation, et soit Ω un domaine (ouvert, borné, connexe, de frontière lipschitzienne) dans \mathbb{R}^d , avec $d \in \{2, 3\}$. Le domaine Ω est découpé en deux sous-domaines disjoints, Ω^F et Ω^S , représentant respectivement les milieux fluide et solide. Ces sous-domaines partagent l'interface $\Gamma := \partial\Omega^F \cap \partial\Omega^S$, dont le vecteur normal unitaire n_{Γ} pointe conventionnellement de Ω^S vers Ω^F . Un exemple de configuration géophysique considérée dans cette thèse est illustré dans la Figure I.2.

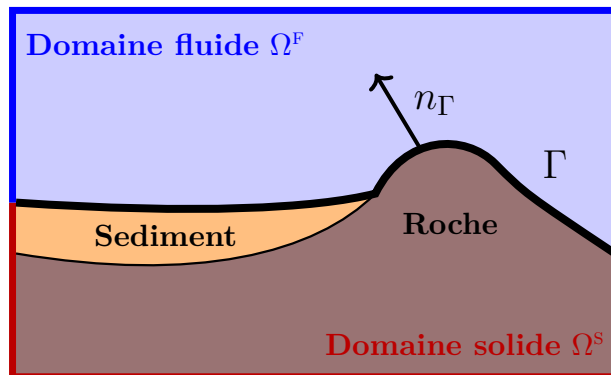


Fig. I.2: Sous-domaine solide Ω^S , sous-domaine fluide Ω^F , et normale unitaire n_{Γ} le long de l'interface Γ (pointant du solide vers le fluide).

L'évolution temporelle d'une onde acoustique, définie par son champ de pression scalaire p [Pa] et son champ de vitesse particulaire \mathbf{m} [$\frac{\text{m}}{\text{s}}$], est décrite par le système d'équations aux dérivées partielles suivant, dans $J \times \Omega^F$,

$$\rho^F \partial_t \mathbf{m} - \nabla p = \mathbf{0}, \quad (\text{I.1a})$$

$$\frac{1}{\kappa} \partial_t p - \nabla \cdot \mathbf{m} = f^F, \quad (\text{I.1b})$$

où ρ^F [$\frac{\text{kg}}{\text{m}^3}$] est la densité du fluide, κ [Pa] le module de compressibilité du fluide, et f^F [$\frac{1}{\text{s}}$] le terme source. Ces équations sont obtenues en considérant un fluide parfait, où le tenseur des contraintes est défini par $\mathbf{s}^F := p \mathbb{I}d$ où $\mathbb{I}d$ est le tenseur identité (au lieu de la convention classique $\mathbf{s}^F := -p \mathbb{I}d$). Ce choix n'a d'autre objet que de simplifier la condition de couplage (I.4). Les propriétés matérielles ρ^F et κ sont généralement constantes par morceaux dans Ω^F . La vitesse des ondes acoustiques est donnée par $c_p^F := \sqrt{\kappa / \rho^F}$ [$\frac{\text{m}}{\text{s}}$]. Les conditions initiales sont spécifiées par $p(0) = p_0$ et $\mathbf{m}(0) = \mathbf{m}_0$ avec les données initiales p_0 et \mathbf{m}_0 .

Soit $\nabla_{\text{sym}} := \frac{1}{2}(\nabla + \nabla^\dagger)$ l'opérateur de gradient symétrique. Les ondes élastiques sont quant à elles décrites par le tenseur des contraintes de Cauchy linéarisé \mathbf{s} [Pa] et le champ de vitesse \mathbf{v} [$\frac{\text{m}}{\text{s}}$], et sont régies par les équations aux dérivées partielles suivantes dans $J \times \Omega^S$:

$$\mathbb{C}^{-1} \partial_t \mathbf{s} - \nabla_{\text{sym}} \mathbf{v} = \mathbf{0}, \quad (\text{I.2a})$$

$$\rho^S \partial_t \mathbf{v} - \nabla \cdot \mathbf{s} = \mathbf{f}^S, \quad (\text{I.2b})$$

où ρ^S [$\frac{\text{kg}}{\text{m}^3}$] est la densité du solide, \mathbb{C} [Pa] le tenseur de Hooke d'ordre quatre, et \mathbf{f}^S [$\frac{\text{Pa}}{\text{m}}$] le terme source. Les propriétés matérielles \mathbb{C} et ρ^S sont généralement constantes par morceaux dans Ω^S avec une valeur fixe dans chaque couche géophysique composant Ω^S . Dans le cadre de l'élasticité isotrope, \mathbb{C} dépend des paramètres de Lamé λ [Pa] et μ [Pa] sous la forme $\mathbb{C}_{ijkl} := \lambda \delta_{ij} \delta_{kl} + \mu (\delta_{ik} \delta_{jl} + \delta_{il} \delta_{jk})$, pour tous $i, j, k, l \in \{1, \dots, d\}$, où δ est le symbole de Kronecker. Ce cadre donne lieu à deux vitesses de propagation des ondes correspondant à deux types d'ondes volumiques, loin des interfaces matérielles :

$$c_p^S := \sqrt{(\lambda + 2\mu) / \rho^S} \quad \left[\frac{\text{m}}{\text{s}} \right] \quad \text{pour les ondes de compression (ondes P),} \quad (\text{I.3a})$$

$$c_s^S := \sqrt{\mu / \rho^S} \quad \left[\frac{\text{m}}{\text{s}} \right] \quad \text{pour les ondes de cisaillement (ondes S).} \quad (\text{I.3b})$$

Nous ne considérons pas la limite incompressible où $\frac{\lambda}{\mu} \gg 1$, de sorte que les deux vitesses d'ondes dans (I.3) sont du même ordre de grandeur. Enfin, les conditions initiales sont spécifiées par $\mathbf{v}(0) = \mathbf{v}_0$ et $\mathbf{s}(0) = \mathbf{s}_0$, avec les données initiales \mathbf{v}_0 et \mathbf{s}_0 .

Des conditions aux limites homogènes de Dirichlet sur p sur $\partial\Omega^F \setminus \Gamma$ et sur \mathbf{v} sur $\partial\Omega^S \setminus \Gamma$ sont imposées. Ce choix implique une réflexion parfaite des ondes acoustiques et élastiques aux frontières du domaine, et d'éventuels retours parasites. Toutes les simulations présentées dans ce manuscrit, ont été réalisées de sorte à ce que ces phases réfléchies sur les bords du domaine de calcul, n'interfèrent aucunement avec les phases d'intérêt.

Les conditions de couplage à l'interface sur $J \times \Gamma$ sont exprimées comme suit :

$$\mathbf{v} \cdot \mathbf{n}_\Gamma = \mathbf{m} \cdot \mathbf{n}_\Gamma, \quad (\text{I.4a})$$

$$\mathbf{s} \cdot \mathbf{n}_\Gamma = p \mathbf{n}_\Gamma, \quad (\text{I.4b})$$

où la première équation impose la continuité de la composante normale de la vitesse à travers l'interface et la deuxième équation exprime l'équilibre des forces.

Nous définissons les espaces fonctionnels suivants :

$$\mathbf{M}^F := \mathbf{L}^2(\Omega^F), \quad P^F := \left\{ p \in H^1(\Omega^F) : p|_{\partial\Omega^F \setminus \Gamma} = 0 \right\}, \quad (\text{I.5a})$$

$$\mathbf{S}^S := \mathbb{L}_{\text{sym}}^2(\Omega^S), \quad \mathbf{V}^S := \left\{ \mathbf{v} \in \mathbf{H}^1(\Omega^S) : \mathbf{v}|_{\partial\Omega^S \setminus \Gamma} = \mathbf{0} \right\}. \quad (\text{I.5b})$$

Le problème couplé consiste à déterminer $(\mathbf{m}, p) : J \rightarrow \mathbf{M}^F \times P^F$ et $(\mathbf{s}, \mathbf{v}) : J \rightarrow \mathbf{S}^S \times \mathbf{V}^S$ tels que, pour tout $t \in J$, les équations faibles suivantes soient satisfaites :

- i) Pour les équations des ondes acoustiques, pour toutes fonctions test $(\mathbf{r}, q) \in \mathbf{M}^F \times P^F$,

$$(\partial_t \mathbf{m}(t), \mathbf{r})_{\mathbf{L}^2(\rho^F; \Omega^F)} - (\nabla p(t), \mathbf{r})_{\mathbf{L}^2(\Omega^F)} = 0, \quad (\text{I.6a})$$

$$(\partial_t p(t), q)_{L^2(\frac{1}{\kappa}; \Omega^F)} + (\mathbf{m}(t), \nabla q)_{\mathbf{L}^2(\Omega^F)} + (\mathbf{v}(t) \cdot \mathbf{n}_\Gamma, q)_{L^2(\Gamma)} = (f^F(t), q)_{L^2(\Omega^F)}. \quad (\text{I.6b})$$

- ii) Pour les équations des ondes élastiques, pour toutes fonctions test $(\mathbf{b}, \mathbf{w}) \in \mathbf{S}^S \times \mathbf{V}^S$,

$$(\partial_t \mathbf{s}(t), \mathbf{b})_{\mathbb{L}^2(\mathbb{C}^{-1}; \Omega^S)} - (\nabla_{\text{sym}} \mathbf{v}(t), \mathbf{b})_{\mathbb{L}^2(\Omega^S)} = 0, \quad (\text{I.7a})$$

$$(\partial_t \mathbf{v}(t), \mathbf{w})_{\mathbf{L}^2(\rho^S; \Omega^S)} + (\mathbf{s}(t), \nabla_{\text{sym}} \mathbf{w})_{\mathbb{L}^2(\Omega^S)} - (p(t) \mathbf{n}_\Gamma, \mathbf{w})_{\mathbf{L}^2(\Gamma)} = (\mathbf{f}^S(t), \mathbf{w})_{\mathbf{L}^2(\Omega^S)}. \quad (\text{I.7b})$$

Les conditions de couplage sont imposées de manière faible, dans la mesure où (I.4a) et (I.4b) sont intégrées respectivement dans (I.6b) et (I.7b).

I.2.2 État de l'art des méthodes numériques

Nous nous intéressons à présent à l'état de l'art des méthodes numériques permettant d'approcher la solution du problème modèle défini par (I.6)–(I.7). L'objectif est de motiver le développement de l'approche HHO proposée dans cette thèse. De manière générale, les principaux défis qui se posent aux méthodes numériques sont leur capacité à prendre en compte des géométries réalistes, caractérisées par des interfaces complexes et de fortes hétérogénéités, tout en permettant l'utilisation d'intégrateurs en temps efficaces.

Différences finies (FD, de l'anglais *Finite Differences*). Les différences finies sont parmi les méthodes les plus largement utilisées en raison de leur simplicité conceptuelle et de leur efficacité numérique. Toutefois, elles présentent plusieurs limitations. En particulier, les méthodes FD rencontrent des difficultés dans les géométries complexes et introduisent des erreurs géométriques aux interfaces [139], bien que des techniques

basées sur des transformations géométriques puissent améliorer leurs performances [8]. De plus, les méthodes FD sont sujettes à la dispersion numérique, que l'on peut atténuer en utilisant des schémas d'ordre élevé. Cependant, ces schémas d'ordre élevé nécessitent des stencils étendus, ce qui nuit à la scalabilité parallèle, et leur discréétisation temporelle explicite est en outre, délicate à mettre en œuvre [127].

Éléments finis continus (FEM, de l'anglais *Finite Element Method*). Une alternative naturelle aux FD sont les éléments finis (voir [77, 78, 79] pour une introduction au sujet, [59, 99] pour des revues sur les applications à la propagation d'ondes ainsi que [15, 75] pour des travaux pionniers sur l'analyse de la méthode dans ce contexte). Les méthodes FEM permettent de traiter naturellement les géométries complexes avec interfaces, mais leur efficacité est limitée par l'utilisation de schémas en temps implicites dus à la non-diagonalité de la matrice de masse globale (des exemples de discréétisation sont donnés à la Figure I.3).

Pour permettre l'utilisation d'intégrateurs explicites en temps, la méthode des Éléments Spectraux (SEM, de l'anglais *Spectral Element Method*) a été introduite. Elle utilise des points de quadrature alignés avec les nœuds d'interpolation tensorisés de Gauss–Lobatto–Legendre (base nodale de type \mathbb{Q}_k , un exemple est donné à la Figure I.3 à droite) sur des maillages quadrangulaires/hexaédriques, menant à une matrice de masse diagonale (mass lumping), sans perte de précision. L'inconvénient principal de SEM est la nécessité de recourir à des maillages structurés rendant difficile la discréétisation de géométries complexes.

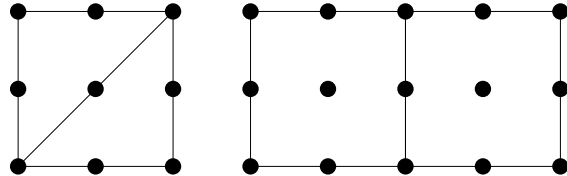


Fig. I.3: **Gauche:** Inconnues discrètes \mathbb{P}_2 -FEM, sur éléments triangulaires. **Droite:** Inconnues discrètes \mathbb{Q}_2 -FEM, sur éléments quadrangulaires.

Maillages généraux. Dans le but d'introduire davantage de flexibilité afin de traiter des géométries réalistes, l'idée est d'utiliser des maillages généraux. De tels maillages sont composés de cellules polyédriques (polygonales en 2D) de forme relativement générale (modulo des contraintes de régularité, voir par exemple [50], [65], [39]). Les maillages généraux sont particulièrement avantageux pour la discréétisation de géométries complexes. Les méthodes numériques capables de prendre en charge de tels maillages, appelées méthodes polytopales, offrent par conséquent une grande flexibilité géométrique. Un exemple simple mais important est celui des maillages non conformes contenant des nœuds orphelins. En effet, les méthodes polytopales vont interpréter la présence d'un nœud orphelin comme une division d'une arête/face formant un angle plat (180°), ce qui revient à augmenter de un le nombre d'arêtes/faces dans les éléments partageant cette arête/face. Ces éléments sont alors traités comme des polyèdres dont certaines arêtes sont alignées (voir

Figure I.4 pour une illustration). La capacité à gérer des maillages généraux constitue un avantage significatif par rapport aux méthodes FEM classiques, car la construction de maillages sans noeuds orphelins est souvent une tâche laborieuse pouvant conduire à des maillages très irréguliers, ce qui peut nuire à la précision de la solution et/ou détériorer le conditionnement de la matrice du système.

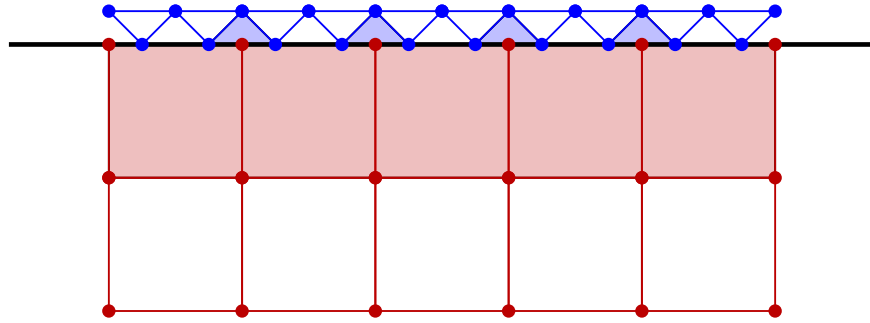


Fig. I.4: Exemple de maillages généraux avec nœuds orphelins. Les cellules à fond bleu sont considérées comme des quadrangles au lieu de triangles, et celles à fond rouge comme des hexagones au lieu de quadrangles.

Deux grandes approches permettant la prise en compte de maillages généraux sont disponibles dans la littérature. La première repose sur une formulation H^1 -conforme, représentée par la méthode des éléments virtuels, qui constitue une généralisation des éléments finis aux maillages généraux. La seconde s'appuie sur une stratégie non H^1 -conforme fondée sur des fonctions discrètes discontinues, permettant elles aussi de traiter des maillages généraux.

Éléments virtuels (VEM, de l'anglais *Virtual Element Method*). Inspirée par les idées des méthodes de différences finies mimétiques [26, 25], la méthode des éléments virtuels (VEM) a été développée dans un cadre de type Galerkin continu [20], dans le but de généraliser la méthode des éléments finis continus aux maillages généraux (voir Figure I.5 pour un exemple de discréttisation). L'idée centrale de cette approche réside dans la définition implicite des espaces d'approximation locaux, d'où l'appellation «virtuelle». Il en résulte que ces espaces incluent généralement des fonctions non polynomiales. Toutefois, ceci n'est pas problématique car VEM ne requiert que la connaissance d'un sous-espace polynomial de l'espace discret local. Cette propriété est rendue possible par la séparation (décomposition orthogonale) de la contribution de ce sous-espace polynomial de celle du sous-espace virtuel non polynomial complémentaire, au moyen d'opérateurs de projection appropriés, calculables uniquement à partir des degrés de liberté. Depuis leur création, les éléments virtuels ont été étendus à un large éventail d'applications [7]. En lien avec la propagation d'ondes, on peut citer en particulier, leur utilisation pour la résolution du problème de Helmholtz dans le cadre d'ondes planes [126], le développement de formulations espace-temps pour l'équation des ondes [144], ainsi qu'une approche basée sur des éléments virtuels aux faces courbes en dimension 2 [61] également pour l'équation des ondes.

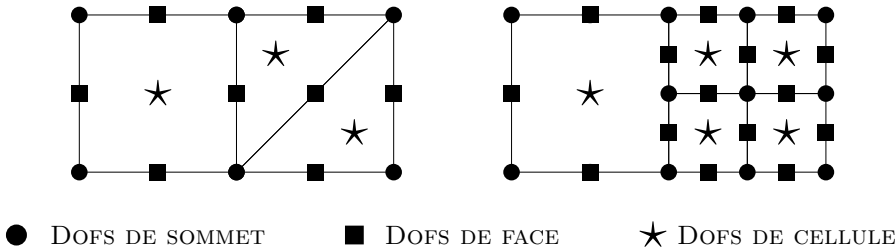


Fig. I.5: Inconnues discrètes VEM d'ordre $k = 2$ sur un maillage conforme (gauche) et non-conforme (droite).

Éléments finis discontinus (dG, de l'anglais *discontinuous Galerkin*). La deuxième possibilité permettant de gagner en flexibilité géométrique est de passer par des méthodes non H^1 -conformes. C'est dans ce cadre qu'ont été introduites les méthodes de Galerkin discontinues, d'abord pour des problèmes de neutronique [130, 110] et hyperboliques [98, 58], puis pour des problèmes elliptiques [9]; voir également les monographies [94, 67]. Plus récemment, ces méthodes ont été appliquées à la propagation d'ondes, en formulations d'ordre un [82, 119] et d'ordre deux [87] en temps (voir [5, 6] pour le couplage élasto-acoustique). En renonçant à produire des solutions H^1 -conformes (continues), les méthodes dG permettent de traiter des maillages généraux (voir Figure I.6 pour un exemple de discréttisation). L'inconvénient principal des méthodes dG est leur coût de calcul élevé en raison du grand nombre de degrés de liberté (dofs) en comparaison à FEM.

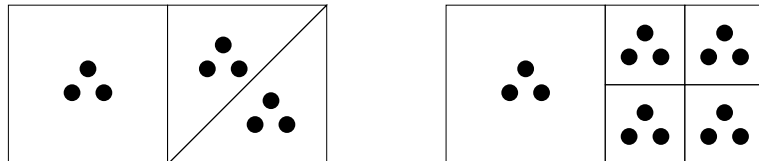


Fig. I.6: Inconnues discrètes dG d'ordre $k = 1$ sur un maillage conforme (gauche) et non-conforme (droite).

Éléments finis hybrides discontinus. Les méthodes hybrides discontinues constituent un développement ultérieur des méthodes dG. Ces méthodes introduisent une inconnue supplémentaire définie sur les faces du maillage. Comparativement aux méthodes dG, ces inconnues de face permettent de réduire les coûts de calcul via une procédure de condensation statique (utilisant un complément de Schur). Cette procédure permet d'éliminer localement les inconnues de cellules, réduisant ainsi la taille du système à résoudre.

On peut considérer que la classe des méthodes hybrides discontinues est composée des méthodes HDG (de l'anglais *Hybridizable Discontinuous Galerkin* [55]), HHO (de l'anglais *Hybrid High-Order* [68]), WG (de l'anglais *Weak Galerkin* [141]) et ncVEM (de l'anglais *non-conforming Virtual Element Methods* [12, 40]). Les méthodes HDG, HHO et WG ont été appliquées avec succès aux problèmes de propagation d'ondes. Dans le cas acoustique, on trouve notamment [122, 134] pour HDG, [32, 81, 135] pour HHO et [96, 147] pour

WG, et pour la propagation d'ondes élastiques, on peut citer [122] pour HDG et [34] pour HHO. De plus, dans le contexte du couplage élasto-acoustique, ces méthodes permettent d'imposer de manière naturelle les conditions de couplage aux interfaces via les inconnues de faces [138].

Les méthodes hybrides discontinues utilisent des polynômes d'ordre arbitraire ($k \geq 1$ pour l'élasticité, sinon $k \geq 0$ pour l'acoustique) associés aux faces du maillage, et des polynômes d'ordre $k' \in \{k, k+1\}$ associés aux cellules (voir Figure I.7 pour un exemple de discréttisation). Elles reposent sur deux opérateurs locaux : un opérateur de reconstruction du gradient et un opérateur de stabilisation. Ces méthodes présentent plusieurs avantages, tels qu'un traitement naturel des maillages généraux, des propriétés de conservativité locale et des taux de convergence optimaux (ordre $(k+1)$ en norme d'énergie et ordre $(k+2)$ en norme L^2), soit un ordre de plus que pour les méthodes dG. De plus, contrairement à ces dernières, elles ne nécessitent pas de seuil minimal pour pondérer la stabilisation. Enfin, dans le cadre de la plasticité, la méthode HHO permet d'éviter de faire appel à la loi de comportement non-linéaire aux points de quadrature sur les faces du maillage [2], ce qui constitue un avantage important par rapport à l'approche dG.

Comme pour les méthodes dG, les méthodes hybrides discontinues reposent sur une formulation discontinue qui conduit naturellement à une matrice de masse bloc-diagonale, permettant l'utilisation efficace d'intégrateurs explicites en temps. En outre, dans le cas d'intégrateurs en temps implicites, les méthodes hybrides discontinues permettent de limiter le coût de calcul élevé des méthodes dG grâce à la procédure de condensation statique mentionnée ci-dessus qui permet l'élimination locale des inconnues de cellule, en ne conservant que les inconnues de face. Par conséquent, les méthodes hybrides discontinues offrent une plus grande flexibilité dans le choix des intégrateurs temporels, tout en maintenant un bon compromis entre précision et efficacité. En outre, la possibilité de monter facilement en ordre, combinée à un taux de convergence légèrement plus élevé que pour dG, permet de limiter les coûts de calcul liés à l'usage de méthodes d'ordre faible, qui nécessitent souvent des raffinements excessifs du maillage pour atteindre une précision comparable.

Les liens entre les méthodes HHO, HDG, WG et ncVEM ont été établis dans [53, 50, 66] et nous les détaillerons ci-dessous. Les travaux de cette thèse portent spécifiquement sur les méthodes HHO, mais en raison de ces liens étroits, ils s'étendent naturellement aux autres méthodes de la classe des méthodes hybrides discontinues.

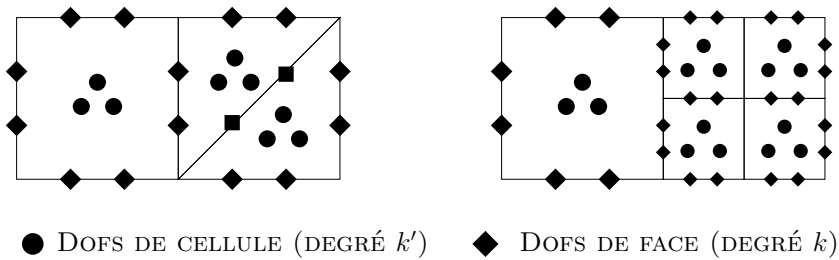


Fig. I.7: Inconnues discrètes HHO d'ordre $k' = k = 1$ sur un maillage conforme (gauche) et non-conforme (droite).

Remarque I.2.1 (Problème fréquentiel). *La propagation d'ondes elasto-acoustiques a également été abordée dans le domaine fréquentiel. En particulier, des formulations mixtes*

ont été proposées dans [85], en utilisant une formulation mixte-duale dans la région solide et une formulation primale standard dans le fluide.

I.3 Introduction aux méthodes Hybrid High-Order (HHO)

Dans cette section, nous présentons la discréétisation HHO d'un problème elliptique puis nous présentons les liens avec les autres méthodes hybrides discontinues. La discréétisation HHO de l'équation des ondes sera abordée au chapitre suivant.

Soit Ω un domaine polyédrique de \mathbb{R}^d , avec $d \in \{2, 3\}$ (ouvert, borné, connexe, à frontière lipschitzienne). Notre objectif est d'approcher la solution $p \in H_0^1(\Omega)$ du problème elliptique suivant :

$$-\nabla \cdot (\kappa \nabla p) = f \quad \text{dans } \Omega, \tag{I.8a}$$

$$p = 0 \quad \text{sur } \partial\Omega, \tag{I.8b}$$

avec $f \in L^2(\Omega)$ et κ un coefficient de diffusion scalaire. Pour simplifier, nous considérons une condition de Dirichlet homogène sur $\partial\Omega$. La formulation faible s'écrit

$$\text{Trouver } p \in H_0^1(\Omega), \quad a(p, q) = \ell(q) \quad \forall q \in H_0^1(\Omega). \tag{I.9}$$

La forme bilinéaire symétrique a et la forme linéaire ℓ sont définies par

$$\begin{cases} a(p, q) := (\nabla p, \nabla q)_{L^2(\kappa; \Omega)}, \\ \ell(q) := (f, q)_{L^2(\Omega)}. \end{cases} \tag{I.10a}$$

$$\begin{cases} a(p, q) := (\nabla p, \nabla q)_{L^2(\kappa; \Omega)}, \\ \ell(q) := (f, q)_{L^2(\Omega)}. \end{cases} \tag{I.10b}$$

Les hypothèses du lemme de Lax-Milgram sont vérifiées, ce qui assure l'existence et l'unicité de la solution de la formulation faible (I.9).

I.3.1 Discréétisation d'un problème elliptique avec HHO

Maillage. Soit \mathcal{T} un maillage polyédrique recouvrant exactement Ω . Les faces du maillage sont regroupées dans l'ensemble \mathcal{F} , que l'on scinde en $\mathcal{F} := \mathcal{F}^\circ \cup \mathcal{F}^\partial$, où \mathcal{F}° contient toutes les interfaces internes du maillage, et \mathcal{F}^∂ contient les faces du maillage situées sur la frontière $\partial\Omega$. Par la suite, nous utiliserons également la notation $\mathcal{M} := (\mathcal{T}, \mathcal{F})$. Une cellule générique du maillage est notée $T \in \mathcal{T}$, son diamètre h_T , son vecteur normal unitaire sortant \mathbf{n}_T , et les faces constituant la frontière de T sont regroupées dans le sous-ensemble $\mathcal{F}_{\partial T} \subset \mathcal{F}$. Enfin, par souci de simplicité, nous supposons que le coefficient de diffusion κ est constant par morceaux. Il est donc constant dans chaque cellule $T \in \mathcal{T}$ et sa valeur y est notée κ_T .

Espaces d'approximations. Soit $k \geq 0$ le degré polynomial. Les inconnues HHO sont constituées d'un couple composé d'une composante cellule et d'une composante face. La composante cellule est un polynôme par morceaux de degré $k' \in \{k, k+1\}$, et la composante face est un polynôme par morceaux de degré k . On parle de discréétisation du même ordre si $k' = k$ et d'ordre différent si $k' = k+1$. On considère les espaces suivants :

$$\hat{P}^k(\mathcal{M}) := P^{k'}(\mathcal{T}) \times P^k(\mathcal{F}), \tag{I.11}$$

où $P^{k'}(\mathcal{T}) := \bigtimes_{T \in \mathcal{T}} P^{k'}(T)$ et $P^k(\mathcal{F}) := \bigtimes_{F \in \mathcal{F}} P^k(F)$. Les éléments de $\widehat{P}^k(\mathcal{M})$ sont notés $\hat{p}_{\mathcal{M}} := (p_{\mathcal{T}}, p_{\mathcal{F}}) \in \widehat{P}^k(\mathcal{M})$, où $p_{\mathcal{T}}$ constitue la composante cellule de $\hat{p}_{\mathcal{M}}$ et $p_{\mathcal{F}}$ sa composante face. Pour tout $T \in \mathcal{T}$, les composantes locales de $\hat{p}_{\mathcal{M}}$ forment la paire

$$\hat{p}_T := (p_T, p_{\partial T}) \in \widehat{P}_T^k := P^{k'}(T) \times P^k(\mathcal{F}_{\partial T}), \quad (\text{I.12})$$

où $p_{\partial T} := (p_F)_{F \in \mathcal{F}_{\partial T}}$ et $P^k(\mathcal{F}_{\partial T}) := \bigtimes_{F \in \mathcal{F}_{\partial T}} P^k(F)$. De plus, afin d'imposer la condition de Dirichlet homogène sur p , nous considérons le sous-espace

$$\widehat{P}_0^k(\mathcal{M}) := \left\{ \hat{p}_{\mathcal{M}} \in \widehat{P}^k(\mathcal{M}) \mid p_F = 0, \forall F \in \mathcal{F}^\theta \right\}. \quad (\text{I.13})$$

Ainsi, nous approchons la pression p par une inconnue HHO $\hat{p}_{\mathcal{M}} \in \widehat{P}_0^k(\mathcal{M})$.

Soit $\Pi_T^{k'}$ (resp. Π_F^k et $\Pi_{\partial T}^k$) la projection L^2 -orthogonale locale sur l'espace $P^{k'}(T)$ (resp. $P^k(F)$ et $P^k(\mathcal{F}_{\partial T})$). On note $\Pi_{\mathcal{T}}^{k'}$ (resp. $\Pi_{\mathcal{F}}^k$) la projection L^2 -orthogonale globale sur $P^{k'}(\mathcal{T})$ (resp. $P^k(\mathcal{F})$). On peut alors définir l'opérateur d'interpolation HHO $\hat{I}_{\mathcal{M}}^{\text{HHO}} : H_0^1(\Omega) \rightarrow \widehat{P}_0^k(\mathcal{M})$ tel que, pour tout $p \in H_0^1(\Omega)$,

$$\hat{I}_{\mathcal{M}}^{\text{HHO}}(p) := (\Pi_{\mathcal{T}}^{k'}(p), \Pi_{\mathcal{F}}^k(p|_{\mathcal{F}})) \in \widehat{P}_0^k(\mathcal{M}). \quad (\text{I.14})$$

On peut également définir son pendant local, $\hat{I}_T^{\text{HHO}} : H_0^1(T) \rightarrow \widehat{P}_T^k(T)$ tel que, pour tout $T \in \mathcal{T}$, tout $p \in H^1(T)$,

$$\hat{I}_T^{\text{HHO}}(p) := (\Pi_T^{k'}(p), \Pi_{\partial T}^k(p|_{\partial T})) \in \widehat{P}_T^k(T). \quad (\text{I.15})$$

Opérateurs de reconstruction. Pour tout $T \in \mathcal{T}$, nous définissons l'opérateur de reconstruction locale du gradient $\mathbf{g}_T : \widehat{P}_T^k \rightarrow \mathbf{P}^k(T)$ (on rappelle que la police en gras fait référence aux champs de vecteurs) tel que, pour tout $\hat{p}_T \in \widehat{P}_T^k$,

$$(\mathbf{g}_T(\hat{p}_T), \mathbf{r})_{\mathbf{L}^2(T)} = (\nabla p_T, \mathbf{r})_{\mathbf{L}^2(T)} - (p_T - p_{\partial T}, \mathbf{r} \cdot \mathbf{n}_T)_{L^2(\partial T)}, \quad \forall \mathbf{r} \in \mathbf{P}^k(T). \quad (\text{I.16})$$

Remarquons que $\mathbf{g}_T(\hat{p}_T)$ repose sur la formule d'intégration par parties et peut être évalué composante par composante en inversant la matrice de masse associée à une base de l'espace des polynômes scalaires $P^k(T)$. On définit l'opérateur global de reconstruction du gradient $\mathbf{g}_{\mathcal{T}} : \widehat{P}^k(\mathcal{M}) \rightarrow \mathbf{M}^k(\mathcal{T})$ par $\mathbf{g}_{\mathcal{T}}(\hat{p}_{\mathcal{M}})|_T := \mathbf{g}_T(\hat{p}_T)$ pour tout $T \in \mathcal{T}$ et tout $\hat{p}_{\mathcal{M}} \in \widehat{P}^k(\mathcal{M})$.

On peut également définir un opérateur de reconstruction du potentiel $R_T^{k+1} : \widehat{P}_T^k \rightarrow P_*^{k+1}(T)$ en résolvant, pour tout $\hat{p}_T \in \widehat{P}_T^k$, le problème de Neumann suivant :

$$(\nabla R_T^{k+1}(\hat{p}_T), \nabla q)_{\mathbf{L}^2(T)} = (\nabla p_T, \nabla q)_{\mathbf{L}^2(T)} + (p_{\partial T} - p_T, \nabla q \cdot \mathbf{n}_T)_{L^2(\partial T)}, \quad \forall q \in P_*^{k+1}(T), \quad (\text{I.17})$$

où $P_*^{k+1}(T) := \left\{ q \in P^{k+1}(T) \mid (q, 1)_T = 0 \right\}$. On impose en outre la condition de valeur moyenne $(R_T^{k+1}(\hat{p}_T), 1)_{L^2(T)} = (p_T, 1)_{L^2(T)}$. On notera que pour les problèmes non linéaires, il est préférable de considérer l'opérateur de reconstruction du gradient \mathbf{g}_T^k plutôt que ∇R_T^{k+1} , comme discuté dans [64, 1].

Remarque I.3.1 (Convergence des opérateurs de reconstruction). *Notons que l'on a les propriétés suivantes, pour tout $T \in \mathcal{T}$ et pour tout $p \in H^1(T)$,*

$$\mathbf{g}_T(\hat{I}_T^{\text{HHO}}(p)) = \Pi_T^k(\nabla p), \quad (\text{I.18a})$$

$$\nabla R_T^{k+1}(\hat{I}_T^{\text{HHO}}(p)) = \nabla \mathcal{E}_T^{k+1}(p), \quad (\text{I.18b})$$

où $\mathcal{E}_T^{k+1} : H^1(T) \rightarrow P^{k+1}(T)$ désigne la projection elliptique. Les opérateurs de reconstruction satisfont donc les propriétés d'approximation suivantes :

$$\|\nabla p - \mathbf{g}_T(\hat{I}_T^{\text{HHO}}(p))\|_{L^2(T)} \lesssim Ch^{k+1}|p|_{H^{k+2}(T)}, \quad (\text{I.19a})$$

$$\|\nabla p - \nabla R_T^{k+1}(\hat{I}_T^{\text{HHO}}(p))\|_{L^2(T)} \lesssim Ch^{k+1}|p|_{H^{k+2}(T)}, \quad (\text{I.19b})$$

pour tout $p \in H^{k+2}(T)$.

Opérateur de stabilisation. Définissons l'opérateur de stabilisation local $S_{\partial T} : \hat{P}_T^k \rightarrow P^k(\mathcal{F}_{\partial T})$ tel que, pour tout $\hat{p}_T \in \hat{P}_T^k$, $S_{\partial T}(\hat{p}_T) := \tilde{S}_{\partial T}(\delta_{\partial T}(\hat{p}_T))$ avec $\delta_{\partial T}(\hat{p}_T) := p_T|_{\partial T} - p_{\partial T}$ où pour tout $\delta \in P^k(\mathcal{F}_{\partial T})$,

$$\tilde{S}_{\delta}(\delta) := \begin{cases} \Pi_{\partial T}^k(\delta + (I - \Pi_T^k)R_T^{k+1}(0, \delta)|_{\partial T}), & \text{si } k' = k, \\ \Pi_{\partial T}^k(\delta), & \text{si } k' = k + 1. \end{cases} \quad (\text{I.20})$$

La forme bilinéaire de stabilisation globale $s_{\mathcal{M}}$ sur $\hat{P}^k(\mathcal{M}) \times \hat{P}^k(\mathcal{M})$ est définie par

$$s_{\mathcal{M}}(\hat{p}_{\mathcal{M}}, \hat{q}_{\mathcal{M}}) := \sum_{T \in \mathcal{T}} \tau_T(S_{\partial T}(\hat{p}_T), S_{\partial T}(\hat{q}_T))_{L^2(\partial T)}, \quad \forall \hat{p}_{\mathcal{M}}, \hat{q}_{\mathcal{M}} \in \hat{P}^k(\mathcal{M}), \quad (\text{I.21})$$

où, pour tout $T \in \mathcal{T}$, le paramètre de stabilisation $\tau_T > 0$ est pris égal à

$$\tau_T := \kappa_T \tilde{h}_T^{-\alpha} \quad (\text{I.22})$$

avec $\alpha \in \{0, 1\}$, $\tilde{h}_T := \frac{h_T}{\ell_{\Omega}}$, (la normalisation par $\ell_{\Omega} := \text{diam}(\Omega)$ est introduite pour des raisons de cohérence dimensionnelle). Le paramètre α est important car il permet de choisir entre une stabilisation $\mathcal{O}(1)$ pour $\alpha = 0$ et une stabilisation $\mathcal{O}(\frac{1}{h})$ pour $\alpha = 1$. Les deux choix s'avèreront utiles dans cette thèse pour l'équation des ondes. Dans le cas des problèmes elliptiques, on considère uniquement le choix $\alpha = 1$.

Remarque I.3.2. La stabilisation dans le cas d'ordre différent est celle introduite par Lehrenfeld–Schöberl dans le cadre des méthodes HDG [108].

Problème global. Le problème discrétisé en espace s'écrit comme suit: Trouver $\hat{p}_{\mathcal{M}} \in \hat{P}_0^k(\mathcal{M})$ tel que pour tout $\hat{q}_{\mathcal{M}} \in \hat{P}_0^k(\mathcal{M})$,

$$a_{\mathcal{M}}(\hat{p}_{\mathcal{M}}, \hat{q}_{\mathcal{M}}) = (f, q_{\mathcal{T}})_{L^2(\Omega)}, \quad (\text{I.23})$$

avec

$$\begin{aligned} a_{\mathcal{M}}(\hat{p}_{\mathcal{M}}, \hat{q}_{\mathcal{M}}) &:= (\mathbf{g}_{\mathcal{T}}(\hat{p}_{\mathcal{M}}), \mathbf{g}_{\mathcal{T}}(\hat{q}_{\mathcal{M}}))_{L^2(\kappa; \Omega)} + s_{\mathcal{M}}(\hat{p}_{\mathcal{M}}, \hat{q}_{\mathcal{M}}), \\ &:= \sum_{T \in \mathcal{T}} \left\{ (\mathbf{g}_T(\hat{p}_T), \mathbf{g}_T(\hat{q}_T))_{L^2(\kappa; T)} + \tau_T(S_{\partial T}(\hat{p}_T), S_{\partial T}(\hat{q}_T))_{L^2(\partial T)} \right\}. \end{aligned} \quad (\text{I.24})$$

On montre que le problème (I.23) est bien posé [69].

Réalisation algébrique. Définissons les dimensions des espaces globaux $P^{k'}(\mathcal{T})$ et $P^k(\mathcal{F}^\circ)$ comme

$$N_{\mathcal{T}}^{k'} := \dim(P^{k'}(\mathcal{T})), \quad N_{\mathcal{F}}^k := \dim(P^k(\mathcal{F}^\circ)), \quad (\text{I.25})$$

et notons leur bases polynomiales respectives comme

$$\{\varphi_i\}_{1 \leq i \leq N_{\mathcal{T}}^{k'}}, \quad \{\psi_i\}_{1 \leq i \leq N_{\mathcal{F}}^k}. \quad (\text{I.26})$$

Soit $(P_{\mathcal{T}}, P_{\mathcal{F}}) \in \mathbb{R}^{N_{\mathcal{T}}^{k'}} \times \mathbb{R}^{N_{\mathcal{F}}^k}$ les vecteurs composantes de $\hat{p}_{\mathcal{M}} = (p_{\mathcal{T}}, p_{\mathcal{F}}) \in \widehat{P}_0^k(\mathcal{M})$. Soit \mathcal{K} la matrice de rigidité globale (symétrique, définie positive), notons $\mathcal{K}_{\mathcal{T}\mathcal{T}}$, $\mathcal{K}_{\mathcal{T}\mathcal{F}}$, $\mathcal{K}_{\mathcal{F}\mathcal{F}}$ les différents blocs de cette matrice. La réalisation algébrique de (I.23) peut être formulée de la manière suivante :

$$\begin{bmatrix} \mathcal{K}_{\mathcal{T}\mathcal{T}} & \mathcal{K}_{\mathcal{T}\mathcal{F}} \\ \mathcal{K}_{\mathcal{T}\mathcal{F}}^\dagger & \mathcal{K}_{\mathcal{F}\mathcal{F}} \end{bmatrix} \begin{bmatrix} P_{\mathcal{T}} \\ P_{\mathcal{F}} \end{bmatrix} = \begin{bmatrix} F_{\mathcal{T}} \\ 0 \end{bmatrix}, \quad (\text{I.27})$$

où $F_{\mathcal{T}}$ a pour composantes $\ell(\varphi_i)$ pour tout $i \in \{1, \dots, N_{\mathcal{T}}^{k'}\}$.

Analyse d'erreur. Nous rappelons maintenant les principaux résultats relatifs à l'analyse d'erreur [69].

Théorème I.3.1 (Estimation d'erreur en norme d'énergie). *Soit $p \in H_0^1(\Omega)$ et $\hat{p}_{\mathcal{M}} \in \widehat{P}_0^k(\mathcal{M})$ les solutions uniques de (I.9) et (I.23) respectivement. Il existe une constante $C > 0$, dépendant de la régularité du maillage et du degré polynomial mais indépendante de h , telle que, en supposant la régularité supplémentaire $p \in H^{k+2}(\Omega)$,*

$$\|\nabla p - g_{\mathcal{T}}(\hat{p}_{\mathcal{M}})\|_{L^2(\Omega)} \leq Ch^{k+1}|p|_{H^{k+2}(\Omega)}. \quad (\text{I.28})$$

Nous avons également une estimation d'erreur L^2 optimale pour le potentiel sous hypothèse de régularité elliptique. Pour simplifier, nous supposons que le coefficient de diffusion κ est constant dans Ω . Dans ces conditions, nous supposons qu'il existe une constante $C_{\text{ell}} > 0$ et un indice de régularité $s \in (1/2, 1]$ ne dépendant que de Ω tels que, pour tout $g \in L^2(\Omega)$, la solution unique $\zeta \in H_0^1(\Omega)$ du problème elliptique adjoint telle que $a(\zeta, q) = (g, q)_{L^2(\Omega)}$ pour tout $q \in H_0^1(\Omega)$ satisfait l'estimation de régularité

$$\|\zeta\|_{H^{1+s}(\Omega)} \leq C_{\text{ell}}\|g\|_{L^2(\Omega)}. \quad (\text{I.29})$$

Théorème I.3.2 (Estimation d'erreur L^2 pour le potentiel). *Outre les hypothèses du théorème I.3.1, supposons que le problème (I.8) vérifie la propriété de régularité elliptique ci-dessus et que $f \in H^1(\Omega)$ dans le cas $k = 0$. Il existe une constante $C > 0$, dépendant de la régularité de Ω et du degré polynomial mais indépendante de h , telle que, pour $k \geq 1$,*

$$\|\Pi_{\mathcal{T}}^{k'}(p) - p_{\mathcal{T}}\|_{L^2(\Omega)} \leq Ch^{k+1+s}|p|_{H^{k+2}(\Omega)}, \quad (\text{I.30a})$$

et pour $s = 1$ et $k' = k = 0$,

$$\|\Pi_{\mathcal{T}}^{k'}(p) - p_{\mathcal{T}}\|_{L^2(\Omega)} \leq Ch^2(|p|_{H^2(\Omega)} + |f|_{H^1(\Omega)}). \quad (\text{I.30b})$$

Le cas optimal dans (I.30a) est obtenu lorsque $s = 1$ (régularité elliptique maximale), auquel cas la borne supérieure dans (I.30a) décroît en h^{k+2} . Lorsque $k' = k+1$, une simple inégalité triangulaire conduit alors à une estimation d'ordre $k+2$ sur $\|p - p_T\|_{L^2(\Omega)}$. En revanche, lorsque $k' = k$ l'estimation (I.30a) s'interprète comme un résultat de superconvergence.

I.3.2 Liens avec les autres méthodes hybrides discontinues

Comme évoqué dans la section précédente, les méthodes HDG, WG et ncVEM présentent des liens étroits avec HHO [53, 66, 50].

Liens avec les méthodes HDG. La principale différence entre les méthodes HHO et HDG est que dans HHO, on approche la paire d'inconnues $(p, p|_{\mathcal{F}})$ et que dans HDG, on approche le triplet d'inconnues $(-\nabla p, p, p|_{\mathcal{F}})$. Ainsi, dans le contexte HDG, on considère explicitement la variable duale $\boldsymbol{\sigma} := -\nabla p$ (souvent appelée flux). Une discréttisation HDG se formule à l'aide des espaces locaux \mathbf{S}_T, V_T et V_F pour tout $T \in \mathcal{T}$ et tout $F \in \mathcal{F}$. En définissant les espaces globaux

$$\mathbf{S}_{\mathcal{T}} := \bigtimes_{T \in \mathcal{T}} \mathbf{S}_T, \quad V_{\mathcal{T}} := \bigtimes_{T \in \mathcal{T}} V_T, \quad V_{\mathcal{F}} := \bigtimes_{F \in \mathcal{F}} V_F \quad (\text{I.31})$$

ainsi que $V_{\mathcal{F}0} := \left\{ \mu_F := (\mu_F)_{F \in \mathcal{F}} \in V_{\mathcal{F}} \mid \mu_F = 0, \forall F \in \mathcal{F}^\partial \right\}$, la méthode HDG consiste à chercher le triplet $(\boldsymbol{\sigma}_T, p_T, \lambda_T) \in \mathbf{S}_T \times V_T \times V_{\mathcal{F}0}$ tel que, pour tout $(\boldsymbol{\tau}_T, w_T, \mu_T) \in \mathbf{S}_T \times V_T \times V_F$, tout $T \in \mathcal{T}$ et tout $F \in \mathcal{F}^\circ$, on ait

$$(\boldsymbol{\sigma}_T, \boldsymbol{\tau}_T)_{L^2(T)} - (p_T, \nabla \cdot \boldsymbol{\tau}_T)_{L^2(T)} + (\lambda_T, \boldsymbol{\tau}_T \cdot \mathbf{n}_T)_{L^2(\partial T)} = 0, \quad (\text{I.32a})$$

$$-(\boldsymbol{\sigma}_T, \nabla w_T)_{L^2(T)} + (\phi_{\partial T} \cdot \mathbf{n}_T, w_T)_{L^2(\partial T)} = (f, w_T)_{L^2(T)}, \quad (\text{I.32b})$$

$$([\![\phi_{\partial T}]\!] \cdot \mathbf{n}_F, \mu_F)_{L^2(F)} = 0, \quad (\text{I.32c})$$

avec $\lambda_{\partial T} := (\lambda_F)_{F \in \mathcal{F}_{\partial T}}$, le flux numérique HDG $\phi_{\partial T} := (\phi_{\partial T})_{T \in \mathcal{T}}$ défini par

$$\phi_{\partial T} := \boldsymbol{\sigma}_T|_{\partial T} + s_{\partial T}^{\text{HDG}}(p_T|_{\partial T} - \lambda_{\partial T})\mathbf{n}_T, \quad \forall T \in \mathcal{T}, \quad (\text{I.33})$$

avec un opérateur de stabilisation $s_{\partial T}^{\text{HDG}}$ et le saut normal à travers l'interface $F = \partial T_- \cap \partial T_+ \in \mathcal{F}^\circ$ défini par

$$[\![\phi_{\partial T}]\!] \cdot \mathbf{n}_F := (\phi_{\partial T_-}|_F - \phi_{\partial T_+}|_F) \cdot \mathbf{n}_F = (\phi_{\partial T_-} \cdot \mathbf{n}_{T_-})|_F + (\phi_{\partial T_+} \cdot \mathbf{n}_{T_+})|_F, \quad (\text{I.34})$$

où \mathbf{n}_F pointe conventionnellement de T_- vers T_+ . L'équation (I.32a) est la contrepartie discrète de $\boldsymbol{\sigma} = -\nabla p$, l'équation (I.32b) celle de $\nabla \cdot \boldsymbol{\sigma} = f$, et l'équation (I.32c) impose faiblement la continuité de la composante normale du flux numérique à travers les interfaces du maillage.

En conclusion, les méthodes HDG sont obtenues en choisissant les espaces locaux \mathbf{S}_T, V_T, V_F et l'opérateur de stabilisation $s_{\partial T}^{\text{HDG}}$. Comme établi dans [53], ce paradigme s'applique à la méthode HHO.

Proposition I.3.1 (Équivalence entre HHO et HDG). *La méthode HHO peut être réécrite comme une méthode HDG en posant*

$$\mathbf{S}_T := \mathbf{P}^k(T), \quad V_T := P^k(T), \quad V_F := P^k(F), \quad (\text{I.35})$$

et l'opérateur de stabilisation HDG

$$s_{\partial T}^{\text{HDG}}(v) := h_T^{-1}(\tilde{S}_{\partial T}^* \circ \tilde{S}_{\partial T})(v), \quad \forall v \in P^k(\mathcal{F}_{\partial T}) := \bigtimes_{F \in \mathcal{F}_{\partial T}} V_F. \quad (\text{I.36})$$

La variable duale HDG est donnée par $\boldsymbol{\sigma}_T = -\mathbf{g}_T(\hat{p}_T)$ pour tout $T \in \mathcal{T}$ et la variable de trace est $\lambda_F = p_F$ pour tout $F \in \mathcal{F}$.

Liens avec les méthodes WG. La méthode Weak Galerkin, introduite dans [142, 141], peut également être interprétée comme une instance particulière des méthodes HDG, comme le démontre [52, Section 6.6]. Les liens avec la méthode HHO sont particulièrement immédiats, puisque les deux méthodes HHO et WG sont formulées à l'aide d'une paire approchant $(p, p|_{\mathcal{F}})$. La seule différence est dans la terminologie : le "gradient faible" dans WG n'est rien d'autre que le gradient reconstruit dans HHO. On notera également que la stabilisation de même ordre dans HHO n'a jamais été considérée dans les méthodes WG, ce qui conduit à une perte d'optimalité (d'un ordre) pour ces dernières. En outre, dans le cas d'ordre différent, l'utilisation de la projection pour définir l'opérateur de stabilisation a souvent été omise dans les méthodes WG, ce qui conduit, à nouveau, à une perte d'optimalité (d'un ordre).

Liens avec les méthodes ncVEM. L'objectif de ce paragraphe est de montrer que la méthode HHO peut s'écrire dans le formalisme ncVEM, en suivant les idées présentées dans [53, 66, 50], voir également [49, 45]. Pour une étude plus systématique, on pourra consulter [109].

Soit $k \geq 0$ le degré polynomial. Considérons l'espace fonctionnel de dimension finie,

$$\mathcal{P}_T^k := \left\{ p \in H^1(T) \mid \Delta p \in P^k(T), \mathbf{n}_T \cdot \nabla p|_{\partial T} \in P^k(F_{\partial T}) \right\}. \quad (\text{I.37})$$

On observe que $P^{k+1}(T) \subset \mathcal{P}_T^k$, mais que \mathcal{P}_T^k contient également d'autres fonctions "virtuelles", i.e. inaccessibles au calcul direct.

Définissons l'espace global de type Crouzeix–Raviart d'ordre élevé

$$\mathcal{P}_{\mathcal{T}}^k := \left\{ p_{\mathcal{T}} \in L^2(\Omega) \mid p_{\mathcal{T}}|_T \in \mathcal{P}_T^k \ \forall T \in \mathcal{T}, \Pi_F^k(\llbracket p_{\mathcal{T}} \rrbracket_F) = 0 \ \forall F \in \mathcal{F}^\circ \right\}, \quad (\text{I.38})$$

où $\llbracket p_{\mathcal{T}} \rrbracket_F$ désigne le saut de $p_{\mathcal{T}}$ à travers l'interface F , et \mathcal{F}° est l'ensemble des faces intérieures, de sorte à avoir une réponse univaluée sur chaque face. On pose également

$$\mathcal{P}_{\mathcal{T}0}^k := \left\{ p_{\mathcal{T}} \in \mathcal{P}_{\mathcal{T}}^k \mid \Pi_F^k(p_{\mathcal{T}}|_F) = 0 \ \forall F \in \mathcal{F}^\partial \right\}. \quad (\text{I.39})$$

Une formulation naturelle pour résoudre le problème (I.8) consiste à chercher

$$p_{\mathcal{T}} \in \mathcal{P}_{\mathcal{T}0}^k, \quad a^{\text{ncVEM}}(p_{\mathcal{T}}, q_{\mathcal{T}}) = \ell(\Pi_{\mathcal{T}}^k(q_{\mathcal{T}})), \quad \forall q_{\mathcal{T}} \in \mathcal{P}_{\mathcal{T}0}^k, \quad (\text{I.40})$$

avec la forme bilinéaire $a^{\text{ncVEM}} : \mathcal{P}_{\mathcal{T}0}^k \times \mathcal{P}_{\mathcal{T}0}^k \rightarrow \mathbb{R}$ définie par

$$a^{\text{ncVEM}}(p_{\mathcal{T}}, q_{\mathcal{T}}) := (\nabla_{\mathcal{T}} p_{\mathcal{T}}, \nabla_{\mathcal{T}} q_{\mathcal{T}})_{L^2(\Omega)}, \quad (\text{I.41})$$

où $\nabla_{\mathcal{T}}$ est l'opérateur gradient brisé.

Pour tout $T \in \mathcal{T}$, nous définissons l'opérateur de reconstruction (virtuelle) $\mathcal{R}_T^{\text{ncVEM}} : \hat{\mathcal{P}}_T^k \rightarrow \mathcal{P}_T^k$ tel que, pour tout $\hat{p}_T \in \hat{\mathcal{P}}_T^k$, la fonction $\mathcal{R}_T^{\text{ncVEM}}(\hat{p}_T) \in \mathcal{P}_T^k$ est définie de manière unique en résolvant le problème de Neumann suivant :

$$(\nabla \mathcal{R}_T^{\text{ncVEM}}(\hat{p}_T), \nabla q)_{L^2(T)} = -(p_T, \Delta q)_{L^2(T)} + (p_{\partial T}, \mathbf{n}_T \cdot \nabla q)_{L^2(\partial T)}, \quad (\text{I.42a})$$

$$(\mathcal{R}_T^{\text{ncVEM}}(\hat{p}_T), 1)_{L^2(T)} = (p_T, 1)_{L^2(T)}. \quad (\text{I.42b})$$

où la relation (I.42a) est satisfaite pour tout $q \in \mathcal{P}_T^k$. Le lien entre les espaces HHO et ncVEM est établi par le diagramme suivant :

$$\begin{array}{ccc} \mathcal{P}_T^k & \xrightleftharpoons[\mathcal{R}_T^{\text{ncVEM}}]{\hat{I}_T^{\text{HHO}}} & \hat{\mathcal{P}}_T^k \end{array} \quad (\text{I.43})$$

avec \hat{I}_T^{HHO} l'opérateur de projection usuel HHO défini en (I.15), la composition des deux opérateurs donnant l'identité.

En utilisant l'opérateur de reconstruction ci-dessus, une reformulation équivalente de (I.40) consiste à chercher

$$\hat{p}_{\mathcal{M}} \in \hat{\mathcal{P}}_0^k(\mathcal{M}), \quad \hat{a}^{\text{ncVEM}}(\hat{p}_{\mathcal{M}}, \hat{q}_{\mathcal{M}}) = \ell(q_{\mathcal{T}}) \quad \forall \hat{q}_{\mathcal{M}} \in \hat{\mathcal{P}}_0^k(\mathcal{M}), \quad (\text{I.44})$$

avec

$$\hat{a}^{\text{ncVEM}}(\hat{p}_{\mathcal{M}}, \hat{q}_{\mathcal{M}}) := (\nabla_{\mathcal{T}} \mathcal{R}_T^{\text{ncVEM}}(\hat{p}_{\mathcal{M}}), \nabla_{\mathcal{T}} \mathcal{R}_T^{\text{ncVEM}}(\hat{q}_{\mathcal{M}}))_{L^2(\Omega)}, \quad (\text{I.45})$$

et $\mathcal{R}_T^{\text{ncVEM}}(\hat{p}_{\mathcal{M}})|_T := \mathcal{R}_T^{\text{ncVEM}}(\hat{p}_T)$ pour tout $T \in \mathcal{T}$.

Pour faire le lien entre les deux méthodes, on remarque tout d'abord qu'une formulation équivalente de la méthode HHO consiste à chercher

$$p_{\mathcal{T}} \in \mathcal{P}_{\mathcal{T}0}^k, \quad a^{\text{HHO}}(p_{\mathcal{T}}, q_{\mathcal{T}}) = \ell(q_{\mathcal{T}}) \quad \forall q_{\mathcal{T}} \in \mathcal{P}_{\mathcal{T}0}^k, \quad (\text{I.46})$$

où la forme bilinéaire $a^{\text{HHO}} : \mathcal{P}_{\mathcal{T}0}^k \times \mathcal{P}_{\mathcal{T}0}^k \rightarrow \mathbb{R}$ est définie par

$$a^{\text{HHO}}(p_{\mathcal{T}}, q_{\mathcal{T}}) := (\nabla R_{\mathcal{T}}^{k+1}(p_{\mathcal{T}}), \nabla R_{\mathcal{T}}^{k+1}(q_{\mathcal{T}}))_{L^2(\Omega)} + s_{\mathcal{M}}(\hat{I}_{\mathcal{M}}^{\text{HHO}}(p_{\mathcal{T}}), \hat{I}_{\mathcal{M}}^{\text{HHO}}(q_{\mathcal{T}})). \quad (\text{I.47})$$

La relation de Pythagore donne,

$$\begin{aligned} & (\nabla_{\mathcal{T}} \mathcal{R}_T^{\text{ncVEM}}(\hat{p}_{\mathcal{M}}), \nabla_{\mathcal{T}} \mathcal{R}_T^{\text{ncVEM}}(\hat{q}_{\mathcal{M}}))_{L^2(\Omega)} \\ &= (\Pi_{\nabla P^{k+1}} \mathcal{R}_T^{\text{ncVEM}}(\hat{p}_{\mathcal{M}}), \Pi_{\nabla P^{k+1}} \mathcal{R}_T^{\text{ncVEM}}(\hat{q}_{\mathcal{M}}))_{L^2(\Omega)} \\ & \quad + ((\mathbf{I} - \Pi_{\nabla P^{k+1}})(\mathcal{R}_T^{\text{ncVEM}}(\hat{p}_{\mathcal{M}})), (\mathbf{I} - \Pi_{\nabla P^{k+1}})(\mathcal{R}_T^{\text{ncVEM}}(\hat{q}_{\mathcal{M}})))_{L^2(\Omega)}, \end{aligned} \quad (\text{I.48})$$

où $\Pi_{\nabla_{\mathcal{T}} P^{k+1}}$ désigne la projection L^2 -orthogonale sur $\nabla P^{k+1}(\mathcal{T})$. En observant que

$$\nabla R_{\mathcal{T}}^{k+1}(\hat{p}_{\mathcal{M}}) = \Pi_{\nabla P^{k+1}} \mathcal{R}_T^{\text{ncVEM}}(\hat{p}_{\mathcal{M}}), \quad (\text{I.49})$$

le lien entre les méthodes HHO et ncVEM est assuré dès lors que

$$s_{\mathcal{M}}(\hat{p}_{\mathcal{M}}, \hat{p}_{\mathcal{M}}) \approx ((I - \Pi_{\nabla P^{k+1}})(\mathcal{R}_{\mathcal{T}}^{\text{ncVEM}}(\hat{p}_{\mathcal{M}})), (I - \Pi_{\nabla P^{k+1}})(\mathcal{R}_{\mathcal{T}}^{\text{ncVEM}}(\hat{p}_{\mathcal{M}})))_{L^2(\Omega)}. \quad (\text{I.50})$$

au sens des formes quadratiques semi-définies positives. Ainsi, le rôle de la stabilisation dans la méthode HHO peut être interprété comme un moyen de garantir que la méthode reste H^1 -coercive dans $\mathcal{P}_{\mathcal{T}0}^k$, dans l'esprit des idées développées dans le cadre de la méthode des éléments virtuels.

I.4 Introduction aux méthodes unfitted

Le maillage des domaines complexes représente un défi important dans la résolution des équations aux dérivées partielles. Il est bien établi que, pour les méthodes classiques d'éléments finis, une adéquation suffisante entre le maillage et la géométrie est nécessaire, sous peine de compromettre la précision des solutions obtenues. Cela est particulièrement crucial pour les méthodes d'ordre élevé. On a vu dans la section précédente que de nombreuses méthodes ont été développées dans le but de simplifier le processus de maillage en permettant un plus grand ensemble de formes géométriques pour les cellules de calcul. Par exemple, l'utilisation de méthodes hybrides discontinues possédant des dofs sur les faces mène à des propriétés avantageuses, comme discuté ci-dessus. Cependant, des difficultés subsistent lors de l'utilisation de méthodes hybrides non conformes en présence de frontières ou d'interfaces courbes, alors que le traitement des cellules avec faces courbes dans les méthodes dG est plus direct. Pour résoudre cette difficulté, une possibilité est d'enrichir (avec des fonctions non polynomiales) l'ensemble des inconnues sur les faces courbes, comme dans [146] pour HHO et dans [21] pour ncVEM. Une autre possibilité est de travailler avec des maillages dont les cellules ont des faces planes, mais de construire la représentation géométrique directement dans la discréttisation, de sorte que même si le maillage n'est pas adapté à l'interface (voir la Figure I.8), la précision de la solution n'est pas dégradée. On parle alors de méthode de discréttisation unfitted. Un problème crucial pour les méthodes unfitted est la gestion des instabilités qui surviennent lorsque l'interface coupe une cellule en produisant une sous-cellule de très petite taille ou très aplatie. On parle de mauvaise coupe. Notre intérêt à poursuivre le développement des méthodes unfitted HHO est motivé par l'objectif de les appliquer à la propagation d'ondes élasto-acoustiques.

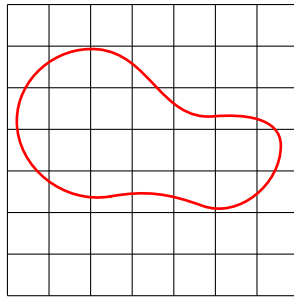


Fig. I.8: Exemple de maillage non-adapté à l'interface.

I.4.1 État de l'art des méthodes unfitted

Dans cette section, nous nous intéressons à l'état de l'art des méthodes unfitted. Dans ce contexte, le principal défi est de parvenir à traiter les mauvaises coupes.

Méthodes continues. Les méthodes unfitted FEM ont été introduites dans [16] en s'inspirant des méthodes de pénalisation [13, 17]. Une avancée majeure dans le développement des méthodes unfitted FEM a été accomplie dans [88] en utilisant la méthode de Nitsche, qui est une méthode de pénalisation consistante conçue à l'origine pour imposer les conditions de Dirichlet au sens faible dans le problème de Poisson [123]. Ces idées ont ensuite été généralisées pour inclure des problèmes de couplage plus complexes, y compris des EDP sur des surfaces et des couplages multiphysiques, conduisant au cadre cutFEM [30] dont un exemple de discrétisation est donné à la Figure I.9; voir également [106, 107]. Le principe général est de doubler les inconnues dans les cellules coupées et d'utiliser la méthode de Nitsche afin d'imposer faiblement les conditions de saut (éventuellement nul) à l'interface. Dans le cadre cutFEM, la gestion des instabilités dues aux mauvaises coupes est effectuée par l'ajout de certains termes stabilisés (dits de pénalisation fantôme) [28] pénalisant le saut des dérivées normales à travers les interfaces proches des cellules mal coupées.

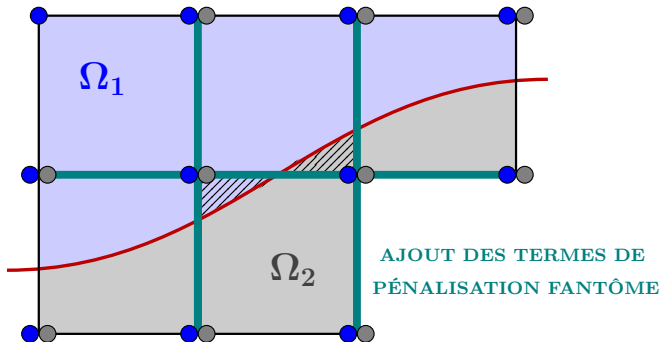


Fig. I.9: Doublement des inconnues Q_1 -FEM, sous-cellules mal coupées (rayés) et ensemble des faces impactées par la pénalisation fantôme.

Méthodes discontinues. Les méthodes unfitted ont également été considérées pour les méthodes dG [19, 97, 113, 91], HDG [56, 129] et HHO [35, 29]. Dans le cadre des méthodes discontinues, l'approche la plus naturelle pour traiter les mauvaises coupes consiste à agglomérer chaque cellule mal coupée avec une cellule voisine qui est bien coupée [97] (cette approche a été étendue aux méthodes FEM conformes dans [14]). Pour les méthodes hybrides discontinues, la combinaison de l'agglomération de cellules et d'un couplage faible local dérivé du cadre HHO a été appliquée avec succès à des problèmes elliptiques avec interface [29], aux écoulements de Stokes incompressibles [31] et à la propagation d'ondes acoustiques [33]. Cependant, il s'avère compliqué d'intégrer la procédure d'agglomération dans un code préexistant puisqu'elle nécessite de modifier une partie du maillage. Il est souvent souhaitable de conserver le maillage sous-jacent fixe et de modifier plutôt la structure algébrique des inconnues. Une technique qui répond à cet objectif

est celle d'extension polynomiale pour stabiliser la méthode. Des idées similaires ont été introduites dans des contextes différents en utilisant des multiplicateurs de Lagrange [89] puis la méthode de Nitsche pour les éléments finis [111, 38], les méthodes isogéométriques [27] et VEM [23, 22, 95].

I.4.2 Présentation de la méthode unfitted HHO

Dans cette section, nous présentons les principaux ingrédients de la méthode unfitted HHO tels que développés dans [29]. On considère une partition de Ω en deux sous-domaines disjoints $\bar{\Omega} = \bar{\Omega}_1 \cup \bar{\Omega}_2$, avec une interface $\Gamma := \partial\Omega_1 \cap \partial\Omega_2$, comme illustré à la Figure I.10. Pour tout $i \in \{1, 2\}$, on pose $\bar{i} := 3 - i$, de sorte que $\Omega \setminus \Omega^i = \Omega^{\bar{i}} \cup \Gamma$. Par souci de simplicité, on suppose que l'interface Γ est de classe C^2 et qu'elle ne touche pas la frontière de Ω . Le vecteur normal unitaire \mathbf{n}_Γ à Γ est orienté conventionnellement de Ω_1 vers Ω_2 . Pour une fonction suffisamment régulière v définie sur $\Omega_1 \cup \Omega_2$, en notant $v_i := v|_{\Omega_i}$ pour tout $i \in \{1, 2\}$, on définit son saut à travers Γ par :

$$[v]_\Gamma := v_1|_\Gamma - v_2|_\Gamma. \quad (\text{I.51})$$

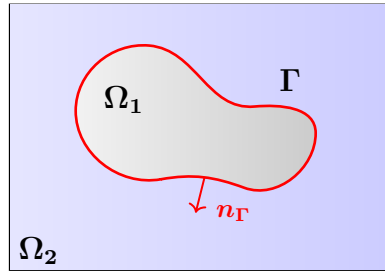


Fig. I.10: Problème modèle.

Problème modèle. Le problème modèle correspond à chercher la solution $p \in H^1(\Omega_1 \cup \Omega_2)$ du problème elliptique avec interface suivant :

$$-\nabla \cdot (\kappa \nabla p) = f \quad \text{dans } \Omega_1 \cup \Omega_2, \quad (\text{I.52a})$$

$$[p]_\Gamma = g_D \quad \text{sur } \Gamma, \quad (\text{I.52b})$$

$$[\kappa \nabla p]_\Gamma \cdot \mathbf{n}_\Gamma = g_N \quad \text{sur } \Gamma, \quad (\text{I.52c})$$

$$p = 0 \quad \text{sur } \partial\Omega, \quad (\text{I.52d})$$

avec $f \in L^2(\Omega)$, $g_D \in H^{\frac{1}{2}}(\Gamma)$ et $g_N \in L^2(\Gamma)$. Pour simplifier, on considère une condition de Dirichlet homogène sur $\partial\Omega$.

On suppose que le coefficient de diffusion κ est scalaire, et que $\kappa_i := \kappa|_{\Omega_i}$ est constant pour tout $i \in \{1, 2\}$. Pour fixer les idées, on suppose que $\kappa_1 \leq \kappa_2$. La méthode couvre le cas fortement contrasté où $\kappa_1 \ll \kappa_2$. Il est important de souligner que c'est la propriété $\kappa_1 \leq \kappa_2$ qui détermine l'orientation de \mathbf{n}_Γ , et non le fait que l'un d'eux sous-domaine touche la frontière. Ainsi, la numérotation dans la Figure I.10 est uniquement illustrative.

On remarque également que les hypothèses précédentes sur Γ et κ peuvent être levées au prix de considérations techniques supplémentaires.

La formulation faible s'écrit :

$$\text{Trouver } p \in V_{g_D}, \quad a(p, q) = \ell(q) \quad \forall q \in V_0, \quad (\text{I.53})$$

avec $V_{g_D} := \{v \in H^1(\Omega_1 \cup \Omega_2) \mid [v]_\Gamma = g_D \text{ sur } \Gamma, v = 0 \text{ sur } \partial\Omega\}$. On note que $V_0 = H_0^1(\Omega)$. La forme bilinéaire symétrique a et la forme linéaire ℓ sont définies par :

$$\left\{ \begin{array}{l} a(p, q) := \sum_{i \in \{1, 2\}} \kappa_i (\nabla p_i, \nabla q_i)_{L^2(\Omega_i)}, \\ \ell(q) := (f, q)_{L^2(\Omega)} + (g_N, q)_{L^2(\Gamma)}. \end{array} \right. \quad (\text{I.54a})$$

$$\left\{ \begin{array}{l} a(p, q) := \sum_{i \in \{1, 2\}} \kappa_i (\nabla p_i, \nabla q_i)_{L^2(\Omega_i)}, \\ \ell(q) := (f, q)_{L^2(\Omega)} + (g_N, q)_{L^2(\Gamma)}. \end{array} \right. \quad (\text{I.54b})$$

On notera que la condition de saut (I.52b) est imposée au sens fort dans (I.53), alors que (I.52c) est imposée au sens faible.

Maillage. Le maillage \mathcal{T} est typiquement composé de mailles de forme simple (bien que cela ne soit pas une hypothèse nécessaire). Un point important est que le maillage \mathcal{T} n'est pas adapté à l'interface Γ , de sorte que cette dernière peut couper arbitrairement une maille quelconque. Une première partition naturelle des mailles est celle entre les mailles coupées et non coupées,

$$\mathcal{T} := \mathcal{T}^{\text{uncut}} \cup \mathcal{T}^{\text{cut}}, \quad (\text{I.55})$$

où $\mathcal{T}^{\text{uncut}}$ désigne l'ensemble des mailles non coupées, \mathcal{T}^{cut} celui des mailles coupées. Pour toute maille $T \in \mathcal{T}$, on définit l'interface locale $T^\Gamma := T \cap \Gamma$ et, pour tout $i \in \{1, 2\}$, $T^i := T \cap \Omega^i$ (certains de ces ensembles peuvent être vides). Nous conservons la notation $\mathcal{M} := (\mathcal{T}, \mathcal{F})$.

Les faces du maillage sont regroupées dans l'ensemble \mathcal{F} , et l'on définit $\mathcal{F}^i := \{F \in \mathcal{F} \mid F \subset \Omega_i\}$ pour tout $i \in \{1, 2\}$. Pour chaque face $F \in \mathcal{F}^\Gamma := \mathcal{F} \setminus (\mathcal{F}^1 \cup \mathcal{F}^2)$ coupée par l'interface Γ , on définit ses deux sous-faces $F^i := F \cap \Omega_i$ pour tout $i \in \{1, 2\}$. Pour toute maille $T \in \mathcal{T}$, on note $\mathcal{F}_{\partial T}$ l'ensemble des faces composant sa frontière ∂T . De plus, pour toute maille coupée $T \in \mathcal{T}^{\text{cut}}$, en rappelant que $T^\Gamma = T \cap \Gamma$, la frontière $\partial(T^i)$ de la sous-maille T^i se décompose comme suit :

$$\partial(T^i) := (\partial T)^i \cup T^\Gamma, \quad (\partial T)^i := \partial T \cap (\overline{\Omega}_i \setminus \Gamma), \quad \forall i \in \{1, 2\}. \quad (\text{I.56})$$

Pour unifier les notations, pour toute maille non coupée $T \in \mathcal{T}^i$ avec $i := \iota(T) \in \{1, 2\}$ (et $\bar{i} := 3 - i$), on pose :

$$T^i := T, \quad T^{\bar{i}} := \emptyset, \quad (\partial T)^i := \partial T, \quad (\partial T)^{\bar{i}} := \emptyset, \quad T^\Gamma := \emptyset. \quad (\text{I.57})$$

Enfin, pour toute maille $T \in \mathcal{T}$ et tout $i \in \{1, 2\}$, l'ensemble (éventuellement vide) $\mathcal{F}_{(\partial T)^i} := \{F^i = F \cap \Omega_i \mid F \in \mathcal{F}_{\partial T}\}$ représente l'ensemble des (sous-)faces composant $(\partial T)^i$.

Degrés de liberté. Dans chaque cellule coupée $T \in \mathcal{T}^{\text{cut}}$, les inconnues HHO sont doublées (comme illustré dans la Figure I.11 à droite) de manière à disposer des inconnues usuelles dans chaque sous-cellule, sauf sur T^Γ où il n'y a pas d'inconnues. L'absence d'inconnues sur l'interface rend nécessaire l'utilisation d'inconnues de cellule de degré $k' = k + 1$ afin de préserver l'ordre de convergence optimal de la méthode unfitted HHO. Ainsi, les inconnues locales HHO dans chaque cellule coupée sont données par

$$\hat{p}_T := (\hat{p}_{T^1}, \hat{p}_{T^2}) := (p_{T^1}, p_{(\partial T)^1}, p_{T^2}, p_{(\partial T)^2}) \in \hat{P}_T^k := \hat{P}_{T^1}^k \times \hat{P}_{T^2}^k. \quad (\text{I.58})$$

avec $\hat{P}_{T^i}^k := P^{k+1}(T^i) \times P^k(\mathcal{F}_{(\partial T)^i})$ et $P^k(\mathcal{F}_{(\partial T)^i}) := \bigtimes_{F^i \in \mathcal{F}_{(\partial T)^i}} P^k(F^i)$, pour tout $i \in \{1, 2\}$. Pour unifier la notation entre cellules coupées et non coupées, on écrit \hat{p}_T dans le même format que dans (I.58) pour chaque cellule non coupée. Ainsi, $\hat{p}_T := (p_{T^1}, p_{(\partial T)^1}, 0, 0)$ pour tout $T \in \mathcal{T}^1$ et $\hat{p}_T := (0, 0, p_{T^2}, p_{(\partial T)^2})$ pour tout $T \in \mathcal{T}^2$.

L'espace global HHO sur le maillage unfitted est

$$\hat{P}^k(\mathcal{M}) := P^k(\mathcal{T}^1) \times P^k(\mathcal{F}^1) \times P^k(\mathcal{T}^2) \times P^k(\mathcal{F}^2), \quad (\text{I.59})$$

où

$$P^k(\mathcal{T}^i) := \bigtimes_{T \in \mathcal{T}} P^{k+1}(T^i), \quad P^k(\mathcal{F}^i) := \bigtimes_{F \in \mathcal{F}} P^k(F^i), \quad \forall i \in \{1, 2\}. \quad (\text{I.60})$$

Pour imposer la condition aux limites de Dirichlet homogène sur $\partial\Omega$, nous considérons le sous-espace

$$\hat{P}_0^k(\mathcal{M}) := P^k(\mathcal{T}^1) \times P_0^k(\mathcal{F}^1) \times P^k(\mathcal{T}^2) \times P_0^k(\mathcal{F}^2), \quad (\text{I.61})$$

où $P_0^k(\mathcal{F}^1)$ et $P_0^k(\mathcal{F}^2)$ sont les sous-espaces de $P^k(\mathcal{F}^1)$ et $P^k(\mathcal{F}^2)$, respectivement, où toutes les inconnues attachées aux faces situées sur $\partial\Omega$ sont nulles. Rappelons que seule l'un des deux sous-domaines Ω_i touche la frontière, de sorte que, en pratique, seul l'un des deux espaces de faces est modifié pour tenir compte des conditions de Dirichlet.

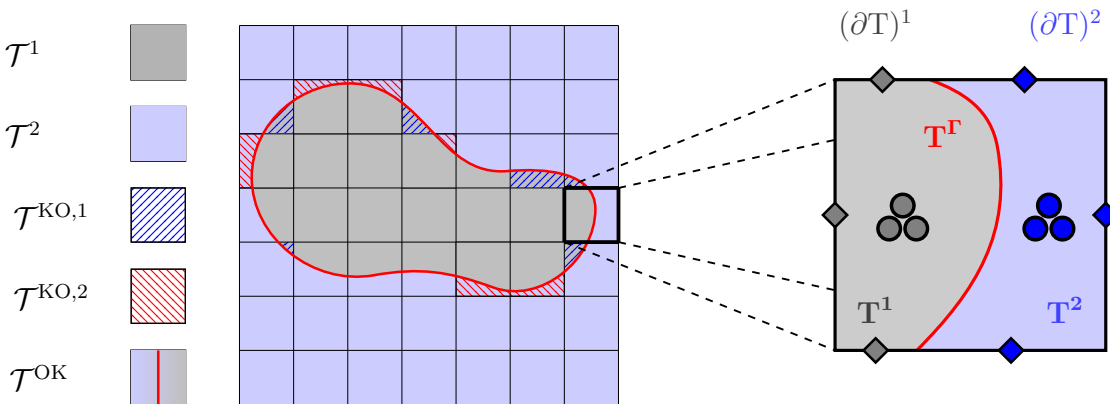


Fig. I.11: **Gauche.** Différent types de cellules dans le cas d'un maillage unfitted. **Droite.** Inconnues locales HHO dans une cellule coupée.

Opérateurs locaux. L'idée est de reconstruire deux gradients, un dans chaque sous-cellule. Ainsi, on définit une paire d'opérateurs locaux $\mathbf{g}_{T^i} : \hat{P}_T^k \rightarrow \mathbf{P}^k(T^i)$, $i \in \{1, 2\}$, tels que, pour tout $\hat{p}_T := (p_{T^1}, p_{(\partial T)^1}, p_{T^2}, p_{(\partial T)^2})$ et tout $\mathbf{q} \in \mathbf{P}^k(T^i)$,

$$(\mathbf{g}_{T^i}(\hat{p}_T), \mathbf{q})_{L^2(T^i)} := (\nabla p_{T^i}, \mathbf{q})_{L^2(T^i)} + (p_{(\partial T)^i} - p_{T^i}, \mathbf{q} \cdot \mathbf{n}_T)_{L^2((\partial T)^i)} - \delta_{i1}([\![p_T]\!]_\Gamma, \mathbf{q} \cdot \mathbf{n}_\Gamma)_{L^2(T^\Gamma)}, \quad (\text{I.62})$$

avec $[\![p_T]\!]_\Gamma := p_{T^1}|_{T^\Gamma} - p_{T^2}|_{T^\Gamma}$ et δ_{i1} désignant le delta de Kronecker. On pourra remarquer que les deux gradients sont reconstruits indépendamment, mais que \mathbf{g}_{T^1} dépend des composantes cellules des deux côtés de l'interface en raison du dernier terme dans (I.62). Ce terme n'est présent que lorsque $i = 1$ afin de garantir la robustesse du schéma dans le cas fortement contrasté où $\kappa_1 \ll \kappa_2$.

Nous considérons deux formes bilinéaires locales de stabilisation. La première est la stabilisation usuelle des méthodes HHO (ici la stabilisation de Lehrenfeld–Schöberl puisque $k' = k + 1$). Son rôle est d'imposer faiblement la consistance entre les inconnues cellules et faces sur les sous-faces des sous-cellules du maillage dans chaque sous-domaine. Pour tous $\hat{p}_M, \hat{q}_M \in \hat{P}_0^k(M)$, on définit

$$s_M^\circ(\hat{p}_M, \hat{q}_M) := \sum_{T \in \mathcal{T}} \sum_{i \in \{1, 2\}} \kappa_i h_T^{-1} (\Pi_{(\partial T)^i}^k(p_{T^i}) - p_{(\partial T)^i}, \Pi_{(\partial T)^i}^k(q_{T^i}) - q_{(\partial T)^i})_{L^2((\partial T)^i)}, \quad (\text{I.63})$$

où $\Pi_{(\partial T)^i}^k$ désigne le projecteur orthogonal L^2 sur $P^k(\mathcal{F}_{(\partial T)^i})$. La seconde forme bilinéaire de stabilisation a pour but de contrôler les sauts à travers l'interface Γ . Plus précisément, pour tous $\hat{p}_M, \hat{q}_M \in \hat{P}_0^k(M)$, on pose

$$s_M^\Gamma(\hat{p}_M, \hat{q}_M) := \sum_{T \in \mathcal{T}^{\text{cut}}} \kappa_1 h_T^{-1} ([\![p_T]\!], [\![q_T]\!])_{L^2(T^\Gamma)}. \quad (\text{I.64})$$

En regroupant les deux termes, on définit, pour tous $\hat{p}_M, \hat{q}_M \in \hat{P}_0^k(M)$,

$$s_M(\hat{p}_M, \hat{q}_M) := s_M^\circ(\hat{p}_M, \hat{q}_M) + s_M^\Gamma(\hat{p}_M, \hat{q}_M). \quad (\text{I.65})$$

Problème global. Le problème discret global s'écrit comme suit : Trouver $\hat{p}_M \in \hat{P}_0^k(M)$ tel que

$$a_M(\hat{p}_M, \hat{q}_M) = \ell_M(\hat{q}_M) \quad \forall \hat{q}_M \in \hat{P}_0^k(M), \quad (\text{I.66})$$

où la forme bilinéaire a_M est définie comme suit :

$$a_M(\hat{p}_M, \hat{q}_M) := b_M(\hat{v}_h, \hat{q}_M) + s_M(\hat{p}_M, \hat{q}_M), \quad (\text{I.67})$$

avec

$$b_M(\hat{p}_M, \hat{q}_M) := \sum_{T \in \mathcal{T}} \sum_{i \in \{1, 2\}} \kappa_i (\mathbf{g}_{T^i}(\hat{p}_T), \mathbf{g}_{T^i}(\hat{q}_T))_{L^2(T^i)}. \quad (\text{I.68})$$

De plus, la forme linéaire ℓ_M est définie par

$$\begin{aligned} \ell_M(\hat{w}_h) &:= \sum_{T \in \mathcal{T}} \sum_{i \in \{1, 2\}} (f, q_{T^i})_{T^i} \\ &\quad + \sum_{T \in \mathcal{T}^{\text{cut}}} \left\{ (g_N, q_{T^2})_{T^\Gamma} + \kappa_1 h_T^{-1} (g_D, [\![q_T]\!]_\Gamma)_{T^\Gamma} - \delta_{i1} \kappa_1 (g_D, \mathbf{g}_{T^i}(\hat{q}_T))_{T^\Gamma} \right\}. \end{aligned} \quad (\text{I.69})$$

On remarque que, dans le problème discret (I.66), seule la condition aux limites de Dirichlet est imposée explicitement (sur les inconnues de face situées sur la frontière $\partial\Omega$), tandis que les deux conditions de saut à travers l'interface, (I.52b) et (I.52c), sont imposées de manière faible.

Cellules mal coupées. Parmi les mailles coupées, on distingue ensuite les mailles bien coupées des mailles mal coupées. Plus précisément, on fixe un paramètre $\vartheta \in (0, 1)$, et on dit qu'une maille coupée T est bien coupée si, pour tout $i \in \{1, 2\}$, T^i contient une boule de rayon ϑh_T ; sinon, la maille T est dite mal coupée. Comme établi dans [29], si ϑ est suffisamment petit et le maillage suffisamment fin (par rapport à la courbure de l'interface), la condition de boule ci-dessus ne peut échouer que au plus dans une des deux sous-cellules. Ces considérations conduisent à la partition suivante :

$$\mathcal{T}^{\text{cut}} := \mathcal{T}^{\text{OK}} \cup \mathcal{T}^{\text{KO}}, \quad (\text{I.70})$$

où \mathcal{T}^{OK} celui des mailles bien coupées, et \mathcal{T}^{KO} celui des mailles mal coupées. En posant $\mathcal{T}^i := \{T \in \mathcal{T} \mid T \subset \Omega_i\}$ pour tout $i \in \{1, 2\}$, on a $\mathcal{T}^{\text{uncut}} = \mathcal{T}^1 \cup \mathcal{T}^2$. Pour toute maille $T \in \mathcal{T}^{\text{uncut}}$, on note $\iota(T) \in \{1, 2\}$ l'indice tel que $T \in \mathcal{T}^{\iota(T)}$. Par ailleurs, pour toute maille $T \in \mathcal{T}^{\text{KO}}$, on définit $\iota(T) \in \{1, 2\}$ comme l'indice pour lequel la condition de boule échoue. On introduit alors la partition $\mathcal{T}^{\text{KO}} = \mathcal{T}_h^{\text{KO},1} \cup \mathcal{T}_h^{\text{KO},2}$, où $T \in \mathcal{T}_h^{\text{KO},i}$ si $\iota(T) = i$. On obtient ainsi une partition plus fine du maillage que celle de (I.55)-(I.70) :

$$\mathcal{T} := \underbrace{\mathcal{T}^1 \cup \mathcal{T}^2}_{\mathcal{T}^{\text{uncut}}} \cup \underbrace{\mathcal{T}^{\text{OK}} \cup \mathcal{T}_h^{\text{KO},1} \cup \mathcal{T}_h^{\text{KO},2}}_{=\mathcal{T}^{\text{cut}}}. \quad (\text{I.71})$$

Un exemple de partitionnement est donné à la Figure I.11 à gauche.

Opérateur d'appariement. Le traitement des mauvaises coupes repose sur un opérateur d'appariement, qui associe à chaque maille mal coupée $T \in \mathcal{T}^{\text{KO}}$ une maille non coupée ou bien coupée appartenant au voisinage $\Delta(T)$. On note cet opérateur \mathcal{N} : $\mathcal{T}^{\text{KO}} \rightarrow \mathcal{T}$, tel que

$$\mathcal{N} : \mathcal{T}^{\text{KO}} \ni S \mapsto T \in (\mathcal{T}^i \cup \mathcal{T}^{\text{OK}} \cup \mathcal{T}^{\text{KO},\bar{i}}) \cap \Delta(S), \quad i := \iota(T). \quad (\text{I.72})$$

En notant $\mathcal{N}_i := \mathcal{N}|_{\mathcal{T}^{\text{KO},i}}$ pour tout $i \in \{1, 2\}$, on a plus précisément :

$$\mathcal{N}_i : \mathcal{T}^{\text{KO},i} \ni S \mapsto T \in (\mathcal{T}^i \cup \mathcal{T}^{\text{OK}} \cup \mathcal{T}^{\text{KO},\bar{i}}) \cap \Delta(S). \quad (\text{I.73})$$

L'ensemble $\mathcal{T}^{\text{KO},i}$ se décompose alors comme suit :

$$\mathcal{T}^{\text{KO},i} = \mathcal{N}_i^{-1}(\mathcal{T}^i) \cup \mathcal{N}_i^{-1}(\mathcal{T}^{\text{OK}}) \cup \mathcal{N}_i^{-1}(\mathcal{T}^{\text{KO},\bar{i}}), \quad \forall i \in \{1, 2\}. \quad (\text{I.74})$$

Une illustration des opérateurs d'appariement \mathcal{N}_1 et \mathcal{N}_2 est présentée sur la Figure I.12.

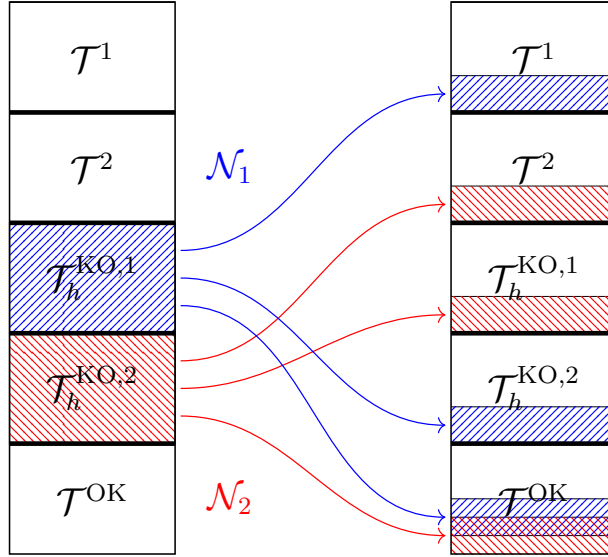


Fig. I.12: Opérateurs d'appariement \mathcal{N}_1 et \mathcal{N}_2 agissant sur les mailles mal coupées.

Stabilisation des mauvaises coupes. Afin d'assurer la stabilité de la méthode, deux stratégies peuvent être envisagées (voir Figure I.13). La première, de nature géométrique, exploite les capacités polyédriques de la méthode HHO : elle consiste à agglomérer une cellule mal coupée $T \in \mathcal{T}^{\text{KO}}$ avec ses voisines $S \in \mathcal{N}_i(T)$. Cette approche permet d'assurer l'optimalité en norme H^1 du schéma HHO, sans nécessiter de modification supplémentaire. Cette approche présente toutefois l'inconvénient de nécessiter une modification de la structure de données du maillage, ce qui peut s'avérer problématique pour une intégration dans un code de calcul préexistant. C'est pourquoi, dans cette thèse, nous explorerons une autre voie pour la stabilisation de ces méthodes. Cette seconde stratégie repose sur l'extension, vers les cellules mal coupées $T \in \mathcal{T}^{\text{KO}}$, des polynômes définis sur les cellules voisines $S \in \mathcal{N}_i(T)$ ne présentant pas de coupe défavorable. Comme évoqué précédemment, ce second choix s'avère moins intrusif dans le cadre d'une intégration dans un code préexistant, mais demande cependant des modifications non-triviales dans la partie assemblage du schéma numérique.

Rappelons qu'un ingrédient central des méthodes HHO est la reconstruction locale du gradient à partir des inconnues locales de cellule et de face. Les propriétés de stabilité de ce gradient reconstruit dépendent fondamentalement d'une inégalité de trace discrète sur les dérivées normales aux faces des cellules. Dans le cas des cellules mal découpées, la constante dans cette inégalité dégénère. La solution explorée ici consiste à utiliser les polynômes de cellules et de faces des cellules mal coupées dans la reconstruction du gradient d'une cellule voisine bien coupée. Avec cette approche, les cellules du maillage restent inchangées, mais le stencil associé à l'opérateur de reconstruction du gradient est légèrement étendu.

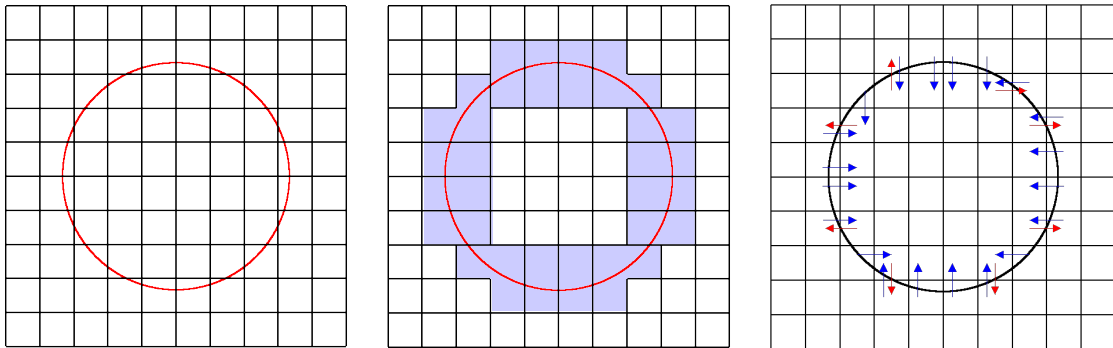


Fig. I.13: **Gauche:** Maillage initial avec interface circulaire. **Centre:** Maillage agglomérée. **Droite:** Modification du stencil pour l'extension polynomiale.

I.5 Plan du manuscrit et contributions

Outre ce chapitre introductif, le manuscrit se compose de trois chapitres techniques puis d'une conclusion.

Le Chapter II, intitulé *HHO methods for elasto-acoustic wave propagation in the time domain*, est consacré au développement des méthodes HHO pour la propagation d'ondes à travers des milieux de nature différente (solide, fluide). Nous dérivons dans un premier temps une estimation d'erreur optimale en norme d'énergie dans un cadre semi-discret en espace. Puis, nous présentons les principaux résultats de l'étude numérique : (i) une analyse spectrale mettant en évidence la nécessité d'une stabilisation d'ordre $\mathcal{O}(1)$ dans le cadre de discrétisations temporelles explicites afin d'éviter des conditions CFL trop restrictives ; (ii) des taux de convergence optimaux d'ordre $(k+1)$ dans les configurations à ordre égal ($k' = k$) et à ordre différent ($k' = k+1$) avec une stabilisation $\mathcal{O}(1)$, et atteignant l'ordre $(k+2)$ pour une discrétisation à ordre différent avec une stabilisation d'ordre $\mathcal{O}(\frac{1}{h})$ et une discrétisation en temps implicite; (iii) des cas tests avec une ondelette de Ricker en condition initiale illustrant la pertinence de la méthode proposée pour la simulation de la propagation d'ondes élasto-acoustiques dans des milieux présentant de forts contrastes de propriétés matérielles. Ce chapitre repose sur un article soumis en 2025 à *ESAIM: Mathematical Modelling and Numerical Analysis (M2AN)* [121].

Le Chapter III, intitulé *Wave propagation in geophysical media using HHO methods on general meshes*, approfondit l'étude numérique menée au chapitre précédent, en montrant qu'il est intéressant d'éliminer localement les inconnues de face dans le cas explicite et les inconnues de cellule dans le cas implicite. Ce chapitre contient également un cas test géophysique réaliste. Les principaux résultats numériques sont les suivants : (i) une procédure de condensation statique dans le cadre implicite et son pendant explicite ; (ii) une étude numérique de stabilité pour divers degrés polynomiaux et diverses formes de mailles, aboutissant à un critère CFL pour le choix du pas de temps ; (iii) une nouvelle étude sur l'ondelette de Ricker afin de comparer l'efficacité des approches implicite et explicite en temps et vérifier également la satisfaction de la condition de couplage (rappelons que celle-ci est satisfaite de manière faible); (iv) des simulations en configuration

géophysique réaliste bidimensionnelle démontrant la grande flexibilité géométrique de la méthode HHO : les maillages hybrides ainsi que les maillages non conformes (avec nœuds orphelins) sont pris en charge sans perte de précision. Ce chapitre repose sur un article soumis en 2025 à *Computer Methods in Applied Mechanics and Engineering (CMAME)* [120].

Le Chapter IV, intitulé *Unfitted HHO methods stabilized by polynomial extension*, apporte une nouvelle contribution au développement des méthodes unfitted HHO. L'objectif est de concevoir et d'analyser une stratégie de stabilisation par extension polynomiale pour ces méthodes. Après avoir présenté les idées principales sur comment intégrer l'extension polynomiale dans les opérateurs locaux de reconstruction du gradient, une analyse de stabilité et d'erreur est menée, suivie d'un ensemble de résultats numériques illustrant le comportement de la méthode. On y trouve notamment : (i) une comparaison des approches par agglomération et par extension polynomiale avec une comparaison des profils de sparsité des matrices de rigidité obtenues par les deux méthodes; (ii) des taux de convergence pour différents centrages des bases polynomiales et différentes valeurs du paramètre ϑ du critère de boule, afin d'analyser la sensibilité de la méthode aux mauvaises coupes; (iii) une étude de robustesse par rapport au contraste et aux sauts à l'interface; (iv) une étude du conditionnement de la matrice de rigidité. Ce chapitre repose sur un article soumis en 2025 à *SIAM Journal on Numerical Analysis (SINUM)* [37].

L'ensemble des développements informatiques et numériques présentés dans les chapitres II et III ont été intégrés au sein du code open-source **disk++**, développé au CERMICS [48]. Les méthodes unfitted nécessitant une structure de données spécifique, les développements associés au chapitre IV ont été réalisés dans la plateforme de prototypage **ProtoN**, également un code open-source du CERMICS. Un portage progressif des outils unfitted vers **disk++** est prévu prochainement. Ces travaux de nature informatique ont donné lieu à la création d'une nouvelle branche dans chacun de ces deux codes, nécessitant des modifications substantielles à de nombreux niveaux : structure des données, opérateurs discrets, processus d'assemblage, interfâçage avec différents solveurs et préconditionneurs, post-traitement des résultats.

HHO methods for elasto-acoustic wave propagation in the time domain

Abstract

We devise a Hybrid High-Order (HHO) method for the coupling between the acoustic and elastic wave equations in the time domain. A first-order formulation in time is considered. The HHO method can use equal-order and mixed-order settings with polynomial degree $k \geq 0$ for the face unknowns, together with $\mathcal{O}(1)$ - or $\mathcal{O}(\frac{1}{h})$ -stabilization. An energy-error estimate is established in the time-continuous case. A numerical spectral analysis is performed, showing that $\mathcal{O}(1)$ -stabilization is required to avoid excessive CFL limitations for explicit time discretizations. Moreover, the spectral radius of the stiffness matrix is found to be fairly independent of the geometry of the mesh cells. For analytical solutions on general meshes, optimal convergence rates of order $(k + 1)$ are shown in both equal- and mixed-order settings using $\mathcal{O}(1)$ -stabilization, whereas order $(k + 2)$ is achieved in the mixed-order setting using $\mathcal{O}(\frac{1}{h})$ -stabilization. Test cases with a Ricker wavelet as an initial condition showcase the relevance of the proposed method for the simulation of elasto-acoustic wave propagation across media with contrasted material properties.

This chapter is based on a paper submitted to *ESAIM: Mathematical Modelling and Numerical Analysis (M2AN)* entitled “Hybrid high-order methods for elasto-acoustic wave propagation in the time domain” [121].

Contents

II.1 Introduction	34
II.2 Model problem	36
II.2.1 Strong formulation	37
II.2.2 Weak formulation	38
II.2.3 Mechanical energy	38
II.3 HHO space semi-discretization	39
II.3.1 Meshing and discrete spaces	39
II.3.2 HHO local operators	41
II.3.3 HHO discretization for the first-order coupling formulation	42
II.4 Error analysis	43
II.4.1 Interpolation operators	43
II.4.2 Energy-error estimate	46
II.5 Algebraic realization of the semi-discrete problem	52

II.6 Numerical results	53
II.6.1 Spectral analysis	54
II.6.2 Time discretization schemes	56
II.6.3 Convergence rates for smooth analytical solutions	56
II.6.4 Numerical study of Ricker wavelet as initial condition	59
II.7 Conclusion	66

II.1 Introduction

The propagation of acoustic and elastic waves plays an important role in the modeling of various physical phenomena in many applications, such as medical imaging and geophysical exploration. In many of these applications, the interaction between solid and fluid domains plays a central role. The main field of application that interests us in this paper is the propagation of waves through rocks, water and air leading to the coupling of elastic and acoustic waves in several media with contrasted material properties. Scenarios of interest range from relatively simple configurations, such as wave propagation in layered media, to complex cases involving heterogeneous domains with intricate geometries. Capturing the wave propagation as well as the dynamics of wave transmission and reflection at fluid-solid interfaces is essential to accurately predict the physical behavior of the phenomena under study. Additionally, employing discretization schemes with moderate numerical dispersion and dissipation is critical to the reliability of simulations. These challenges motivate the development of advanced numerical methods that can address the complexity of coupled wave problems in the time domain.

Finite Differences (FD) are one of the most widely used methods for space discretization due to their conceptual simplicity and computational efficiency. However, they have several limitations. In particular, FD methods meet with difficulties in complex geometries and are subject to geometrical errors by committing inaccuracies at interfaces [139], although geometric mappings can enhance flexibility [8]. Moreover, FD methods are also subject to numerical dispersion, which can be tempered by using high-order schemes. However, high-order FD schemes require large stencils which can hinder parallel scalability, and their explicit time discretization can be challenging [127]. An alternative to high-order FD methods are high-order continuous finite elements (see [59] for a review). These methods provide a natural way to handle non-planar complex geometries with interfaces. However, their efficiency is hampered by implicit time-stepping due to a global non-diagonal mass matrix, and the simulations can be polluted by spurious modes [112]. To make explicit time-stepping possible, Spectral Element Methods (SEM) were introduced. These methods align quadrature points with Lagrangian interpolation nodes that are Gauss–Lobatto–Legendre points, leading to a diagonal mass matrix (mass lumping), without loss in accuracy. The main drawback of SEM is to rely almost exclusively on quadrangular/hexahedral meshes with tensorization of quadrature nodes to be very efficient, making the discretization of complicated geometries quite challenging.

To obtain more geometric flexibility, discontinuous Galerkin (dG) methods were introduced both in first-order [82, 119] and second-order time formulations [87] of the wave

equation (see [5, 6] for the elasto-acoustic coupled problem). In general, in dG schemes for the first-order formulation in time, stabilization acts as a dissipative mechanism, whereas it is possible to identify a discrete energy that is conserved for the second-order time formulation. For an energy-conserving dG discretization of the first-order formulation, see [47] where some continuity of the unknowns is enforced. The main drawback of dG methods is their computational cost since they involve much more degrees of freedom than continuous finite element methods. Hybridizable Discontinuous Galerkin (HDG) methods [55] introduce an additional unknown defined over the mesh skeleton and offer a reduction of the computational cost by the use of static condensation. Moreover, in a coupling wave context, HDG methods weakly enforce in a seamless way the transmission conditions at the interface [138]. In comparison with the second-order formulation, the first-order formulation allows to approximate the primal and dual variables simultaneously. Furthermore, the first-order formulation offers a wider choice of high-order time-discrete schemes, such as Runge-Kutta schemes, whereas high-order approximation schemes of the second-order time derivative are less straightforward.

Coupled elasto-acoustic wave propagation has also been addressed in the frequency domain. In particular, mixed finite element formulations have been proposed in [85] using a dual-mixed formulation in the solid region, and a standard primal formulation in the fluid region. In this context, the key challenge lies in coupling the solid stress tensor with the Helmholtz equation governing the fluid pressure. This is achieved by enforcing one of the transmission conditions weakly using a Lagrange multiplier.

The present work focuses on the coupling between elastic and acoustic wave equations in the time domain in the first-order formulation within the framework of hybrid high-order (HHO) methods for space semi-discretization. HHO methods make use of polynomials of arbitrary order ($k \geq 1$ for elasticity, $k \geq 0$ for diffusion) attached to the mesh faces and polynomials of order $k' \in \{k, k+1\}$ attached to the mesh cells [50, 65]. Initially developed for linear diffusion problems [69] and locking-free linear elasticity [68], HHO methods offer several advantages, including the natural handling of polyhedral and nonconforming meshes, local conservativity, and optimal convergence rates (order $(k+1)$ in the energy norm). Additionally, a static condensation procedure enables the local elimination of the cell unknowns, enhancing computational efficiency. HHO methods rely on two locally defined operators: a gradient reconstruction operator and a stabilization operator. The close connection between HHO, HDG and Weak Galerkin (WG) methods has been established in [53]. HHO methods have been extended to wave propagation in [34, 32] for both first- and second-order time formulations, see also [81, 135] for further developments on explicit time schemes for the second-order in time formulation of the wave equation. As HDG methods, a key advantage of HHO methods is their easy handling of coupling conditions through face-based degrees of freedom, which enables a natural and efficient treatment of interface conditions in multiphysics problems.

The present work brings several advances in the development and analysis of Hybrid High-Order (HHO) methods for coupled elasto-acoustic wave propagation. Our first contribution is an energy-error estimate in the space semi-discrete case. In particular, we leverage the fact that the coupling terms exhibit an anti-symmetric, and thus non-dissipative, structure. We improve on the analysis in [34] since we treat coupled elasto-acoustic wave

problems, and we simplify the error estimate by exploiting tighter consistency properties of the method. Our second contribution is a spectral analysis of the resulting algebraic formulation, that reveals a behavior of the spectral radius of the stiffness matrix as $\min(\eta, 1/\eta)$ with η the scaling of the stabilization. Interestingly, this scaling is fairly independent of the geometry of the mesh cells (triangular, quadrangular or polygonal). Thus, explicit time schemes are recommended with $\mathcal{O}(1)$ -stabilization, whereas implicit time schemes can be combined with either $\mathcal{O}(1)$ - or $\mathcal{O}(\frac{1}{h})$ -stabilization (see Remark II.3.1 for the scaling of the stabilization). The third contribution concerns optimal convergence rates for smooth solutions where we observe that $\mathcal{O}(\frac{1}{h})$ -stabilization leads to improved rates in the energy norm (order $(k + 2)$ instead of $(k + 1)$). The last contribution is a more realistic study featuring interface, Rayleigh-type waves and complex transmission phenomena where we perform a comparison of HHO solutions with a reference solution obtained by a numerical computation using Green functions. Notice that our discretization method differs from [138] since the primal variable in the fluid domain is the pressure here, whereas it is the fluid velocity in [138]. Moreover, we allow for implicit and explicit schemes as well as $\mathcal{O}(1)$ - and $\mathcal{O}(\frac{1}{h})$ -stabilizations, whereas [138] focuses on explicit time schemes and $\mathcal{O}(1)$ -stabilization.

The paper is organized as follows. In Section II.2, we present the model problem for the elasto-acoustic coupling as well as its weak formulation. In Section II.3, we detail the HHO space semi-discretization. In Section II.4 we present the energy-error analysis in the time-continuous setting. In Section II.5, the algebraic realization of the space semi-discrete problem is discussed. Finally, numerical results are presented in Section II.6.

II.2 Model problem

This section introduces the domain configuration, and the coupling of the acoustic and elastic wave equations. We use boldface (resp. blackboard) fonts for vectors (resp. tensors), as well as for vector-valued (resp. tensor-valued) fields and spaces composed of such fields.

Let $J := (0, T_f)$ be the time interval with the final time $T_f > 0$, and Ω be a polyhedral domain in \mathbb{R}^d , $d \in \{2, 3\}$ (open, bounded, connected, Lipschitz subset of \mathbb{R}^d). We consider a partition of Ω such that $\overline{\Omega} := \overline{\Omega^S} \cup \overline{\Omega^F}$ into two disjoint, open, polyhedral subdomains Ω^S and Ω^F constituting the elastic medium and the acoustic medium, respectively, sharing the polygonal interface $\Gamma := \partial\Omega^S \cap \partial\Omega^F$. We fix the unit normal vector \mathbf{n}_Γ to Γ as conventionally pointing from Ω^S to Ω^F .

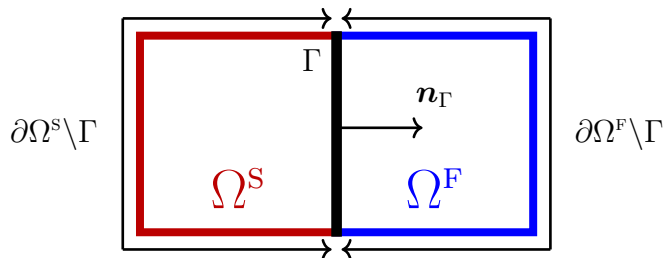


Fig. II.1: Elastic domain Ω^S , acoustic domain Ω^F , and unit normal \mathbf{n}_Γ along the interface Γ

II.2.1 Strong formulation

Acoustic wave equation. The acoustic wave equation governs the scalar pressure field p [Pa] and the velocity field \mathbf{m} [$\frac{\text{m}}{\text{s}}$] solving the following PDE system in $J \times \Omega^F$:

$$\rho^F \partial_t \mathbf{m} - \nabla p = \mathbf{0}, \quad (\text{II.1a})$$

$$\frac{1}{\kappa} \partial_t p - \nabla \cdot \mathbf{m} = f^F, \quad (\text{II.1b})$$

with the fluid density ρ^F [$\frac{\text{kg}}{\text{m}^3}$], the fluid bulk modulus κ [Pa], and the source term f^F [$\frac{1}{\text{s}}$]. The celerity of the acoustic waves is $c_p^F := \sqrt{\kappa / \rho^F}$ [$\frac{\text{m}}{\text{s}}$]. We assign the initial conditions

$$p(0) = p_0 \quad \text{and} \quad \mathbf{m}(0) = \mathbf{m}_0, \quad (\text{II.2})$$

with given data p_0 and \mathbf{m}_0 . For simplicity, we enforce homogeneous Dirichlet boundary conditions on p on $\partial\Omega^F \setminus \Gamma$.

Elastic wave equation. Let $\nabla_{\text{sym}} := \frac{1}{2}(\nabla + \nabla^\dagger)$ be the symmetric gradient operator. The elastic wave equation governs the (linearized) Cauchy stress tensor \mathbf{s} [Pa] and the velocity field \mathbf{v} [$\frac{\text{m}}{\text{s}}$] solving the following PDE system in $J \times \Omega^S$:

$$\mathbb{C}^{-1} \partial_t \mathbf{s} - \nabla_{\text{sym}} \mathbf{v} = \mathbf{0}, \quad (\text{II.3a})$$

$$\rho^S \partial_t \mathbf{v} - \nabla \cdot \mathbf{s} = \mathbf{f}^S, \quad (\text{II.3b})$$

with the solid density ρ^S [$\frac{\text{kg}}{\text{m}^3}$] and the source term \mathbf{f}^S [$\frac{\text{Pa}}{\text{m}}$]. In the framework of isotropic elasticity, the 4th-order Hooke tensor \mathbb{C} [Pa] only depends on the Lamé parameters λ [Pa] and μ [Pa], and is such that $\mathbb{C}_{ijkl} := \lambda \delta_{ij} \delta_{kl} + \mu (\delta_{ik} \delta_{jl} + \delta_{il} \delta_{jk})$, where the δ 's are Kronecker symbols. In this setting, there are two wave speeds [$\frac{\text{m}}{\text{s}}$] related to two types of body waves, far from material interfaces:

$$c_p^S := \sqrt{(\lambda + 2\mu) / \rho^S} \quad \text{for compressional (or P-) waves,} \quad (\text{II.4a})$$

$$c_s^S := \sqrt{\mu / \rho^S} \quad \text{for shear (or S-) waves.} \quad (\text{II.4b})$$

We do not consider here the incompressible limit as $\frac{\lambda}{\mu} \gg 1$, so that both wave speeds in (II.4) are of similar magnitude. We assign the initial conditions

$$\mathbf{v}(0) = \mathbf{v}_0 \quad \text{and} \quad \mathbf{s}(0) = \mathbf{s}_0, \quad (\text{II.5})$$

with given data \mathbf{v}_0 and \mathbf{s}_0 . For simplicity, we enforce homogeneous Dirichlet boundary conditions on \mathbf{v} on $\partial\Omega^S \setminus \Gamma$.

Coupled problem. The interface conditions on $J \times \Gamma$ are

$$\mathbf{v} \cdot \mathbf{n}_\Gamma = \mathbf{m} \cdot \mathbf{n}_\Gamma, \quad (\text{II.6a})$$

$$\mathbf{s} \cdot \mathbf{n}_\Gamma = p \mathbf{n}_\Gamma, \quad (\text{II.6b})$$

where the first equation is a kinematic condition and the second equation is a balance of forces per unit surface (namely, tractions) at the interface.

We mention that (II.1a)-(II.1b) can be interpreted as the momentum balance and the (linearized) mass conservation equations in the fluid domain, and (II.3a)-(II.3b) as the constitutive assumption and momentum balance equation in the solid domain. Finally, we notice that in (II.6), only the normal component of the velocity is continuous at the interface.

II.2.2 Weak formulation

We define the functional spaces

$$H_{0\Gamma}^1(\Omega^F) := \{p \in H^1(\Omega^F) : p|_{\partial\Omega^F \setminus \Gamma} = 0\}, \quad (\text{II.7a})$$

$$\mathbf{H}_{0\Gamma}^1(\Omega^S) := \{\mathbf{v} \in \mathbf{H}^1(\Omega^S) : \mathbf{v}|_{\partial\Omega^S \setminus \Gamma} = \mathbf{0}\}, \quad (\text{II.7b})$$

taking into account the homogeneous Dirichlet boundary conditions. For weighted Lebesgue spaces, we use the notation $(u, v)_{L^2(\kappa; \Omega)} := \int_{\Omega} \kappa u v \, d\Omega$ for all $u, v \in L^2(\Omega)$ and for a bounded and uniformly positive weight κ . A similar notation is used for inner products involving vector- and tensor-valued fields. Focusing for simplicity on a smooth solution in time, which requires initial conditions $(\mathbf{m}_0, p_0) \in \mathbf{L}^2(\Omega^F) \times H_{0\Gamma}^1(\Omega^F)$ and $(\mathbf{s}_0, \mathbf{v}_0) \in \mathbb{L}_{\text{sym}}^2(\Omega^S) \times \mathbf{H}_{0\Gamma}^1(\Omega^S)$, the coupled elasto-acoustic wave problem consists of finding $(\mathbf{m}, p) \in C^1(\overline{J}; \mathbf{L}^2(\Omega^F)) \times (C^1(\overline{J}; L^2(\Omega^F)) \cap C^0(\overline{J}; H_{0\Gamma}^1(\Omega^F)))$ and $(\mathbf{s}, \mathbf{v}) \in C^1(\overline{J}; \mathbb{L}_{\text{sym}}^2(\Omega^S)) \times (C^1(\overline{J}; \mathbf{L}^2(\Omega^S)) \cap C^0(\overline{J}; \mathbf{H}_{0\Gamma}^1(\Omega^S)))$ such that, for all $(\mathbf{r}, q) \in \mathbf{L}^2(\Omega^F) \times H_{0\Gamma}^1(\Omega^F)$, all $(\mathbf{b}, \mathbf{w}) \in \mathbb{L}_{\text{sym}}^2(\Omega^S) \times \mathbf{H}_{0\Gamma}^1(\Omega^S)$, and all $t \in \overline{J}$,

$$(\partial_t \mathbf{m}(t), \mathbf{r})_{\mathbf{L}^2(\rho^F; \Omega^F)} - (\nabla p(t), \mathbf{r})_{\mathbf{L}^2(\Omega^F)} = 0, \quad (\text{II.8a})$$

$$(\partial_t p(t), q)_{L^2(\frac{1}{\kappa}; \Omega^F)} + (\mathbf{m}(t), \nabla q)_{\mathbf{L}^2(\Omega^F)} + (\mathbf{v}(t) \cdot \mathbf{n}_\Gamma, q)_{L^2(\Gamma)} = (f^F(t), q)_{L^2(\Omega^F)}, \quad (\text{II.8b})$$

and

$$(\partial_t \mathbf{s}(t), \mathbf{b})_{\mathbb{L}^2(\mathbb{C}^{-1}; \Omega^S)} - (\nabla_{\text{sym}} \mathbf{v}(t), \mathbf{b})_{\mathbb{L}^2(\Omega^S)} = 0, \quad (\text{II.9a})$$

$$(\partial_t \mathbf{v}(t), \mathbf{w})_{\mathbf{L}^2(\rho^S; \Omega^S)} + (\mathbf{s}(t), \nabla_{\text{sym}} \mathbf{w})_{\mathbb{L}^2(\Omega^S)} - (p(t) \mathbf{n}_\Gamma, \mathbf{w})_{L^2(\Gamma)} = (\mathbf{f}^S(t), \mathbf{w})_{\mathbf{L}^2(\Omega^S)}. \quad (\text{II.9b})$$

Notice that the coupling condition (II.6a) is enforced weakly in (II.8b), and the coupling condition (II.6b) is enforced weakly in (II.9b).

II.2.3 Mechanical energy.

The total mechanical energy $\mathcal{E}(t) := \mathcal{E}^S(t) + \mathcal{E}^F(t)$ of a wave propagating through an elasto-acoustic medium is expressed as the sum of the mechanical energy in each medium involving the kinetic and the potential energy as follows:

$$\mathcal{E}^F(t) := \frac{1}{2} \|\mathbf{m}(t)\|_{\mathbf{L}^2(\rho^F; \Omega^F)}^2 + \frac{1}{2} \|p(t)\|_{L^2(\frac{1}{\kappa}; \Omega^F)}^2, \quad \mathcal{E}^S(t) := \frac{1}{2} \|\mathbf{v}(t)\|_{\mathbf{L}^2(\rho^S; \Omega^S)}^2 + \frac{1}{2} \|\mathbf{s}(t)\|_{\mathbb{L}^2(\mathbb{C}^{-1}; \Omega^S)}^2.$$

The following result is well-known, but we present it for completeness.

Lemma II.2.1 (Energy balance). *The following energy balance holds: For all $t \in \overline{J}$,*

$$\mathcal{E}(t) = \mathcal{E}(0) + \int_0^t \left\{ (f^F(\tau), p(\tau))_{L^2(\Omega^F)} + (\mathbf{f}^S(\tau), \mathbf{v}(\tau))_{\mathbf{L}^2(\Omega^S)} \right\} d\tau. \quad (\text{II.10})$$

Proof. Testing (II.8) with $(\mathbf{m}(t), p(t))$ and (II.9) with $(\mathbf{s}(t), \mathbf{v}(t))$ gives

$$(\partial_t \mathbf{m}(t), \mathbf{m}(t))_{L^2(\rho^F; \Omega^F)} - (\nabla p(t), \mathbf{m}(t))_{L^2(\Omega^F)} = 0, \quad (\text{II.11a})$$

$$(\partial_t p(t), p(t))_{L^2(\frac{1}{\kappa}; \Omega^F)} + (\mathbf{m}(t), \nabla p(t))_{L^2(\Omega^F)} + (\mathbf{v}(t) \cdot \mathbf{n}_\Gamma, p(t))_{L^2(\Gamma)} = (f^F(t), p(t))_{L^2(\Omega^F)}, \quad (\text{II.11b})$$

and

$$(\partial_t \mathbf{s}(t), \mathbf{s}(t))_{\mathbb{L}^2(\mathbb{C}^{-1}; \Omega^S)} - (\nabla_{\text{sym}} \mathbf{v}(t), \mathbf{s}(t))_{\mathbb{L}^2(\Omega^S)} = \mathbf{0}, \quad (\text{II.12a})$$

$$(\partial_t \mathbf{v}(t), \mathbf{v}(t))_{L^2(\rho^S; \Omega^S)} + (\mathbf{s}(t), \nabla_{\text{sym}} \mathbf{v}(t))_{\mathbb{L}^2(\Omega^S)} - (p(t) \mathbf{n}_\Gamma, \mathbf{v}(t))_{L^2(\Gamma)} = (\mathbf{f}^S(t), \mathbf{v}(t))_{L^2(\Omega^S)}. \quad (\text{II.12b})$$

Summing (II.11a)-(II.11b) and (II.12a)-(II.12b), we get

$$\begin{aligned} \frac{d}{dt} \mathcal{E}^F(t) &= (f^F(t), p(t))_{L^2(\Omega^F)} - (\mathbf{v}(t) \cdot \mathbf{n}_\Gamma, p(t))_{L^2(\Gamma)}, \\ \frac{d}{dt} \mathcal{E}^S(t) &= (\mathbf{f}^S(t), \mathbf{v}(t))_{L^2(\Omega^S)} + (p(t) \mathbf{n}_\Gamma, \mathbf{v}(t))_{L^2(\Gamma)}. \end{aligned}$$

Summing the two equations and integrating over $(0, t)$ for all $t \in \bar{J}$ proves the claim. \square

II.3 HHO space semi-discretization

This section presents the key ingredients of the HHO discretization, namely the discrete spaces and the discrete operators leading to the space semi-discrete HHO formulation.

II.3.1 Meshing and discrete spaces

Admissible mesh. Let \mathcal{T} be a polyhedral mesh of Ω that fits the partition of Ω into Ω^S and Ω^F . For simplicity, we assume that all the material properties are piecewise constant on \mathcal{T} . We define the two sub-meshes \mathcal{T}^S and \mathcal{T}^F which cover exactly Ω^S and Ω^F , respectively. The mesh faces are collected in the set \mathcal{F} which is split into $\mathcal{F} := \mathcal{F}^\circ \cup \mathcal{F}^\partial$, where \mathcal{F}° collects all the mesh interfaces (inside Ω , including on Γ) and \mathcal{F}^∂ collects all the mesh boundary faces on $\partial\Omega$. With obvious notation, we further decompose $\mathcal{F}^\circ := \mathcal{F}^{OF} \cup \mathcal{F}^{OS} \cup \mathcal{F}^F$ and $\mathcal{F}^\partial := \mathcal{F}^{\partial F} \cup \mathcal{F}^{\partial S}$. Later on, we also use the notation $\mathcal{M}^F := (\mathcal{T}^F, \mathcal{F}^F)$ and $\mathcal{M}^S := (\mathcal{T}^S, \mathcal{F}^S)$ where $\mathcal{F}^F := \mathcal{F}^{OF} \cup \mathcal{F}^{\partial F} \cup \mathcal{F}^F$ and $\mathcal{F}^S := \mathcal{F}^{OS} \cup \mathcal{F}^{\partial S} \cup \mathcal{F}^F$. A generic mesh cell is denoted $T \in \mathcal{T}$, its diameter h_T , its unit outward normal \mathbf{n}_T , and the faces composing the boundary of T are collected in the subset $\mathcal{F}_{\partial T} \subset \mathcal{F}$. We also set $\tilde{h}_T := \frac{h_T}{\ell_\Omega}$, where the scaling by $\ell_\Omega := \text{diam}(\Omega)$ is introduced for dimensional consistency.

Approximation spaces. In each subdomain, we consider a mixed formulation with one primal variable (p and \mathbf{v}) and one dual variable (\mathbf{m} and \mathbf{s}). The idea is to discretize the primal variables using the HHO method and the dual variables using a classical dG approach. Let $k \geq 1$ be the polynomial degree. The dG variables are piecewise polynomials of order k , whereas the HHO variables are composed of a pair with one cell component and one face component. The cell component is a piecewise polynomial of order $k' \in \{k, k+1\}$

and the face component is a piecewise polynomial of order $k \geq 1$. The HHO discretization is said to be of equal-order if $k' = k$ and of mixed-order if $k' = k + 1$.

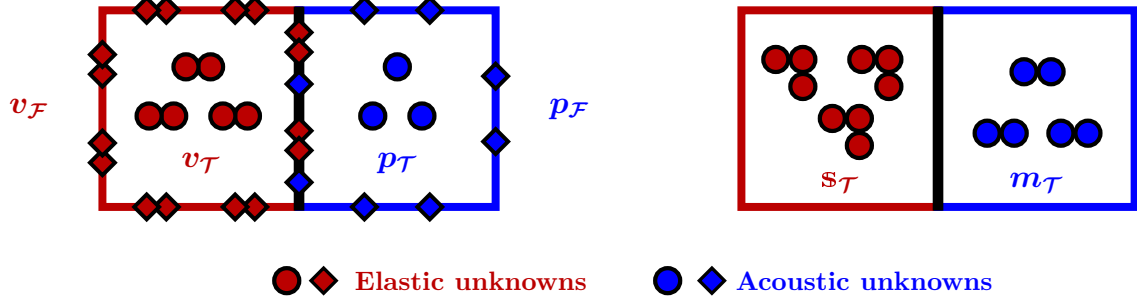


Fig. II.2: Elasto-acoustic unknowns with a equal-order discretization ($k' = k = 1$). **Left panel:** Primal variables discretized using HHO. **Right panel:** Dual variables discretized using dG.

Let $\ell \geq 0$. We introduce the local polynomial spaces $\mathbb{P}_{\text{sym}}^\ell(T)$, $\mathbf{P}^\ell(T)$ and $P^\ell(T)$ (resp. $\mathbf{P}^\ell(F)$ and $P^\ell(F)$) as the restrictions to T (resp. F) of symmetric tensor-, vector- and scalar-valued d -variate polynomials of degree at most ℓ (resp. $(d - 1)$ -variate polynomials of degree at most ℓ).

Acoustic wave equation. The discrete dG and HHO spaces are

$$\mathbf{M}^k(\mathcal{T}^F) := \bigtimes_{T \in \mathcal{T}^F} \mathbf{P}^k(T), \quad \widehat{\mathbf{P}}^k(\mathcal{M}^F) := P^{k'}(\mathcal{T}^F) \times P^k(\mathcal{F}^F), \quad (\text{II.13})$$

where $P^{k'}(\mathcal{T}^F) := \bigtimes_{T \in \mathcal{T}^F} P^{k'}(T)$ and $P^k(\mathcal{F}^F) := \bigtimes_{F \in \mathcal{F}^F} P^k(F)$. The global and local generic elements in $\widehat{\mathbf{P}}^k(\mathcal{M}^F)$ are denoted by

$$\begin{aligned} \hat{p}_{\mathcal{M}^F} &:= (p_{\mathcal{T}^F}, p_{\mathcal{F}^F}) \in \widehat{\mathbf{P}}^k(\mathcal{M}^F), \\ \hat{p}_T &:= (p_T, p_{\partial T}) \in \widehat{P}_T^k := P^{k'}(T) \times P^k(\mathcal{F}_{\partial T}) \quad \forall T \in \mathcal{T}^F, \end{aligned} \quad (\text{II.14})$$

where $p_{\partial T} := (p_F)_{F \in \mathcal{F}_{\partial T}}$ and $P^k(\mathcal{F}_{\partial T}) := \bigtimes_{F \in \mathcal{F}_{\partial T}} P^k(F)$. Moreover, to enforce the homogeneous Dirichlet boundary condition on p , we consider the subspace

$$\widehat{P}_0^k(\mathcal{M}^F) := \left\{ \hat{p}_{\mathcal{M}^F} \in \widehat{\mathbf{P}}^k(\mathcal{M}^F) \mid p_F = 0, \forall F \in \mathcal{F}^{\partial F} \right\}. \quad (\text{II.15})$$

For all $t \in \bar{J}$, we approximate the pressure $p(t)$ by a HHO unknown $\hat{p}_{\mathcal{M}^F}(t) \in \widehat{P}_0^k(\mathcal{M}^F)$ and the velocity $\mathbf{m}(t)$ by a dG unknown $\mathbf{m}_{\mathcal{T}^F}(t) \in \mathbf{M}^k(\mathcal{T}^F)$.

Elastic wave equation. The discrete dG and HHO spaces are

$$\mathbb{S}_{\text{sym}}^k(\mathcal{T}^S) := \bigtimes_{T \in \mathcal{T}_h^S} \mathbb{P}_{\text{sym}}^k(T), \quad \widehat{\mathbf{V}}^k(\mathcal{M}^S) := \mathbf{V}^{k'}(\mathcal{T}^S) \times \mathbf{V}^k(\mathcal{F}^S), \quad (\text{II.16})$$

where $\mathbf{V}^{k'}(\mathcal{T}^S) := \bigtimes_{T \in \mathcal{T}^S} \mathbf{P}^{k'}(T)$ and $\mathbf{V}^k(\mathcal{F}^S) := \bigtimes_{F \in \mathcal{F}^S} \mathbf{P}^k(F)$. The global and local generic elements in $\widehat{\mathbf{V}}^k(\mathcal{M}^S)$ are denoted by

$$\begin{aligned}\widehat{\mathbf{v}}_{\mathcal{M}^S} &:= (\mathbf{v}_{\mathcal{T}^S}, \mathbf{v}_{\mathcal{F}^S}) \in \widehat{\mathbf{V}}^k(\mathcal{M}^S), \\ \widehat{\mathbf{v}}_T &:= (\mathbf{v}_T, \mathbf{v}_{\partial T}) \in \widehat{\mathbf{V}}_T^k := \mathbf{P}^{k'}(T) \times \mathbf{P}^k(\mathcal{F}_{\partial T}) \quad \forall T \in \mathcal{T}^S,\end{aligned}\tag{II.17}$$

where $\mathbf{v}_{\partial T} := (\mathbf{v}_F)_{F \in \mathcal{F}_{\partial T}}$ and $\mathbf{P}^k(\mathcal{F}_{\partial T}) := \bigtimes_{F \in \mathcal{F}_{\partial T}} \mathbf{P}^k(F)$. Moreover, to enforce the homogeneous Dirichlet boundary condition on \mathbf{v} , we consider the subspace

$$\widehat{\mathbf{V}}_0^k(\mathcal{M}^S) := \left\{ \widehat{\mathbf{v}}_{\mathcal{M}^S} \in \widehat{\mathbf{V}}^k(\mathcal{M}^S) \mid \mathbf{v}_F = \mathbf{0}, \forall F \in \mathcal{F}^{\partial S} \right\}.\tag{II.18}$$

For all $t \in \overline{J}$, we approximate the velocity $\mathbf{v}(t)$ by a HHO unknown $\widehat{\mathbf{v}}_{\mathcal{M}^S}(t) \in \widehat{\mathbf{V}}_0^k(\mathcal{M}^S)$ and the stress tensor $\mathbf{s}(t)$ by a dG unknown $\mathbf{s}_{\mathcal{T}^S}(t) \in \mathbb{S}_{\text{sym}}^k(\mathcal{T}^S)$.

L^2 -orthogonal projections. Let $\Pi_T^{k'}$ (resp., Π_F^k and $\Pi_{\partial T}^k$) be the local $L^2(T)$ - (resp., $L^2(F)$ - and $L^2(\partial T)$ -) orthogonal projection onto $P^{k'}(T)$ (resp., $P^k(F)$ and $P^k(\mathcal{F}_{\partial T})$). Let $\Pi_{\mathcal{T}^\bullet}^{k'}$ (resp. $\Pi_{\mathcal{F}^\bullet}^k$) be the global L^2 -orthogonal projections onto $P^{k'}(\mathcal{T}^\bullet)$ (resp. $P^k(\mathcal{F}^\bullet)$) with $\bullet \in \{F, S\}$. A similar notation is used for vector- and tensor-valued fields.

II.3.2 HHO local operators

The HHO discretization is formulated locally using the following two key operators:

- i) a local gradient reconstruction operator for the acoustic wave equation and a local symmetric gradient reconstruction operator for the elastic wave equation;
- ii) a stabilization operator that penalizes the difference between the trace of the cell unknowns and the face unknowns for the HHO components on both subdomains.

The discrete problem is then assembled by summing the contributions of all the mesh cells.

Acoustic wave equation. We define the local gradient reconstruction operator $\mathbf{g}_T : \widehat{P}_T^k \rightarrow \mathbf{P}^k(T)$ such that, for all $\hat{p}_T \in \widehat{P}_T^k$,

$$(\mathbf{g}_T(\hat{p}_T), \mathbf{r})_{L^2(T)} = (\nabla p_T, \mathbf{r})_{L^2(T)} - (p_T - p_{\partial T}, \mathbf{r} \cdot \mathbf{n}_T)_{L^2(\partial T)}, \quad \forall \mathbf{r} \in \mathbf{P}^k(T).\tag{II.19}$$

Notice that $\mathbf{g}_T(\hat{p}_T)$ can be evaluated componentwise by inverting the mass matrix associated with a basis of the scalar-valued polynomial space $P^k(T)$.

We define the local stabilization operator $S_{\partial T} : \widehat{P}_T^k \rightarrow P^k(\mathcal{F}_{\partial T})$ such that, for all $\hat{p}_T \in \widehat{P}_T^k$,

$$S_{\partial T}(\hat{p}_T) := \Pi_{\partial T}^k(\delta_{\partial T}(\hat{p}_T)) \quad \text{with} \quad \delta_{\partial T}(\hat{p}_T) := p_T|_{\partial T} - p_{\partial T}.\tag{II.20}$$

We define the global gradient reconstruction operator $\mathbf{g}_{\mathcal{T}^F} : \widehat{P}^k(\mathcal{M}^F) \rightarrow \mathbf{M}^k(\mathcal{T}^F)$ as $\mathbf{g}_{\mathcal{T}^F}(\hat{p}_{\mathcal{M}^F})|_T := \mathbf{g}_T(\hat{p}_T)$ for all $T \in \mathcal{T}^F$ and all $\hat{p}_{\mathcal{M}^F} \in \widehat{P}^k(\mathcal{M}^F)$, and the global stabilization bilinear form $s_{\mathcal{M}^F}$ on $\widehat{P}^k(\mathcal{M}^F) \times \widehat{P}^k(\mathcal{M}^F)$ as

$$s_{\mathcal{M}^F}(\hat{p}_{\mathcal{M}^F}, \hat{q}_{\mathcal{M}^F}) := \sum_{T \in \mathcal{T}^F} \tau_T^F(S_{\partial T}(\hat{p}_T), S_{\partial T}(\hat{q}_T))_{L^2(\partial T)}, \quad \forall \hat{p}_{\mathcal{M}^F}, \hat{q}_{\mathcal{M}^F} \in \widehat{P}^k(\mathcal{M}^F),\tag{II.21}$$

where, for all $T \in \mathcal{T}^F$, the stabilization parameter $\tau_T^F > 0$ is taken equal to (see also Remark II.3.1 below)

$$\tau_T^F := \zeta^F \tilde{h}_T^{-\alpha} \quad \text{with} \quad \zeta^F := (\rho^F c_p^F)^{-1} = c_p^F \kappa^{-1}, \quad \alpha \in \{0, 1\}. \quad (\text{II.22})$$

Elastic wave equation. We define the local symmetric gradient reconstruction operator $\mathbf{g}_T^{\text{sym}} : \widehat{\mathbf{V}}_T^k \rightarrow \mathbb{P}_{\text{sym}}^k(T)$ such that, for all $\hat{\mathbf{v}}_T \in \widehat{\mathbf{V}}_T^k$,

$$(\mathbf{g}_T^{\text{sym}}(\hat{\mathbf{v}}_T), \mathbf{b})_{\mathbf{L}^2(T)} = (\nabla_{\text{sym}} \mathbf{v}_T, \mathbf{b})_{\mathbf{L}^2(T)} - (\mathbf{v}_T - \mathbf{v}_{\partial T}, \mathbf{b} \cdot \mathbf{n}_T)_{\mathbf{L}^2(\partial T)}, \quad \forall \mathbf{b} \in \mathbb{P}_{\text{sym}}^k(T). \quad (\text{II.23})$$

Notice that $\mathbf{g}_T^{\text{sym}}(\hat{\mathbf{v}}_T)$ can be evaluated componentwise by inverting the mass matrix associated with a basis of the scalar-valued polynomial space $P^k(T)$.

We define the local stabilization operator $\mathbf{S}_{\partial T} : \widehat{\mathbf{V}}_T^k \rightarrow \mathbf{P}^k(\mathcal{F}_{\partial T})$ such that, for all $\hat{\mathbf{v}}_T \in \widehat{\mathbf{V}}_T^k$,

$$\mathbf{S}_{\partial T}(\hat{\mathbf{v}}_T) := \boldsymbol{\Pi}_{\partial T}^k(\boldsymbol{\delta}_{\partial T}(\hat{\mathbf{v}}_T)) \quad \text{with} \quad \boldsymbol{\delta}_{\partial T}(\hat{\mathbf{v}}_T) := \mathbf{v}_T|_{\partial T} - \mathbf{v}_{\partial T}. \quad (\text{II.24})$$

We define the global symmetric gradient reconstruction operator $\mathbf{g}_{\mathcal{T}^S}^{\text{sym}} : \widehat{\mathbf{V}}^k(\mathcal{M}^S) \rightarrow \mathbb{S}_{\text{sym}}^k(\mathcal{T}^S)$ as $\mathbf{g}_{\mathcal{T}^S}^{\text{sym}}(\hat{\mathbf{v}}_{\mathcal{M}^S})|_T := \mathbf{g}_T^{\text{sym}}(\hat{\mathbf{v}}_T)$ for all $T \in \mathcal{T}^S$ and all $\hat{\mathbf{v}}_{\mathcal{M}^S} \in \widehat{\mathbf{V}}^k(\mathcal{M}^S)$, and the global stabilization bilinear form $s_{\mathcal{M}^S}$ on $\widehat{\mathbf{V}}^k(\mathcal{M}^S) \times \widehat{\mathbf{V}}^k(\mathcal{M}^S)$ as

$$s_{\mathcal{M}^S}(\hat{\mathbf{v}}_{\mathcal{M}^S}, \hat{\mathbf{w}}_{\mathcal{M}^S}) := \sum_{T \in \mathcal{T}^S} \tau_T^S (\mathbf{S}_{\partial T}(\hat{\mathbf{v}}_T), \mathbf{S}_{\partial T}(\hat{\mathbf{w}}_T))_{\mathbf{L}^2(\partial T)}, \quad \forall \hat{\mathbf{v}}_{\mathcal{M}^S}, \hat{\mathbf{w}}_{\mathcal{M}^S} \in \widehat{\mathbf{V}}^k(\mathcal{M}^S), \quad (\text{II.25})$$

where, for all $T \in \mathcal{T}^S$, the stabilization parameter $\tau_T^S > 0$ is taken equal to

$$\tau_T^S = \zeta^S \tilde{h}_T^{-\alpha} \quad \text{with} \quad \zeta^S := \rho^S c^S, \quad \alpha \in \{0, 1\}, \quad (\text{II.26})$$

and c^S can be any of the two wave speeds defined in (II.4).

Remark II.3.1 (Stabilization parameter). *Notice from (II.20) and (II.24) that the stabilization operators considered in the paper are the same regardless of the discretization setting (equal- or mixed-order) and correspond to plain least-squares stabilization in the equal-order setting. This choice is standard for $\mathcal{O}(1)$ -stabilization ($\alpha = 0$) in the first-order formulation of wave problems discretized using dG method and was also considered recently in [80] in the context of HHO methods. However, $\mathcal{O}(\frac{1}{h})$ -stabilization ($\alpha = 1$) can be useful in certain situations (see Remark II.4.4 and numerical results from Section II.6 for further discussion). Notice also that the scaling of ζ^F in (II.22) and ζ^S in (II.26) differs; this is actually the physically consistent scaling and stems from the fact that the primal variables in both subdomains have different physical dimensions.*

II.3.3 HHO discretization for the first-order coupling formulation

The space semi-discrete problem for the coupled elasto-acoustic wave problem reads as follows: Find $(\mathbf{m}_{\mathcal{T}^F}, \hat{p}_{\mathcal{M}^F}) \in C^1(\overline{J}; \mathbf{M}^k(\mathcal{T}^F) \times \widehat{P}_0^k(\mathcal{M}^F))$ and $(\mathbf{s}_{\mathcal{T}^S}, \hat{\mathbf{v}}_{\mathcal{M}^S}) \in C^1(\overline{J}; \mathbb{S}_{\text{sym}}^k(\mathcal{T}^S) \times \widehat{\mathbf{V}}_0^k(\mathcal{M}^S))$ such that, for all $(\mathbf{r}_{\mathcal{T}^F}, \hat{q}_{\mathcal{M}^F}) \in \mathbf{M}^k(\mathcal{T}^F) \times \widehat{P}_0^k(\mathcal{M}^F)$ and all $(\mathbf{b}_{\mathcal{T}^S}, \hat{\mathbf{w}}_{\mathcal{M}^S}) \in$

$\$_{\text{sym}}^k(\mathcal{T}^s) \times \widehat{\mathbf{V}}_0^k(\mathcal{M}^s)$, and all $t \in \bar{J}$,

$$(\partial_t \mathbf{m}_{\mathcal{T}^F}(t), \mathbf{r}_{\mathcal{T}^F})_{L^2(\rho^F; \Omega^F)} - (\mathbf{g}_{\mathcal{T}^F}(\hat{p}_{\mathcal{M}^F}(t)), \mathbf{r}_{\mathcal{T}^F})_{L^2(\Omega^F)} = 0, \quad (\text{II.27a})$$

$$\begin{aligned} & (\partial_t p_{\mathcal{T}^F}(t), q_{\mathcal{T}^F})_{L^2(\frac{1}{\kappa}; \Omega^F)} + (\mathbf{m}_{\mathcal{T}^F}(t), \mathbf{g}_{\mathcal{T}^F}(\hat{q}_{\mathcal{M}^F}))_{L^2(\Omega^F)} \\ & + s_{\mathcal{M}^F}(\hat{p}_{\mathcal{M}^F}(t), \hat{q}_{\mathcal{M}^F}) + (\mathbf{v}_{\mathcal{F}^s}(t) \cdot \mathbf{n}_\Gamma, q_{\mathcal{F}^F})_{L^2(\Gamma)} = (f^F(t), q_{\mathcal{T}^F})_{L^2(\Omega^F)}, \end{aligned} \quad (\text{II.27b})$$

and

$$(\partial_t \$_{\mathcal{T}^s}(t), \$_{\mathcal{T}^s})_{\mathbb{L}^2(\mathbb{C}^{-1}; \Omega^s)} - (\mathbf{g}_{\mathcal{T}^s}^{\text{sym}}(\hat{\mathbf{v}}_{\mathcal{M}^s}(t)), \$_{\mathcal{T}^s})_{\mathbb{L}^2(\Omega^s)} = 0, \quad (\text{II.28a})$$

$$\begin{aligned} & (\partial_t \mathbf{v}_{\mathcal{T}^s}(t), \mathbf{w}_{\mathcal{T}^s})_{L^2(\rho^s; \Omega^s)} + (\$,_{\mathcal{T}^s}(t), \mathbf{g}_{\mathcal{T}^s}^{\text{sym}}(\hat{\mathbf{w}}_{\mathcal{M}^s}))_{\mathbb{L}^2(\Omega^s)} \\ & + s_{\mathcal{M}^s}(\hat{\mathbf{v}}_{\mathcal{M}^s}(t), \hat{\mathbf{w}}_{\mathcal{M}^s}) - (p_{\mathcal{F}^F}(t) \mathbf{n}_\Gamma, \mathbf{w}_{\mathcal{F}^s})_{L^2(\Gamma)} = (f^s(t), \mathbf{w}_{\mathcal{T}^s})_{L^2(\Omega^s)}. \end{aligned} \quad (\text{II.28b})$$

The initial conditions for the discrete coupled problem $\mathbf{m}_{\mathcal{T}^F}(0), \hat{p}_{\mathcal{M}^F}(0), \$_{\mathcal{T}^s}(0)$, and $\hat{\mathbf{v}}_{\mathcal{M}^s}(0)$ are further discussed in Section 4.

We emphasize the seamless enforcement of the coupling conditions in (II.27b) and (II.28b) exploiting the fact that face unknowns are readily available on Γ in the HHO setting. Moreover, the total discrete mechanical energy over the elasto-acoustic domain Ω is defined as $\mathcal{E}_h(t) := \mathcal{E}_h^F(t) + \mathcal{E}_h^S(t)$ with

$$\begin{aligned} \mathcal{E}_h^F(t) &:= \frac{1}{2} \|\mathbf{m}_{\mathcal{T}^F}(t)\|_{L^2(\rho^F; \Omega^F)}^2 + \frac{1}{2} \|p_{\mathcal{T}^F}(t)\|_{L^2(\frac{1}{\kappa}; \Omega^F)}^2, \\ \mathcal{E}_h^S(t) &:= \frac{1}{2} \|\mathbf{v}_{\mathcal{T}^s}(t)\|_{L^2(\rho^s; \Omega^s)}^2 + \frac{1}{2} \|\$,_{\mathcal{T}^s}(t)\|_{\mathbb{L}^2(\mathbb{C}^{-1}; \Omega^s)}^2. \end{aligned}$$

Lemma II.3.1 (Semi-discrete energy balance). *The following discrete energy balance holds: For all $t \in \bar{J}$,*

$$\begin{aligned} \mathcal{E}_h(t) + \int_0^t \left\{ s_{\mathcal{M}^F}(\hat{p}_{\mathcal{M}^F}(\tau), \hat{p}_{\mathcal{M}^F}(\tau)) + s_{\mathcal{M}^s}(\hat{\mathbf{v}}_{\mathcal{M}^s}(\tau), \hat{\mathbf{v}}_{\mathcal{M}^s}(\tau)) \right\} d\tau = \\ \mathcal{E}_h(0) + \int_0^t \left\{ (f^F(\tau), p_{\mathcal{T}^F}(\tau))_{L^2(\Omega^F)} + (f^s(\tau), \mathbf{v}_{\mathcal{T}^s}(\tau))_{L^2(\Omega^s)} \right\} d\tau. \end{aligned} \quad (\text{II.29})$$

Proof. Similar to the proof of Lemma II.2.1. \square

II.4 Error analysis

In this section, we prove an energy-error estimate for the space semi-discrete problem (II.27)-(II.28) by using suitable interpolation operators. Here onwards, the inequality $a \leq Cb$ for positive numbers a and b is abbreviated as $a \lesssim b$, where the value of C is independent of the mesh-size h , the material parameters, the length scale ℓ_Ω , and the time scale T_f . The value of C can depend on the mesh shape-regularity, the polynomial degree, the space dimension, and the ratio $\frac{\lambda}{\mu}$.

II.4.1 Interpolation operators

Inspired by [80], we use, in both subdomains, the H^+ interpolation operator from [72] to approximate the dG variable and the classical HHO interpolation operator (based on L^2 -orthogonal projections) to approximate the HHO variable.

In the acoustic part, we employ the H^+ interpolation operator $\mathbf{I}_T^{H+} : \mathbf{H}^\nu(T) \rightarrow \mathbf{P}^k(T)$, $\nu \in (\frac{1}{2}, 1]$, defined for all $T \in \mathcal{T}^F$ as follows: We consider the L^2 -orthogonal decomposition

$$\mathbf{P}^k(T) = \nabla P_*^{k+1}(T) \oplus \mathbf{Z}^k(T), \quad (\text{II.30})$$

where $P_*^{k+1}(T) := \{q \in P^{k+1}(T) : (q, 1)_{L^2(T)} = 0\}$ and $\mathbf{Z}^k(T) := \nabla P_*^{k+1}(T)^\perp \cap \mathbf{P}^k(T)$ (orthogonalities are understood in \mathbf{L}^2). Then, for all $\mathbf{m} \in \mathbf{H}^\nu(T)$, we define $\mathbf{I}_T^{H+}(\mathbf{m}) \in \mathbf{P}^k(T)$ from the following conditions:

$$(\mathbf{I}_T^{H+}(\mathbf{m}) - \mathbf{m}, \mathbf{r})_{\mathbf{L}^2(T)} = 0 \quad \forall \mathbf{r} \in \mathbf{Z}^k(T), \quad (\text{II.31a})$$

$$(\mathbf{I}_T^{H+}(\mathbf{m}) - \mathbf{m}, \nabla q)_{\mathbf{L}^2(T)} = (\Pi_{\partial T}^k(\mathbf{m} \cdot \mathbf{n}_T) - \mathbf{m} \cdot \mathbf{n}_T, q)_{L^2(\partial T)} \quad \forall q \in P_*^{k+1}(T). \quad (\text{II.31b})$$

Notice that (II.31b) actually holds true for all $q \in P^{k+1}(T)$. For all $T \in \mathcal{T}^F$, the interpolation operator \mathbf{I}_T^{H+} is well-defined and the following holds for all $\ell_{\mathbf{m}} \in [\nu, k + 1]$ (see [72, Prop. 2.1] for a proof):

$$\|\mathbf{I}_T^{H+}(\mathbf{m}) - \mathbf{m}\|_{\mathbf{L}^2(T)} + h_T^{\frac{1}{2}} \|\mathbf{I}_T^{H+}(\mathbf{m}) - \mathbf{m}\|_{\mathbf{L}^2(\partial T)} \lesssim h_T^{\ell_{\mathbf{m}}} |\mathbf{m}|_{\mathbf{H}^{\ell_{\mathbf{m}}}(T)}. \quad (\text{II.32})$$

The global interpolation operator $\mathbf{I}_{\mathcal{T}^F}^{H+} : \mathbf{H}^\nu(\Omega^F) \rightarrow \mathbf{P}^k(\mathcal{T}^F)$ is defined as $(\mathbf{I}_{\mathcal{T}^F}^{H+}(\mathbf{m}))|_T := \mathbf{I}_T^{H+}(\mathbf{m}|_T)$ for all $T \in \mathcal{T}^F$ and all $\mathbf{m} \in \mathbf{H}^\nu(\Omega^F)$. For the HHO variable, we employ the standard HHO interpolation operator $\hat{I}_{\mathcal{M}^F}^{\text{HHO}} : H_{0\Gamma}^1(\Omega^F) \rightarrow \hat{P}_0^k(\mathcal{M}^F)$ defined, for all $p \in H_{0\Gamma}^1(\Omega^F)$, by

$$\hat{I}_{\mathcal{M}^F}^{\text{HHO}}(p) := (\Pi_{\mathcal{F}^F}^{k'}(p), \Pi_{\mathcal{F}^F}^k(p|_{\mathcal{F}^F})) \in \hat{P}_0^k(\mathcal{M}^F). \quad (\text{II.33})$$

In the elastic part, we employ the H^+ interpolation operator $\mathbb{I}_{\mathcal{T}^S}^{H+} : \mathbb{H}_{\text{sym}}^\nu(\Omega^S) \rightarrow \mathbb{P}_{\text{sym}}^k(\mathcal{T}^S)$, $\nu \in (\frac{1}{2}, 1]$, defined for all $T \in \mathcal{T}^S$ as follows: We consider the L^2 -orthogonal decomposition

$$\mathbb{P}_{\text{sym}}^k(T) = \nabla_{\text{sym}} \mathbf{P}_*^{k+1}(T) \oplus \mathbb{Z}_{\text{sym}}^k(T), \quad (\text{II.34})$$

where $\mathbf{P}_*^{k+1}(T) := [P_*^{k+1}(T)]^d := \{\mathbf{q} \in \mathbf{P}^{k+1}(T) : (\mathbf{q}, \mathbf{e}_i)_{\mathbf{L}^2(T)} = 0 \quad \forall i \in \{1, \dots, d\}\}$ with the canonical basis $(\mathbf{e}_i)_{i \in \{1, \dots, d\}}$ of \mathbb{R}^d , and $\mathbb{Z}_{\text{sym}}^k(T) := \nabla_{\text{sym}} \mathbf{P}_*^{k+1}(T)^\perp \cap \mathbb{P}_{\text{sym}}^k(T)$. Then, for all $\mathbf{s} \in \mathbb{H}_{\text{sym}}^\nu(\Omega^S)$, we define $\mathbb{I}_T^{H+}(\mathbf{s}) \in \mathbb{P}_{\text{sym}}^k(T)$ from the following conditions:

$$(\mathbb{I}_T^{H+}(\mathbf{s}) - \mathbf{s}, \mathbf{b})_{\mathbf{L}^2(T)} = 0 \quad \forall \mathbf{b} \in \mathbb{Z}_{\text{sym}}^k(T), \quad (\text{II.35a})$$

$$(\mathbb{I}_T^{H+}(\mathbf{s}) - \mathbf{s}, \nabla_{\text{sym}} \mathbf{w})_{\mathbf{L}^2(T)} = (\Pi_{\partial T}^k(\mathbf{s} \cdot \mathbf{n}_T) - \mathbf{s} \cdot \mathbf{n}_T, \mathbf{w})_{\mathbf{L}^2(\partial T)} \quad \forall \mathbf{w} \in \mathbf{P}_*^{k+1}(T). \quad (\text{II.35b})$$

For all $T \in \mathcal{T}^S$, the interpolation operator \mathbb{I}_T^{H+} is well-defined and the following holds for all $\ell_{\mathbf{s}} \in [\nu, k + 1]$ (see [72, Prop. 3.1] for a proof):

$$\|\mathbb{I}_T^{H+}(\mathbf{s}) - \mathbf{s}\|_{\mathbf{L}^2(T)} + h_T^{\frac{1}{2}} \|\mathbb{I}_T^{H+}(\mathbf{s}) - \mathbf{s}\|_{\mathbf{L}^2(\partial T)} \lesssim h_T^{\ell_{\mathbf{s}}} |\mathbf{s}|_{\mathbb{H}^{\ell_{\mathbf{s}}}(T)}. \quad (\text{II.36})$$

The global interpolation operator $\mathbb{I}_{\mathcal{T}^S}^{H+} : \mathbb{H}_{\text{sym}}^\nu(\Omega^S) \rightarrow \mathbb{P}_{\text{sym}}^k(\mathcal{T}^S)$ is defined as $(\mathbb{I}_{\mathcal{T}^S}^{H+}(\mathbf{s}))|_T := \mathbb{I}_T^{H+}(\mathbf{s}|_T)$ for all $T \in \mathcal{T}^S$ and all $\mathbf{s} \in \mathbb{H}_{\text{sym}}^\nu(\Omega^S)$. For the HHO variable, we employ the HHO interpolation operator $\hat{I}_{\mathcal{M}^S}^{\text{HHO}} : \mathbf{H}_{0\Gamma}^1(\Omega^S) \rightarrow \widehat{\mathbf{V}}_0^k(\mathcal{M}^S)$ defined, for all $\mathbf{v} \in \mathbf{H}_{0\Gamma}^1(\Omega^S)$, by

$$\hat{I}_{\mathcal{M}^S}^{\text{HHO}}(\mathbf{v}) := (\Pi_{\mathcal{F}^S}^{k'}(\mathbf{v}), \Pi_{\mathcal{F}^S}^k(\mathbf{v}|_{\mathcal{F}^S})) \in \widehat{\mathbf{V}}_0^k(\mathcal{M}^S). \quad (\text{II.37})$$

Now, we define some notation to be used for the error analysis in the next section. For all $\hat{p}_{\mathcal{M}^F} \in \widehat{P}_0^k(\mathcal{M}^F)$ and all $\hat{\mathbf{v}}_{\mathcal{M}^S} \in \widehat{\mathbf{V}}_0^k(\mathcal{M}^S)$, the HHO norms are (classically) defined as follows:

$$\|\hat{p}_{\mathcal{M}^F}\|_{\text{HHO},F}^2 := \sum_{T \in \mathcal{T}^F} \zeta^F \left(\|\nabla p_T\|_{\mathbf{L}^2(T)}^2 + h_T^{-1} \|p_{\partial T} - p_T\|_{L^2(\partial T)}^2 \right), \quad (\text{II.38})$$

and

$$\|\hat{\mathbf{v}}_{\mathcal{M}^S}\|_{\text{HHO},S}^2 := \sum_{T \in \mathcal{T}^S} \zeta^S \left(\|\nabla_{\text{sym}} \mathbf{v}_T\|_{\mathbb{L}^2(T)}^2 + h_T^{-1} \|\mathbf{v}_{\partial T} - \mathbf{v}_T\|_{\mathbf{L}^2(\partial T)}^2 \right), \quad (\text{II.39})$$

where ζ^F and ζ^S are defined in (II.22) and (II.26), respectively. We set

$$|\hat{p}_{\mathcal{M}^F}|_{S^F}^2 := s_{\mathcal{M}^F}(\hat{p}_{\mathcal{M}^F}, \hat{p}_{\mathcal{M}^F}) \quad \text{and} \quad |\hat{\mathbf{v}}_{\mathcal{M}^S}|_{S^S}^2 := s_{\mathcal{M}^S}(\hat{\mathbf{v}}_{\mathcal{M}^S}, \hat{\mathbf{v}}_{\mathcal{M}^S}). \quad (\text{II.40})$$

For linear functionals $\phi_{\mathcal{M}^F} \in (\widehat{P}_0^k(\mathcal{M}^F))'$ and $\phi_{\mathcal{M}^S} \in (\widehat{\mathbf{V}}_0^k(\mathcal{M}^S))'$, we define the following quantities:

$$\|\phi_{\mathcal{M}^F}\|_{(\text{HHO},F)'} := \sup_{\hat{q}_{\mathcal{M}^F} \in \widehat{P}_0^k(\mathcal{M}^F)} \frac{|\phi_{\mathcal{M}^F}(q_{\mathcal{M}^F})|}{\|\hat{q}_{\mathcal{M}^F}\|_{\text{HHO},F}}, \quad (\text{II.41a})$$

$$\|\phi_{\mathcal{M}^S}\|_{(\text{HHO},S)'} := \sup_{\hat{\mathbf{w}}_{\mathcal{M}^S} \in \widehat{\mathbf{V}}_0^k(\mathcal{M}^S)} \frac{|\phi_{\mathcal{M}^S}(\hat{\mathbf{w}}_{\mathcal{M}^S})|}{\|\hat{\mathbf{w}}_{\mathcal{M}^S}\|_{\text{HHO},S}},$$

$$\|\phi_{\mathcal{M}^F}\|_{(S^F)'} := \sup_{\hat{q}_{\mathcal{M}^F} \in \widehat{P}_0^k(\mathcal{M}^F)} \frac{|\phi_{\mathcal{M}^F}(\hat{q}_{\mathcal{M}^F})|}{|\hat{q}_{\mathcal{M}^F}|_{S^F}}, \quad (\text{II.41b})$$

$$\|\phi_{\mathcal{M}^S}\|_{(S^S)'} := \sup_{\hat{\mathbf{w}}_{\mathcal{M}^S} \in \widehat{\mathbf{V}}_0^k(\mathcal{M}^S)} \frac{|\phi_{\mathcal{M}^S}(\hat{\mathbf{w}}_{\mathcal{M}^S})|}{|\hat{\mathbf{w}}_{\mathcal{M}^S}|_{S^S}}.$$

The seminorms in (II.41) may be unbounded for general linear functionals $\phi_{\mathcal{M}^F}$ and $\phi_{\mathcal{M}^S}$, but we will see that they remain bounded for the consistency errors. For all $(\mathbf{m}, p) \in \mathbf{H}^\nu(\Omega^F) \times H_{0\Gamma}^1(\Omega^F)$, $\nu \in (\frac{1}{2}, 1]$, we define the augmented seminorm

$$|(\mathbf{m}, p)|_{\#,F}^2 := \sum_{T \in \mathcal{T}^F} \left\{ \tilde{h}_T^\alpha \|\mathbf{B}_{\partial T}(\mathbf{m}) \cdot \mathbf{n}_T\|_{L^2(\frac{1}{\zeta^F}; \partial T)}^2 + h_T \tilde{h}_T^{-\alpha} \|\nabla B_T(p)\|_{L^2(\zeta^F; T)}^2 \right\}, \quad (\text{II.42})$$

with $\mathbf{B}_{\partial T}(\mathbf{m}) := (\mathbf{m} - \mathbf{I}_T^{H+}(\mathbf{m}))|_{\partial T}$ and $B_T(p) := p - \Pi_T^{k'}(p)$ for all $T \in \mathcal{T}^F$. For all $(\mathbf{s}, \mathbf{v}) \in \mathbb{H}^\nu(\Omega^S) \times \mathbf{H}_{0\Gamma}^1(\Omega^S)$, $\nu \in (\frac{1}{2}, 1]$, we define the augmented seminorm

$$|(\mathbf{s}, \mathbf{v})|_{\#,S}^2 := \sum_{T \in \mathcal{T}^S} \left\{ \tilde{h}_T^\alpha \|\mathbb{B}_{\partial T}(\mathbf{s}) \cdot \mathbf{n}_T\|_{L^2(\frac{1}{\zeta^S}; \partial T)}^2 + h_T \tilde{h}_T^{-\alpha} \|\nabla_{\text{sym}} \mathbf{B}_T(\mathbf{v})\|_{\mathbb{L}^2(\zeta^S; T)}^2 \right\}, \quad (\text{II.43})$$

with $\mathbb{B}_{\partial T}(\mathbf{s}) := (\mathbf{s} - \mathbb{I}_T^{H+}(\mathbf{s}))|_{\partial T}$ and $\mathbf{B}_T(\mathbf{v}) := \mathbf{v} - \Pi_T^{k'}(\mathbf{v})$ for all $T \in \mathcal{T}^S$.

Finally, for all $t \in (0, T_f]$ and the time interval $J_t := (0, t)$, we set the following notation:

$$\|q\|_{L^p(J_t; *)}^p := \int_{J_t} \|q(\tau)\|_*^p d\tau \quad \text{for all } p \in [1, \infty), \quad \|q\|_{C^0(\bar{J}_t; *)} := \sup_{s \in \bar{J}_t} \|q(s)\|_*, \quad (\text{II.44})$$

where $\|\cdot\|_*$ is a seminorm or a norm depending on the context.

II.4.2 Energy-error estimate

We are now ready to state and prove our main error estimate.

Theorem II.4.1 (Energy-error estimate). *Let (\mathbf{m}, p) and (\mathbf{s}, \mathbf{v}) solve (II.8) and (II.9) with the initial conditions (II.2) and (II.5), respectively, and assume that $\mathbf{m} \in C^1(\bar{J}; \mathbf{H}^\nu(\Omega^F))$ and $\mathbf{s} \in C^1(\bar{J}; \mathbb{H}^\nu(\Omega^S))$, $\nu \in (\frac{1}{2}, 1]$. Let $(\mathbf{m}_{\mathcal{T}^F}, \hat{p}_{\mathcal{M}^F})$ and $(\mathbf{s}_{\mathcal{T}^S}, \hat{\mathbf{v}}_{\mathcal{M}^S})$ solve (II.27) and (II.28) with the initial conditions $\hat{p}_{\mathcal{M}^F}(0) = \hat{I}_{\mathcal{M}^F}^{\text{HHO}}(p_0)$, $\mathbf{m}_{\mathcal{T}^F}(\mathbf{0}) = \mathbf{I}_{\mathcal{T}^F}^{\text{H+}}(\mathbf{m}_0)$, $\hat{\mathbf{v}}_{\mathcal{M}^S}(\mathbf{0}) = \hat{I}_{\mathcal{M}^S}^{\text{HHO}}(\mathbf{v}_0)$, and $\mathbf{s}_{\mathcal{T}^S}(0) = \mathbb{I}_{\mathcal{T}^S}^{\text{H+}}(\mathbf{s}_0)$, respectively. The following holds for all $t \in (0, T_f]$:*

$$\begin{aligned} & \| \mathbf{m} - \mathbf{m}_{\mathcal{T}^F} \|_{C^0(\bar{J}_t; \mathbf{L}^2(\rho^F; \Omega^F))}^2 + \| p - p_{\mathcal{T}^F} \|_{C^0(\bar{J}_t; L^2(\frac{1}{\kappa}; \Omega^F))}^2 \\ & + \| \mathbf{s} - \mathbf{s}_{\mathcal{T}^S} \|_{C^0(\bar{J}_t; \mathbb{L}^2(\mathbb{C}^{-1}; \Omega^S))}^2 + \| \mathbf{v} - \mathbf{v}_{\mathcal{T}^S} \|_{C^0(\bar{J}_t; \mathbf{L}^2(\rho^S; \Omega^S))}^2 \\ & \lesssim \| \mathbf{m} - \mathbf{I}_{\mathcal{T}^F}^{\text{H+}}(\mathbf{m}) \|_{C^0(\bar{J}_t; \mathbf{L}^2(\rho^F; \Omega^F))}^2 + \| \partial_t \mathbf{m} - \mathbf{I}_{\mathcal{T}^F}^{\text{H+}}(\partial_t \mathbf{m}) \|_{L^1(J_t; \mathbf{L}^2(\rho^F; \Omega^F))}^2 \\ & + \| \mathbf{s} - \mathbb{I}_{\mathcal{T}^S}^{\text{H+}}(\mathbf{s}) \|_{C^0(\bar{J}_t; \mathbb{L}^2(\mathbb{C}^{-1}; \Omega^S))}^2 + \| \partial_t \mathbf{s} - \mathbb{I}_{\mathcal{T}^S}^{\text{H+}}(\partial_t \mathbf{s}) \|_{L^1(J_t; \mathbb{L}^2(\mathbb{C}^{-1}; \Omega^S))}^2 \\ & + \| p - \Pi_{\mathcal{T}^F}^k(p) \|_{C^0(\bar{J}_t; L^2(\frac{1}{\kappa}; \Omega^F))}^2 + \| \mathbf{v} - \Pi_{\mathcal{T}^S}^k(\mathbf{v}) \|_{C^0(\bar{J}_t; \mathbf{L}^2(\rho^S; \Omega^S))}^2 \\ & + \| (\mathbf{m}, p) \|_{L^2(J_t; \#; F)}^2 + \| (\mathbf{s}, \mathbf{v}) \|_{L^2(J_t; \#; S)}^2. \end{aligned} \quad (\text{II.45})$$

Proof. (1) Error equations. For all $t \in \bar{J}$, we define the discrete errors as follows:

$$\mathbf{N}_{\mathcal{T}^F}(t) := \mathbf{m}_{\mathcal{T}^F}(t) - \mathbf{I}_{\mathcal{T}^F}^{\text{H+}}(\mathbf{m}(t)), \quad \mathbf{N}_{\mathcal{T}^S}(t) := \mathbf{s}_{\mathcal{T}^S}(t) - \mathbb{I}_{\mathcal{T}^S}^{\text{H+}}(\mathbf{s}(t)), \quad (\text{II.46a})$$

$$\hat{e}_{\mathcal{M}^F}(t) := \hat{p}_{\mathcal{M}^F}(t) - \hat{I}_{\mathcal{M}^F}^{\text{HHO}}(p(t)), \quad \hat{\mathbf{e}}_{\mathcal{M}^S}(t) := \hat{\mathbf{v}}_{\mathcal{M}^S}(t) - \hat{I}_{\mathcal{M}^S}^{\text{HHO}}(\mathbf{v}(t)). \quad (\text{II.46b})$$

The first equation (II.27a) in the discrete problem leads, for all $\mathbf{r}_{\mathcal{T}^F} \in \mathbf{M}^k(\mathcal{T}^F)$ and all $t \in \bar{J}$, to

$$\begin{aligned} & (\partial_t \mathbf{N}_{\mathcal{T}^F}(t), \mathbf{r}_{\mathcal{T}^F})_{\mathbf{L}^2(\rho^F; \Omega^F)} - (\mathbf{g}_{\mathcal{T}^F}(\hat{e}_{\mathcal{M}^F}(t)), \mathbf{r}_{\mathcal{T}^F})_{\mathbf{L}^2(\Omega^F)} \\ & = -(\mathbf{I}_{\mathcal{T}^F}^{\text{H+}}(\partial_t \mathbf{m}(t)), \mathbf{r}_{\mathcal{T}^F})_{\mathbf{L}^2(\rho^F; \Omega^F)} + (\mathbf{g}_{\mathcal{T}^F}(\hat{I}_{\mathcal{M}^F}^{\text{HHO}}(p(t))), \mathbf{r}_{\mathcal{T}^F})_{\mathbf{L}^2(\Omega^F)} \\ & = (\partial_t \mathbf{m}(t) - \mathbf{I}_{\mathcal{T}^F}^{\text{H+}}(\partial_t \mathbf{m}(t)), \mathbf{r}_{\mathcal{T}^F})_{\mathbf{L}^2(\rho^F; \Omega^F)}, \end{aligned} \quad (\text{II.47})$$

where we used that $\mathbf{I}_{\mathcal{T}^F}^{\text{H+}}(\partial_t \bullet) = \partial_t \mathbf{I}_{\mathcal{T}^F}^{\text{H+}}(\bullet)$, $\mathbf{g}_{\mathcal{T}^F}(\hat{I}_{\mathcal{M}^F}^{\text{HHO}}(p(t))) = \Pi_{\mathcal{T}^F}^k(\nabla p(t)) = \Pi_{\mathcal{T}^F}^k(\rho^F \partial_t \mathbf{m}(t))$ (the first equality follows from the definition of $\mathbf{g}_{\mathcal{T}^F}$ and the second from (II.1a)), and the \mathbf{L}^2 -orthogonality of $\Pi_{\mathcal{T}^F}^k$. Analogously, using (II.28a), $\mathbb{I}_{\mathcal{T}^S}^{\text{H+}}(\partial_t \bullet) = \partial_t \mathbb{I}_{\mathcal{T}^S}^{\text{H+}}(\bullet)$ and the identity $\mathbf{g}_{\mathcal{T}^S}^{\text{sym}}(\hat{I}_{\mathcal{M}^S}^{\text{HHO}}(\mathbf{v}(t))) = \Pi_{\mathcal{T}^S}^k(\nabla_{\text{sym}} \mathbf{v}(t)) = \Pi_{\mathcal{T}^S}^k(\mathbb{C}^{-1} \partial_t \mathbf{s}(t))$, Analogously, using (II.28a), $\mathbb{I}_{\mathcal{T}^S}^{\text{H+}}(\partial_t \bullet) = \partial_t \mathbb{I}_{\mathcal{T}^S}^{\text{H+}}(\bullet)$ and the identity $\mathbf{g}_{\mathcal{T}^S}^{\text{sym}}(\hat{I}_{\mathcal{M}^S}^{\text{HHO}}(\mathbf{v}(t))) = \Pi_{\mathcal{T}^S}^k(\nabla_{\text{sym}} \mathbf{v}(t)) = \Pi_{\mathcal{T}^S}^k(\mathbb{C}^{-1} \partial_t \mathbf{s}(t))$, we have, for all $\mathbf{b}_{\mathcal{T}^S} \in \mathbb{S}_{\text{sym}}^k(\mathcal{T}^S)$ and all $t \in \bar{J}$,

$$\begin{aligned} & (\partial_t \mathbf{N}_{\mathcal{T}^S}(t), \mathbf{b}_{\mathcal{T}^S})_{\mathbb{L}^2(\mathbb{C}^{-1}; \Omega^S)} - (\mathbf{g}_{\mathcal{T}^S}^{\text{sym}}(\hat{\mathbf{e}}_{\mathcal{M}^S}(t)), \mathbf{b}_{\mathcal{T}^S})_{\mathbb{L}^2(\Omega^S)} \\ & = (\partial_t \mathbf{s}(t) - \mathbb{I}_{\mathcal{T}^S}^{\text{H+}}(\partial_t \mathbf{s}(t)), \mathbf{b}_{\mathcal{T}^S})_{\mathbb{L}^2(\mathbb{C}^{-1}; \Omega^S)}. \end{aligned} \quad (\text{II.48})$$

The second equation (II.27b) in the discrete problem and (II.1b) in the continuous problem

show that, for all $\hat{q}_{\mathcal{M}^F} \in \hat{P}_0^k(\mathcal{M}^F)$ and all $t \in \bar{J}$,

$$\begin{aligned}
 & (\partial_t e_{\mathcal{T}^F}(t), q_{\mathcal{T}^F})_{L^2(\frac{1}{\kappa}; \Omega^F)} + (\mathbf{N}_{\mathcal{T}^F}(t), \mathbf{g}_{\mathcal{T}^F}(\hat{q}_{\mathcal{M}^F}))_{L^2(\Omega^F)} + (\mathbf{e}_{\mathcal{F}^S}(t) \cdot \mathbf{n}_\Gamma, q_{\mathcal{F}^F})_{L^2(\Gamma)} \\
 & \quad + s_{\mathcal{M}^F}(\hat{e}_{\mathcal{M}^F}(t), \hat{q}_{\mathcal{M}^F}) \\
 &= (\frac{1}{\kappa} \partial_t p(t) - \nabla \cdot \mathbf{m}(t), q_{\mathcal{T}^F})_{L^2(\Omega^F)} - (\partial_t \Pi_{\mathcal{T}^F}^{k'}(p(t)), q_{\mathcal{T}^F})_{L^2(\frac{1}{\kappa}; \Omega^F)} \\
 & \quad - (\mathbf{I}_{\mathcal{T}^F}^{H+}(\mathbf{m}(t)), \mathbf{g}_{\mathcal{T}^F}(\hat{q}_{\mathcal{M}^F}))_{L^2(\Omega^F)} - (\boldsymbol{\Pi}_{\mathcal{F}^S}^k(\mathbf{v}(t)) \cdot \mathbf{n}_\Gamma, q_{\mathcal{F}^F})_{L^2(\Gamma)} - s_{\mathcal{M}^F}(\hat{I}_{\mathcal{M}^F}^{HHO}(p(t)), \hat{q}_{\mathcal{M}^F}) \\
 &= \sum_{T \in \mathcal{T}^F} \left\{ (\partial_t(p(t) - \Pi_T^{k'}(p(t))), q_T)_{L^2(\frac{1}{\kappa}; \Omega^F)} + (\mathbf{m}(t) - \mathbf{I}_T^{H+}(\mathbf{m}(t)), \nabla q_T)_{L^2(T)} \right. \\
 & \quad \left. - (\mathbf{m}(t) \cdot \mathbf{n}_T, q_T)_{L^2(\partial T)} + (\mathbf{I}_T^{H+}(\mathbf{m}(t)) \cdot \mathbf{n}_T, q_T - q_{\partial T})_{L^2(\partial T)} \right\} \\
 & \quad - (\boldsymbol{\Pi}_{\mathcal{F}^S}^k(\mathbf{v}(t)) \cdot \mathbf{n}_\Gamma, q_{\mathcal{F}^F})_{L^2(\Gamma)} - s_{\mathcal{M}^F}(\hat{I}_{\mathcal{M}^F}^{HHO}(p(t)), \hat{q}_{\mathcal{M}^F}) \\
 &= \sum_{T \in \mathcal{T}^F} \left\{ - (\Pi_{\partial T}^k(\mathbf{m}(t) \cdot \mathbf{n}_T), q_T)_{L^2(\partial T)} + (\mathbf{I}_T^{H+}(\mathbf{m}(t)) \cdot \mathbf{n}_T, q_T - q_{\partial T})_{L^2(\partial T)} \right\} \\
 & \quad - s_{\mathcal{M}^F}(\hat{I}_{\mathcal{M}^F}^{HHO}(p(t)), \hat{q}_{\mathcal{M}^F}) - (\Pi_{\mathcal{F}^S}^k(\mathbf{v}(t) \cdot \mathbf{n}_\Gamma), q_{\mathcal{F}^F})_{L^2(\Gamma)}, \tag{II.49}
 \end{aligned}$$

with an integration by parts and the definition of $\mathbf{g}_{\mathcal{T}^F}$ from (II.19) in the second step (since $\mathbf{I}_{\mathcal{T}^F}^{H+}(\mathbf{m}(t)) \in \mathbf{P}^k(\mathcal{T}^F)$), and the L^2 -orthogonality of $\Pi_T^{k'}$ and the definition (II.31b) of \mathbf{I}_T^{H+} in the last step. Since $\boldsymbol{\Pi}_{\partial T}^k(\mathbf{m}(t))$ and $q_{\partial T}$ are single-valued and since $q_F = 0$ for all $F \in \mathcal{F}_h^{\partial F}$, we have

$$\sum_{T \in \mathcal{T}^F} (\Pi_{\partial T}^k(\mathbf{m}(t) \cdot \mathbf{n}_T), q_{\partial T})_{L^2(\partial T)} = -(\Pi_{\mathcal{F}^S}^k(\mathbf{m}(t) \cdot \mathbf{n}_\Gamma), q_{\mathcal{F}^F})_{L^2(\Gamma)} = -(\Pi_{\mathcal{F}^S}^k(\mathbf{v}(t) \cdot \mathbf{n}_\Gamma), q_{\mathcal{F}^F})_{L^2(\Gamma)},$$

where we also used that $\mathbf{n}_T|_{\partial T \cap \Gamma} = -\mathbf{n}_\Gamma$, and the coupling condition (II.6a). This in (II.49) and the observation that $(\boldsymbol{\Pi}_{\partial T}^k(\mathbf{m}(t)) - \mathbf{I}_T^{H+}(\mathbf{m}(t))|_{\partial T}) \cdot \mathbf{n}_T \in P^k(\mathcal{F}_{\partial T})$ result in

$$\begin{aligned}
 & (\partial_t e_{\mathcal{T}^F}(t), q_{\mathcal{T}^F})_{L^2(\frac{1}{\kappa}; \Omega^F)} + (\mathbf{N}_{\mathcal{T}^F}(t), \mathbf{g}_{\mathcal{T}^F}(\hat{q}_{\mathcal{M}^F}))_{L^2(\Omega^F)} + s_{\mathcal{M}^F}(\hat{e}_{\mathcal{M}^F}(t), \hat{q}_{\mathcal{M}^F}) \\
 & \quad + (\mathbf{e}_{\mathcal{F}^S}(t) \cdot \mathbf{n}_\Gamma, q_{\mathcal{F}^F})_{L^2(\Gamma)} \\
 &= \sum_{T \in \mathcal{T}^F} ((\boldsymbol{\Pi}_{\partial T}^k(\mathbf{m}(t)) - \mathbf{I}_T^{H+}(\mathbf{m}(t))) \cdot \mathbf{n}_T, q_{\partial T} - q_T)_{L^2(\partial T)} - s_{\mathcal{M}^F}(\hat{I}_{\mathcal{M}^F}^{HHO}(p(t)), \hat{q}_{\mathcal{M}^F}) \\
 &= \sum_{T \in \mathcal{T}^F} ((\mathbf{m}(t) - \mathbf{I}_T^{H+}(\mathbf{m}(t))) \cdot \mathbf{n}_T, \Pi_{\partial T}^k(q_{\partial T} - q_T))_{L^2(\partial T)} - s_{\mathcal{M}^F}(\hat{I}_{\mathcal{M}^F}^{HHO}(p(t)), \hat{q}_{\mathcal{M}^F}). \tag{II.50}
 \end{aligned}$$

Similarly, for the elastic problem, the second equation (II.28b) in the discrete problem and

(II.3b) in the continuous problem show that, for all $\hat{\mathbf{w}}_{\mathcal{M}^s} \in \widehat{\mathbf{V}}_0^k(\mathcal{M}^s)$ and all $t \in \overline{J}$,

$$\begin{aligned}
 & (\partial_t \mathbf{e}_{\mathcal{T}^s}(t), \mathbf{w}_{\mathcal{T}^s})_{\mathbf{L}^2(\rho^s; \Omega^s)} + (\mathbf{N}_{\mathcal{T}^s}(t), \mathbf{g}_{\mathcal{T}^s}^{\text{sym}}(\hat{\mathbf{w}}_{\mathcal{M}^s}))_{\mathbb{L}^2(\Omega^s)} \\
 & + s_{\mathcal{M}^s}(\hat{\mathbf{e}}_{\mathcal{M}^s}(t), \hat{\mathbf{w}}_{\mathcal{M}^s}) - (e_{\mathcal{F}^s}(t) \mathbf{n}_\Gamma, \mathbf{w}_{\mathcal{F}^s})_{\mathbf{L}^2(\Gamma)} = (\rho^s \partial_t \mathbf{v}(t) - \nabla \cdot \mathbf{s}(t), \mathbf{w}_{\mathcal{T}^s})_{\mathbf{L}^2(\Omega^s)} \\
 & - (\partial_t \boldsymbol{\Pi}_{\mathcal{T}^s}^{k'}(\mathbf{v}(t)), \mathbf{w}_{\mathcal{T}^s})_{\mathbf{L}^2(\rho^s; \Omega^s)} - (\mathbb{I}_{\mathcal{T}^s}^{\text{H+}}(\mathbf{s}(t)), \mathbf{g}_{\mathcal{T}^s}^{\text{sym}}(\hat{\mathbf{w}}_{\mathcal{M}^s}))_{\mathbb{L}^2(\Omega^s)} - s_{\mathcal{M}^s}(\hat{\mathbf{I}}_{\mathcal{M}^s}^{\text{HHO}}(\mathbf{v}(t)), \hat{\mathbf{w}}_{\mathcal{M}^s}) \\
 & + (\Pi_{\mathcal{F}^s}^k(p(t)) \mathbf{n}_\Gamma, \mathbf{w}_{\mathcal{F}^s})_{\mathbf{L}^2(\Gamma)} = \sum_{T \in \mathcal{T}^s} \left\{ (\partial_t(\mathbf{v}(t) - \boldsymbol{\Pi}_T^{k'}(\mathbf{v}(t))), \mathbf{w}_{\mathcal{T}^s})_{\mathbf{L}^2(\rho^s; \Omega^s)} \right. \\
 & + (\mathbf{s}(t) - \mathbb{I}_T^{\text{H+}}(\mathbf{s}(t)), \nabla_{\text{sym}} \mathbf{w}_T)_{\mathbb{L}^2(T)} - (\mathbf{s}(t) \cdot \mathbf{n}_T, \mathbf{w}_T)_{\mathbf{L}^2(\partial T)} \\
 & \left. + (\mathbb{I}_T^{\text{H+}}(\mathbf{s}(t)) \cdot \mathbf{n}_T, \mathbf{w}_T - \mathbf{w}_{\partial T})_{\mathbf{L}^2(\partial T)} \right\} - s_{\mathcal{M}^s}(\hat{\mathbf{I}}_{\mathcal{M}^s}^{\text{HHO}}(\mathbf{v}(t)), \hat{\mathbf{w}}_{\mathcal{M}^s}) + (\Pi_{\mathcal{F}^s}^k(p(t)) \mathbf{n}_\Gamma, \mathbf{w}_{\mathcal{F}^s})_{\mathbf{L}^2(\Gamma)} \\
 & = \sum_{T \in \mathcal{T}^s} \left\{ - (\boldsymbol{\Pi}_{\partial T}^k(\mathbf{s}(t) \cdot \mathbf{n}_T), \mathbf{w}_T)_{\mathbf{L}^2(\partial T)} + (\mathbb{I}_T^{\text{H+}}(\mathbf{s}(t)) \cdot \mathbf{n}_T, \mathbf{w}_T - \mathbf{w}_{\partial T})_{\mathbf{L}^2(\partial T)} \right\} \\
 & - s_{\mathcal{M}^s}(\hat{\mathbf{I}}_{\mathcal{M}^s}^{\text{HHO}}(\mathbf{v}(t)), \hat{\mathbf{w}}_{\mathcal{M}^s}) + (\boldsymbol{\Pi}_{\mathcal{F}^s}^k(p(t)) \mathbf{n}_\Gamma, \mathbf{w}_{\mathcal{F}^s})_{\mathbf{L}^2(\Gamma)}, \tag{II.51}
 \end{aligned}$$

with an integration by parts and the definition of $\mathbf{g}_{\mathcal{T}^s}^{\text{sym}}$ from (II.23) in the second step, and the L^2 -orthogonality of $\boldsymbol{\Pi}_T^{k'}$ and the definition (II.35b) of $\mathbb{I}_T^{\text{H+}}$ in the last step. Since $\boldsymbol{\Pi}_{\partial T}^k(\mathbf{s}(t))$ and $\mathbf{w}_{\partial T}$ are single-valued and since $\mathbf{w}_F = \mathbf{0}$ for all $F \in \mathcal{F}_h^{\partial s}$, we have

$$\sum_{T \in \mathcal{T}^s} (\boldsymbol{\Pi}_{\partial T}^k(\mathbf{s}(t) \cdot \mathbf{n}_T), \mathbf{w}_{\partial T})_{\mathbf{L}^2(\partial T)} = (\boldsymbol{\Pi}_{\mathcal{F}^s}^k(\mathbf{s}(t) \cdot \mathbf{n}_\Gamma), \mathbf{w}_{\mathcal{F}^s})_{\mathbf{L}^2(\Gamma)} = (\boldsymbol{\Pi}_{\mathcal{F}^s}^k(p(t)) \mathbf{n}_\Gamma, \mathbf{w}_{\mathcal{F}^s})_{\mathbf{L}^2(\Gamma)},$$

where we also used that $\mathbf{n}_T|_{\partial T \cap \Gamma} = \mathbf{n}_\Gamma$, and the coupling condition (II.6b). This in (II.51) and the observation that $(\boldsymbol{\Pi}_{\partial T}^k(\mathbf{s}(t) - \boldsymbol{\Pi}_T^k(\mathbf{s}(t)))|_{\partial T}) \cdot \mathbf{n}_T \in \mathbf{P}^k(\mathcal{F}_{\partial T})$ result in

$$\begin{aligned}
 & (\partial_t \mathbf{e}_{\mathcal{T}^s}(t), \mathbf{w}_{\mathcal{T}^s})_{\mathbf{L}^2(\rho^s; \Omega^s)} + (\mathbf{N}_{\mathcal{T}^s}(t), \mathbf{g}_{\mathcal{T}^s}^{\text{sym}}(\hat{\mathbf{w}}_{\mathcal{M}^s}))_{\mathbb{L}^2(\Omega^s)} + s_{\mathcal{M}^s}(\hat{\mathbf{e}}_{\mathcal{M}^s}(t), \hat{\mathbf{w}}_{\mathcal{M}^s}) \\
 & \quad - (e_{\mathcal{F}^s}(t) \mathbf{n}_\Gamma, \mathbf{w}_{\mathcal{F}^s})_{\mathbf{L}^2(\Gamma)} \\
 & = \sum_{T \in \mathcal{T}^s} ((\boldsymbol{\Pi}_{\partial T}^k(\mathbf{s}(t)) - \mathbb{I}_T^{\text{H+}}(\mathbf{s}(t))) \cdot \mathbf{n}_T, \mathbf{w}_{\partial T} - \mathbf{w}_T)_{\mathbf{L}^2(\partial T)} - s_{\mathcal{M}^s}(\hat{\mathbf{I}}_{\mathcal{M}^s}^{\text{HHO}}(\mathbf{v}(t)), \hat{\mathbf{w}}_{\mathcal{M}^s}) \\
 & = \sum_{T \in \mathcal{T}^s} ((\mathbf{s}(t) - \mathbb{I}_T^{\text{H+}}(\mathbf{s}(t))) \cdot \mathbf{n}_T, \boldsymbol{\Pi}_{\partial T}^k(\mathbf{w}_{\partial T} - \mathbf{w}_T))_{\mathbf{L}^2(\partial T)} - s_{\mathcal{M}^s}(\hat{\mathbf{I}}_{\mathcal{M}^s}^{\text{HHO}}(\mathbf{v}(t)), \hat{\mathbf{w}}_{\mathcal{M}^s}). \tag{II.52}
 \end{aligned}$$

The combination of (II.50) and (II.52) leads, for all $\hat{q}_{\mathcal{M}^f} \in \hat{P}_0^k(\mathcal{M}^f)$ and all $\hat{\mathbf{w}}_{\mathcal{M}^s} \in \widehat{\mathbf{V}}_0^k(\mathcal{M}^s)$, to

$$\begin{aligned}
 & (\partial_t e_{\mathcal{T}^f}(t), q_{\mathcal{T}^f})_{\mathbf{L}^2(\frac{1}{\kappa}; \Omega^f)} + (\mathbf{N}_{\mathcal{T}^f}(t), \mathbf{g}_{\mathcal{T}^f}(\hat{q}_{\mathcal{M}^f}))_{\mathbf{L}^2(\Omega^f)} + s_{\mathcal{M}^f}(\hat{\mathbf{e}}_{\mathcal{M}^f}(t), \hat{q}_{\mathcal{M}^f}) \\
 & + (\mathbf{e}_{\mathcal{F}^f}(t) \cdot \mathbf{n}_\Gamma, q_{\mathcal{F}^f})_{\mathbf{L}^2(\Gamma)} + (\partial_t \mathbf{e}_{\mathcal{T}^s}(t), \mathbf{w}_{\mathcal{T}^s})_{\mathbf{L}^2(\rho^s; \Omega^s)} + (\mathbf{N}_{\mathcal{T}^s}(t), \mathbf{g}_{\mathcal{T}^s}^{\text{sym}}(\hat{\mathbf{w}}_{\mathcal{M}^s}))_{\mathbb{L}^2(\Omega^s)} \\
 & + s_{\mathcal{M}^s}(\hat{\mathbf{e}}_{\mathcal{M}^s}(t), \hat{\mathbf{w}}_{\mathcal{M}^s}) - (e_{\mathcal{F}^s}(t) \mathbf{n}_\Gamma, \mathbf{w}_{\mathcal{F}^s})_{\mathbf{L}^2(\Gamma)} \\
 & =: \psi_{\mathcal{M}^f}((\mathbf{m}(t), p(t)); \hat{q}_{\mathcal{M}^f}) + \psi_{\mathcal{M}^s}((\mathbf{s}(t), \mathbf{v}(t)); \hat{\mathbf{w}}_{\mathcal{M}^s}), \tag{II.53}
 \end{aligned}$$

where the linear functionals $\psi_{\mathcal{M}^f}((\mathbf{m}(t), p(t)); \cdot) \in (\hat{P}_0^k(\mathcal{M}^f))'$ and $\psi_{\mathcal{M}^s}((\mathbf{s}(t), \mathbf{v}(t)); \cdot) \in (\widehat{\mathbf{V}}_0^k(\mathcal{M}^s))'$ denote the consistency errors such that

$$\begin{aligned}
 \psi_{\mathcal{M}^f}((\mathbf{m}(t), p(t)); \hat{q}_{\mathcal{M}^f}) & := \sum_{T \in \mathcal{T}^f} ((\mathbf{m}(t) - \boldsymbol{\Pi}_T^{\text{H+}}(\mathbf{m}(t))) \cdot \mathbf{n}_T, \boldsymbol{\Pi}_{\partial T}^k(q_{\partial T} - q_T))_{\mathbf{L}^2(\partial T)} \\
 & \quad - s_{\mathcal{M}^f}(\hat{\mathbf{I}}_{\mathcal{M}^f}^{\text{HHO}}(p(t)), \hat{q}_{\mathcal{M}^f}), \\
 \psi_{\mathcal{M}^s}((\mathbf{s}(t), \mathbf{v}(t)); \hat{\mathbf{w}}_{\mathcal{M}^s}) & := \sum_{T \in \mathcal{T}^s} ((\mathbf{s}(t) - \mathbb{I}_T^{\text{H+}}(\mathbf{s}(t))) \cdot \mathbf{n}_T, \boldsymbol{\Pi}_{\partial T}^k(\mathbf{w}_{\partial T} - \mathbf{w}_T))_{\mathbf{L}^2(\partial T)} \\
 & \quad - s_{\mathcal{M}^s}(\hat{\mathbf{I}}_{\mathcal{M}^s}^{\text{HHO}}(\mathbf{v}(t)), \hat{\mathbf{w}}_{\mathcal{M}^s}),
 \end{aligned}$$

for all $\hat{q}_{\mathcal{M}^F} \in \widehat{P}_0^k(\mathcal{M}^F)$ and all $\hat{\mathbf{w}}_{\mathcal{M}^S} \in \widehat{\mathbf{V}}_0^k(\mathcal{M}^S)$.

(2) Stability. Choosing $\hat{q}_{\mathcal{M}^F} := \hat{e}_{\mathcal{M}^F}(t)$ and $\hat{\mathbf{w}}_{\mathcal{M}^S} := \hat{\mathbf{e}}_{\mathcal{M}^S}(t)$ in the error equation (II.53) for all $t \in \bar{J}$, and using (II.47) and (II.48) with $\mathbf{r}_{\mathcal{T}^F} := \mathbf{N}_{\mathcal{T}^F}(t)$ and $\mathbf{b}_{\mathcal{T}^S} := \mathbb{N}_{\mathcal{T}^S}(t)$, we obtain

$$\begin{aligned} & \frac{1}{2} \frac{d}{dt} \left\{ \|e_{\mathcal{T}^F}(t)\|_{L^2(\frac{1}{\kappa}; \Omega^F)}^2 + \|\mathbf{e}_{\mathcal{T}^S}(t)\|_{L^2(\rho^S; \Omega^S)}^2 + \|\mathbf{N}_{\mathcal{T}^F}(t)\|_{L^2(\rho^F; \Omega^F)}^2 + \|\mathbb{N}_{\mathcal{T}^S}(t)\|_{L^2(\mathbb{C}^{-1}; \Omega^S)}^2 \right\} \\ & + s_{\mathcal{M}^F}(\hat{e}_{\mathcal{M}^F}(t), \hat{e}_{\mathcal{M}^F}(t)) + s_{\mathcal{M}^S}(\hat{\mathbf{e}}_{\mathcal{M}^S}(t), \hat{\mathbf{e}}_{\mathcal{M}^S}(t)) \\ & = (\partial_t \mathbf{m}(t) - \mathbf{I}_{\mathcal{T}^F}^{H+}(\partial_t \mathbf{m}(t)), \mathbf{N}_{\mathcal{T}^F}(t))_{L^2(\rho^F; \Omega^F)} + (\partial_t \mathbf{s}(t) - \mathbb{I}_{\mathcal{T}^S}^{H+}(\partial_t \mathbf{s}(t)), \mathbb{N}_{\mathcal{T}^S}(t))_{L^2(\mathbb{C}^{-1}; \Omega^S)} \\ & + \psi_{\mathcal{M}^F}((\mathbf{m}(t), p(t)); \hat{e}_{\mathcal{M}^F}(t)) + \psi_{\mathcal{M}^S}((\mathbf{s}(t), \mathbf{v}(t)); \hat{\mathbf{e}}_{\mathcal{M}^S}(t)). \end{aligned} \quad (\text{II.54})$$

This is the critical step where the errors at the interface cancel, as do the interface terms in the energy balance. Integrating from 0 to t , and noticing that $e_{\mathcal{T}^F}(0) = 0$, $\mathbf{N}_{\mathcal{T}^F}(0) = \mathbf{0} = \mathbf{e}_{\mathcal{T}^S}(0)$, and $\mathbb{N}_{\mathcal{T}^S}(0) = \mathbf{0}$ owing to the initial conditions lead to

$$\begin{aligned} & \frac{1}{2} \left\{ \|e_{\mathcal{T}^F}(t)\|_{L^2(\frac{1}{\kappa}; \Omega^F)}^2 + \|\mathbf{e}_{\mathcal{T}^S}(t)\|_{L^2(\rho^S; \Omega^S)}^2 + \|\mathbf{N}_{\mathcal{T}^F}(t)\|_{L^2(\rho^F; \Omega^F)}^2 + \|\mathbb{N}_{\mathcal{T}^S}(t)\|_{L^2(\mathbb{C}^{-1}; \Omega^S)}^2 \right\} \\ & + \|\hat{e}_{\mathcal{M}^F}\|_{L^2(J_t; S^F)}^2 + \|\hat{\mathbf{e}}_{\mathcal{M}^S}\|_{L^2(J_t; S^S)}^2 = \int_{J_t} \left\{ (\partial_t \mathbf{m}(\tau) - \mathbf{I}_{\mathcal{T}^F}^{H+}(\partial_t \mathbf{m}(\tau)), \mathbf{N}_{\mathcal{T}^F}(\tau))_{L^2(\rho^F; \Omega^F)} \right. \\ & \left. + (\partial_t \mathbf{s}(\tau) - \mathbb{I}_{\mathcal{T}^S}^{H+}(\partial_t \mathbf{s}(\tau)), \mathbb{N}_{\mathcal{T}^S}(\tau))_{L^2(\mathbb{C}^{-1}; \Omega^S)} + \psi_{\mathcal{M}^F}((\mathbf{m}(\tau), p(\tau)); \hat{e}_{\mathcal{M}^F}(\tau)) \right. \\ & \left. + \psi_{\mathcal{M}^S}((\mathbf{s}(\tau), \mathbf{v}(\tau)); \hat{\mathbf{e}}_{\mathcal{M}^S}(\tau)) \right\} d\tau. \end{aligned}$$

Hölder's inequality in time for the first two terms on the right hand-side, the Cauchy-Schwarz inequality in time for the last two terms, and Young's inequality imply that

$$\begin{aligned} & \frac{1}{2} \left\{ \|e_{\mathcal{T}^F}(t)\|_{L^2(\frac{1}{\kappa}; \Omega^F)}^2 + \|\mathbf{e}_{\mathcal{T}^S}(t)\|_{L^2(\rho^S; \Omega^S)}^2 + \|\mathbf{N}_{\mathcal{T}^F}(t)\|_{L^2(\rho^F; \Omega^F)}^2 + \|\mathbb{N}_{\mathcal{T}^S}(t)\|_{L^2(\mathbb{C}^{-1}; \Omega^S)}^2 \right\} \\ & \frac{3}{4} \left\{ \|\hat{e}_{\mathcal{M}^F}\|_{L^2(J_t; S^F)}^2 + \|\hat{\mathbf{e}}_{\mathcal{M}^S}\|_{L^2(J_t; S^S)}^2 \right\} \leq \|\partial_t \mathbf{m} - \mathbf{I}_{\mathcal{T}^F}^{H+}(\partial_t \mathbf{m})\|_{L^1(J_t; L^2(\rho^F; \Omega^F))}^2 \\ & + \|\partial_t \mathbf{s} - \mathbb{I}_{\mathcal{T}^S}^{H+}(\partial_t \mathbf{s})\|_{L^1(J_t; L^2(\mathbb{C}^{-1}; \Omega^S))}^2 + \frac{1}{4} \left\{ \|\mathbf{N}_{\mathcal{T}^F}\|_{C^0(\bar{J}_t; L^2(\rho^F; \Omega^F))}^2 + \|\mathbb{N}_{\mathcal{T}^S}\|_{C^0(\bar{J}_t; L^2(\mathbb{C}^{-1}; \Omega^S))}^2 \right\} \\ & + \|\psi_{\mathcal{M}^F}((\mathbf{m}, p); \cdot)\|_{L^2(J_t; (S^F)')}^2 + \|\psi_{\mathcal{M}^S}((\mathbf{s}, \mathbf{v}); \cdot)\|_{L^2(J_t; (S^S)')}^2. \end{aligned}$$

(3) Bound on consistency errors. Rewriting the definition of $\psi_{\mathcal{M}^F}$ leads to

$$\begin{aligned} & \psi_{\mathcal{M}^F}((\mathbf{m}(t), p(t)); \hat{q}_{\mathcal{M}^F}) \\ & = \sum_{T \in \mathcal{T}^F} ((\tau_T^F)^{-\frac{1}{2}} (\mathbf{m}(t) - \mathbf{I}_T^{H+}(\mathbf{m}(t))) \cdot \mathbf{n}_T, (\tau_T^F)^{\frac{1}{2}} \Pi_{\partial T}^k (q_{\partial T} - q_T))_{L^2(\partial T)} \\ & \quad - s_{\mathcal{M}^F}(\hat{I}_{\mathcal{M}^F}^{\text{HHO}}(p(t)), \hat{q}_{\mathcal{M}^F}). \end{aligned}$$

The Cauchy-Schwarz inequality and the definition (II.20) of $S_{\partial T}$ imply that

$$\begin{aligned} & |\psi_{\mathcal{M}^F}((\mathbf{m}(t), p(t)); \hat{q}_{\mathcal{M}^F})| \\ & \lesssim \left\{ \sum_{T \in \mathcal{T}^F} \left(\tilde{h}_T^\alpha \|\mathbf{B}_{\partial T}(\mathbf{m}(t)) \cdot \mathbf{n}_T\|_{L^2(\frac{1}{\kappa^F}; \partial T)}^2 + s_T^F(\hat{I}_T^{\text{HHO}}(p(t)), \hat{I}_T^{\text{HHO}}(p(t))) \right) \right\}^{\frac{1}{2}} s_{\mathcal{M}^F}(\hat{q}_{\mathcal{M}^F}, \hat{q}_{\mathcal{M}^F})^{\frac{1}{2}}. \end{aligned}$$

where s_T^F is the local contribution to $s_{\mathcal{M}^F}$ defined in (II.21). Using the L^2 -stability of $\Pi_{\partial T}^k$, a multiplicative trace inequality, and the Poincaré inequality on T , we infer that

$$\begin{aligned} s_T^F(\hat{I}_T^{\text{HHO}}(p(t)), \hat{I}_T^{\text{HHO}}(p(t))) &\leq \tau_T^F \|p(t) - \Pi_T^{k'}(p(t))\|_{L^2(\partial T)}^2 \\ &\lesssim \tau_T^F (h_T^{-1} \|p(t) - \Pi_T^{k'}(p(t))\|_{L^2(T)}^2 + h_T \|\nabla(p(t) - \Pi_T^{k'}(p(t)))\|_{L^2(T)}^2) \\ &\lesssim \tau_T^F h_T \|\nabla(p(t) - \Pi_T^{k'}(p(t)))\|_{L^2(T)}^2 = h_T \tilde{h}_T^{-\alpha} \|\nabla B_T(p(t))\|_{L^2(\zeta^F; T)}^2, \end{aligned}$$

where we also used the definition of τ_T^F from (II.22). Hence, we obtain $\|\psi_{\mathcal{M}^F}((\mathbf{m}(t), p(t)); \cdot)\|_{(S^F)'} \lesssim |(\mathbf{m}(t), p(t))|_{\#, F}$, and similarly, $\|\psi_{\mathcal{M}^S}((\mathbf{s}(t), \mathbf{v}(t)); \cdot)\|_{(S^S)'} \lesssim |(\mathbf{s}(t), \mathbf{v}(t))|_{\#, S}$.

(4) Conclusion: Combining Step (2) and Step (3) gives

$$\begin{aligned} &\frac{1}{2} \left\{ \|e_{\mathcal{T}^F}(t)\|_{L^2(\frac{1}{\kappa}; \Omega^F)}^2 + \|\mathbf{e}_{\mathcal{T}^S}(t)\|_{L^2(\rho^S; \Omega^S)}^2 + \|\mathbf{N}_{\mathcal{T}^F}(t)\|_{L^2(\rho^F; \Omega^F)}^2 + \|\mathbf{N}_{\mathcal{T}^S}(t)\|_{L^2(\mathbb{C}^{-1}; \Omega^S)}^2 \right\} \\ &+ \frac{3}{4} \left\{ \|\hat{\mathbf{e}}_{\mathcal{M}^F}\|_{L^2(J_t; S^F)}^2 + \|\hat{\mathbf{e}}_{\mathcal{M}^S}\|_{L^2(J_t; S^S)}^2 \right\} \lesssim \|\partial_t \mathbf{m} - \mathbf{I}_{\mathcal{T}^F}^{H+}(\partial_t \mathbf{m})\|_{L^1(J_t; L^2(\rho^F; \Omega^F))}^2 \\ &+ \|\partial_t \mathbf{s} - \mathbb{I}_{\mathcal{T}^S}^{H+}(\partial_t \mathbf{s})\|_{L^1(J_t; L^2(\mathbb{C}^{-1}; \Omega^S))}^2 + \frac{1}{4} \left\{ \|\mathbf{N}_{\mathcal{T}^F}\|_{C^0(\bar{J}_t; L^2(\rho^F; \Omega^F))}^2 + \|\mathbf{N}_{\mathcal{T}^S}\|_{C^0(\bar{J}_t; L^2(\mathbb{C}^{-1}; \Omega^S))}^2 \right\} \\ &+ \|(\mathbf{m}, p)\|_{L^2(J_t; \#, F)}^2 + \|(\mathbf{s}, \mathbf{v})\|_{L^2(J_t; \#, S)}^2. \end{aligned}$$

Since the left-hand side evaluated at any $t \in J_t$ is bounded by the right-hand side, we have

$$\begin{aligned} &\frac{1}{2} \left\{ \|e_{\mathcal{T}^F}\|_{C^0(\bar{J}_t; L^2(\frac{1}{\kappa}; \Omega^F))}^2 + \|\mathbf{e}_{\mathcal{T}^S}\|_{C^0(\bar{J}_t; L^2(\rho^S; \Omega^S))}^2 \right\} + \frac{1}{4} \left\{ \|\mathbf{N}_{\mathcal{T}^F}\|_{C^0(\bar{J}_t; L^2(\rho^F; \Omega^F))}^2 \right. \\ &\quad \left. + \|\mathbf{N}_{\mathcal{T}^S}\|_{C^0(\bar{J}_t; L^2(\mathbb{C}^{-1}; \Omega^S))}^2 \right\} \lesssim \|\partial_t \mathbf{m} - \mathbf{I}_{\mathcal{T}^F}^{H+}(\partial_t \mathbf{m})\|_{L^1(J_t; L^2(\rho^F; \Omega^F))}^2 \\ &+ \|\partial_t \mathbf{s} - \mathbb{I}_{\mathcal{T}^S}^{H+}(\partial_t \mathbf{s})\|_{L^1(J_t; L^2(\mathbb{C}^{-1}; \Omega^S))}^2 + \|(\mathbf{m}, p)\|_{L^2(J_t; \#, F)}^2 + \|(\mathbf{s}, \mathbf{v})\|_{L^2(J_t; \#, S)}^2, \end{aligned}$$

where we dropped the positive stabilization terms on the left-hand side for simplicity. This and the triangle inequality result in (II.4.1). \square

Remark II.4.1 (Gronwall's lemma). *Our proof of Theorem II.4.1 avoids the need to invoke Gronwall's lemma. The key argument is the fact that the consistency errors are controlled by the stabilization semi-norms of the discrete errors. This is the main reason for choosing the H^+ interpolation operators from [72] instead of the usual L^2 -projections for dG variables as in [34].*

Remark II.4.2 (Convergence rates). *If there are $\ell_1 \in \{1, \dots, k+1\}$ and $\ell_2 \in \{1, \dots, k' + 1\}$ such that $\mathbf{m} \in C^1(\bar{J}; \mathbf{H}^{\ell_1}(\Omega^F))$, $p \in C^0(\bar{J}; H^{\ell_2}(\Omega^F))$ and $\mathbf{s} \in C^1(\bar{J}; \mathbb{H}^{\ell_1}(\Omega^S))$, $\mathbf{v} \in C^0(\bar{J}; \mathbf{H}^{\ell_2}(\Omega^S))$, we have*

$$\begin{aligned} &\|\mathbf{m} - \mathbf{m}_{\mathcal{T}^F}\|_{C^0(\bar{J}; L^2(\rho^F; \Omega^F))} + \|p - p_{\mathcal{T}^F}\|_{C^0(\bar{J}; L^2(\frac{1}{\kappa}; \Omega^F))} + \|\mathbf{s} - \mathbf{s}_{\mathcal{T}^S}\|_{C^0(\bar{J}; L^2(\mathbb{C}^{-1}; \Omega^S))} \\ &+ \|\mathbf{v} - \mathbf{v}_{\mathcal{T}^S}\|_{C^0(\bar{J}; L^2(\rho^S; \Omega^S))} \lesssim \mathcal{O}(\tilde{h}^{\frac{\alpha}{2}} h^{\ell_1 - \frac{1}{2}} + \tilde{h}^{-\frac{\alpha}{2}} h^{\ell_2 - \frac{1}{2}}). \end{aligned} \tag{II.55}$$

In the case where $\ell_1 = k+1$ and $\ell_2 = k'+1$, this gives $\mathcal{O}(h^{k+\frac{1}{2}})$ for $\mathcal{O}(1)$ -stabilization (i.e., $\alpha = 0$ in (II.22) and (II.26)), and $\mathcal{O}(h^{k+1} + h^{k'})$ for $\mathcal{O}(\frac{1}{h})$ -stabilization (i.e., $\alpha = 1$ in

(II.22) and (II.26)), that is, $\mathcal{O}(h^k)$ for equal-order and $\mathcal{O}(h^{k+1})$ for mixed-order. Finally, notice from Step (4) of the proof of Theorem II.4.1 that we can also bound the stabilization semi-norms of the discrete errors as

$$\|\hat{p}_{\mathcal{M}^F}\|_{L^2(J; S^F)} + \|\hat{\mathbf{v}}_{\mathcal{M}^S}\|_{L^2(J; S^S)} \lesssim \mathcal{O}(\tilde{h}^{\frac{\alpha}{2}} h^{\ell_1 - \frac{1}{2}} + \tilde{h}^{-\frac{\alpha}{2}} h^{\ell_2 - \frac{1}{2}}). \quad (\text{II.56})$$

Moreover, as shown in [80], the above rates for $\alpha = 0$ can be improved to $\mathcal{O}(h^{k+1})$ on simplices. A discussion of the above regularity assumption on the exact solution for smooth data and computational domain can be found in [4, Section 8.5.1].

Remark II.4.3 (Initial condition). *For the dG variables, the initial conditions $\mathbf{m}_{\mathcal{T}^F}(\mathbf{0}) = \mathbf{I}_{\mathcal{T}^F}^{H^+}(\mathbf{m}_0)$ and $\mathbf{s}_{\mathcal{T}^S}(0) = \mathbb{I}_{\mathcal{T}^S}^{H^+}(\mathbf{s}_0)$ are chosen for simplicity. Instead, we can set the initial conditions to $\mathbf{m}_{\mathcal{T}^F}(\mathbf{0}) = \boldsymbol{\Pi}_{\mathcal{T}^F}^k(\mathbf{m}_0)$ and $\mathbf{s}_{\mathcal{T}^S}(0) = \boldsymbol{\Pi}_{\mathcal{T}^S}^k(\mathbf{s}_0)$ using the usual L^2 -projections, and this will only lead to the two extra contributions $\|\mathbf{I}_{\mathcal{T}^F}^{H^+}(\mathbf{m}_0) - \boldsymbol{\Pi}_{\mathcal{T}^F}^k(\mathbf{m}_0)\|_{L^2(\rho^F; \Omega^F)}$ and $\|\mathbb{I}_{\mathcal{T}^S}^{H^+}(\mathbf{s}_0) - \boldsymbol{\Pi}_{\mathcal{T}^S}^k(\mathbf{s}_0)\|_{L^2(\rho^S; \Omega^S)}$ in the error estimate. The triangle inequalities $\|\mathbf{I}_{\mathcal{T}^F}^{H^+}(\mathbf{m}_0) - \boldsymbol{\Pi}_{\mathcal{T}^F}^k(\mathbf{m}_0)\|_{L^2(\rho^F; \Omega^F)} \leq \|\mathbf{I}_{\mathcal{T}^F}^{H^+}(\mathbf{m}_0) - \mathbf{m}_0\|_{L^2(\rho^F; \Omega^F)} + \|\mathbf{m}_0 - \boldsymbol{\Pi}_{\mathcal{T}^F}^k(\mathbf{m}_0)\|_{L^2(\rho^F; \Omega^F)}$ and $\|\mathbb{I}_{\mathcal{T}^S}^{H^+}(\mathbf{s}_0) - \boldsymbol{\Pi}_{\mathcal{T}^S}^k(\mathbf{s}_0)\|_{L^2(\rho^S; \Omega^S)} \leq \|\mathbb{I}_{\mathcal{T}^S}^{H^+}(\mathbf{s}_0) - \mathbf{s}_0\|_{L^2(\rho^S; \Omega^S)} + \|\mathbf{s}_0 - \boldsymbol{\Pi}_{\mathcal{T}^S}^k(\mathbf{s}_0)\|_{L^2(\rho^S; \Omega^S)}$ followed by interpolation estimates show that these additional terms converge optimally.*

Remark II.4.4 (Equal-order setting with HHO stabilization). *For equal-order setting with the high-order HHO stabilization, the stabilization operator in the acoustic domain is defined as*

$$S_{\partial T}(\hat{p}_T) := \boldsymbol{\Pi}_{\partial T}^k(\delta_{\partial T}(\hat{p}_T) + ((\mathbf{I} - \boldsymbol{\Pi}_T^k)R_T(0, \delta_{\partial T}(\hat{p}_T)))|_{\partial T}) \quad \forall \hat{p}_T \in \hat{P}_T^k, \quad (\text{II.57})$$

and in the elastic domain as

$$\mathbf{S}_{\partial T}(\hat{\mathbf{v}}_T) := \boldsymbol{\Pi}_{\partial T}^k(\boldsymbol{\delta}_{\partial T}(\hat{\mathbf{v}}_T) + ((\mathbf{I} - \boldsymbol{\Pi}_T^k)\mathbf{R}_T(\mathbf{0}, \boldsymbol{\delta}_{\partial T}(\hat{\mathbf{v}}_T)))|_{\partial T}) \quad \forall \hat{\mathbf{v}}_T \in \hat{\mathbf{V}}_T^k, \quad (\text{II.58})$$

using suitable reconstruction operators $R_T : \hat{P}_T^k \rightarrow P^{k+1}(T)$ and $\mathbf{R}_T : \hat{\mathbf{V}}_T^k \rightarrow \mathbf{P}^{k+1}(T)$ respectively (see, e.g., [68]). These choices combined with $\mathcal{O}(\frac{1}{h})$ -stabilization improve the convergence rate to $\mathcal{O}(h^{k+1})$ even on polyhedra in contrast to the stabilization operators (II.20) and (II.24). However, as discussed in [80, Sec. 7.1], this choice of stabilization is generally suitable only for implicit time-stepping schemes.

Remark II.4.5 (Comparison with [34]). *The arguments in [34] for uncoupled acoustic or elastic waves are based on the L^2 -orthogonal projection for the dual variable instead of the H^+ interpolation operator used herein. The analysis in [34] requires to bound the consistency errors $\psi_{\mathcal{M}^F}((\mathbf{m}(t), p(t)); \cdot)$ and $\psi_{\mathcal{M}^S}((\mathbf{s}(t), \mathbf{v}(t)); \cdot)$ by means of the HHO norm, instead of the stabilization seminorm as done in the proof of Theorem II.4.1. Both approaches (using either the L^2 -projection or the H^+ interpolation operator for the dual variable) lead to the same convergence rates. However, in the context of explicit timeschemes, the analysis crucially hinges on bounding the consistency errors in terms of the stabilization seminorms only, as highlighted in [80]. This is why we preferred to use the H^+ interpolation operator in the present work although its focus is on the time-continuous case.*

II.5 Algebraic realization of the semi-discrete problem

This section details the algebraic realization of the space semi-discrete system (II.27)-(II.28). For the acoustic wave equation, we define the dimensions of the following polynomial spaces:

$$N_{\mathcal{T}^F}^{k'} := \dim(\mathcal{P}^{k'}(\mathcal{T}^F)), \quad N_{\mathcal{F}^F}^k := \dim(\mathcal{P}^k(\mathcal{F}^F)), \quad M_{\mathcal{T}^F}^k := \dim(\mathbf{M}^k(\mathcal{T}^F)), \quad (\text{II.59})$$

and denote the respective bases as

$$\{\varphi_i\}_{1 \leq i \leq N_{\mathcal{T}^F}^{k'}}, \quad \{\psi_i\}_{1 \leq i \leq N_{\mathcal{F}^F}^k}, \quad \{\zeta_k\}_{1 \leq k \leq M_{\mathcal{T}^F}^k}. \quad (\text{II.60})$$

The basis $\{\zeta_k\}_{1 \leq k \leq M_{\mathcal{T}^F}^k}$ is constructed as products of Cartesian basis vectors in \mathbb{R}^d with scalar-valued basis functions of $\mathcal{P}^k(\mathcal{T}^F)$. Let $(P_{\mathcal{T}^F}(t), P_{\mathcal{F}^F}(t)) \in \mathbb{R}^{N_{\mathcal{T}^F}^{k'}} \times \mathbb{R}^{N_{\mathcal{F}^F}^k}$ and $M_{\mathcal{T}^F}(t) \in \mathbb{R}^{M_{\mathcal{T}^F}^k}$ be the time-dependent component vectors of $(p_{\mathcal{T}^F}(t), p_{\mathcal{F}^F}(t)) \in \widehat{P}_0^k(\mathcal{M}^F)$ and $\mathbf{m}_{\mathcal{T}^F}(t) \in \mathbf{M}^k(\mathcal{T}^F)$, respectively, in these bases. Let $\mathcal{M}_{\mathcal{T}^F}^{\rho^F}$ and $\mathcal{M}_{\mathcal{T}^F}^{\frac{1}{\kappa}}$ denote the mass matrices associated with the inner products in $L^2(\rho^F; \Omega^F)$ and $L^2(\frac{1}{\kappa}; \Omega^F)$, respectively, using the above bases. Let $\mathcal{G}_{\mathcal{T}^F} \in \mathbb{R}^{M_{\mathcal{T}^F}^k \times N_{\mathcal{T}^F}^{k'}}$ and $\mathcal{G}_{\mathcal{T}^F \mathcal{F}^F} \in \mathbb{R}^{M_{\mathcal{T}^F}^k \times N_{\mathcal{F}^F}^k}$ denote the two blocks of the gradient reconstruction matrix, so that

$$(\mathbf{g}_{\mathcal{T}}(\hat{p}_{\mathcal{M}^F}(t)), \mathbf{r}_{\mathcal{T}^F})_{L^2(\Omega^F)} = (\mathcal{G}_{\mathcal{T}^F} P_{\mathcal{T}^F} + \mathcal{G}_{\mathcal{T}^F \mathcal{F}^F} P_{\mathcal{F}^F})^\dagger R_{\mathcal{T}^F}, \quad (\text{II.61})$$

for all $\mathbf{r}_{\mathcal{T}^F} \in \mathbf{M}^k(\mathcal{T}^F)$ with components $R_{\mathcal{T}^F} \in \mathbb{R}^{M_{\mathcal{T}^F}^k}$. Finally, let $\Sigma_{\mathcal{T}^F}, \Sigma_{\mathcal{T}^F \mathcal{F}^F}, \Sigma_{\mathcal{T}^F \mathcal{F}^F}^\dagger, \Sigma_{\mathcal{F}^F}$ represent the four blocks of the matrix associated with the stabilization bilinear form $s_{\mathcal{M}^F}$ defined in (II.21).

For the elastic wave equation, we define the dimensions of the following polynomial spaces:

$$L_{\mathcal{T}^S}^{k'} := \dim(\mathbf{V}^{k'}(\mathcal{T}^S)), \quad L_{\mathcal{F}^S}^k := \dim(\mathbf{V}^k(\mathcal{F}^S)), \quad H_{\mathcal{T}^S}^k := \dim(\mathbb{S}_{\text{sym}}^k(\mathcal{T}^S)), \quad (\text{II.62})$$

and denote the respective bases as

$$\{\phi_i\}_{1 \leq i \leq L_{\mathcal{T}^S}^{k'}}, \quad \{\theta_i\}_{1 \leq i \leq L_{\mathcal{F}^S}^k}, \quad \{\mathbb{Y}_k\}_{1 \leq k \leq H_{\mathcal{T}^S}^k}. \quad (\text{II.63})$$

The basis $\{\mathbb{Y}_k\}_{1 \leq k \leq H_{\mathcal{T}^S}^k}$ is naturally built as tensor products of basis vectors in $\mathbb{R}_{\text{sym}}^{d \times d}$ and scalar-valued basis functions in $\mathcal{P}^k(\mathcal{T}^S)$. Let $(V_{\mathcal{T}^S}(t), V_{\mathcal{F}^S}(t)) \in \mathbb{R}^{L_{\mathcal{T}^S}^{k'}} \times \mathbb{R}^{L_{\mathcal{F}^S}^k}$ and $S_{\mathcal{T}^S} \in \mathbb{R}^{H_{\mathcal{T}^S}^k}$ represent the time-dependent component vectors of $(v_{\mathcal{T}^S}(t), v_{\mathcal{F}^S}(t)) \in \widehat{\mathbf{V}}_0^k(\mathcal{M}^S)$ and $s_{\mathcal{T}^S}(t) \in \mathbb{S}_{\text{sym}}^k(\mathcal{T}^S)$, respectively, in these bases. Let $\mathcal{M}_{\mathcal{T}^S}^{\mathbb{C}^{-1}}$ and $\mathcal{M}_{\mathcal{T}^S}^{\rho^S}$ denote the mass matrices for the inner products in $\mathbb{L}^2(\mathbb{C}^{-1}; \Omega^S)$ and $\mathbf{L}^2(\rho^S; \Omega^S)$, respectively, in these bases. Let $\mathcal{H}_{\mathcal{T}^S} \in \mathbb{R}^{H_{\mathcal{T}^S}^k \times L_{\mathcal{T}^S}^{k'}}$ and $\mathcal{H}_{\mathcal{T}^S \mathcal{F}^S} \in \mathbb{R}^{H_{\mathcal{T}^S}^k \times L_{\mathcal{F}^S}^k}$ denote the two blocks of the symmetric gradient reconstruction matrix, so that

$$(\mathbf{g}_{\mathcal{T}^S}^{\text{sym}}(\hat{v}_{\mathcal{M}^S}(t)), \mathbf{b}_{\mathcal{T}^S})_{\mathbb{L}^2(\Omega^S)} = (\mathcal{H}_{\mathcal{T}^S} V_{\mathcal{T}^S} + \mathcal{H}_{\mathcal{T}^S \mathcal{F}^S} V_{\mathcal{F}^S})^\dagger B_{\mathcal{T}^S}. \quad (\text{II.64})$$

for all $\mathbf{b}_{\mathcal{T}^S} \in \mathbb{S}_{\text{sym}}^k(\mathcal{T}^S)$ with components $B_{\mathcal{T}^S} \in \mathbb{R}^{H_{\mathcal{T}^S}^k}$. Finally, let $\Sigma_{\mathcal{T}^S}, \Sigma_{\mathcal{T}^S \mathcal{F}^S}, \Sigma_{\mathcal{F}^S \mathcal{T}^S}, \Sigma_{\mathcal{F}^S}$ denote the four blocks of the matrix associated with the stabilization bilinear form $s_{\mathcal{M}^S}$ defined in (II.25).

Let $\mathcal{C}_{\mathcal{F}^{\Gamma}}$ be the matrix representing the coupling terms, so that

$$(\mathbf{v}_{\mathcal{F}^s} \cdot \mathbf{n}_{\Gamma}, q_{\mathcal{F}^{\Gamma}})_{L^2(\Gamma)} = \mathbf{Q}_{\mathcal{F}^{\Gamma}}^{\dagger} \mathcal{C}_{\mathcal{F}^{\Gamma}} \mathbf{V}_{\mathcal{F}^s}. \quad (\text{II.65})$$

for all $q_{\mathcal{F}^{\Gamma}} \in \mathcal{P}^k(\mathcal{F}^{\Gamma})$ with components $\mathbf{Q}_{\mathcal{F}^{\Gamma}} \in \mathbb{R}^{N_{\mathcal{F}^{\Gamma}}^k}$ and all $\mathbf{v}_{\mathcal{F}^s} \in \mathbf{P}^k(\mathcal{F}^s)$ with components $\mathbf{V}_{\mathcal{F}^s} \in \mathbb{R}^{L_{\mathcal{F}^s}^k}$. Notice that $\mathcal{C}_{\mathcal{F}^{\Gamma}}$ is block-diagonal with a nonzero block only for all $F \in \mathcal{F}^{\Gamma}$.

Altogether, the algebraic realization of (II.27) and (II.28) can be formulated in the following way: For all $t \in \bar{J}$,

$$\begin{bmatrix} \mathcal{M}_{\mathcal{T}^p}^{\rho^p} & 0 & 0 & 0 & 0 & 0 \\ 0 & \mathcal{M}_{\mathcal{T}^p}^{\frac{1}{\kappa}} & 0 & 0 & 0 & 0 \\ 0 & 0 & 0 & 0 & 0 & 0 \\ 0 & 0 & 0 & \mathcal{M}_{\mathcal{T}^s}^{\mathcal{C}^{-1}} & 0 & 0 \\ 0 & 0 & 0 & 0 & \mathcal{M}_{\mathcal{T}^s}^{\rho^s} & 0 \\ 0 & 0 & 0 & 0 & 0 & 0 \end{bmatrix} \frac{d}{dt} \begin{bmatrix} \mathbf{M}_{\mathcal{T}^p} \\ \mathbf{P}_{\mathcal{T}^p} \\ \mathbf{P}_{\mathcal{T}^s} \\ \mathbf{S}_{\mathcal{T}^s} \\ \mathbf{V}_{\mathcal{T}^s} \\ \mathbf{V}_{\mathcal{F}^s} \end{bmatrix} + \begin{bmatrix} 0 & \mathcal{G}_{\mathcal{T}^p} & \mathcal{G}_{\mathcal{T}^p \mathcal{F}^p} & 0 & 0 & 0 \\ -\mathcal{G}_{\mathcal{T}^p}^{\dagger} & \Sigma_{\mathcal{T}^p} & -\Sigma_{\mathcal{T}^p \mathcal{F}^p} & 0 & 0 & 0 \\ -\mathcal{G}_{\mathcal{T}^p \mathcal{F}^p}^{\dagger} & \Sigma_{\mathcal{T}^p \mathcal{F}^p}^{\dagger} & \Sigma_{\mathcal{F}^p} & 0 & 0 & \mathcal{C}_{\mathcal{F}^{\Gamma}} \\ 0 & 0 & 0 & 0 & \mathcal{H}_{\mathcal{T}^s} & \mathcal{H}_{\mathcal{T}^s \mathcal{F}^s} \\ 0 & 0 & 0 & -\mathcal{H}_{\mathcal{T}^s}^{\dagger} & \Sigma_{\mathcal{T}^s} & \Sigma_{\mathcal{T}^s \mathcal{F}^s} \\ 0 & 0 & 0 & -\mathcal{C}_{\mathcal{F}^{\Gamma}}^{\dagger} & -\mathcal{H}_{\mathcal{T}^s \mathcal{F}^s}^{\dagger} & \Sigma_{\mathcal{F}^s \mathcal{T}^s} \end{bmatrix} \begin{bmatrix} \mathbf{M}_{\mathcal{T}^p} \\ \mathbf{P}_{\mathcal{T}^p} \\ \mathbf{P}_{\mathcal{T}^s} \\ \mathbf{S}_{\mathcal{T}^s} \\ \mathbf{V}_{\mathcal{T}^s} \\ \mathbf{V}_{\mathcal{F}^s} \end{bmatrix} = \begin{bmatrix} 0 \\ \mathbf{F}_{\mathcal{T}^p} \\ 0 \\ 0 \\ \mathbf{F}_{\mathcal{T}^s} \\ 0 \end{bmatrix}. \quad (\text{II.66})$$

Notice that, as shown in the discrete energy balance (II.29), the coupling between acoustic and elastic waves produces no energy, resulting in antisymmetric coupling matrices in (II.66). For convenience, we re-arrange the unknowns by grouping first the (elastic and acoustic) cell unknowns and then the (elastic and acoustic) face unknowns. Then, (II.66) rewrites as

$$\begin{bmatrix} \mathcal{M}_{\mathcal{T}^p}^{\rho^p} & 0 & 0 & 0 & 0 & 0 \\ 0 & \mathcal{M}_{\mathcal{T}^p}^{\frac{1}{\kappa}} & 0 & 0 & 0 & 0 \\ 0 & 0 & \mathcal{M}_{\mathcal{T}^s}^{\mathcal{C}^{-1}} & 0 & 0 & 0 \\ 0 & 0 & 0 & \mathcal{M}_{\mathcal{T}^s}^{\rho^s} & 0 & 0 \\ 0 & 0 & 0 & 0 & 0 & 0 \\ 0 & 0 & 0 & 0 & 0 & 0 \end{bmatrix} \frac{d}{dt} \begin{bmatrix} \mathbf{M}_{\mathcal{T}^p} \\ \mathbf{P}_{\mathcal{T}^p} \\ \mathbf{S}_{\mathcal{T}^s} \\ \mathbf{V}_{\mathcal{T}^s} \\ \mathbf{P}_{\mathcal{F}^s} \\ \mathbf{V}_{\mathcal{F}^s} \end{bmatrix} + \begin{bmatrix} 0 & \mathcal{G}_{\mathcal{T}^p} & 0 & 0 & \mathcal{G}_{\mathcal{T}^p \mathcal{F}^p} & 0 \\ -\mathcal{G}_{\mathcal{T}^p}^{\dagger} & \Sigma_{\mathcal{T}^p} & 0 & 0 & \Sigma_{\mathcal{T}^p \mathcal{F}^p} & 0 \\ 0 & 0 & 0 & \mathcal{H}_{\mathcal{T}^s} & 0 & \mathcal{H}_{\mathcal{T}^s \mathcal{F}^s} \\ 0 & 0 & -\mathcal{H}_{\mathcal{T}^s}^{\dagger} & \Sigma_{\mathcal{T}^s} & 0 & \Sigma_{\mathcal{T}^s \mathcal{F}^s} \\ -\mathcal{G}_{\mathcal{T}^p \mathcal{F}^p}^{\dagger} & \Sigma_{\mathcal{T}^p \mathcal{F}^p} & 0 & 0 & \Sigma_{\mathcal{F}^p} & \mathcal{C}_{\mathcal{F}^{\Gamma}} \\ 0 & 0 & -\mathcal{H}_{\mathcal{T}^s \mathcal{F}^s}^{\dagger} & \Sigma_{\mathcal{F}^s \mathcal{T}^s} & -\mathcal{C}_{\mathcal{F}^{\Gamma}}^{\dagger} & \Sigma_{\mathcal{F}^s} \end{bmatrix} \begin{bmatrix} \mathbf{M}_{\mathcal{T}^p} \\ \mathbf{P}_{\mathcal{T}^p} \\ \mathbf{S}_{\mathcal{T}^s} \\ \mathbf{V}_{\mathcal{T}^s} \\ \mathbf{P}_{\mathcal{F}^s} \\ \mathbf{V}_{\mathcal{F}^s} \end{bmatrix} = \begin{bmatrix} 0 \\ \mathbf{F}_{\mathcal{T}^p} \\ 0 \\ 0 \\ \mathbf{F}_{\mathcal{T}^s} \\ 0 \end{bmatrix}. \quad (\text{II.67})$$

This system can be rewritten in the following compact form:

$$\begin{bmatrix} \mathcal{M}_{\mathcal{T}} & 0 \\ 0 & 0 \end{bmatrix} \partial_t \mathbf{U} + \begin{bmatrix} \mathcal{K}_{\mathcal{T}} & \mathcal{K}_{\mathcal{T}\mathcal{F}} \\ \mathcal{K}_{\mathcal{F}\mathcal{T}} & \mathcal{K}_{\mathcal{F}} \end{bmatrix} \mathbf{U} = \mathbf{F}, \quad (\text{II.68})$$

where \mathbf{U} is the vector of unknowns, the blocks with index \mathcal{T} corresponds to the 4×4 upper-left submatrices in the mass and stiffness matrices, the block with index $\mathcal{T}\mathcal{F}$ to the 4×2 upper-right submatrices in the stiffness matrix (II.67), the block with index $\mathcal{F}\mathcal{T}$ to the 2×4 lower-left submatrices, and the block with index \mathcal{F} to the 2×2 lower-right submatrices. Notice that $\mathcal{K}_{\mathcal{F}}$ has a block-diagonal structure.

II.6 Numerical results

In this section, we present 2D numerical results obtained using the HHO-dG discretizations of the elasto-acoustic problem described above. In particular, we compare equal- and mixed-order settings for the HHO variables and $\mathcal{O}(1)$ - and $\mathcal{O}(\frac{1}{h})$ -stabilizations. We analyze first the spectral properties of the algebraic problem (II.68). Next, we focus on a test case with analytical solution, so as to verify convergence rates. Finally, we study the case of a Ricker wavelet as an initial condition and we compare our results to a reference solution obtained by a numerical computation using Green functions.

The implementation is carried out in the open-source software Diskpp (available at <https://github.com/wareHHOuse/diskpp>), which is described in [48].

In the following, to precisely specify the level of discretization for each test case, we introduce two computational parameters: the spatial refinement level ℓ , defined as $h = 2^{-\ell}$, and the time refinement level n , defined as $\Delta t = 0.1 \times 2^{-n}$. All the test cases are set up in space-time domains so that $\ell_\Omega \approx 1$ and $T_f \approx 1$.

II.6.1 Spectral analysis

The goal here is to conduct a numerical spectral analysis of the space semi-discrete problem (II.68). For that purpose, we consider the generalized eigenvalue problem associated with (II.68). We define the Schur complement with respect to the face-face block of the stiffness matrix as

$$\mathcal{K}_{\text{SCHUR}} := \mathcal{K}_T - \mathcal{K}_{TF} \mathcal{K}_F^{-1} \mathcal{K}_{FT}. \quad (\text{II.69})$$

The corresponding eigenvalue problem is expressed as

$$\mathcal{K}_{\text{SCHUR}}^\dagger \mathcal{M}_T^{-1} \mathcal{K}_{\text{SCHUR}} \mathbf{X} = \gamma \mathcal{M}_T \mathbf{X}, \quad (\text{II.70})$$

where \mathbf{X} is the eigenvector and γ the eigenvalue. We define the spectral radius as the largest eigenvalue from (II.70).

Our objective is to investigate the influence of the stabilization on the spectral radius in both equal- and mixed-order settings. To this end, we consider $\mathcal{O}(1)$ -stabilizations, and we introduce additional weights η^F and η^S scaling the stabilization bilinear forms. Specifically, we set

$$\tilde{s}_{\mathcal{M}^F}(\hat{p}_h, \hat{q}_h) := \eta^F s_{\mathcal{M}^F}(\hat{p}_h, \hat{q}_h), \quad \tilde{s}_{\mathcal{M}^S}(\hat{\mathbf{v}}_h, \hat{\mathbf{w}}_h) := \eta^S s_{\mathcal{M}^S}(\hat{\mathbf{v}}_h, \hat{\mathbf{w}}_h). \quad (\text{II.71})$$

First, in Figure II.3, this analysis is conducted for three settings: pure acoustic with weight

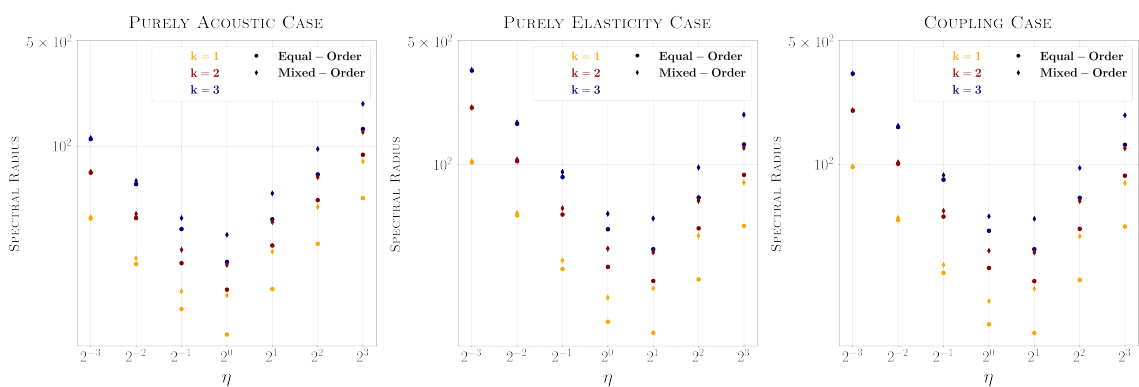


Fig. II.3: Spectral radius in the equal-Order and mixed-Order settings for the pure acoustic, pure linear elasticity, and elasto-acoustic coupling cases with $k \in \{1:3\}$

η^F , pure elastic with weight η^S , and elasto-acoustic coupling with weight $\eta^F = \eta^S = \eta$. All the spectral radii are normalized by the size of the mesh, evaluated as $\sqrt{\#\text{cells}}$. The first observation is that the spectral radius essentially behaves as $\max(\eta + c_1, \frac{1}{\eta} + c_2)$ for some

suitable constants c_1 and c_2 . Therefore, choosing an $\mathcal{O}(\frac{1}{h})$ -stabilization, which corresponds to selecting a high value for η , leads to a large spectral radius. This is unfavorable if explicit time-stepping schemes are used as it tightens the CFL restriction. Therefore, for an explicit time discretization, a stabilization of order $\mathcal{O}(1)$ is preferable. The second observation is that, regardless of the chosen discretization (equal- or mixed-order), the spectral radius in the purely elastic case is higher than in the purely acoustic case. This observation is consistent with the fact that elastic waves propagate at higher velocities than acoustic waves. Moreover, the behavior observed in the coupled elasto-acoustic case essentially aligns with that of the purely elastic case. The third observation is that, in all cases, the spectral radius for the equal-order setting is lower than the one for the mixed-order setting, indicating a potentially better CFL condition for the equal-order scheme.

According to the spectral analysis of the two pure cases, we can set the weights for the acoustic and elastic stabilizations, η_*^F and η_*^S , as follows so as to minimize the spectral radius in each pure case:

$$\eta_*^F = \begin{cases} 0.88, & \text{equal-order,} \\ 0.80, & \text{mixed-order.} \end{cases} \quad \eta_*^S = \begin{cases} 1.54, & \text{equal-order,} \\ 1.38, & \text{mixed-order.} \end{cases} \quad (\text{II.72})$$

In the rest of the paper we keep these settings. Table II.1 then reports the spectral radius in the coupled elasto-acoustic case for equal- and mixed-order settings, $k \in \{1:3\}$ and with weights prescribed as $\eta^F = 2^w \eta_*^F$ and $\eta^S = 2^w \eta_*^S$ with $w \in \{-3:3\}$ and η_*^F, η_*^S from (II.72). We observe that, in all cases, the lowest spectral radius is obtained for $w = 0$.

	η/η_*	1/8	1/4	1/2	1	2	4	8
	k	1	2	3	1	2	4	8
EQUAL-ORDER	1	55.3	27.8	14.2	9.9	19.7	39.5	78.9
	2	114.8	57.8	29.5	19.5	38.3	76.3	152.5
	3	185.2	93.2	47.7	29.6	57.3	113.9	227.3
MIXED-ORDER	1	94.2	48.3	26.3	16.5	20.7	41.0	81.7
	2	195.0	99.3	53.0	31.8	33.2	64.7	128.7
	3	314.3	159.6	84.3	50.0	51.3	99.4	197.4

Tab. II.1: Spectral radius in the equal- and mixed-order settings for the elasto-acoustic coupling with reference weights given by (II.72) and $k \in \{1:3\}$

Another interesting aspect is the influence of the mesh geometry on the spectral radius. Table II.2 reports the spectral radius for polynomial degrees $k \in \{1:6\}$ on simplicial, quadrilateral, and polygonal meshes. The latter are generated using the software PolyMesher [137]. We can see that, for an equal-order setting, the spectral radius on quadrangles is slightly better than that on simplices and polygons, with the latter being slightly worse. However, in the mixed-order setting, quadrangles and simplices appear to be roughly equivalent and at higher orders, simplices slightly outperform quadrangles in terms of spectral radius. Polygons remain the worst case in the mixed-order setting, but the difference is not that significant (about 15% increase).

	SIMPLICIAL MESHES \triangle		QUADRANGULAR MESHES \square		POLYGONAL MESHES \diamond	
	EQUAL-ORDER	MIXED-ORDER	EQUAL-ORDER	MIXED-ORDER	EQUAL-ORDER	MIXED-ORDER
$k = 1$	11.6	17.6	9.9	16.5	10.5	20.1
$k = 2$	21.3	31.4	19.5	31.8	20.7	37.2
$k = 3$	33.4	47.8	29.6	50.0	35.2	59.4
$k = 4$	49.2	69.5	45.3	74.0	53.9	86.6
$k = 5$	68.0	93.7	61.5	100.6	76.6	118.9
$k = 6$	90.1	123.2	83.0	134.0	103.5	156.3

Tab. II.2: Spectral radius for different cell geometries in equal- and mixed-order settings with $k \in \{1:6\}$ and optimal setting for η^F and η^S from (II.72)

II.6.2 Time discretization schemes

We consider both implicit and explicit time-stepping schemes. In the implicit case, we allow for both $\mathcal{O}(1)$ - and $\mathcal{O}(\frac{1}{h})$ -stabilizations, and for simplicity we focus on the mixed-order setting since the equal-order setting appears to be slightly more expensive in the static case [50]. We consider s -stage Singly Diagonally Implicit Runge–Kutta (SDIRK) schemes of order $(s+1)$ with $s \in \{2, 3\}$. The associated Butcher tableaux are reported in (II.73a) where the SDIRK(3, 4) scheme corresponds to the values $\nu := \frac{1}{\sqrt{3}} \cos(\frac{\pi}{18}) + \frac{1}{2}$ and $\xi := \frac{1}{6(2\nu-1)^2}$. In the explicit case, owing to the CFL restriction, we only consider $\mathcal{O}(1)$ -stabilization, but we include both equal- and mixed-order settings. We consider s -stage Explicit Runge–Kutta (ERK) schemes of order s with $s \in \{2, 3, 4\}$. The Butcher tableaux are reported in (II.73b).

$$\begin{array}{c|cc}
 \frac{1}{4} & \frac{1}{4} & 0 \\
 \frac{3}{4} & \frac{1}{2} & \frac{1}{4} \\
 \hline
 & \frac{1}{2} & \frac{1}{2}
 \end{array}
 \quad
 \begin{array}{c|ccc}
 \theta & \theta & 0 & 0 \\
 \frac{1}{2} & \frac{1}{2} - \theta & \theta & 0 \\
 1 - \theta & 2\theta & 1 - 4\theta & \theta \\
 \hline
 & \xi & 1 - 2\xi & \xi
 \end{array} \tag{II.73a}$$

$$\begin{array}{c|cc}
 0 & 0 & 0 \\
 \frac{1}{2} & \frac{1}{2} & 0 \\
 \hline
 & 0 & 1
 \end{array}
 \quad
 \begin{array}{c|ccc}
 0 & 0 & 0 & 0 \\
 \frac{1}{2} & \frac{1}{2} & 0 & 0 \\
 1 & -1 & 2 & 0 \\
 \hline
 & \frac{1}{6} & \frac{2}{3} & \frac{1}{6}
 \end{array}
 \quad
 \begin{array}{c|cccc}
 0 & 0 & 0 & 0 & 0 \\
 \frac{1}{2} & \frac{1}{2} & 0 & 0 & 0 \\
 \frac{1}{2} & 0 & \frac{1}{2} & 0 & 0 \\
 1 & 0 & 0 & 1 & 0 \\
 \hline
 & \frac{1}{6} & \frac{1}{3} & \frac{1}{3} & \frac{1}{6}
 \end{array} \tag{II.73b}$$

II.6.3 Convergence rates for smooth analytical solutions

In this section, we study the convergence rates on smooth analytical solutions. Both the acoustic and elastic media have the same density and similar wave speeds. Specifically, we consider the simulation time $T_f = 1$ and

- $\Omega^F := (0, 1) \times (0, 1)$, with density $\rho^F := 1$, fluid bulk modulus $\kappa := 1$, and velocity of the pressure waves $c_p^F := 1$,
- $\Omega^S := (-1, 0) \times (0, 1)$, with density $\rho^S := 1$, and Lamé parameters so that $c_p^S := \sqrt{3}$ and $c_S := 1$.

The analytical solution is expressed in terms of the potentials u (acoustic) and $\mathbf{u} := (u_x, u_y)$ (elastic) so that

$$p := \partial_t u \quad \mathbf{m} := \nabla u \quad \text{in } \Omega^F, \quad (\text{II.74a})$$

$$\mathbf{v} := \partial_t \mathbf{u} \quad \mathbb{C}^{-1} : \mathbf{s} := \nabla_{\text{sym}} \mathbf{u} \quad \text{in } \Omega^S. \quad (\text{II.74b})$$

The source terms, the (non)homogeneous Dirichlet boundary conditions, and the initial conditions are defined according to the following choices for the potentials, which indeed satisfy the coupling conditions (II.6a)-(II.6b):

1. Polynomial in space, so that the temporal error is the only error component:

$$u := (1-x)x^2(1-y)y \sin(\sqrt{2}\pi t) \quad u_x = u_y := (1+x)x^2(1-y)y \sin(\sqrt{2}\pi t); \quad (\text{II.75a})$$

2. Polynomial in time, so that the spatial error is the only error component:

$$u = u_x = u_y := x \sin(\pi x) \sin(\pi y) t^2. \quad (\text{II.75b})$$

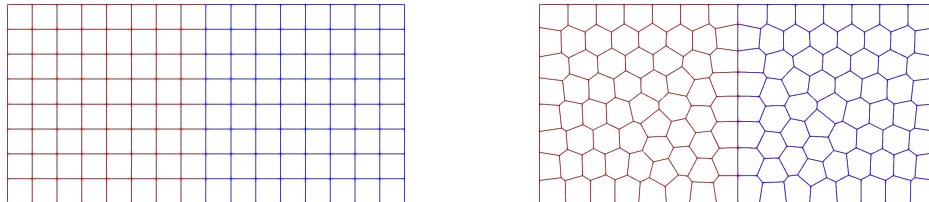


Fig. II.4: Cartesian and polygonal meshes for $\ell = 2$

We consider two types of meshes: Cartesian and polygonal meshes. Some examples are shown in Figure II.4 for $\ell = 2$, with the elastic subdomain mesh on the left side in red, and the acoustic subdomain mesh on the right side in blue. In each subdomain, two types of unknowns contribute to the mechanical energy: (i) the cell components of the HHO unknowns; (ii) the dG unknowns. Thus, we set

$$\|p_{\mathcal{T}^F}, \mathbf{v}_{\mathcal{T}^S}\|_{\text{HHO}}^2 := \|p_{\mathcal{T}^F}(t)\|_{L^2(\frac{1}{\kappa}; \Omega^F)}^2 + \|\mathbf{v}_{\mathcal{T}^S}(t)\|_{\mathbf{L}^2(\rho^S; \Omega^S)}^2, \quad (\text{II.76a})$$

$$\|\mathbf{m}_{\mathcal{T}^F}, \mathbf{s}_{\mathcal{T}^S}\|_{\text{dG}}^2 := \|\mathbf{m}_{\mathcal{T}^F}(t)\|_{\mathbf{L}^2(\rho^F; \Omega^F)}^2 + \|\mathbf{s}_{\mathcal{T}^S}(t)\|_{\mathbb{L}^2(\mathbb{C}^{-1}; \Omega^S)}^2. \quad (\text{II.76b})$$

In what follows, we report these two contributions separately, since they can feature different convergence rates.

We first consider convergence rates in time. For this purpose, we use the analytical solution (II.75a). Figure II.5 shows that, as expected, optimal convergence rates in time are reached in the mixed-order setting and $\mathcal{O}(\frac{1}{h})$ -stabilization: order s for ERK(s) schemes

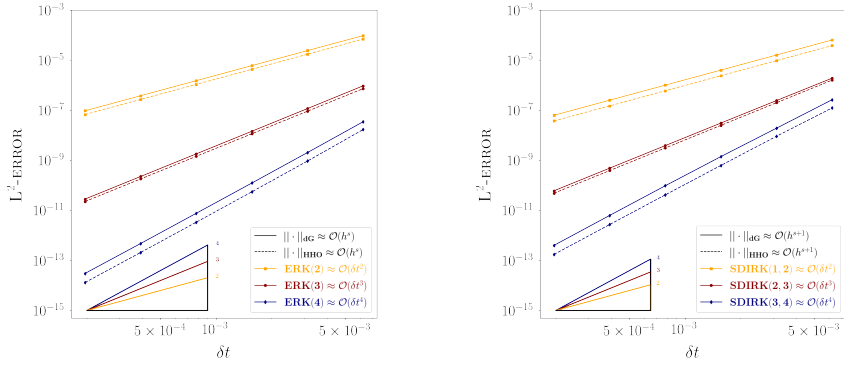


Fig. II.5: Errors as a function of the time step for the analytical solution (II.75a) with a mixed-order discretization, $k = 4$, $\ell = 1$, $n \in \{4, 5, 6, 7, 8, 9, 10\}$ and $\mathcal{O}(\frac{1}{h})$ -stabilization. **Left:** SDIRK($s, s+1$) with $s \in \{1, 2, 3\}$. **Right:** ERK(s) with $s \in \{2, 3, 4\}$.

and order $(s+1)$ for SDIRK($s, s+1$) schemes. The same results are obtained in the equal-order setting, for $\mathcal{O}(1)$ -stabilization, or on polyhedral meshes (results omitted for brevity).

We consider now convergence rates in space on Cartesian meshes. For this purpose, we use the analytical solution (II.75b). The left and central panels of Figure II.6 present the errors (II.76b) as a function of the mesh size for ERK schemes with $\mathcal{O}(1)$ -stabilization in both equal- and mixed-order settings. The right panel of Figure II.6, reports errors (II.76b) as a function of the mesh size for SDIRK schemes in mixed-order setting with $\mathcal{O}(\frac{1}{h})$ -stabilization are reported. For ERK schemes with $\mathcal{O}(1)$ -stabilization in equal- and mixed-order settings, both HHO and dG unknowns exhibit the expected convergence rate of order $(k+1)$ (with sometimes a slight suboptimality for the dG unknowns). In contrast, SDIRK schemes with $\mathcal{O}(\frac{1}{h})$ -stabilization achieve improved convergence rates on the HHO unknowns which now converge at order $(k+2)$, whereas dG unknowns still converge at order $(k+1)$. We still notice a superconvergence phenomenon at lower polynomial orders for the dG unknowns.

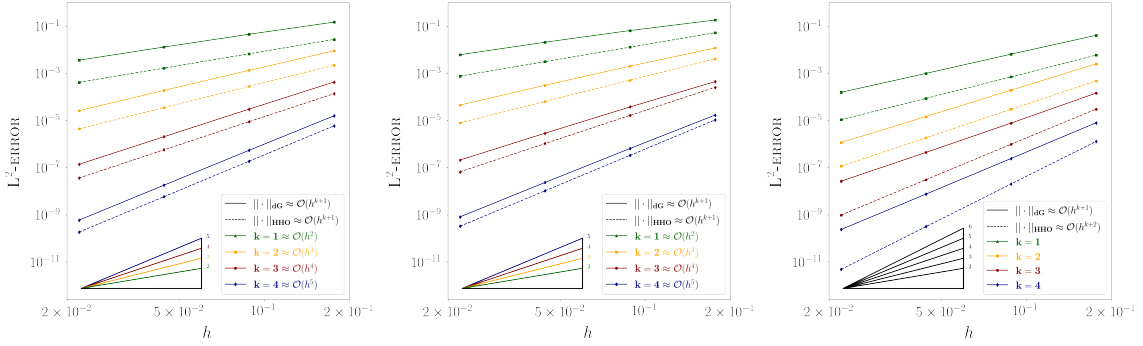


Fig. II.6: Errors (II.76b) as a function of the mesh-size (Cartesian meshes) for the analytical solution (II.75b). **Left:** Equal-order with $\mathcal{O}(1)$ -stabilization. **Center:** Mixed-order with $\mathcal{O}(1)$ -stabilization. **Right:** Mixed-order with $\mathcal{O}(\frac{1}{h})$ -stabilization. Computational parameters: $n = 8$, $\ell \in \{2, 3, 4, 5\}$.

Finally, we evaluate spatial convergence rates on polyhedral meshes. Figure II.7 presents the results for ERK schemes in equal- and mixed-order settings with $\mathcal{O}(1)$ -stabilization and SDIRK schemes in mixed-order setting with $\mathcal{O}(\frac{1}{h})$ -stabilization. The conclusions on polyhedral meshes corroborate those on Cartesian meshes.

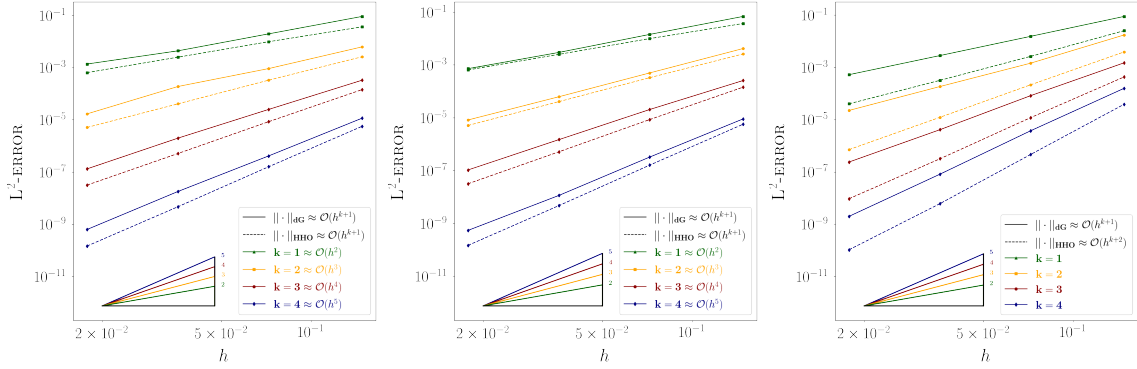


Fig. II.7: Errors (II.76b) as a function of the mesh size (Polyhedral meshes) for the analytical solution (II.75b). **Left:** Equal-order with $\mathcal{O}(1)$ -stabilization. **Center:** Mixed-order with $\mathcal{O}(1)$ -stabilization. **Right:** Mixed-order with $\mathcal{O}(\frac{1}{h})$ -stabilization. Computational parameters: $n = 8$, $\ell \in \{2, 3, 4, 5\}$.

II.6.4 Numerical study of Ricker wavelet as initial condition

This test case deals with the propagation of an elasto-acoustic wave through a heterogeneous domain. Referring to Figure II.8, let H be the height of the domain, H_e the height of the elastic subdomain and L the length of both subdomains. We set $\Omega^F := (0, L) \times (0, H - H_e)$ and $\Omega^S := (0, L) \times (-H_e, 0)$. Two sensors \mathcal{S}^F and \mathcal{S}^S are positioned on a vertical line as in the Figure II.8 so as to have one sensor in each subdomain. For the acoustic sensor \mathcal{S}^F , the acoustic pressure $p_{\mathcal{T}^F}$ is considered, and for the elastic sensor \mathcal{S}^S the x - and y -components of the elastic velocity $\mathbf{v}_{\mathcal{T}^S}$ are considered. Homogeneous Dirichlet boundary conditions are enforced, the source terms are null, and the initial condition corresponds to a velocity Ricker wavelet centered at the point $(x_c, y_c) \in \Omega^F$ (in purple on Figure II.8) given by the following expression:

$$\mathbf{m}_0(x, y) := \theta \exp \left(-\pi^2 \frac{r^2}{\lambda^2} \right) (x - x_c, y - y_c)^\dagger \quad (\text{II.77})$$

with $\theta := 10 \left[\frac{1}{\text{s}} \right]$, $\lambda := \frac{c_p^F}{f_c} [\text{m}]$ with $f_c := 10 \left[\frac{1}{\text{s}} \right]$ and $r^2 := (x - x_c)^2 + (y - y_c)^2$. This initial condition corresponds to a velocity Ricker wave centered at the point $(x_c, y_c) \in \Omega$.

II.6.4.1 Academic setting

We first consider an academic case in which the acoustic and elastic media have the same density and propagate S-waves at the same speed as compressional acoustic waves, *i.e.*,

$$\rho^F = \rho^S = 1, \quad c_p^S = \sqrt{3}, \quad c_p^F = c_s^S = 1. \quad (\text{II.78})$$

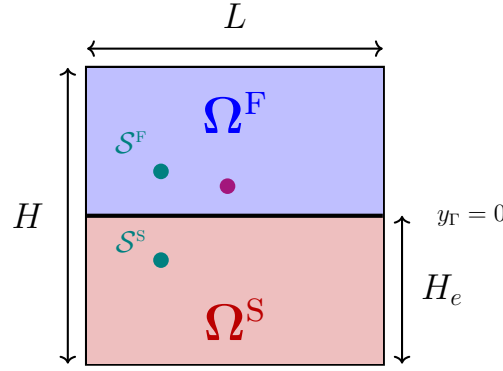


Fig. II.8: Ricker wavelet test case

As the material properties are similar, we consider two subdomains of the same dimension, with $L = H = 1$, $H_e = 0.5$ and $x_c := 0$, $y_c := 0.125$ for the origin of the pulse in the acoustic subdomain. The simulation time is set to $T_f := 10$.

The following results are obtained using the SDIRK(3, 4) time scheme with a mixed-order setting and $\mathcal{O}(1)$ -stabilization. Figure II.9 displays the two-dimensional pressure distribution in the acoustic subdomain and the Euclidean norm of the velocity in the elastic subdomain at times $t \in \{0, 0.25, 0.27, 0.32\}$. We can see that the simulation propagates correctly the acoustic Ricker wavelet through the elasto-acoustic interface. The difference in properties, intrinsic to the nature of the media, causes a small reflection of the acoustic wave when it meets the interface. Moreover, we observe the transmission of the compressional wave as a P-wave (with the larger celerity), as well as the creation of an S-wave in the elastic part of the domain.

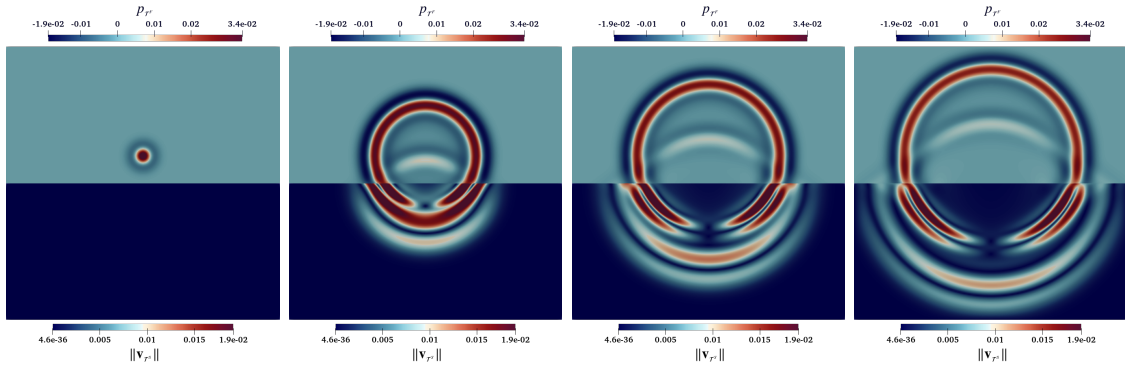


Fig. II.9: Spatial distribution of the acoustic pressure (upper side) and the elastic velocity norm (lower side) at times $t \in \{0, 0.25, 0.27, 0.32\}$ predicted by SDIRK(3, 4) scheme with mixed-order setting, $\mathcal{O}(\frac{1}{h})$ -stabilization, $k = 1$, $\ell = 7$, and $n = 9$.

A comparison to a semi-analytical solution provided by the open source software Gar6more (<https://gitlab.inria.fr/jdiaz/gar6more2d>) is performed in Figure II.10. For two-dimensional infinite or semi-infinite domains, this code computes the analytical solution of elasto-acoustic waves propagating in homogeneous or heterogeneous media. In particular, the software analytically convolves the Green function of the problem with the source function. The solution is called semi-analytical since the convolution is done by

a numerical integration. In Figure II.10, we report the solution for times $t \in [0, 0.25]$ at the two sensors $\mathcal{S}^F := (-0.15, 0.1)$ and $\mathcal{S}^S := (-0.15, -0.1)$ with the material properties defined in (II.78), for two rather coarse meshes: $\ell = 4$ on the left column and $\ell = 5$ on the right column. Figure II.10 shows that, for a moderate property contrast, even on the rather coarse mesh corresponding to $\ell = 4$, we can approximate the analytical solution with high accuracy by increasing the polynomial order. Altogether, only the case $k = 1$ on the coarse mesh does not allow to obtain an accurate representation of the solution.

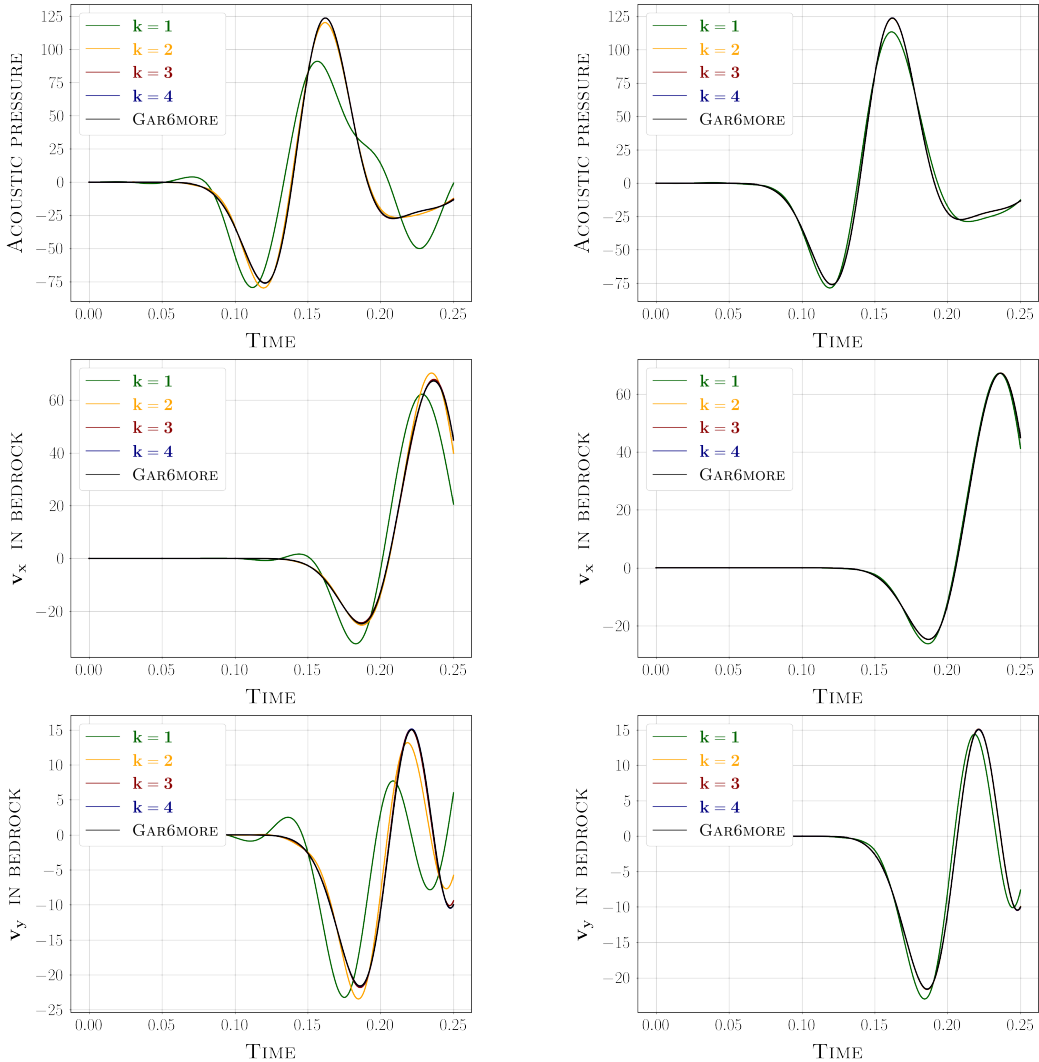


Fig. II.10: Ricker wavelet with homogeneous material properties (see (II.78)). Comparison of the solution over time with the semi-analytical solution at sensors \mathcal{S}^F (1^{st} row), and \mathcal{S}^S (2^{nd} and 3^{rd} rows) for $n = 9$ and $\ell = 4$ (left column) and $\ell = 5$ (right column).

II.6.4.2 Realistic (contrasted) setting

We now investigate a test case with a strong property contrast focusing on two cases corresponding to granite and water (II.79a) and granite and air (II.79b):

$$\rho^S = 2.6\rho^F = 1.3, \quad c_p^S = 4c_p^F = 2, \quad c_s^S = 2c_p^F = 1, \quad (\text{II.79a})$$

$$\rho^S = 2200\rho^F = 800, \quad c_p^S = 17.5c_p^F = 6.36, \quad c_s^S = 9c_p^F = 3.27. \quad (\text{II.79b})$$

We report the solution for times $t \in [0, 0.5]$ at the two sensors $\mathcal{S}^F := (-0.05, 0.1)$ and $\mathcal{S}^S := (-0.05, -0.1)$. Figure II.11 reports the results for case (II.79a) and Figure II.12 those for (II.79b) on two meshes: $\ell = 5$ on the left column and $\ell = 6$ on the right column (this corresponds to one more level of refinement than for the low-contrast case).

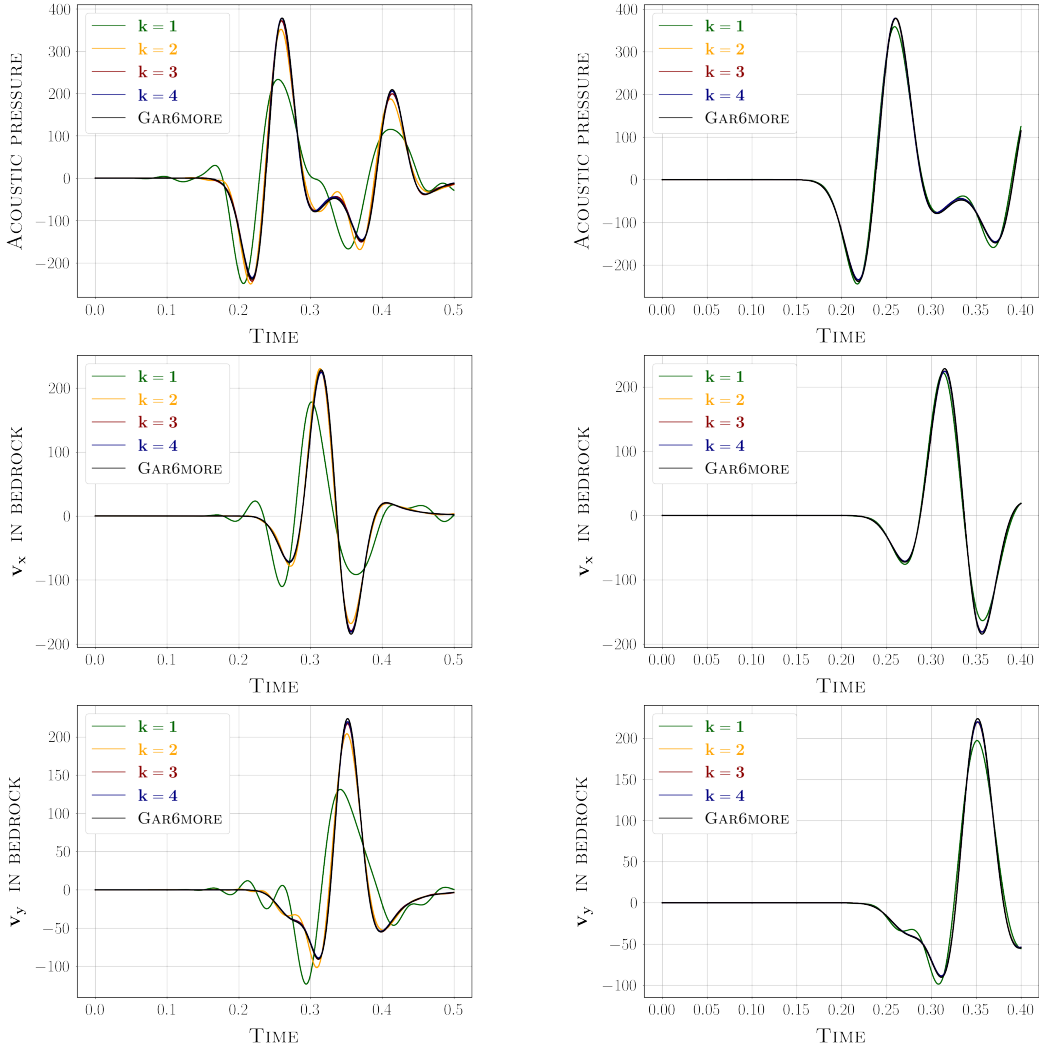


Fig. II.11: Ricker wavelet with granite-water contrast (see (II.79a)). Comparison of the solution over time with the semi-analytical solution at sensors \mathcal{S}^F (1^{st} row) and \mathcal{S}^S (2^{nd} and 3^{rd} rows) for $n = 9$ and $\ell = 5$ (left column) and $\ell = 6$ (right column).

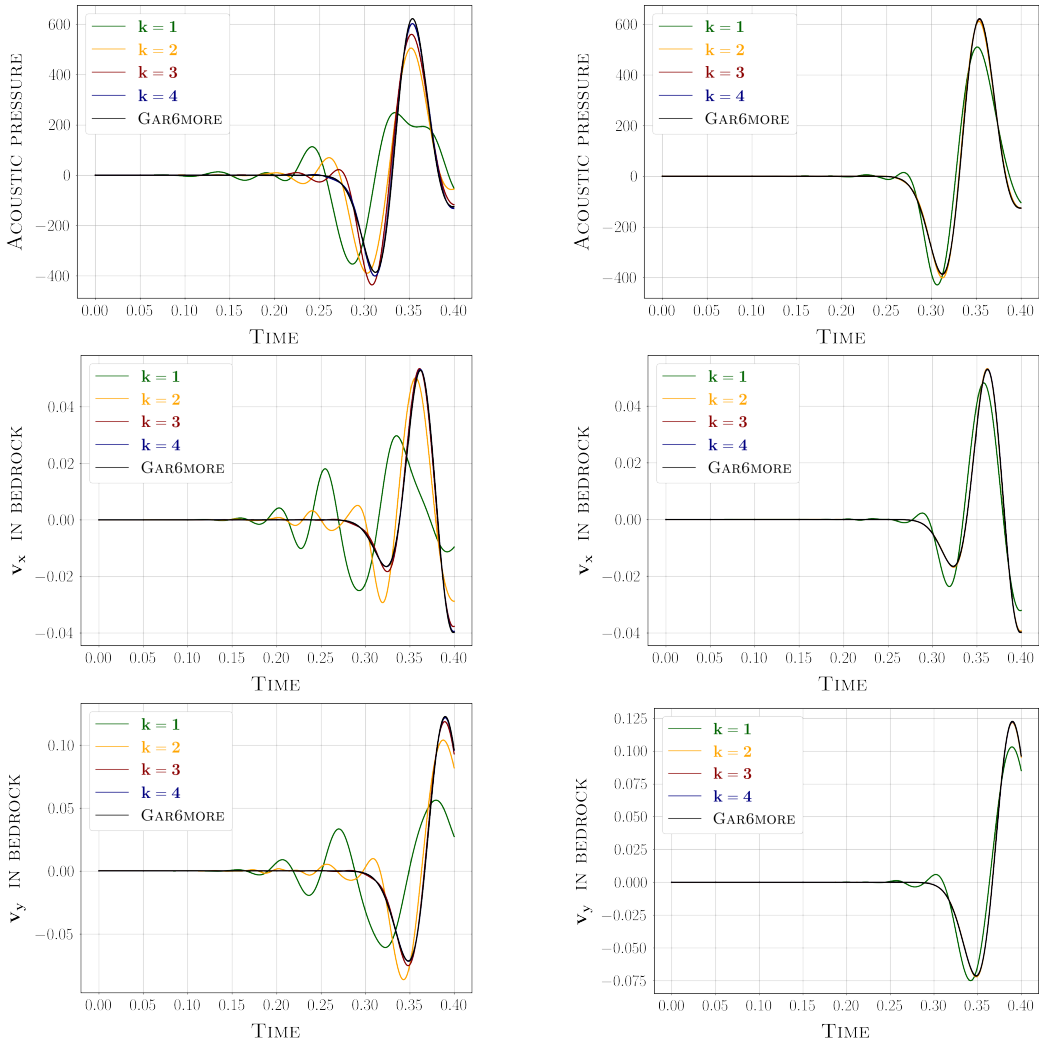


Fig. II.12: Ricker wavelet with granite-air contrast (see (II.79b)). Comparison of the solution over time with the semi-analytical solution at sensors \mathcal{S}^F (1^{st} row) and \mathcal{S}^S (2^{nd} and 3^{rd} rows) for $n = 9$ and $\ell = 5$ (left column) and $\ell = 6$ (right column).

The results reported in Figures II.11 and II.12 exhibit the same characteristics as in the previous case, thus demonstrating that the present scheme effectively handles strong property contrasts by accurately describing the solution (excluding the case $k = 1$ on the coarse mesh). Finally, as expected, the greater the contrast, the larger the amplitude difference between the acoustic and elastic signals. Indeed, while the signals in Figure II.10 have similar amplitudes, Figure II.11 and Figure II.12 show that as the contrast increases, the signals in the receiving medium become weaker due to strong wave reflections at the interface.

In Figures II.13 and II.14, we focus on the time evolution of the discrete energy of the global system. In Figure II.13, the left panel shows the energy repartition as a function of time for $t \in [0, 10]$, polynomial order $k = 3$ space refinement $\ell = 6$, and time refinement $n = 9$. In the right panel, we study the relative energy loss as the ratio of energy at times $t \in [0, 1]$ with the energy at initial time for different polynomial degrees $k \in \{1, 2, 3\}$

and space refinement levels $\ell \in \{4, 5, 6\}$. In the left panel, we observed that, in the absence of contrast, the energy initially concentrated in the acoustic subdomain is partially transferred to the elastic subdomain. On longer time scales, energy oscillates with a moderate amplitude around an equal distribution between the two subdomains. In the right panel, we can see that increasing the polynomial order and/or the space refinement level significantly reduces energy dissipation. For all reasonable discretizations, the energy dissipation stays below 1% for all $t \in [0, 1]$. In the left panel of Figure II.14, we show the energy repartition for the contrasted case (II.79a) with $\ell = 6$ and $k = 3$. We observe that, owing to the increase in property contrast, significantly less energy is transmitted from the acoustic medium to the elastic medium, which is consistent with the decrease in signal amplitude observed in Figures II.11 and II.12. The same test cases were conducted with the initial pulse located in the elastic medium, and a similar distribution of the energy was observed between the emitting medium and the receiving medium. For the sake of brevity, these results are not reported here.

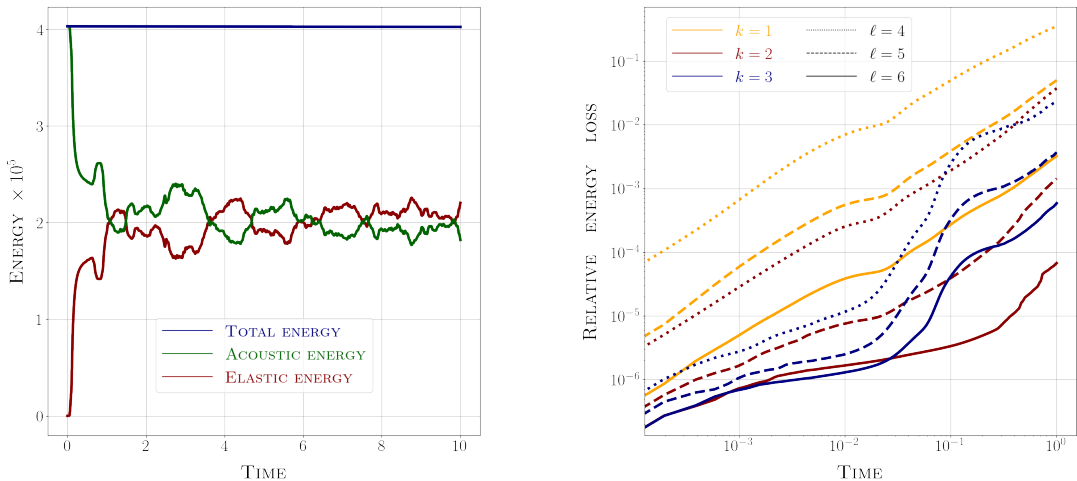


Fig. II.13: SDIRK(3, 4) scheme with $n = 9$. **Left:** Energy repartition as a function of the time for $k = 3$ and $\ell = 6$. **Right:** Relative energy loss as function of the time for $k \in \{1, 2, 3\}$ and $\ell \in \{4, 5, 6\}$.

To conclude, we perform the granite-water test case (II.79a) with scaled values for the material properties and the geometry. We set

$$\begin{aligned} \rho^F &:= 1025 \text{ kg.m}^{-3}, & c_p^F &:= 1500 \text{ m.s}^{-1}, \\ \rho^S &:= 2690 \text{ kg.m}^{-3}, & c_p^S &:= 6000 \text{ m.s}^{-1}, & c_s^S &:= 3000 \text{ m.s}^{-1}, \end{aligned} \quad (\text{II.80})$$

as well as $L := 5000$ m, $H := 3500$ m, $H_e := 2500$ m for the dimensions of the domain and $x_c := 0$ m, $y_c := 500$ m for the center of the pulse in the acoustic subdomain, and a simulation time $T_f := 0.425$ s. Figure II.15 displays the two-dimensional distributions of the pressure in the acoustic region and of the velocity norm in the elastic region at times $t \in \{0.1275, 0.3825\}$ predicted by the SDIRK(3, 4) scheme, with computational parameters $k = 3$ and $n = 8$. A quadrangular mesh is considered with $h_x = 8.93$ m and $h_y = 6.25$ m. The computational domain has been chosen sufficiently large in order to

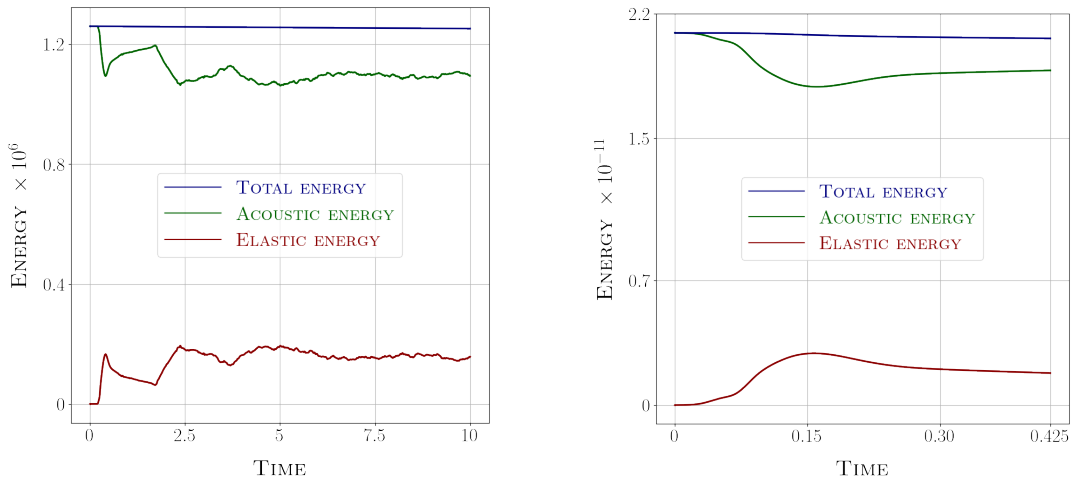


Fig. II.14: Ricker wavelet for granite-water test case: Energy repartition as a function of the time predicted by SDIRK(3,4) scheme. **Left:** Test case (II.79a), $k = 3$, $n = 9$ and $\ell = 6$. **Right:** Test case (II.80), $k = 3$, $n = 8$, $h_x = 8.93$ m and $h_y = 6.25$ m.

avoid the bouncing off the walls due to the homogeneous Dirichlet conditions and to allow the waves to develop. We can see that the simulation captures well the penetration of the

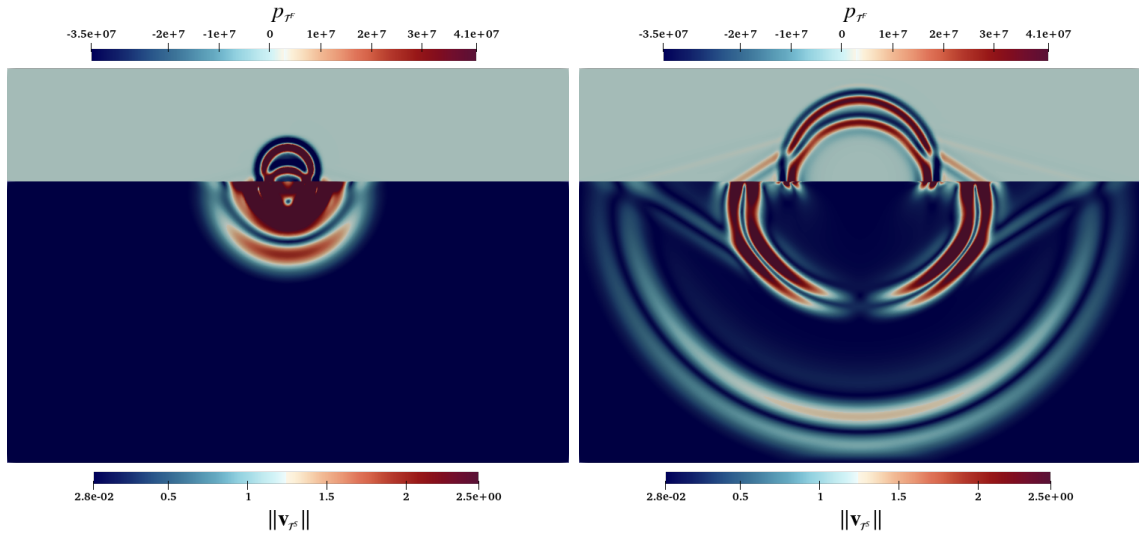


Fig. II.15: Ricker wavelet for granite-water test case (II.80): Spatial distribution of the acoustic pressure (upper side) and the elastic velocity norm (lower side) at times at times $t \in \{0.1275, 0.3825\}$ predicted by SDIRK(3,4) with mixed-order setting, $\mathcal{O}(\frac{1}{h})$ -stabilization, $k = 3$, $n = 8$, $h_x = 8.93$ m and $h_y = 6.25$ m.

wave into the elastic domain. The lateral conical wavefronts are accurately represented, along with the interface, Rayleigh-type waves, which are characterized by the constructive interferences between P-waves and polarized S-waves at the interface. The right panel of Figure II.14 shows the energy repartition related to this test case.

In conclusion, all these results highlight the robustness of the proposed scheme in

accurately modeling wave propagation through media with significant density and wave velocity contrasts.

II.7 Conclusion

In this paper, we studied the elasto-acoustic coupled wave problem in first-order form approximated using dG (for the dual variable) and HHO (for the primal variable) space discretizations including several variants for HHO: equal- or mixed-order and stabilization parameters $\mathcal{O}(1)$ or $\mathcal{O}(\frac{1}{h})$. We performed a space semi-discrete analysis based on the H^+ interpolation operator for the dual variable instead of the standard L^2 projection operator. This choice makes the time-continuous analysis simpler than in [34]. Compared to dG which stabilizes both primal and dual variables and achieves $\mathcal{O}(h^{k+\frac{1}{2}})$ convergence rates (see, e.g. [36]), we stabilize only the primal variable and achieve $\mathcal{O}(h^{k+1})$ convergence rates. The spectral analysis study in Section 6.1 showcases the effect of different stabilization weights on the CFL condition. In the numerical experiments of Section 6.3, we considered both implicit and explicit time-stepping schemes, and confirmed the theoretical convergence rates on an academic test case. Moreover, we observed $\mathcal{O}(h^{k+2})$ convergence rates for the primal variable in the L^2 -norm when using the mixed-order HHO method with $\mathcal{O}(\frac{1}{h})$ -stabilization. In Section 6.4, we presented a realistic Ricker wavelet test case with contrasted material properties and demonstrated that our scheme accurately captures wave propagation across interfaces. An interesting perspective for further work is to explore nonlinear coupled wave models. One of the advantages of HHO with respect to dG in this context is that the integration of nonlinear behavior laws is only required at the quadrature nodes in the cells, but not on the faces [1]. Another perspective for future work is to analyze the fully discrete scheme involving a DIRK time scheme combined with the HHO space discretization.

Wave propagation in geophysical media using HHO methods on general meshes

Abstract

Hybrid high-order (HHO) methods are numerical methods characterized by several interesting properties such as local conservativity, geometric flexibility and high-order accuracy. Here, HHO schemes are studied for the space semi-discretization of coupled elasto-acoustic waves in the time domain using a first-order formulation. Explicit and singly diagonal implicit Runge–Kutta (ERK & SDIRK) schemes are used for the time discretization. We show that an efficient implementation of explicit (resp. implicit) time schemes calls for a static condensation of the face (resp. cell) unknowns. Crucially, both static condensation procedures only involve block-diagonal matrices. Then, we provide numerical estimates for the CFL stability limit of ERK schemes and present a comparative study on the efficiency of explicit versus implicit schemes. Our findings indicate that implicit time schemes remain competitive in many situations. Finally, simulations in a 2D realistic geophysical configuration are performed, illustrating the geometrical flexibility of the HHO method: both hybrid (triangular and quadrangular) and nonconforming (with hanging nodes) meshes are easily handled, delivering results of comparable accuracy to a reference spectral element software based on tensorized elements.

This chapter is based on a paper submitted to *Computer Methods in Applied Mechanics and Engineering (CMAME)* entitled “Elasto-acoustic wave propagation in geophysical media using hybrid high-order methods on general meshes” [120].

Contents

III.1 Introduction	68
III.2 Model problem	71
III.2.1 Strong formulation	71
III.2.2 Weak formulation	73
III.3 HHO space semi-discretization	73
III.3.1 Mesh	73
III.3.2 Degrees of freedom	74
III.3.3 Space semi-discrete formulation and algebraic realization	75
III.4 Fully discrete schemes	80
III.4.1 Singly Diagonal Implicit Runge-Kutta (SDIRK) schemes	81
III.4.2 Explicit Runge–Kutta (ERK) schemes	82

III.5 Numerical results	83
III.5.1 CFL and efficiency study on a sinusoidal test case	83
III.5.2 Accuracy study and efficiency on a Ricker wavelet	89
III.5.3 Geometric flexibility of HHO: a realistic simulation	92
III.6 Conclusion	97

III.1 Introduction

The accurate computation of mechanical wave propagation is crucial in numerous scientific fields, such as medical imaging [136], non-destructive testing [104], or geophysics [103]. In geophysics for instance, seismic (*i.e.*, elastic), hydroacoustic or infrasonic waves are used to probe the Earth at the local (petroleum and marine exploration) and global scales. Owing to a broad suite of recording instruments deployed in various Earth's environments, these wavefields jointly provide insights into the Earth's internal structure [84], seismic source properties, or help monitoring natural hazards [10]. The success of these endeavors strongly depends on the ability to compute and understand how an elasto-acoustic wavefield propagates through media that are heterogeneous and different in nature (solid, fluid). Closed-form or semi-analytical solutions are available only for the simplest geometrical configurations [3], while asymptotic methods often rely on assumptions that may not be fulfilled in more complex scenarios (*e.g.*, ray theory or single-scattering approximations). Consequently, numerical methods that accurately simulate the partial differential equations describing elasto-acoustic waves are required to simulate wave propagation in realistic media of complex geometry.

Advances in high-performance computing have triggered the emergence of various numerical methods. The finite difference method (FDM) is still widely used [118], evolving from regular-grid to staggered-grid approaches with improved accuracy [140]. Despite its efficiency on rectilinear meshes, FDM has long struggled with complex geometries and strong material contrasts. Extensions to more intricate domains have been developed [127], but requiring an increased computational effort. Additionally, higher-order FDM introduce larger stencils, negatively impacting parallel scalability.

A natural alternative to FDM are continuous finite element methods (FEM), which accommodate unstructured meshes and intricate boundaries. However, low-order FEM is computationally inefficient [112], and its high-order extension can suffer from aliasing issues. The spectral element method (SEM), introduced in [125] for fluid dynamics and later adapted to time-domain wave equations [101], leverages the accuracy of spectral methods owing to high-order polynomial approximations based on Lagrangian basis functions whose nodes coincide with the tensorized Gauss-Lobatto-Legendre (GLL) quadrature points. This choice ensures a diagonal mass matrix and efficient explicit time-stepping while retaining high-order accuracy. SEM have been successfully applied to coupled elasto-acoustic wave propagation [100, 44] with a description of the fluid velocity using a potential field. However, SEM essentially relies on a space discretization with quadrilateral/hexahedral elements, which poses meshing challenges for realistic 3D applications. Different extensions to simplicial meshes [60, 116] have demonstrated good dispersion

properties [115], yet they may introduce additional computational overheads, difficulties in increasing the order of accuracy, or a loss of mass matrix diagonalization [116]. Moreover, handling severe wavespeed discontinuities necessitates multiscale discretizations in space (nonconforming meshes with h - or p -adaptivity) or time (multiple-time stepping), leading to increased algorithmic complexity, higher computational costs [42], and potential instabilities [71].

These limitations have sparked interest in discontinuous methods, such as finite volume (FV) and discontinuous Galerkin (dG) methods. Both methods rely on local information exchanges through fluxes at mesh interfaces, thereby relaxing the classical FEM C^0 -continuity constraint, and accommodating more naturally meshes with hanging nodes for instance. Some dG methods adopt a second-order formulation in time (*e.g.*, interior penalty methods [87, 62, 5]), whereas others (including FV) adopt a first-order formulation in time, solving for both primal (pressure in acoustics, velocity in elastodynamics) and dual (velocity in acoustics, stress in elastodynamics) variables. Several dG variants exist, depending on the fluxes (some based on Godunov-type upwind fluxes [73, 143], others on central fluxes [117] or modified upwind [145]) and on the polynomial setting (*e.g.*, dG-SEM combinations [143, 6]). While dG methods achieve FEM-like convergence rates, their high computational costs due to the substantial amount of degrees of freedom generally remain a drawback.

Thus, there is room for alternative numerical strategies. Among others, like the Distributional Finite-Difference Method (DFDM) [114], or the Virtual Element Method (VEM) [61], one promising approach is the family of hybrid nonconforming methods, which leverage ideas from both FEM and dG. Hybrid nonconforming methods can achieve higher-order accuracy through a consistent gradient reconstruction based on an additional unknown field defined on the mesh skeleton, hence the term "hybrid". Compared to dG methods, hybrid nonconforming methods have several advantages: (i) They include a built-in and robust stabilization that is less sensitive to parameter tuning than the one used in dG methods; (ii) In the context of elliptic problems, they achieve H^1 -convergence of order $(k + 1)$ and L^2 -convergence of order $(k + 2)$, *i.e.* one order higher than dG methods. For the wave equation in first-order form, they can achieve L^2 -convergence of order $(k + 2)$ under a post-processing for the primal variable [57] (although it may be insufficient in elastodynamics [138]). Moreover, these methods allow for a natural enforcement of coupling conditions by means of the unknowns attached to the mesh skeleton.

The most salient example of hybrid nonconforming method is the Hybridizable dG method (HDG). This method was first proposed in [122] for the wave equation in first-order form, following the seminal work [55] on HDG methods for elliptic problems (see also [54] for a second-order formulation in time). HDG methods allow for efficient implicit time-stepping by leveraging static condensation (*i.e.* the local elimination of the cell unknowns). Efficient explicit time-stepping is also possible whenever the stabilization bilinear form leads to a block-diagonal face-face matrix. Explicit and implicit HDG schemes for the wave equation are compared in [102], where explicit schemes were found more efficient for various configurations. Different conclusions are drawn in the present work, allowing at least to say that the explicit and implicit approaches are both relevant.

Another compelling instance in the class of hybrid nonconforming methods is the

Hybrid High-Order (HHO) method. The HHO method approximates the solution within the mesh cells and its trace on the mesh skeleton, both by polynomial unknowns. The setting is of equal-order when the cell and face polynomials are of the same order $k \geq 0$, whereas the setting is of mixed-order when the cell polynomials are one order higher than the face polynomials. The two devising principles of HHO methods are: (i) a gradient reconstruction in each mesh cell from the local cell and face unknowns; (ii) a stabilization that weakly enforces locally the matching of the trace of the cell unknowns with the corresponding face unknowns. Although the devising principles in HHO differ from those in HDG, it has been shown in [53] (see also [50]) that tight connections exist between both approaches, as well as with other hybrid nonconforming methods such as Weak Galerkin and nonconforming VEM. HHO methods were introduced in [68] for linear elasticity and in [69] for linear diffusion. Since then, HHO methods have been applied to a broad range of problems. We refer the reader to the two textbooks [50, 65] and to [32, 33, 135] for the development of HHO methods applied to the (purely) acoustic or elastic wave equation in first- and second-order form (see also [81, 80] for further analysis results).

The approximation of coupled elasto-acoustic waves using HHO methods in space and Runge–Kutta (RK) schemes in time has been started in [121]. Therein, the devising principles of the method were established, and an error analysis in the space semi-discrete setting was proposed. Moreover, numerical results, mostly on academic test cases, were presented to showcase the stability and accuracy properties of the proposed method. Let us briefly summarize the main findings. On the one hand, if explicit RK (ERK) time-stepping schemes are considered, it is recommended to scale the stabilization by an $\mathcal{O}(1)$ -weight (to alleviate the CFL restriction) and to use a plain Least-Squares stabilization. Because of this, it is natural to consider an equal-order setting for the cell and face unknowns. On the other hand, for implicit RK (IRK) schemes, one can consider tighter stabilizations to obtain higher-order convergence rates. Namely, one can scale the stabilization by an $\mathcal{O}(\frac{1}{h})$ -weight (where h is the mesh size) and employ any of the high-order HHO stabilization operators. As discussed in [48] for elliptic problems, the mixed-order setting with Lehrenfeld–Schöberl stabilization appears to be more computationally effective.

In this work, we further develop the above methodology, addressing important computational aspects and assessing the approach on more realistic geophysical settings. The HHO formulations for the explicit and implicit time schemes are those discussed above. Our first main contribution in the paper is to recast the fully discrete problem in algebraic form, so as to show that an efficient implementation of implicit (resp. explicit) time schemes calls for a static condensation of the cell (resp. face) unknowns. Crucially, both static condensation procedures only involve block-diagonal matrices. Our second main contribution is to estimate numerically the CFL stability limit for explicit time schemes and to provide a comparative study on the efficiency of explicit versus implicit time schemes. This is performed on test cases with manufactured solutions and in bilayered problems with an initial Ricker wavelet. As mentioned above, our findings indicate that implicit time schemes remain competitive in many situations. Our third main contribution is to consider a realistic test case including waves trapped in a sedimentary basin, and to show that the proposed methodology delivers accurate solutions, while offering the capability of handling general meshes with hanging nodes. Reference solutions for this latter test case

are obtained using a spectral element software using tensorized elements.

The paper is organized as follows. Section III.2 introduces the coupled elasto-acoustic model and presents its first-order weak formulation. Section III.3 presents the HHO space semi-discretization. Section III.4 describes the fully discrete problem, incorporating both explicit and implicit RK schemes and showing the relevance of static condensation procedures in both cases. Section III.5 (i) investigates numerically the CFL stability limit for ERK and compared the efficiency (error vs. CPU time) of both explicit and implicit time schemes ; (ii) verifies the accuracy of the proposed methodology on a Ricker wavelet test case (with realistic material properties) for which a semi-analytical solution is available, and performs a further comparative study of explicit vs. implicit time schemes; (iii) showcases the performances of the proposed method on a two-dimensional test case inspired by recent seismoacoustic observations, focusing on the emission of acoustic energy due to the interaction between seismic waves and a sedimentary basin [93, 11]. Numerical results obtained on quadrilateral, simplicial, hybrid, and nonconforming meshes (with hanging nodes) are compared to those produced by a reference spectral element solver based on tensorized elements, thus highlighting the versatility of the HHO method to handle general meshes in complex geological media.

III.2 Model problem

This section presents the model problem. We use boldface (resp. blackboard) fonts for vectors (resp. tensors), and for vector-valued (resp. tensor-valued) fields and spaces composed of such fields. For a bounded and uniformly positive weight κ , we define the κ -weighted L^2 -inner product as $(u, v)_{L^2(\kappa; \Omega)} := \int_{\Omega} \kappa u v \, d\Omega$ for all $u, v \in L^2(\Omega)$. A similar notation is used for inner products involving vector- and tensor-valued fields.

III.2.1 Strong formulation

Let $J := (0, T_f)$ denotes the time interval of interest, where $T_f > 0$ represents the final time, and let Ω be a polyhedral domain (open, bounded, connected, Lipschitz set) in \mathbb{R}^d , with $d \in \{2, 3\}$. We partition Ω into two disjoint, polyhedral subdomains, Ω^F and Ω^S (of boundaries $\partial\Omega^F$ and $\partial\Omega^S$), representing the solid and fluid media, respectively. These subdomains share the interface $\Gamma := \partial\Omega^F \cap \partial\Omega^S$, and the unit normal vector \mathbf{n}_Γ on Γ conventionally points from Ω^S to Ω^F . A simplified representation of this setting is displayed in Figure III.1 illustrating the geophysical application considered in Section III.5.

The linear acoustic wave propagation is defined by the evolution of its scalar pressure field p [Pa] and velocity field \mathbf{m} [$\frac{\text{m}}{\text{s}}$], which are described by the following system of partial differential equations in $J \times \Omega^F$:

$$\rho^F \partial_t \mathbf{m} - \nabla p = \mathbf{0}, \quad (\text{III.1a})$$

$$\frac{1}{\kappa} \partial_t p - \nabla \cdot \mathbf{m} = f^F, \quad (\text{III.1b})$$

where ρ^F [$\frac{\text{kg}}{\text{m}^3}$] is the fluid density, κ [Pa] is the fluid bulk modulus, and f^F [Hz] is the source term. The equation (III.1b) is derived by considering a perfect fluid, where the stress tensor is given by $\mathbf{s}^F := p \mathbb{I} d$, instead of the classical convention $\mathbf{s}^F := -p \mathbb{I} d$, where

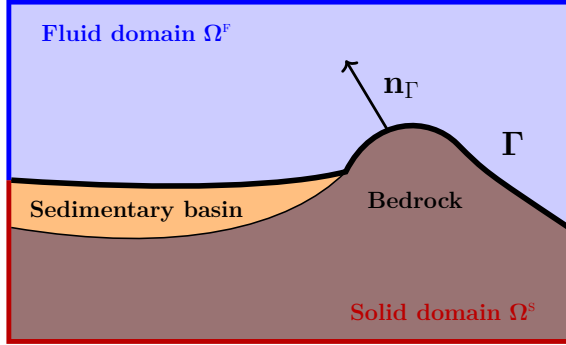


Fig. III.1: Solid subdomain Ω^S composed of the sedimentary basin and the bedrock, fluid subdomain Ω^F , and unit normal \mathbf{n}_Γ along the interface Γ (highlighted with a thick black line)

$\mathbb{I}d$ is the identity tensor. The material properties ρ^F and κ are typically piecewise constant in Ω^F , although it is not mandatory (they can smoothly evolve in space). The speed of the acoustic waves is given by $c_p^F := \sqrt{\kappa/\rho^F}$ [$\frac{m}{s}$]. The initial conditions are specified as $p(0) = p_0$ and $\mathbf{m}(0) = \mathbf{m}_0$ with initial data p_0 and \mathbf{m}_0 .

Let $\nabla_{\text{sym}} := \frac{1}{2}(\nabla + \nabla^\dagger)$ denote the symmetric gradient operator. The elastic wave equations, which describe the evolution of the linearized Cauchy stress tensor \mathbf{s} [Pa] and the velocity field \mathbf{v} [$\frac{m}{s}$], consist of the following partial differential equations in $J \times \Omega^S$:

$$\mathbb{C}^{-1} \partial_t \mathbf{s} - \nabla_{\text{sym}} \mathbf{v} = \emptyset, \quad (\text{III.2a})$$

$$\rho^S \partial_t \mathbf{v} - \nabla \cdot \mathbf{s} = \mathbf{f}^S, \quad (\text{III.2b})$$

where ρ^S [$\frac{kg}{m^3}$] is the solid density, \mathbb{C} [Pa] is the fourth-order Hooke tensor, and \mathbf{f}^S [$\frac{N}{m^3}$] is the source term. The material properties \mathbb{C} and ρ^S can be considered piecewise constant in Ω^S . In the framework of isotropic elasticity, \mathbb{C} depends on the Lamé parameters λ [Pa] and μ [Pa] as $\mathbb{C}_{ijkl} := \lambda \delta_{ij} \delta_{kl} + \mu (\delta_{ik} \delta_{jl} + \delta_{il} \delta_{jk})$, for all $i, j, k, l \in \{1, \dots, d\}$, where δ is the Kronecker symbol. This setting gives rise to two wave speeds [$\frac{m}{s}$] corresponding to two types of body waves, far from material interfaces:

$$c_p^S := \sqrt{(\lambda + 2\mu)/\rho^S} \quad \text{for compressional (P-) waves}, \quad (\text{III.3a})$$

$$c_s^S := \sqrt{\mu/\rho^S} \quad \text{for shear (S-) waves}. \quad (\text{III.3b})$$

We do not consider the incompressible limit where $\frac{\lambda}{\mu} \gg 1$, so that the two wave speeds in (III.3) are expected to be of similar magnitude. The initial conditions are specified as $\mathbf{v}(0) = \mathbf{v}_0$ and $\mathbf{s}(0) = \mathbf{s}_0$, with initial data \mathbf{v}_0 and \mathbf{s}_0 .

For simplicity, we impose homogeneous Dirichlet boundary conditions on p on $\partial\Omega^F \setminus \Gamma$ and on \mathbf{v} on $\partial\Omega^S \setminus \Gamma$, which lead to perfect wave reflection at the domain boundaries. The computational domain and time are chosen appropriately, so as to avoid any spurious reflection that could interfere with the main phenomena we want to simulate.

The interface conditions on $J \times \Gamma$ are expressed as follows:

$$\mathbf{v} \cdot \mathbf{n}_\Gamma = \mathbf{m} \cdot \mathbf{n}_\Gamma, \quad (\text{III.4a})$$

$$\mathbf{s} \cdot \mathbf{n}_\Gamma = p \mathbf{n}_\Gamma, \quad (\text{III.4b})$$

where the first equation enforces the continuity of the normal velocity component across the interface (kinematic condition on a perfect fluid-solid boundary where tangential slip is allowed, but there is no separation or interpenetration), and the second equation (dynamic condition) expresses the balance of forces.

III.2.2 Weak formulation

We define the following functional spaces:

$$\mathbf{M}^F := \mathbf{L}^2(\Omega^F), \quad P^F := \left\{ p \in H^1(\Omega^F) : p|_{\partial\Omega^F \setminus \Gamma} = 0 \right\}, \quad (\text{III.5a})$$

$$\mathbf{S}^S := \mathbb{L}_{\text{sym}}^2(\Omega^S), \quad \mathbf{V}^S := \left\{ \mathbf{v} \in \mathbf{H}^1(\Omega^S) : \mathbf{v}|_{\partial\Omega^S \setminus \Gamma} = \mathbf{0} \right\}. \quad (\text{III.5b})$$

The coupled elasto-acoustic wave problem then consists of finding $(\mathbf{m}, p) : J \rightarrow \mathbf{M}^F \times P^F$ and $(\mathbf{s}, \mathbf{v}) : J \rightarrow \mathbf{S}^S \times \mathbf{V}^S$ such that, for all $t \in J$, the following weak equations hold:

- i) For the acoustic wave equations, for all test functions $(\mathbf{r}, q) \in \mathbf{M}^F \times P^F$,

$$(\partial_t \mathbf{m}(t), \mathbf{r})_{\mathbf{L}^2(\rho^F; \Omega^F)} - (\nabla p(t), \mathbf{r})_{\mathbf{L}^2(\Omega^F)} = 0, \quad (\text{III.6a})$$

$$(\partial_t p(t), q)_{L^2(\frac{1}{\kappa}; \Omega^F)} + (\mathbf{m}(t), \nabla q)_{\mathbf{L}^2(\Omega^F)} + (\mathbf{v}(t) \cdot \mathbf{n}_\Gamma, q)_{L^2(\Gamma)} = (f^F(t), q)_{L^2(\Omega^F)}. \quad (\text{III.6b})$$

- ii) For the elastic wave equations, for all test functions $(\mathbf{b}, \mathbf{w}) \in \mathbf{S}^S \times \mathbf{V}^S$,

$$(\partial_t \mathbf{s}(t), \mathbf{b})_{\mathbb{L}^2(\mathbb{C}^{-1}; \Omega^S)} - (\nabla_{\text{sym}} \mathbf{v}(t), \mathbf{b})_{\mathbb{L}^2(\Omega^S)} = 0, \quad (\text{III.7a})$$

$$(\partial_t \mathbf{v}(t), \mathbf{w})_{\mathbf{L}^2(\rho^S; \Omega^S)} + (\mathbf{s}(t), \nabla_{\text{sym}} \mathbf{w})_{\mathbb{L}^2(\Omega^S)} - (p(t) \mathbf{n}_\Gamma, \mathbf{w})_{L^2(\Gamma)} = (\mathbf{f}^S(t), \mathbf{w})_{\mathbf{L}^2(\Omega^S)}. \quad (\text{III.7b})$$

The coupling conditions (III.4a) and (III.4b) are directly incorporated into (III.6b) and (III.7b), respectively. Thus, they are weakly imposed.

III.3 HHO space semi-discretization

In this section, we introduce a simple description of the space semi-discretization of (III.6)-(III.7) in the HHO framework. Namely, we take a quick look at the way the method deals with general meshes, and how (III.6)-(III.7) are approximated with HHO operators. Our goal is to provide the set of ODEs that drive the time-evolution of the space semi-discrete system in algebraic form, using a generic choice for the local polynomial bases.

III.3.1 Mesh

Let \mathcal{T} be a polygonal mesh of the domain Ω , constructed so as to align with the partition of Ω into the subdomains Ω^F and Ω^S . The mesh cells are supposed to have

planar faces, constructed so as to align with the different boundaries of the subdomains Ω^F and Ω^S . Thus, we generate a piecewise affine approximation of the interface Γ and of the subdomains Ω^S and Ω^F . We assume that the mesh is fine enough to neglect the geometric error introduced by this approximation. Consistently with this assumption, we also assume that all material properties are piecewise constant on \mathcal{T} . For latter use, we define the two sub-meshes, \mathcal{T}^F and \mathcal{T}^S , which cover exactly the subdomains Ω^F and Ω^S , respectively.

The set of mesh faces \mathcal{F} is partitioned as $\mathcal{F} := \mathcal{F}^\circ \cup \mathcal{F}^\partial$, where \mathcal{F}° collects all the interior faces, including those lying on the interface Γ , and \mathcal{F}^∂ collects all the boundary faces on $\partial\Omega$. The set of interior faces is further split as $\mathcal{F}^\circ := \mathcal{F}^{\circ F} \cup \mathcal{F}^{\circ S} \cup \mathcal{F}^\Gamma$, whereas the set of boundary faces is split as $\mathcal{F}^\partial := \mathcal{F}^{\partial F} \cup \mathcal{F}^{\partial S}$, with obvious notation. To simplify later expressions, we define $\mathcal{F}^F := \mathcal{F}^{\circ F} \cup \mathcal{F}^{\partial F} \cup \mathcal{F}^\Gamma$ and $\mathcal{F}^S := \mathcal{F}^{\circ S} \cup \mathcal{F}^{\partial S} \cup \mathcal{F}^\Gamma$ for the sets of faces lying in $\overline{\Omega^F}$ and $\overline{\Omega^S}$, respectively.

We consider general meshes which can contain hanging nodes (see Figure III.2). These meshes can be handled in a seamless fashion by any discretization method supporting polyhedral cells, as HHO and dG methods. For instance, in the example shown in Figure III.2, elements sharing an edge with the solid-fluid interface and containing hanging nodes from the other mesh (filled elements) are no longer considered as triangles in the fluid region or as quadrilaterals in the solid region, but are treated as quadrilaterals and hexagons, respectively. This approach greatly simplifies the meshing of the domain, particularly at the fluid-solid interface, since it allows for independent meshing of the two subdomains.

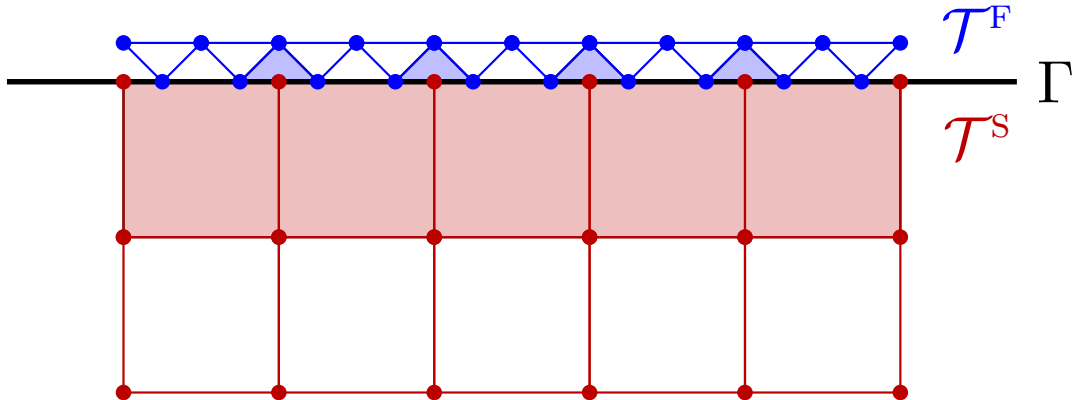


Fig. III.2: Generic example of a mesh with hanging nodes at the interface Γ . Filled elements are reinterpreted: filled squares as hexagons and filled triangles as quadrilaterals. Unfilled elements are treated for what they are: squares and triangles.

III.3.2 Degrees of freedom

Recall that the coupled problem (III.6)-(III.7) relies on primal (p and \mathbf{v}) and on dual (\mathbf{m} and \mathbf{s}) variables. Here, the primal variables are discretized using the HHO method, whereas the dual variables are discretized via a standard dG approach. The dG variables are thus piecewise polynomials of degree k (only a cell component), whereas the HHO variables consist of a pair: a cell component and a face component. The cell component is

a piecewise polynomial of degree $k' \in \{k, k+1\}$, whereas the face component is a piecewise polynomial of degree k . The HHO discretization is referred to as equal-order when $k' = k$ and as mixed-order when $k' = k + 1$. A polynomial degree $k \geq 1$ is required in the solid subdomain to control the rigid body motions [68]. For simplicity, we consider the same polynomial degree k in both subdomains, although it is not mandatory (we can take $k \geq 0$ in the fluid subdomain).

A generic mesh cell is denoted by $T \in \mathcal{T}$, with its diameter h_T , its outward unit normal \mathbf{n}_T , and the set of its boundary faces $\mathcal{F}_{\partial T}$. A generic mesh face is denoted by $F \in \mathcal{F}$. We define the local polynomial spaces $\mathbb{P}_{\text{sym}}^k(T)$, $\mathbf{P}^k(T)$ and $P^k(T)$ (resp. $\mathbf{P}^k(F)$ and $P^k(F)$) as the restrictions to the mesh cell T (resp. the mesh face F) of symmetric tensor-, vector- and scalar-valued d -variate polynomials of degree at most k (resp. $(d-1)$ -variate polynomials of degree at most k). Altogether, we consider the following dofs:

- i) from a local point of view, we have

$$p_T \in P^{k'}(T), \quad p_{\partial T} \in P^k(\mathcal{F}_{\partial T}) := \bigtimes_{F \in \mathcal{F}_{\partial T}} P^k(F), \quad \mathbf{m}_T \in \mathbf{P}^k(T), \quad \forall T \in \mathcal{T}^F, \quad (\text{III.8a})$$

$$\mathbf{v}_T \in \mathbf{P}^{k'}(T), \quad \mathbf{v}_{\partial T} \in \mathbf{P}^k(\mathcal{F}_{\partial T}) := \bigtimes_{F \in \mathcal{F}_{\partial T}} \mathbf{P}^k(F), \quad \mathbf{s}_T \in \mathbb{P}_{\text{sym}}^k(T), \quad \forall T \in \mathcal{T}^S. \quad (\text{III.8b})$$

- ii) from a global point of view, we have

$$p_{\mathcal{T}^F} \in P^{k'}(\mathcal{T}^F) := \bigtimes_{T \in \mathcal{T}^F} P^{k'}(T), \quad p_{\mathcal{F}^F} \in P^k(\mathcal{F}^F) := \bigtimes_{F \in \mathcal{F}^F} P^k(F), \quad (\text{III.9a})$$

$$\mathbf{v}_{\mathcal{T}^S} \in \mathbf{V}^{k'}(\mathcal{T}^S) := \bigtimes_{T \in \mathcal{T}^S} \mathbf{P}^{k'}(T), \quad \mathbf{v}_{\mathcal{F}^S} \in \mathbf{V}^k(\mathcal{F}^S) := \bigtimes_{F \in \mathcal{F}^S} \mathbf{P}^k(F), \quad (\text{III.9b})$$

$$\mathbf{m}_{\mathcal{T}^F} \in \mathbf{M}^k(\mathcal{T}^F) := \bigtimes_{T \in \mathcal{T}^F} \mathbf{P}^k(T), \quad \mathbf{s}_{\mathcal{T}^S} \in \mathbb{S}^k(\mathcal{T}^S) := \bigtimes_{T \in \mathcal{T}^S} \mathbb{P}_{\text{sym}}^k(T). \quad (\text{III.9c})$$

In Figure III.3, we illustrate the dofs involved in the space discretization of a 2D domain near a solid-fluid interface, for hexagonal meshes and polynomial degrees $k' = k = 1$. There are 9 cell unknowns in each fluid cell (3 for the primal variable and 6 for the dual variable), and there are 2 unknowns for each face $F \in \mathcal{F}^{\text{OF}}$. There are 15 cell unknowns in each solid cell (6 for the primal variable and 9 for the dual variable), and there are 4 unknowns for each face $F \in \mathcal{F}^{\text{OS}}$. Finally, there are 6 unknowns for each face $F \in \mathcal{F}^{\Gamma}$ (2 from the fluid part and 4 from the solid part).

III.3.3 Space semi-discrete formulation and algebraic realization

The space semi-discrete formulation of the model problem (III.6)-(III.7) consists in finding $(p_{\mathcal{T}^F}(t), p_{\mathcal{F}^F}(t), \mathbf{m}_{\mathcal{T}^F}(t)) : J \longrightarrow P^{k'}(\mathcal{T}^F) \times P^k(\mathcal{F}^F) \times \mathbf{M}^k(\mathcal{T}^F)$ in the fluid subdomain and $(\mathbf{v}_{\mathcal{T}^S}(t), \mathbf{v}_{\mathcal{F}^S}(t), \mathbf{s}_{\mathcal{T}^S}(t)) : J \longrightarrow \mathbf{V}^{k'}(\mathcal{T}^S) \times \mathbf{V}^k(\mathcal{F}^S) \times \mathbb{S}^k(\mathcal{T}^S)$ in the solid subdomain,

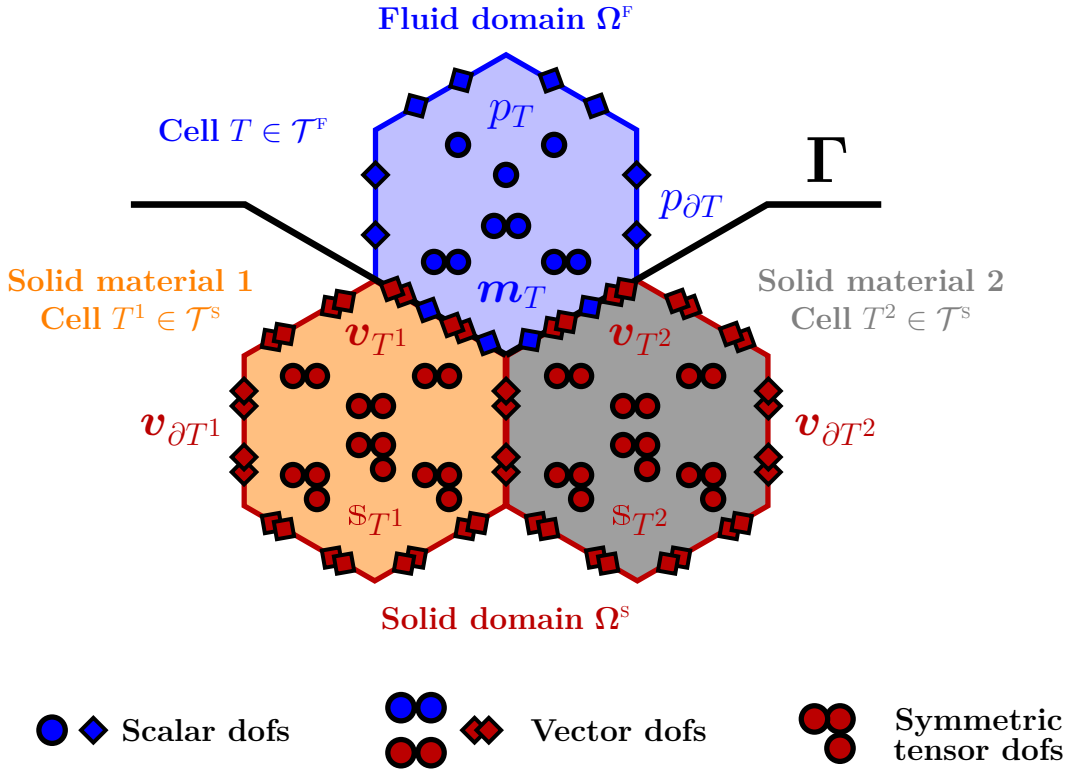


Fig. III.3: Elasto-acoustic dofs along a solid-fluid interface, with hexagonal mesh cells and lowest equal-order discretization ($k' = k = 1$).

such that, for all $t \in \bar{J}$,

$$(\partial_t \mathbf{m}_{\mathcal{T}^F}(t), \mathbf{r}_{\mathcal{T}^F})_{\mathbf{L}^2(\rho^F; \Omega^F)} - (\mathbf{g}_{\mathcal{T}^F}(p_{\mathcal{T}^F}(t), p_{\mathcal{F}^F}(t)), \mathbf{r}_{\mathcal{T}^F})_{\mathbf{L}^2(\Omega^F)} = 0, \quad (\text{III.10a})$$

$$\begin{aligned} & (\partial_t p_{\mathcal{T}^F}(t), q_{\mathcal{T}^F})_{L^2(\frac{1}{\kappa}; \Omega^F)} + (\mathbf{m}_{\mathcal{T}^F}(t), \mathbf{g}_{\mathcal{T}^F}(q_{\mathcal{T}^F}, q_{\mathcal{F}^F}))_{\mathbf{L}^2(\Omega^F)} \\ & + s^F((p_{\mathcal{T}^F}(t), p_{\mathcal{F}^F}(t)), (q_{\mathcal{T}^F}, q_{\mathcal{F}^F})) + (\mathbf{v}_{\mathcal{F}^S}(t) \cdot \mathbf{n}_\Gamma, q_{\mathcal{F}^F})_{L^2(\Gamma)} = (f^F(t), q_{\mathcal{T}^F})_{L^2(\Omega^F)}, \end{aligned} \quad (\text{III.10b})$$

for all $\mathbf{r}_{\mathcal{T}^F} \in \mathbf{M}^k(\mathcal{T}^F)$ and all $(q_{\mathcal{T}^F}, q_{\mathcal{F}^F}) \in P^{k'}(\mathcal{T}^F) \times P^k(\mathcal{F}^F)$, and

$$(\partial_t \mathbf{s}_{\mathcal{T}^S}(t), \mathbf{b}_{\mathcal{T}^S})_{\mathbb{L}^2(\mathbb{C}^{-1}; \Omega^S)} - (\mathbf{g}_{\mathcal{T}^S}^{\text{sym}}(\mathbf{v}_{\mathcal{T}^S}(t), \mathbf{v}_{\mathcal{F}^S}(t)), \mathbf{b}_{\mathcal{T}^S})_{\mathbb{L}^2(\Omega^S)} = 0, \quad (\text{III.11a})$$

$$\begin{aligned} & (\partial_t \mathbf{v}_{\mathcal{T}^S}(t), \mathbf{w}_{\mathcal{T}^S})_{\mathbf{L}^2(\rho^S; \Omega^S)} + (\mathbf{s}_{\mathcal{T}^S}(t), \mathbf{g}_{\mathcal{T}^S}^{\text{sym}}(\mathbf{w}_{\mathcal{T}^S}, \mathbf{w}_{\mathcal{F}^S}))_{\mathbb{L}^2(\Omega^S)} \\ & + s^S((\mathbf{v}_{\mathcal{T}^S}(t), \mathbf{v}_{\mathcal{F}^S}(t)), (\mathbf{w}_{\mathcal{T}^S}, \mathbf{w}_{\mathcal{F}^S})) - (p_{\mathcal{F}^S}(t) \mathbf{n}_\Gamma, \mathbf{w}_{\mathcal{F}^S})_{L^2(\Gamma)} = (\mathbf{f}^S(t), \mathbf{w}_{\mathcal{T}^S})_{\mathbf{L}^2(\Omega^S)}, \end{aligned} \quad (\text{III.11b})$$

for all $\mathbf{b}_{\mathcal{T}^S} \in \mathbb{S}^k(\mathcal{T}^S)$ and all $(\mathbf{w}_{\mathcal{T}^S}, \mathbf{w}_{\mathcal{F}^S}) \in \mathbf{V}^{k'}(\mathcal{T}^S) \times \mathbf{V}^k(\mathcal{F}^S)$. Here, $\mathbf{g}_{\mathcal{T}^F}$, $\mathbf{g}_{\mathcal{T}^S}^{\text{sym}}$, s^F , and s^S are the global (symmetric) gradient reconstruction operators and global stabilization bilinear forms whose expressions are given by the right-hand sides of equations (III.16)-(III.17) below. The main ideas are the following: the (symmetric) gradient reconstruction allows to consistently and locally build the (symmetric) gradient of the primal variable using both its cell and face dofs; the stabilization bilinear form weakly enforces locally the matching of the trace of the cell dofs with the face dofs. The reader is referred to [121] for further insight into the HHO formulation.

To derive the algebraic realization of (III.10)-(III.11), we consider the following generic bases:

$$\{\varphi_i\}_{1 \leq i \leq N_{\mathcal{T}^F}^{k'}}, \quad \{\psi_i\}_{1 \leq i \leq N_{\mathcal{F}^F}^k}, \quad \{\zeta_k\}_{1 \leq k \leq M_{\mathcal{T}^F}^k}, \quad (\text{III.12a})$$

$$\{\phi_i\}_{1 \leq i \leq L_{\mathcal{T}^S}^{k'}}, \quad \{\theta_i\}_{1 \leq i \leq L_{\mathcal{F}^S}^k}, \quad \{\mathbb{Y}_k\}_{1 \leq k \leq H_{\mathcal{T}^S}^k}, \quad (\text{III.12b})$$

with the corresponding dimensions

$$N_{\mathcal{T}^F}^{k'} := \dim(P^{k'}(\mathcal{T}^F)), \quad N_{\mathcal{F}^F}^k := \dim(P^k(\mathcal{F}^F)), \quad M_{\mathcal{T}^F}^k := \dim(\mathbf{M}^k(\mathcal{T}^F)), \quad (\text{III.13a})$$

$$L_{\mathcal{T}^S}^{k'} := \dim(\mathbf{V}^{k'}(\mathcal{T}^S)), \quad L_{\mathcal{F}^S}^k := \dim(\mathbf{V}^k(\mathcal{F}^S)), \quad H_{\mathcal{T}^S}^k := \dim(\mathbb{S}^k(\mathcal{T}^S)). \quad (\text{III.13b})$$

The basis $\{\zeta_k\}_{1 \leq k \leq M_{\mathcal{T}^F}^k}$ is build by combining Cartesian basis vectors of \mathbb{R}^d with scalar basis functions of $P^k(\mathcal{T}^F)$. Similarly, the bases $\{\phi_i\}_{1 \leq i \leq L_{\mathcal{T}^S}^{k'}}$, $\{\theta_i\}_{1 \leq i \leq L_{\mathcal{F}^S}^k}$ and $\{\mathbb{Y}_k\}_{1 \leq k \leq H_{\mathcal{T}^S}^k}$ are built by combining Cartesian basis vectors of \mathbb{R}^d , \mathbb{R}^d and $\mathbb{R}_{\text{sym}}^{d \times d}$, respectively, with scalar basis functions of $P^{k'}(\mathcal{T}^S)$, $P^k(\mathcal{F}^S)$ and $P^k(\mathcal{T}^S)$, respectively. For all the scalar-valued polynomial spaces, we use a local modal basis composed of monomials centered at the barycenter of the corresponding geometric object.

Degrees of freedom. Let $(\mathbf{P}_{\mathcal{T}^F}(t), \mathbf{P}_{\mathcal{F}^F}(t)) \in \mathbb{R}^{N_{\mathcal{T}^F}^{k'} \times N_{\mathcal{F}^F}^k}$ and $\mathbf{M}_{\mathcal{T}^F}(t) \in \mathbb{R}^{M_{\mathcal{T}^F}^k}$ represent the time-dependent component vectors of $(p_{\mathcal{T}^F}(t), p_{\mathcal{F}^F}(t)) \in P^{k'}(\mathcal{T}^F) \times P^k(\mathcal{F}^F)$ and $\mathbf{m}_{\mathcal{T}^F}(t) \in \mathbf{M}^k(\mathcal{T}^F)$ in the fluid subdomain Ω^F , respectively. Let $(\mathbf{V}_{\mathcal{T}^S}(t), \mathbf{V}_{\mathcal{F}^S}(t)) \in \mathbb{R}^{L_{\mathcal{T}^S}^{k'} \times L_{\mathcal{F}^S}^k}$ and $\mathbf{S}_{\mathcal{T}^S} \in \mathbb{R}^{H_{\mathcal{T}^S}^k}$ represent the time-dependent component vectors of $(\mathbf{v}_{\mathcal{T}^S}(t), \mathbf{v}_{\mathcal{F}^S}(t)) \in \mathbf{V}^{k'}(\mathcal{T}^S) \times \mathbf{V}^k(\mathcal{F}^S)$ and $\mathbf{s}_{\mathcal{T}^S} \in \mathbb{S}^k(\mathcal{T}^S)$ in the solid subdomain Ω^S , respectively. The algebraic realization of (III.10)-(III.11) is, for all $t \in \bar{J}$,

$$\begin{bmatrix} \mathcal{M}_{\mathcal{T}^F}^{\rho^F} & 0 \\ 0 & \mathcal{M}_{\mathcal{T}^F}^{\frac{1}{\kappa}} \end{bmatrix} \begin{bmatrix} 0 & 0 & 0 & 0 \\ 0 & 0 & 0 & 0 \\ \vdots & \vdots & \vdots & \vdots \\ 0 & 0 & \mathcal{M}_{\mathcal{T}^S}^{\mathbb{C}^{-1}} & 0 \\ 0 & 0 & 0 & \mathcal{M}_{\mathcal{T}^S}^{\rho^S} \\ 0 & 0 & 0 & 0 \\ 0 & 0 & 0 & 0 \end{bmatrix} \begin{bmatrix} \mathbf{M}_{\mathcal{T}^F} \\ \mathbf{P}_{\mathcal{T}^F} \\ \mathbf{S}_{\mathcal{T}^S} \\ \mathbf{V}_{\mathcal{T}^S} \\ \mathbf{P}_{\mathcal{F}^F} \\ \mathbf{V}_{\mathcal{F}^F} \end{bmatrix} + \begin{bmatrix} 0 & \mathcal{G}_{\mathcal{T}^F} & 0 & 0 & \mathcal{G}_{\mathcal{T}^F \mathcal{F}^F} & 0 \\ -\mathcal{G}_{\mathcal{T}^F}^\dagger & \Sigma_{\mathcal{T}^F} & 0 & 0 & \Sigma_{\mathcal{T}^F \mathcal{F}^F} & 0 \\ 0 & 0 & 0 & \mathcal{H}_{\mathcal{T}^S} & 0 & \mathcal{H}_{\mathcal{T}^S \mathcal{F}^S} \\ 0 & 0 & -\mathcal{H}_{\mathcal{T}^S}^\dagger & \Sigma_{\mathcal{T}^S} & 0 & \Sigma_{\mathcal{T}^S \mathcal{F}^S} \\ -\mathcal{G}_{\mathcal{T}^F \mathcal{F}^F}^\dagger & \Sigma_{\mathcal{T}^F \mathcal{F}^F}^\dagger & 0 & 0 & \Sigma_{\mathcal{F}^F} & \mathcal{C}_{\mathcal{F}^F} \\ 0 & 0 & -\mathcal{H}_{\mathcal{T}^S \mathcal{F}^S}^\dagger & \Sigma_{\mathcal{T}^S \mathcal{F}^S}^\dagger & -\mathcal{C}_{\mathcal{F}^S}^\dagger & \Sigma_{\mathcal{F}^S} \end{bmatrix} \begin{bmatrix} \mathbf{M}_{\mathcal{T}^F} \\ \mathbf{P}_{\mathcal{T}^F} \\ \mathbf{S}_{\mathcal{T}^S} \\ \mathbf{V}_{\mathcal{T}^S} \\ \mathbf{P}_{\mathcal{F}^F} \\ \mathbf{V}_{\mathcal{F}^F} \end{bmatrix} = \begin{bmatrix} 0 \\ \mathbf{F}_{\mathcal{T}^F} \\ 0 \\ \mathbf{F}_{\mathcal{T}^S} \\ 0 \\ \mathbf{F}_{\mathcal{F}^S} \end{bmatrix}, \quad (\text{III.14})$$

where the different blocks are defined as follows.

Mass matrices. The mass matrices $\mathcal{M}_{\mathcal{T}^F}^{\rho^F} \in \mathbb{R}^{M_{\mathcal{T}^F}^k \times M_{\mathcal{T}^F}^k}$ and $\mathcal{M}_{\mathcal{T}^F}^{\frac{1}{\kappa}} \in \mathbb{R}^{N_{\mathcal{T}^F}^{k'} \times N_{\mathcal{T}^F}^{k'}}$ are associated with the inner products in $\mathbf{L}^2(\rho^F; \Omega^F)$ and $L^2(\frac{1}{\kappa}; \Omega^F)$, respectively, and the mass matrices $\mathcal{M}_{\mathcal{T}^S}^{\mathbb{C}^{-1}} \in \mathbb{R}^{H_{\mathcal{T}^S}^k \times H_{\mathcal{T}^S}^k}$ and $\mathcal{M}_{\mathcal{T}^S}^{\rho^S} \in \mathbb{R}^{L_{\mathcal{T}^S}^{k'} \times L_{\mathcal{T}^S}^{k'}}$ are associated with the inner products in $\mathbb{L}_{\text{sym}}^2(\mathbb{C}^{-1}; \Omega^S)$ and $\mathbf{L}^2(\rho^S; \Omega^S)$, respectively. Their (classical) expressions are as follows:

$$\mathbf{M}_{\mathcal{T}^F}^\dagger \mathcal{M}_{\mathcal{T}^F}^{\rho^F} \mathbf{R}_{\mathcal{T}^F} = \sum_{T \in \mathcal{T}^F} \rho^F(\mathbf{m}_T, \mathbf{r})_{\mathbf{L}^2(T)}, \quad \mathbf{P}_{\mathcal{T}^F}^\dagger \mathcal{M}_{\mathcal{T}^F}^{\frac{1}{\kappa}} \mathbf{Q}_{\mathcal{T}^F} = \sum_{T \in \mathcal{T}^F} \frac{1}{\kappa} (p_T, q)_{L^2(T)}, \quad (\text{III.15a})$$

$$\mathbf{S}_{\mathcal{T}^S}^\dagger \mathcal{M}_{\mathcal{T}^S}^{\mathbb{C}^{-1}} \mathbf{B}_{\mathcal{T}^S} = \sum_{T \in \mathcal{T}^S} \mathbb{C}^{-1}(\mathbf{s}_T, \mathbf{b})_{\mathbb{L}^2(T)}, \quad \mathbf{V}_{\mathcal{T}^S}^\dagger \mathcal{M}_{\mathcal{T}^S}^{\rho^S} \mathbf{W}_{\mathcal{T}^S} = \sum_{T \in \mathcal{T}^S} \rho^S(\mathbf{v}_T, \mathbf{w})_{\mathbf{L}^2(T)}, \quad (\text{III.15b})$$

for all $\mathbf{m}_{\mathcal{T}^F}, \mathbf{r} \in \mathbf{P}^k(\mathcal{T}^F)$ and all $p_{\mathcal{T}^F}, q \in P^{k'}(\mathcal{T}^F)$ with component vectors $\mathbf{M}_{\mathcal{T}^F}$, $\mathbf{R}_{\mathcal{T}^F}$ and $\mathbf{P}_{\mathcal{T}^F}$, $\mathbf{Q}_{\mathcal{T}^F}$, respectively, and all $\mathbf{s}_{\mathcal{T}^S}, \mathbf{b} \in \mathbb{S}^k(\mathcal{T}^S)$ and all $\mathbf{v}_{\mathcal{T}^S}, \mathbf{w} \in \mathbf{P}^{k'}(\mathcal{T}^S)$ with component vectors $\mathbf{S}_{\mathcal{T}^S}$, $\mathbf{B}_{\mathcal{T}^S}$ and $\mathbf{V}_{\mathcal{T}^S}$, $\mathbf{W}_{\mathcal{T}^S}$, respectively.

Gradient reconstruction blocks. The gradient reconstruction blocks $\mathcal{G}_{\mathcal{T}^F} \in \mathbb{R}^{M_{\mathcal{T}^F}^k \times N_{\mathcal{T}^F}^{k'}}$ and $\mathcal{G}_{\mathcal{T}^F \mathcal{F}^F} \in \mathbb{R}^{M_{\mathcal{T}^F}^k \times N_{\mathcal{F}^F}^k}$ and the symmetric gradient reconstruction blocks $\mathcal{H}_{\mathcal{T}^S} \in \mathbb{R}^{H_{\mathcal{T}^S}^k \times L_{\mathcal{T}^S}^{k'}}$ and $\mathcal{H}_{\mathcal{T}^S \mathcal{F}^S} \in \mathbb{R}^{H_{\mathcal{T}^S}^k \times L_{\mathcal{F}^S}^k}$ are defined so that they satisfy

$$(\mathcal{G}_{\mathcal{T}^F} \mathbf{P}_{\mathcal{T}^F} + \mathcal{G}_{\mathcal{T}^F \mathcal{F}^F} \mathbf{P}_{\mathcal{F}^F})^\dagger \mathbf{R}_{\mathcal{T}^F} = \sum_{T \in \mathcal{T}^F} \left\{ (\nabla p_T, \mathbf{r})_{L^2(T)} - (p_T - p_{\partial T}, \mathbf{r} \cdot \mathbf{n}_T)_{L^2(\partial T)} \right\}, \quad (\text{III.16a})$$

$$(\mathcal{H}_{\mathcal{T}^S} \mathbf{V}_{\mathcal{T}^S} + \mathcal{H}_{\mathcal{T}^S \mathcal{F}^S} \mathbf{V}_{\mathcal{F}^S})^\dagger \mathbf{B}_{\mathcal{T}^S} = \sum_{T \in \mathcal{T}^S} \left\{ (\nabla_{\text{sym}} \mathbf{v}_T, \mathbf{b})_{\mathbb{L}_{\text{sym}}^2(T)} - (\mathbf{v}_T - \mathbf{v}_{\partial T}, \mathbf{b} \cdot \mathbf{n}_T)_{L^2(\partial T)} \right\}, \quad (\text{III.16b})$$

for all $(p_{\mathcal{T}^F}, p_{\mathcal{F}^F}) \in P^{k'}(\mathcal{T}^F) \times P^k(\mathcal{F}^F)$, all $(\mathbf{v}_{\mathcal{T}^S}, \mathbf{v}_{\mathcal{F}^S}) \in \mathbf{V}^{k'}(\mathcal{T}^S) \times \mathbf{V}^k(\mathcal{F}^S)$ with component vectors $\mathbf{P}_{\mathcal{T}^F}$, $\mathbf{P}_{\mathcal{F}^F}$ and $\mathbf{V}_{\mathcal{T}^S}$, $\mathbf{V}_{\mathcal{F}^S}$, respectively, and for all $\mathbf{r} \in \mathbf{M}^k(\mathcal{T}^F)$, all $\mathbf{b} \in \mathbb{S}^k(\mathcal{T}^S)$ with component vectors $\mathbf{R}_{\mathcal{T}^F}$ and $\mathbf{B}_{\mathcal{T}^S}$, respectively.

Stabilization blocks. The fluid stabilization blocks $\Sigma_{\mathcal{T}^F} \in \mathbb{R}^{N_{\mathcal{T}^F}^{k'} \times N_{\mathcal{T}^F}^{k'}}$, $\Sigma_{\mathcal{T}^F \mathcal{F}^F} \in \mathbb{R}^{N_{\mathcal{T}^F}^{k'} \times N_{\mathcal{F}^F}^k}$, and $\Sigma_{\mathcal{F}^F} \in \mathbb{R}^{N_{\mathcal{F}^F}^k \times N_{\mathcal{F}^F}^k}$ and the solid stabilization blocks $\Sigma_{\mathcal{T}^S} \in \mathbb{R}^{L_{\mathcal{T}^S}^{k'} \times L_{\mathcal{T}^S}^{k'}}$, $\Sigma_{\mathcal{T}^S \mathcal{F}^S} \in \mathbb{R}^{L_{\mathcal{T}^S}^{k'} \times L_{\mathcal{F}^S}^k}$, and $\Sigma_{\mathcal{F}^S} \in \mathbb{R}^{L_{\mathcal{F}^S}^k \times L_{\mathcal{F}^S}^k}$ are defined so that they satisfy

$$(\Sigma_{\mathcal{T}^F} \mathbf{P}_{\mathcal{T}^F} + \Sigma_{\mathcal{T}^F \mathcal{F}^F} \mathbf{P}_{\mathcal{F}^F})^\dagger \mathbf{Q}_{\mathcal{T}^F} + (\Sigma_{\mathcal{T}^F \mathcal{F}^F}^\dagger \mathbf{P}_{\mathcal{T}^F} + \Sigma_{\mathcal{F}^F} \mathbf{P}_{\mathcal{F}^F})^\dagger \mathbf{Q}_{\mathcal{F}^F} = \sum_{T \in \mathcal{T}^F} \tau_T^F(S_{\partial T}(p_T, p_{\partial T}), S_{\partial T}(q_T, q_{\partial T}))_{L^2(\partial T)}, \quad (\text{III.17a})$$

$$(\Sigma_{\mathcal{T}^S} \mathbf{V}_{\mathcal{T}^S} + \Sigma_{\mathcal{T}^S \mathcal{F}^S} \mathbf{V}_{\mathcal{F}^S})^\dagger \mathbf{W}_{\mathcal{T}^S} + (\Sigma_{\mathcal{T}^S \mathcal{F}^S}^\dagger \mathbf{V}_{\mathcal{T}^S} + \Sigma_{\mathcal{F}^S} \mathbf{V}_{\mathcal{F}^S})^\dagger \mathbf{W}_{\mathcal{F}^S} = \sum_{T \in \mathcal{T}^S} \tau_T^S(S_{\partial T}(\mathbf{v}_T, \mathbf{v}_{\partial T}), S_{\partial T}(\mathbf{w}_T, \mathbf{w}_{\partial T}))_{L^2(\partial T)}, \quad (\text{III.17b})$$

for all $(p_{\mathcal{T}^F}, p_{\mathcal{F}^F}) \in P^{k'}(\mathcal{T}^F) \times P^k(\mathcal{F}^F)$ and all $(\mathbf{v}_{\mathcal{T}^S}, \mathbf{v}_{\mathcal{F}^S}) \in \mathbf{V}^{k'}(\mathcal{T}^S) \times \mathbf{V}^k(\mathcal{F}^S)$ with component vectors $\mathbf{P}_{\mathcal{T}^F}$, $\mathbf{P}_{\mathcal{F}^F}$ and $\mathbf{V}_{\mathcal{T}^S}$, $\mathbf{V}_{\mathcal{F}^S}$, respectively, and for all $(q_{\mathcal{T}^F}, q_{\mathcal{F}^F}) \in P^{k'}(\mathcal{T}^F) \times P^k(\mathcal{F}^F)$ and all $(\mathbf{w}_{\mathcal{T}^S}, \mathbf{w}_{\mathcal{F}^S}) \in \mathbf{V}^{k'}(\mathcal{T}^S) \times \mathbf{V}^k(\mathcal{F}^S)$ with component vectors $\mathbf{Q}_{\mathcal{T}^F}$, $\mathbf{Q}_{\mathcal{F}^F}$ and $\mathbf{W}_{\mathcal{T}^S}$, $\mathbf{W}_{\mathcal{F}^S}$, respectively. The stabilization parameters are defined as follows:

$$\tau_T^F := (\rho^F c_P^F)|_T^{-1} \tilde{h}_T^{-\alpha}, \quad \tau_T^S := (\rho^S c_S^S)|_T \tilde{h}_T^{-\alpha}, \quad (\text{III.18})$$

where the local scaling by $(\rho^F c_P^F)|_T^{-1}$ and $(\rho^S c_S^S)|_T$ follows from physical consistency, the parameter $\alpha \in \{0, 1\}$ is used to shift from $\mathcal{O}(1)$ -stabilization ($\alpha = 0$) to $\mathcal{O}(\frac{1}{h})$ -stabilization ($\alpha = 1$), and $\tilde{h}_T := \frac{h_T}{\ell_\Omega}$ is a normalized cell diameter, where the global length scale $\ell_\Omega := \text{diam}(\Omega)$ is introduced for dimensional consistency.

Regarding the local stabilization operators $S_{\partial T} : P^{k'}(T) \times P^k(\mathcal{F}_{\partial T}) \rightarrow P^k(\mathcal{F}_{\partial T})$ and $\mathbf{S}_{\partial T} : \mathbf{P}^{k'}(T) \times \mathbf{P}^k(\mathcal{F}_{\partial T}) \rightarrow \mathbf{P}^k(\mathcal{F}_{\partial T})$, we consider two configurations:

- The first one, which we use in the equal-order HHO discretization ($k' = k$), corresponds to a plain Least-Squares stabilization:

$$S_{\partial T}(p_T, p_{\partial T}) := p_T|_{\partial T} - p_{\partial T}, \quad \mathbf{S}_{\partial T}(\mathbf{v}_T, \mathbf{v}_{\partial T}) := \mathbf{v}_T|_{\partial T} - \mathbf{v}_{\partial T}. \quad (\text{III.19})$$

This stabilization will be used with the scaling $\alpha = 0$ and explicit time-stepping schemes.

- The second one, which we use in the mixed-order HHO discretization ($k' = k + 1$), corresponds to the Lehrenfeld–Schöberl stabilization [105]:

$$S_{\partial T}(p_T, p_{\partial T}) := \Pi_{\partial T}^k(p_T|_{\partial T}) - p_{\partial T}, \quad S_{\partial T}(\mathbf{v}_T, \mathbf{v}_{\partial T}) := \Pi_{\partial T}^k(\mathbf{v}_T|_{\partial T}) - \mathbf{v}_{\partial T}, \quad (\text{III.20})$$

where $\Pi_{\partial T}^k$ is the local $L^2(\partial T)$ -orthogonal projection onto $P^k(\mathcal{F}_{\partial T})$. This stabilization will be used with the scaling $\alpha = 1$ and implicit time-stepping schemes.

Coupling blocks. The matrix $\mathcal{C}_{\mathcal{F}^\Gamma} \in \mathbb{R}^{N_{\mathcal{F}^\Gamma}^k \times L_{\mathcal{F}^s}^k}$ representing the coupling terms is defined so that

$$\mathbf{Q}_{\mathcal{F}^\Gamma}^\dagger \mathcal{C}_{\mathcal{F}^\Gamma} \mathbf{V}_{\mathcal{F}^s} = (\mathbf{v}_{\mathcal{F}^s} \cdot \mathbf{n}_\Gamma, q_{\mathcal{F}^s})_{L^2(\Gamma)}, \quad (\text{III.21})$$

for all $q_{\mathcal{F}^s} \in P^k(\mathcal{F}^s)$ with component vector $\mathbf{Q}_{\mathcal{F}^s} \in \mathbb{R}^{N_{\mathcal{F}^s}^k}$ and all $\mathbf{v}_{\mathcal{F}^s} \in \mathbf{P}^k(\mathcal{F}^s)$ with component vector $\mathbf{V}_{\mathcal{F}^s} \in \mathbb{R}^{L_{\mathcal{F}^s}^k}$. Notice that $\mathcal{C}_{\mathcal{F}^\Gamma}$ is block-diagonal with a nonzero block only for all $F \in \mathcal{F}^\Gamma$.

Source terms. The source terms $\mathbf{F}_{\mathcal{T}^F}(t) \in \mathbb{R}^{N_{\mathcal{T}^F}^{k'}}$ and $\mathbf{F}_{\mathcal{T}^s}(t) \in \mathbb{R}^{L_{\mathcal{T}^s}^{k'}}$ are time-dependent and correspond to the algebraic realization of the linear forms

$$\mathbf{F}_{\mathcal{T}^F}^\dagger(t) \mathcal{M}_{\mathcal{T}^F} \mathbf{Q}_{\mathcal{T}^F} = \sum_{T \in \mathcal{T}^F} (f^F(t), q)_{L^2(T)}, \quad (\text{III.22a})$$

$$\mathbf{F}_{\mathcal{T}^s}^\dagger(t) \mathcal{M}_{\mathcal{T}^s} \mathbf{W}_{\mathcal{T}^s} = \sum_{T \in \mathcal{T}^s} (\mathbf{f}^s(t), \mathbf{w})_{L^2(T)}, \quad (\text{III.22b})$$

for all $q \in P^{k'}(\mathcal{T}^F)$ and all $\mathbf{w} \in \mathbf{P}^{k'}(\mathcal{T}^s)$ with component vectors $\mathbf{Q}_{\mathcal{T}^F}$ and $\mathbf{W}_{\mathcal{T}^s}$, respectively, and $\mathcal{M}_{\mathcal{T}^F}$ and $\mathcal{M}_{\mathcal{T}^s}$ are the mass matrices associated with the canonical inner products in $L^2(\Omega^F)$ and $\mathbf{L}^2(\Omega^s)$, respectively.

Equation (III.14) can be rewritten in a more compact form by regrouping all the cell unknowns on the one hand, and all the face unknowns on the other hand. With obvious notation, we obtain

$$\begin{bmatrix} \mathcal{M}_{\mathcal{T}} & 0 \\ 0 & 0 \end{bmatrix} \partial_t \begin{bmatrix} \mathbf{U}_{\mathcal{T}} \\ \mathbf{U}_{\mathcal{F}} \end{bmatrix} + \begin{bmatrix} \mathcal{K}_{\mathcal{T}} & \mathcal{K}_{\mathcal{T}\mathcal{F}} \\ \mathcal{K}_{\mathcal{F}\mathcal{T}} & \mathcal{K}_{\mathcal{F}} \end{bmatrix} \begin{bmatrix} \mathbf{U}_{\mathcal{T}} \\ \mathbf{U}_{\mathcal{F}} \end{bmatrix} = \begin{bmatrix} \mathbf{F}_{\mathcal{T}} \\ 0 \end{bmatrix}, \quad (\text{III.23})$$

where $\mathcal{M}_{\mathcal{T}}$ is the cell mass matrix, $\mathcal{K}_{\mathcal{T}}$, $\mathcal{K}_{\mathcal{T}\mathcal{F}}$, $\mathcal{K}_{\mathcal{F}\mathcal{T}}$, $\mathcal{K}_{\mathcal{F}}$, are the blocks of the stiffness matrix, $\mathbf{U}_{\mathcal{T}}$ and $\mathbf{U}_{\mathcal{F}}$ are the components of the vector of unknowns and $\mathbf{F}_{\mathcal{T}}$ is the cell source term (the face source term is null). A crucial observation is that both $\mathcal{K}_{\mathcal{T}}$ and $\mathcal{K}_{\mathcal{F}}$ are block diagonal. This important property will be exploited in Section 4 in the context of implicit and explicit time-stepping schemes. While the block-diagonal structure of $\mathcal{K}_{\mathcal{T}}$ is obvious, let us briefly motivate why $\mathcal{K}_{\mathcal{F}}$ is also block-diagonal. First, this is the case for all $F \in \mathcal{F}^{\text{OF}} \cup \mathcal{F}^{\text{OS}}$ since the stabilization bilinear forms are local to each interior face for both fluid and solid subdomains, with local diagonal blocks of size $\dim P^k(F)$ or $\dim \mathbf{P}^k(F)$, respectively. Furthermore, for all $F \in \mathcal{F}^\Gamma$, the couplings are also local to the face, but the diagonal block in $\mathcal{K}_{\mathcal{F}}$ is of larger size, namely $\dim P^k(F) + \dim \mathbf{P}^k(F)$.

III.4 Fully discrete schemes

The time discretization is based on Runge–Kutta (RK) schemes. Butcher tableaux are a classical way to define RK schemes by means of the coefficients $\{a_{ij}\}_{1 \leq i,j \leq s}$, $\{b_i\}_{1 \leq i \leq s}$, and $\{c_i\}_{1 \leq i \leq s}$, where $s \geq 1$ is the number of stages. For explicit RK schemes with s stages and order s (ERK(s)), the matrix $\{a_{ij}\}_{1 \leq i,j \leq s}$ is strictly lower-triangular. For singly diagonal implicit RK schemes with s stages and order $(s+1)$ (SDIRK($s, s+1$)), the matrix is lower-triangular with $a_{11} = \dots = a_{ss} := a_*$. The corresponding Butcher tableaux are as follows:

$$\begin{array}{c|cccc} c_1 & a_* & 0 & \cdots & 0 \\ c_2 & a_{21} & a_* & \ddots & 0 \\ \vdots & \vdots & \ddots & \ddots & \vdots \\ c_s & a_{s1} & \cdots & a_{s,s-1} & a_* \\ \hline b_1 & \cdots & b_{s-1} & b_s \end{array} \quad \begin{array}{c|ccccc} c_1 & 0 & \cdots & \cdots & 0 \\ c_2 & a_{21} & 0 & \cdots & 0 \\ \vdots & \vdots & \ddots & \ddots & \vdots \\ c_s & a_{s1} & \cdots & a_{s,s-1} & 0 \\ \hline b_1 & \cdots & b_{s-1} & b_s \end{array} \quad (\text{III.24})$$

To simplify the writing of SDIRK and ERK schemes, we define $a_{s+1,i} := b_i$ for all $i \in \{1, \dots, s\}$ and set $a_{s+1,s+1} := 0$.

We now detail the time discretization of (III.23) by SDIRK and ERK schemes. We show that an effective SDIRK implementation is obtained by the local elimination of the cell unknowns, whereas an effective ERK implementation is obtained by the local elimination of the face unknowns. The outcome of this elimination is illustrated in Figure III.4. Let $(t^n)_{n \in \{0, \dots, N\}}$ with $t^0 = 0$ and $t^N = T_f$ be the discrete time nodes, and let $\Delta t^n := t^n - t^{n-1}$ be the time step. For simplicity, we consider that the time-step is constant and drop the superscript n .

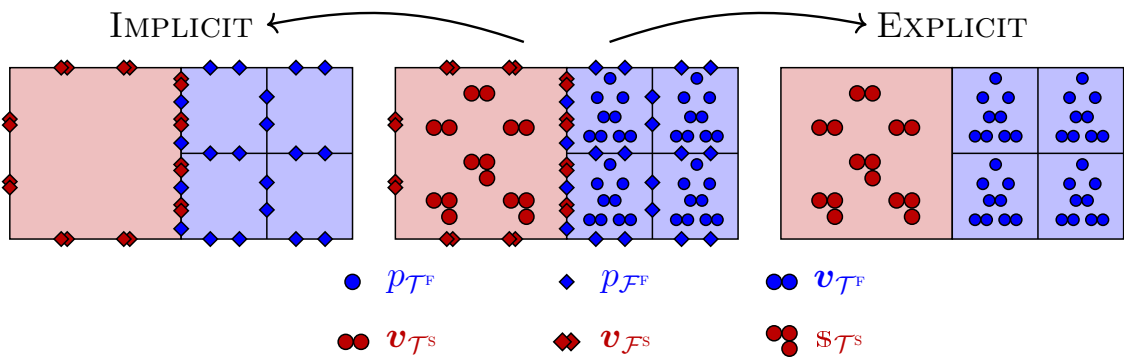


Fig. III.4: Fully coupled unknowns after static condensation for SDIRK schemes (left) and for ERK schemes (right) for the lowest equal-order discretization ($k' = k = 1$).

We observe from Figure III.4 that the number of cell dofs appears to be larger than the face dofs. Let us give a more quantitative estimate. Neglecting the number of boundary faces, and assuming that each cell has n faces (e.g., $n = 3$ for triangles and $n = 4$ for tetrahedra), the asymptotic ratio between the number of cells and the number of faces is n .

$\#CELLS \approx 2\#FACES$. Under this assumption, Table III.1 reports the expected percentage of dofs associated with faces for triangular and tetrahedral meshes, and for equal- and mixed-order HHO settings. A first observation is, as expected, that the proportion of face dofs decreases with the polynomial degree. A second observation is that, in the mixed-order case (used with implicit time schemes), the share of cell dofs is at least 75%. In this setting, static condensation — which eliminates the cell dofs — allows for a significant reduction in the size of the global linear system. In the equal-order case (used with explicit time schemes), the proportion of cell dofs is smaller but remains dominant (at least 67%). Here, the static condensation eliminates face dofs instead, which still reduces the system size, albeit less substantially. Altogether, we can conclude that the reduction in computational costs by static condensation is much more impactful when using implicit time schemes.

			GENERAL k	$k = 1$	$k = 2$	$k = 3$
EQUAL-ORDER	2D	ACOUSTIC	$\frac{1}{k+3}$	25%	20%	17%
		ELASTIC	$\frac{6}{5k+16}$	29%	23%	19%
	3D	ACOUSTIC	$\frac{3}{2k+9}$	27%	23%	20%
		ELASTIC	$\frac{2}{k+5}$	33%	29%	25%
MIXED-ORDER	2D	ACOUSTIC	$\frac{3(k+1)}{3k^2+14k+13}$	20%	17%	15%
		ELASTIC	$\frac{6(k+1)}{5k^2+25k+24}$	22%	19%	17%
	3D	ACOUSTIC	$\frac{6(k+1)(k+2)}{4k^3+33k^2+77k+54}$	21%	19%	17%
		ELASTIC	$\frac{6(k+1)(k+2)}{3k^3+27k^2+66k+48}$	25%	23%	21%

Tab. III.1: Percentage of face dofs for purely acoustic and elastic cases, in 2D and 3D, for equal- and mixed-order settings, for various polynomial degrees k .

III.4.1 Singly Diagonal Implicit Runge-Kutta (SDIRK) schemes

Given $\mathbf{U}_{\mathcal{T}}^{n-1}$ from the previous time step or the initial condition, the time discretization of (III.23) by SDIRK($s, s + 1$) schemes is as follows: We solve sequentially for all $i \in \{1, \dots, s + 1\}$,

$$\begin{bmatrix} \mathcal{M}_{\mathcal{T}} & 0 \\ 0 & 0 \end{bmatrix} \begin{bmatrix} \mathbf{U}_{\mathcal{T}}^{n,i} \\ \mathbf{U}_{\mathcal{F}}^{n,i} \end{bmatrix} = \begin{bmatrix} \mathcal{M}_{\mathcal{T}} & 0 \\ 0 & 0 \end{bmatrix} \begin{bmatrix} \mathbf{U}_{\mathcal{T}}^{n-1} \\ \mathbf{U}_{\mathcal{F}}^{n-1} \end{bmatrix} + \Delta t \sum_{j=1}^i a_{ij} \left(\begin{bmatrix} \mathbf{F}_{\mathcal{T}}^{n-1+c_j} \\ 0 \end{bmatrix} - \begin{bmatrix} \mathcal{K}_{\mathcal{T}} & \mathcal{K}_{\mathcal{T}\mathcal{F}} \\ \mathcal{K}_{\mathcal{F}\mathcal{T}} & \mathcal{K}_{\mathcal{F}} \end{bmatrix} \begin{bmatrix} \mathbf{U}_{\mathcal{T}}^{n,j} \\ \mathbf{U}_{\mathcal{F}}^{n,j} \end{bmatrix} \right), \quad (\text{III.25})$$

where $\mathbf{F}_{\mathcal{T}}^{n-1+c_j} := \mathbf{F}_{\mathcal{T}}(t_{n-1} + c_j \Delta t)$. Notice that the last stage ($i = s + 1$) only requires a mass matrix inversion. Finally, we set $\mathbf{U}_{\mathcal{T}}^{n+1} := \mathbf{U}_{\mathcal{T}}^{n,s+1}$. For all $i \in \{1, \dots, s\}$, each stage in (III.25) can be rewritten as

$$\begin{bmatrix} \mathcal{M}_{\mathcal{T}} + a_* \Delta t \mathcal{K}_{\mathcal{T}} & a_* \Delta t \mathcal{K}_{\mathcal{T}\mathcal{F}} \\ a_* \Delta t \mathcal{K}_{\mathcal{F}\mathcal{T}} & a_* \Delta t \mathcal{K}_{\mathcal{F}} \end{bmatrix} \begin{bmatrix} \mathbf{U}_{\mathcal{T}}^{n,i} \\ \mathbf{U}_{\mathcal{F}}^{n,i} \end{bmatrix} = \begin{bmatrix} \mathbf{B}_{\mathcal{T}}^{n,i} \\ \mathbf{B}_{\mathcal{F}}^{n,i} \end{bmatrix}, \quad (\text{III.26})$$

with

$$\begin{bmatrix} B_{\mathcal{T}}^{n,i} \\ B_{\mathcal{F}}^{n,i} \end{bmatrix} := \begin{bmatrix} \mathcal{M}_{\mathcal{T}} U_{\mathcal{T}}^{n-1} + a_* \Delta t F_{\mathcal{T}}^{n-1+c_i} + \Delta t \sum_{j=1}^{i-1} a_{ij} (F_{\mathcal{T}}^{n-1+c_j} - \mathcal{K}_{\mathcal{T}} U_{\mathcal{T}}^{n,j} - \mathcal{K}_{\mathcal{F}} U_{\mathcal{F}}^{n,j}) \\ -\Delta t \sum_{j=1}^{i-1} a_{ij} (\mathcal{K}_{\mathcal{F}} U_{\mathcal{T}}^{n,j} + \mathcal{K}_{\mathcal{F}} U_{\mathcal{F}}^{n,j}) \end{bmatrix}. \quad (\text{III.27})$$

A key observation is that the cell-cell submatrix in (III.26) (associated with all the fluid and solid cell unknowns) is block-diagonal. Hence, a static condensation procedure can be performed, leading to a global problem coupling only the face unknowns. This strategy enhances computational efficiency by eliminating locally all the cell unknowns. Therefore, (III.25) is solved by performing sequentially the following two solves:

$$a_* \Delta t (\mathcal{K}_{\mathcal{F}} - a_* \Delta t \mathcal{K}_{\mathcal{F}} \mathcal{T} (\mathcal{M}_{\mathcal{T}} + a_* \Delta t \mathcal{K}_{\mathcal{T}})^{-1} \mathcal{K}_{\mathcal{F}} \mathcal{T}) U_{\mathcal{F}}^{n,i} = B_{\mathcal{F}}^{n,i} - a_* \Delta t \mathcal{K}_{\mathcal{F}} \mathcal{T} (\mathcal{M}_{\mathcal{T}} + a_* \Delta t \mathcal{K}_{\mathcal{T}})^{-1} B_{\mathcal{T}}^{n,i}, \quad (\text{III.28a})$$

$$U_{\mathcal{T}}^{n,i} = (\mathcal{M}_{\mathcal{T}} + a_* \Delta t \mathcal{K}_{\mathcal{T}})^{-1} (B_{\mathcal{T}}^{n,i} - a_* \Delta t \mathcal{K}_{\mathcal{F}} \mathcal{T} U_{\mathcal{F}}^{n,i}). \quad (\text{III.28b})$$

Owing to the singly diagonal structure of the Butcher tableau, all the stages share the same system matrix allowing to re-use matrix factorizations. Moreover, for a constant time step, matrix factorizations can be re-used throughout the whole time integration. Notice also that the second step (III.28b) is local and embarrassingly parallel.

In this work, we employ s -stage Singly Diagonally Implicit Runge–Kutta (SDIRK) methods of order $(s+1)$, with $s \in \{2, 3\}$. The associated Butcher tableaux are reported in (III.29) where the SDIRK(3, 4) scheme corresponds to the values $\nu := \frac{1}{\sqrt{3}} \cos(\frac{\pi}{18}) + \frac{1}{2}$ and $\xi := \frac{1}{6(2\nu-1)^2}$:

$$\begin{array}{c|cc} \frac{1}{4} & \frac{1}{4} & 0 \\ \frac{3}{4} & \frac{1}{2} & \frac{1}{4} \\ \hline & \frac{1}{2} & \frac{1}{2} \end{array} \qquad \begin{array}{c|ccc} \nu & \nu & 0 & 0 \\ \frac{1}{2} & \frac{1}{2} - \nu & \nu & 0 \\ 1 - \nu & 2\nu & 1 - 4\nu & \nu \\ \hline & \xi & 1 - 2\xi & \xi \end{array} \quad (\text{III.29})$$

III.4.2 Explicit Runge–Kutta (ERK) schemes

Given $U_{\mathcal{T}}^{n-1}$ from the previous time step or the initial condition, the time discretization of (III.23) by ERK(s) schemes is as follows: We solve sequentially for all $i \in \{1, \dots, s+1\}$,

$$\begin{bmatrix} \mathcal{M}_{\mathcal{T}} & 0 \\ 0 & 0 \end{bmatrix} \begin{bmatrix} U_{\mathcal{T}}^{n,i} \\ U_{\mathcal{F}}^{n,i} \end{bmatrix} = \begin{bmatrix} \mathcal{M}_{\mathcal{T}} & 0 \\ 0 & 0 \end{bmatrix} \begin{bmatrix} U_{\mathcal{T}}^{n-1} \\ U_{\mathcal{F}}^{n-1} \end{bmatrix} + \Delta t \sum_{j=1}^{i-1} a_{ij} \left(\begin{bmatrix} F_{\mathcal{T}}^{n-1+c_j} \\ 0 \end{bmatrix} - \begin{bmatrix} \mathcal{K}_{\mathcal{T}} & \mathcal{K}_{\mathcal{F}} \\ \mathcal{K}_{\mathcal{F}} & \mathcal{K}_{\mathcal{F}} \end{bmatrix} \begin{bmatrix} U_{\mathcal{T}}^{n,j} \\ U_{\mathcal{F}}^{n,j} \end{bmatrix} \right), \quad (\text{III.30})$$

recalling that $F_{\mathcal{T}}^{n-1+c_j} := F_{\mathcal{T}}(t_{n-1} + c_j \Delta t)$. Finally, we set $U_{\mathcal{T}}^{n+1} := U_{\mathcal{T}}^{n,s+1}$. This time, we exploit the fact that the face-face submatrix $\mathcal{K}_{\mathcal{F}}$ is block-diagonal and we eliminate locally all the face unknowns. Thus, we rewrite (III.30) only in terms of the cell unknowns (this procedure is called dG rewriting in the context of HDG methods). We first set $U_{\mathcal{T}}^{n,1} = U_{\mathcal{T}}^{n-1}$. Then, for all $i \in \{1, \dots, s+1\}$, we first solve:

$$\mathcal{K}_{\mathcal{F}} U_{\mathcal{F}}^{n,i} = -\mathcal{K}_{\mathcal{F}} \mathcal{T} U_{\mathcal{T}}^{n,i}, \quad (\text{III.31a})$$

followed by

$$\mathcal{M}_{\mathcal{T}} \mathbf{U}_{\mathcal{T}}^{n,i} = \mathcal{M}_{\mathcal{T}} \mathbf{U}_{\mathcal{T}}^{n-1} + \Delta t \sum_{j=1}^{i-1} a_{ij} \left(\mathbf{F}_{\mathcal{T}}^{n-1+c_j} - (\mathcal{K}_{\mathcal{T}} - \mathcal{K}_{\mathcal{T}\mathcal{F}} \mathcal{K}_{\mathcal{F}}^{-1} \mathcal{K}_{\mathcal{F}\mathcal{T}}) \mathbf{U}_{\mathcal{T}}^{n,j} \right). \quad (\text{III.31b})$$

We emphasize that both solves in (III.31) are block-diagonal.

In this work, we use s -stage Explicit Runge–Kutta (ERK) schemes of order s , with $s \in \{2, 3, 4\}$. The corresponding Butcher tableaux are reported in (III.32). We recall that ERK(s) schemes are subject to a CFL stability condition. This point is further discussed in Section III.5.1 below.

$\begin{array}{c cc} & 0 & 0 \\ 0 & \hline & \frac{1}{2} \\ \hline \frac{1}{2} & \frac{1}{2} & 0 \\ \hline & 0 & 1 \end{array}$	$\begin{array}{c ccc} & 0 & 0 & 0 \\ \hline \frac{1}{2} & \frac{1}{2} & 0 & 0 \\ \hline 1 & -1 & 2 & 0 \\ \hline & \frac{1}{6} & \frac{2}{3} & \frac{1}{6} \end{array}$	$\begin{array}{c cccc} & 0 & 0 & 0 & 0 \\ \hline \frac{1}{2} & \frac{1}{2} & 0 & 0 & 0 \\ \hline \frac{1}{2} & 0 & \frac{1}{2} & 0 & 0 \\ \hline 1 & 0 & 0 & 1 & 0 \\ \hline & \frac{1}{6} & \frac{1}{3} & \frac{1}{3} & \frac{1}{6} \end{array}$
---	---	---

(III.32)

III.5 Numerical results

In this section, we present 2D numerical results obtained with the HHO discretization of the elasto-acoustic problem described above. Our goal is threefold. Our first goal is to analyze the CFL condition of the explicit schemes and to perform a computational efficiency study comparing explicit and implicit schemes, in order to identify the most effective time-stepping strategy. To this purpose, we consider manufactured solutions. Our second goal is to assess the accuracy of the method using a classical test case with a Ricker wavelet as the initial condition, comparing the numerical results to a semi-analytical solution. Moreover, we provide a further comparison between explicit and implicit schemes using this second test case. Our third goal is to showcase the geometric flexibility of the method. To this purpose, we consider a geophysical application involving the propagation of a seismic wavefield through complex media.

Recall that, for explicit time-stepping, we use an equal-order HHO discretization with $O(1)$ Least-Squares stabilization whereas, for implicit time-stepping, we use a mixed-order HHO discretization with Lehrenfeld-Schöberl $O(\frac{1}{h})$ -stabilization. To solve the resulting linear systems, both a direct LU solver and an iterative Biconjugate Gradient (BiCG) solver preconditioned by an incomplete LU (ILU) factorization are used. The former is considered so as to enable a fair comparison with the explicit schemes.

The implementation is carried out in the open-source software `disk++`, available at <https://github.com/wareHHOuse/diskpp>, and further detailed in [48].

III.5.1 CFL and efficiency study on a sinusoidal test case

To define the discretization level we introduce two computational parameters: the spatial refinement level ℓ , so that $h = 2^{-\ell}$, and the time refinement level n , so that $\Delta t = 0.1 \times 2^{-n}$. We consider three types of meshes: Cartesian, simplicial and polygonal.

Some examples are shown in Figure III.5 for $\ell = 2$, with the solid subdomain mesh on the left side in red, and the fluid subdomain mesh on the right side in blue.

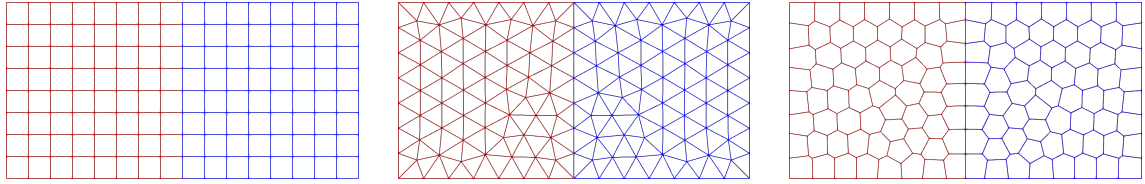


Fig. III.5: Cartesian, simplicial, and polygonal meshes for $\ell = 2$.

Test case setting. The fluid and solid media have the same density and similar wave speeds. Specifically, we consider a simulation time $T_f := 1$ and

- $\Omega^F := (0, 1) \times (0, 1)$, with density $\rho^F := 1$, compressibility modulus $\kappa := 1$, so that the velocity of the pressure waves is $c_p^F = 1$;
- $\Omega^S := (-1, 0) \times (0, 1)$, with density $\rho^S := 1$, and Lamé parameters so that $c_p^S := \sqrt{3}$ and $c_s = 1$.

The sinusoidal solution is expressed in terms of the potential u (acoustic) and the displacement $\mathbf{u} := (u_x, u_y)$ (elastic) so that

$$p := \partial_t u, \quad \mathbf{m} := \nabla u, \quad \text{in } \Omega^F, \quad (\text{III.33a})$$

$$\mathbf{v} := \partial_t \mathbf{u}, \quad \mathbb{C}^{-1} \mathbf{s} := \nabla_{\text{sym}} \mathbf{u}, \quad \text{in } \Omega^S. \quad (\text{III.33b})$$

If not specified, the source terms, the (non)homogeneous Dirichlet boundary conditions, and the initial conditions are defined according to

$$u(t, x, y) := x^2 \sin(\omega \pi x) \sin(\omega \pi y) \sin(\theta \pi t), \quad (\text{III.34a})$$

$$u_x(t, x, y) = u_y(t, x, y) := x^2 \cos(\omega \frac{\pi}{2} x) \sin(\omega \pi y) \cos(\theta \pi t), \quad (\text{III.34b})$$

where ω and θ are the spatial and temporal frequencies, respectively. We consider two main configurations: a dominant spatial evolution with $\omega := 5$ and $\theta := \sqrt{2}$ and a dominant temporal evolution with $\omega := 1$ and $\theta := 10$.

Stability study of explicit time schemes. We first study the stability of ERK(s) schemes with $s \in \{2, 3, 4\}$. We consider additional weighting parameters, η^F and η^S , which scale the stabilization bilinear forms appearing on the right-hand sides of (III.17). The stability condition for the ERK(s) schemes can be written in the following form,

$$c_{\sharp} \frac{\Delta t}{h} \leq \text{CFL}^*(s, k, \eta^F, \eta^S), \quad (\text{III.35})$$

where CFL^* denotes the critical value for stability and c_{\sharp} is the largest velocity in the domain. To determine the value of CFL^* , we use an empirical procedure based on energy conservation. To this purpose, we slightly modify the test case so that the energy of the

system remains constant. Specifically, we consider the functions in (III.34) only to prescribe the initial condition, take homogeneous Dirichlet boundary conditions and impose null source terms. Stability is assessed based on the relative energy increase, limited to $\varepsilon := 5\%$ of the initial or previous time-step energy. At the time step t^n , the energy is evaluated as

$$E^n := \frac{1}{2} \|\mathbf{m}\tau(t^n)\|_{L^2(\rho^F; \Omega^F)}^2 + \frac{1}{2} \|p\tau(t^n)\|_{L^2(\frac{1}{\kappa}; \Omega^F)}^2 + \frac{1}{2} \|\mathbf{v}\tau(t^n)\|_{L^2(\rho^S; \Omega^S)}^2 + \frac{1}{2} \|\mathbf{s}\tau(t^n)\|_{L^2(\mathbb{C}^{-1}; \Omega^S)}^2. \quad (\text{III.36})$$

The value of CFL^* is determined by reducing iteratively the total number of time steps by $\delta := 1\%$ after each stable simulation. The value of CFL^* is then identified by bracketing the transition between stability and instability. The procedure is summarized in Algorithm 1.

Algorithm 1 Bounding of the CFL Stability Limit

```

1: while simulation is stable do
2:   for  $n = 1$  to  $N$  do
3:     Compute energy  $E_n$ 
4:     Compute relative energy increase  $\Delta E := \max_n \left( \frac{|E_n - E_0|}{E_0}, \frac{|E_n - E_{n-1}|}{E_{n-1}} \right)$ 
5:     if  $\Delta E > \varepsilon$  then
6:       Flag  $N$  as the first unstable time step
7:       Break
8:     end if
9:   end for
10:  Flag  $N$  as the last stable time step
11:  Decrease  $N$  by  $\delta N$ 
12: end while

```

In Figure III.6, we first analyze the stability of the pure acoustic and elastic problems to determine the optimal values of η^F and η^S in each subdomain, *i.e.* the values that maximize CFL^* . We obtain $\eta_*^F = 0.8$ and $\eta_*^S = 1.5$. These values are retained in the rest of the paper. We also notice that the stability coefficient CFL^* behaves as $\min(\eta + c_1, \frac{1}{\eta} + c_2)$ for suitable constants c_1 and c_2 , consistently with the observations reported in [121] for the spectral radius of the stiffness matrix.

In Table III.2, we report the CFL^* values determined using Algorithm 1. These tables also provide the ratios of the CFL^* coefficients between the different number of stages of the ERK(s) schemes and the different polynomial orders, respectively. It can be observed that these ratios slightly increase with s , showing that increasing the number of stages improves stability. Moreover, as expected, CFL^* decreases with the polynomial degree, essentially as k^{-1} . Finally, in Table III.3, we analyze the impact of the mesh geometry on the value of CFL^* . This value is only mildly sensitive to the mesh geometry, although meshes with higher face counts seem to slightly enhance the scheme stability.

Efficiency study. We now assess the efficiency of the explicit and implicit schemes using the analytical solution (III.34). Accuracy is quantified by computing the error in

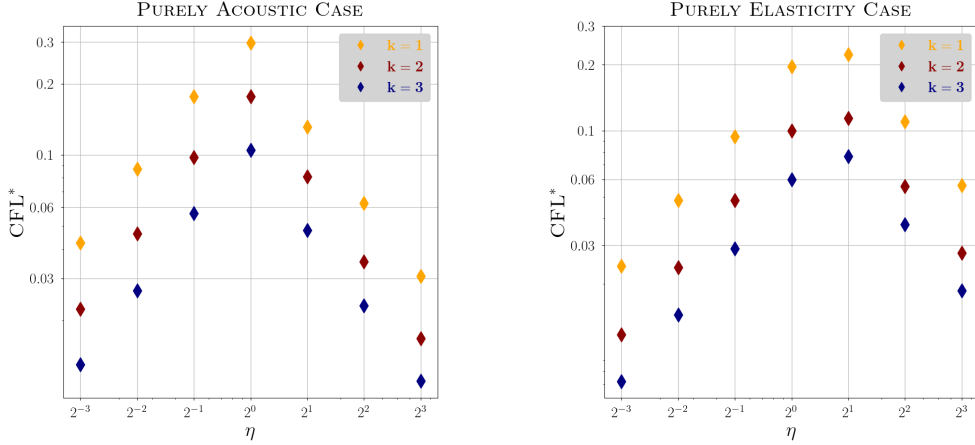


Fig. III.6: CFL* in the equal-order setting for the pure acoustic and elastic cases for $k \in \{1, 2, 3\}$.

	$k = 1$			$k = 2$			$k = 3$		
	$s = 2$	$s = 3$	$s = 4$	$s = 2$	$s = 3$	$s = 4$	$s = 2$	$s = 3$	$s = 4$
CFL*	0.205	0.253	0.282	0.099	0.123	0.138	0.063	0.079	0.087
RATIO WRT s	1	1.23	1.38	1	1.24	1.39	1	1.25	1.38
RATIO WRT k	1	1	1	0.48	0.49	0.49	0.31	0.31	0.31

Tab. III.2: CFL* coefficient (and ratios thereof) for ERK(s), $s \in \{2, 3, 4\}$ and $k \in \{1, 2, 3\}$.

MESHES	$s = 2$			$s = 3$			$s = 4$			
	\triangle	\square	\diamond	\triangle	\square	\diamond	\triangle	\square	\diamond	
$k = 1$	CFL*	0.191	0.205	0.264	0.238	0.253	0.329	0.265	0.282	0.363
	RATIO	1	1.07	1.38	1	1.06	1.38	1	1.06	1.37
$k = 2$	CFL*	0.106	0.099	0.136	0.133	0.123	0.170	0.147	0.138	0.188
	RATIO	1	0.93	1.28	1	0.92	1.28	1	0.94	1.28
$k = 3$	CFL*	0.072	0.063	0.082	0.090	0.079	0.102	0.100	0.087	0.115
	RATIO	1	0.88	1.13	1	0.88	1.13	1	0.87	1.15

Tab. III.3: CFL* coefficient (and ratios thereof) for ERK(s), $s \in \{2, 3, 4\}$ and $k \in \{1, 2, 3\}$.

the L^2 -norm of the dG variables at the final time step over the computational domain. The efficiency of the various schemes is compared in terms of error versus CPU time. For a fair comparison, implicit schemes employ an iterative solver with a tolerance defined as $TOL_\ell := 2^{-\ell(k+1)}TOL_0$ so that at each level of space refinement, the convergence criterion for the iterative solver is decreased appropriately. Moreover, for both implicit and explicit schemes of order s , the time steps are defined as $\Delta t_\ell := 2^{-\ell\frac{k+1}{s+1}}\Delta t_0$ so as to ensure that, at each level of space refinement, the space and time discretization errors remain balanced. The reference parameters TOL_0 and Δt_0 are determined empirically. Specifically, we compute the error associated with various time step values and observe a stagnation of the total error once the time discretization error becomes negligible compared to the spatial

discretization error. We then define Δt_0 as the largest time step for which this stagnation is observed. The reference tolerance TOL_0 is selected slightly smaller than the spatial discretization error to ensure that the iterative solver does not dominate the total error. This procedure, which is only considered for $\ell = 0$, yields an optimized implicit time step for solving the problem. The time step for explicit schemes is instead dictated by the CFL condition (III.35) for all $\ell \geq 0$.

In Figure III.7 and Figure III.8, we first consider the test case in which the spatial discretization error dominates. In Figure III.7, our objective is to compare explicit schemes on the one hand, and implicit schemes on the other hand. The first observation, valid for both explicit and implicit schemes, is that increasing the polynomial degree significantly improves efficiency. The second observation is that, in the regime where the spatial error dominates, all the explicit schemes exhibit similar efficiency, and the same holds for implicit schemes. Nevertheless, ERK(2) and SDIRK(3,4) appear to be slightly more efficient than the other schemes within their respective category. In Figure III.8, the left panel compares the efficiency of ERK(2) and SDIRK(3,4) schemes. We observe that the implicit scheme is more efficient than the explicit one. This gain is due to the larger time steps allowed by the implicit scheme and the elimination of cell unknowns by static condensation, which compensates for the additional cost of solving the linear system. In the right panel, we evaluate the efficiency of ERK(4) on meshes composed of different cell geometries: simplices, polygons, and squares. We observe that, overall, the efficiency remains similar across the three mesh types. However, at low polynomial orders, polygonal meshes appear to be slightly more efficient, as their more favorable CFL condition allows for somewhat larger time steps. Conversely, at higher orders, the large number of faces in polygonal meshes becomes a drawback. Indeed, the better CFL condition no longer offsets the additional computational cost due to the handling of extra faces. Hence, while the overall efficiency remains comparable, we can conclude that polygonal meshes are preferable at low order, whereas at higher order, it is advantageous to favor cell geometries with fewer faces, such as simplices.

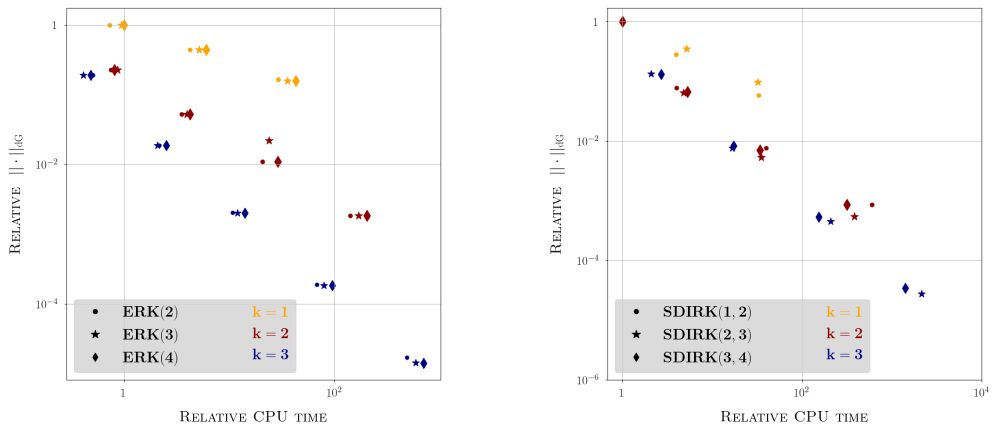


Fig. III.7: Test case with dominant spatial error. **Left panel:** Efficiency comparison for $ERK(s)$ for $s \in \{2, 3, 4\}$. **Right panel:** Efficiency for $SDIRK(s, s + 1)$ for $s \in \{1, 2, 3\}$.

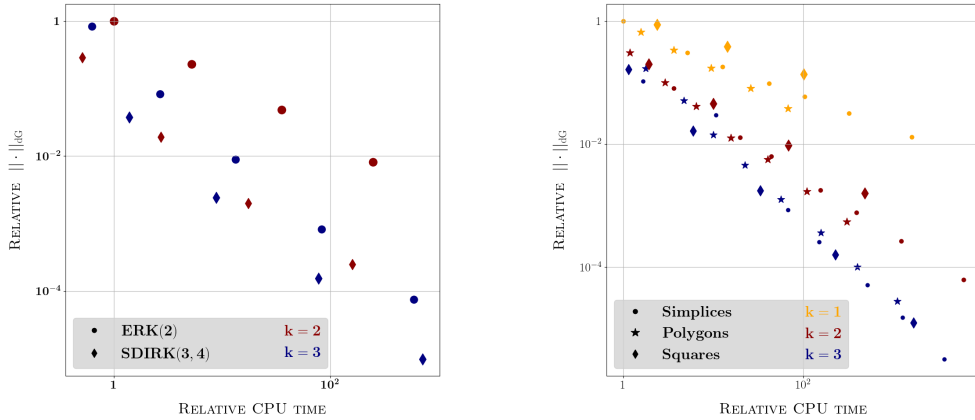


Fig. III.8: Test case with dominant spatial error. **Left panel:** Efficiency comparison for ERK(2) and SDIRK(3, 4). **Right panel:** Efficiency comparison for ERK(4) on meshes composed of different cell geometries.

In Figure III.9, we now consider the test case where the time error is dominant. In this setting, the time steps used for the implicit schemes are smaller than the stability limit enforced by (III.35). Therefore, there is no advantage in using implicit schemes. Regarding the cell geometry, since the stability constraint is no longer the limiting factor, reducing the number of faces is the most effective approach, regardless of the approximation order.

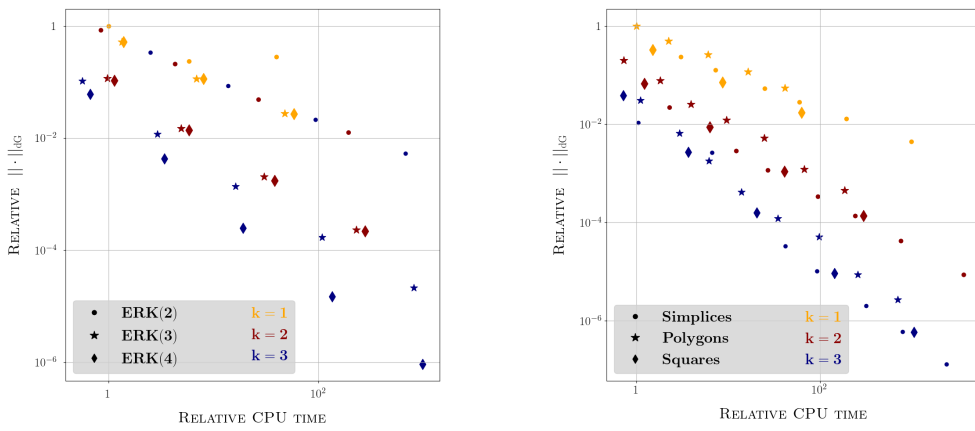


Fig. III.9: Test case with dominant time error. **Left panel:** Efficiency comparison for ERK(s) for $s \in \{2, 3, 4\}$. **Right panel:** Efficiency comparison for ERK(4) on meshes composed of different cell geometries.

III.5.2 Accuracy study and efficiency on a Ricker wavelet

Here, we investigate the accuracy of the proposed method to simulate the propagation of an elasto-acoustic wave through a bilayered, stratified medium. Referring to Figure III.10, let H denote the height of the whole domain, H^F and H^S the height of the fluid and solid subdomain respectively, and L the width of both subdomains. We define $\Omega^F := (0, L) \times (0, H^F)$ for the fluid subdomain and $\Omega^S := (0, L) \times (-H^S, 0)$ for the solid subdomain. Homogeneous Dirichlet boundary conditions are applied, the source terms are set to zero, and the perturbation to quiescence is due to the initial velocity field that is a Ricker wavelet centered at the point $(x_c, y_c) \in \Omega^F$ (indicated in purple in Figure III.10), expressed as

$$\mathbf{m}_0(x, y) := \theta \exp\left(-\pi^2 \frac{r^2}{\lambda^2}\right) (x - x_c, y - y_c)^\dagger, \quad (\text{III.37})$$

where $\theta := 1 \text{ [Hz]}$, $\lambda := \frac{c_p}{f_c} \text{ [m]}$ with $f_c := 10 \text{ [Hz]}$, and $r^2 := (x - x_c)^2 + (y - y_c)^2$.

Three virtual sensors record the properties of the propagating elasto-acoustic wavefield: \mathcal{S}^F , \mathcal{S}^S and \mathcal{S}^I , located in the fluid subdomain, in the solid subdomain and at the interface, respectively. The acoustic sensor \mathcal{S}^F records the acoustic pressure $p_{\mathcal{T}^F}$ and the fluid velocity $\mathbf{m}_{\mathcal{T}^F}$, whereas the elastic sensor \mathcal{S}^S records the elastic velocity $\mathbf{v}_{\mathcal{T}^S}$ and the stress tensor $\mathbf{s}_{\mathcal{T}^S}$. The sensor located at the interface records the four quantities $p_{\mathcal{F}^F}$, $\mathbf{m}_{\mathcal{T}^F}$, $\mathbf{v}_{\mathcal{F}^S}$ and $\mathbf{s}_{\mathcal{T}^S}$.

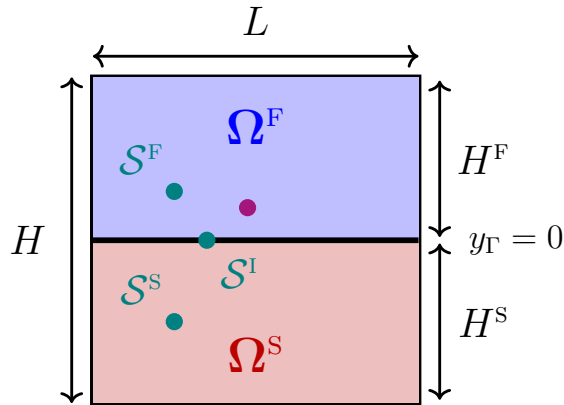


Fig. III.10: General setting for the accuracy tests with a Ricker wavelet as an initial condition. Turquoise dots indicate the position of the three sensors and the magenta dot indicates the localization of the center of the initial source.

III.5.2.1 Academic material properties

We first consider an academic case in which the acoustic and elastic media exhibit identical densities and propagate the acoustic waves and the elastic S-waves at the same velocity as compressional acoustic waves, *i.e.*,

$$\rho^F := \rho^S := 1, \quad c_p^S := \sqrt{3}, \quad c_p^F := c_s^S := 1. \quad (\text{III.38})$$

Concerning the geometry, we set $L := H := 1$ [m], $H^F := H^S := 0.5$ [m], and the pulse is located at $x_c := 0$ [m], $y_c := 0.125$ [m] in the fluid subdomain. The simulation time is set to $T_f := 1$ [s].

As observed below equations (III.6)-(III.7), the coupling conditions on Γ are weakly imposed. Here, we take a closer look at what happens at the interface so as to illustrate numerically the convergence results established in [121]. To this purpose, we use the sensor $S^I := (-0.3, 0)$ [m] and we set, for all $t \in \bar{J}$,

$$\Delta_{\text{KIN}}(t, S^I) := |(\mathbf{v}_{\mathcal{F}^S}(t, S^I) - \mathbf{m}_{\mathcal{T}^F}(t, S^I)) \cdot \mathbf{n}_\Gamma|, \quad (\text{III.39a})$$

$$\Delta_{\text{DYN}}(t, S^I) := \|p_{\mathcal{F}^F}(t, S^I)\mathbf{n}_\Gamma - \mathbf{s}_{\mathcal{T}^S}(t, S^I) \cdot \mathbf{n}_\Gamma\|, \quad (\text{III.39b})$$

The numerical results are obtained using SDIRK(3, 4) and the time step is set to $\Delta t = 0.1 \times 2^{-8}$ (this value is small enough so that space discretization errors dominate). Figure III.11 reports the evolution at the discrete time nodes of the errors defined in (III.39), for various mesh refinement levels ℓ . The left column shows the kinematic errors (III.39a), whereas the right column shows the dynamic errors (III.39b). The top row corresponds to the polynomial degree $k = 1$ and the bottom row to $k = 3$. As expected, the numerical error on the pointwise satisfaction of the coupling conditions decreases significantly when increasing the mesh refinement and/or the polynomial degree

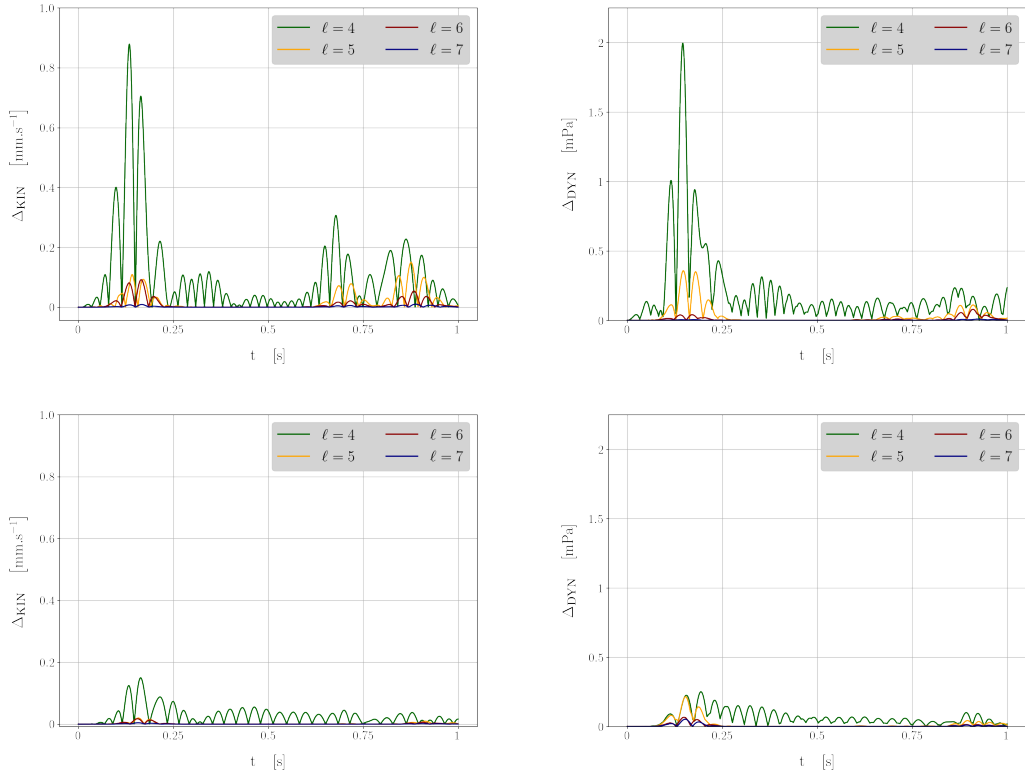


Fig. III.11: Errors on the coupling conditions as a function of the time predicted by SDIRK(3, 4) for $k = 1$ (top row) and $k = 3$ (bottom row). **Left:** Kinematic errors (see (III.39a)). **Right:** Dynamic errors (see (III.39b)).

III.5.2.2 Realistic (strongly contrasted) material properties

We now consider a test case with a strong contrast of material properties, specifically focusing on hard rock (granite) overlaid by a water layer with the following material properties:

$$\begin{aligned} \rho^F &:= 1025 \text{ kg.m}^{-3}, & c_p^F &:= 1500 \text{ m.s}^{-1}, \\ \rho^S &:= 2690 \text{ kg.m}^{-3}, & c_p^S &:= 6000 \text{ m.s}^{-1}, & c_s^S &:= 3000 \text{ m.s}^{-1}. \end{aligned} \quad (\text{III.40})$$

The geometric setup is now $L := 7.5$ [km], $H := 5.25$ [km], $H^F := 1.5$ [km] and $H^S := 3.75$ [km], and the pulse is located at $x_c := 0$ [km], $y_c := 0.1$ [km] in the fluid subdomain. The simulation time is set to $T_f := 0.625$ [s]. The mesh is composed of quadrangular elements with size of $h_x = 23.3$ [m] and $h_y = 16.3$ [m].

The results are obtained using SDIRK(3, 4) and the time step is set to $\Delta t = 0.1 \times 2^{-6}$. A semi-analytical reference solution, valid until reflections occur at the domain boundaries, is computed using the open source software Gar6more (<https://gitlab.inria.fr/jdiaz/gar6more2d>). Figure III.12 displays the particularly rich structure of the pressure field in the fluid subdomain and of the Euclidian norm of the velocity field in the solid subdomain, both at final time. We observe the presence of conical and interface (Rayleigh, Scholte) waves, whose accurate capture is commonly used to assess the accuracy of a numerical method.

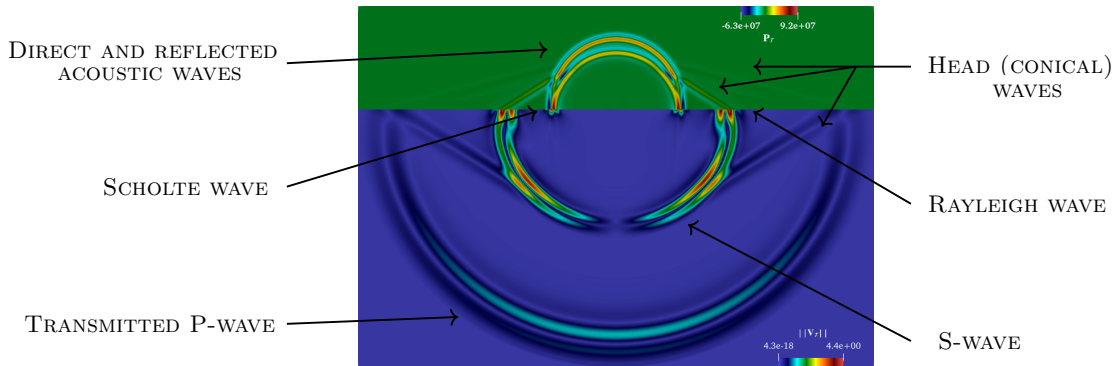


Fig. III.12: Spatial distribution of the acoustic pressure (upper side) and the elastic velocity norm (lower side) at $t = 0.625$ [s].

In Table III.4 and Figure III.13, we evaluate the accuracy of the numerical predictions at the three sensors located at $\mathcal{S}^F := (-2.3, 0.1)$ [km], $\mathcal{S}^S := (-2.3, -0.2)$ [km] and $\mathcal{S}^I := (-1.3, 0)$ [km]. The sensors \mathcal{S}^F and \mathcal{S}^S located within the two subdomains are positioned so as to capture only the conical waves, whereas the sensor \mathcal{S}^I located at the interface also captures the main phases. We compare ERK(4) and SDIRK(3, 4) and to avoid the proliferation of results, we focus on the polynomial degrees $k \in \{2, 3\}$ in Table III.4 and $k \in \{1, 3\}$ in Figure III.13. CPU times and relative errors with respect to the reference solution, measured at the sensors \mathcal{S}^F and \mathcal{S}^S , are reported in Table III.4. The relative

error is defined as

$$\text{ERR} := \frac{\|p_{\mathcal{T}^F}(t, \mathcal{S}^F) - p_{\text{REF}}(t, \mathcal{S}^F)\|_{\ell^2(J)}}{\|p_{\text{REF}}(t, \mathcal{S}^F)\|_{\ell^2(J)}} + \frac{\|\mathbf{v}_{\mathcal{T}^S}(t, \mathcal{S}^S) - \mathbf{v}_{\text{REF}}(t, \mathcal{S}^S)\|_{\ell^2(J)}}{\|\mathbf{v}_{\text{REF}}(t, \mathcal{S}^S)\|_{\ell^2(J)}}. \quad (\text{III.41})$$

Notice that all the methods compared in Table III.4 lead to comparable errors, so that the CPU comparison is meaningful concerning their efficiency. For the explicit scheme, we consider time steps just slightly below the stability limit. Instead, for the implicit scheme, we can consider larger time steps. In each case, the time step Δt is reported in nondimensional form as $\widetilde{\Delta t} := c_p^S \frac{\Delta t}{h}$, where c_p^S is defined in (III.40) and is the largest velocity in the domain. We observe in Table III.4 that the difference is significant between implicit and explicit time schemes. In particular, for $k = 3$, the CPU ratio reaches nearly 5, since much smaller time steps are required for explicit schemes. This negatively impacts the overall CPU time, confirming as in the previous section the higher efficiency reached by implicit schemes. Referring now to Figure III.13, we notice that, for $k = 1$, the spatial resolution is insufficient to accurately capture the solution, whereas, for $k = 3$, accurate solutions are captured when $\widetilde{\Delta t} \leq 0.414$.

SCHEMES	SOLVER	CFL*	$\widetilde{\Delta t}$	RATIO	CPU [s]	RATIO	ERR
SDIRK(3, 4)	direct	n/a	0.414	6.90	1125	1	3.15e-02
			0.414	6.90	2284	2.03	2.52e-02
SDIRK(3, 4)	iterative	n/a	0.414	6.90	2228	1.98	3.91e-02
			0.414	6.90	4216	3.75	3.11e-02
ERK(4)	n/a	0.138	0.095	1.36	1533	1.27	2.01e-2
		0.087	0.060	1	5664	5.03	1.90e-2

Tab. III.4: Times step $\widetilde{\Delta t}$ (normalized as CFL*), CPU times and errors (see (III.41)) for ERK(s) for $s \in \{2, 3, 4\}$ and $k \in \{2, 3\}$.

III.5.3 Geometric flexibility of HHO: a realistic simulation

Finally, we present a realistic test case of seismoacoustics coupling that is relevant in some geophysical applications. Namely, we are interested in the propagation of seismic waves that can be trapped in a sedimentary basin embedded in a hard rock, or bedrock, and such that large part of the energy can leak into the atmosphere. This phenomenon seems to have already been observed in [93, 11], and may be important for the monitoring of natural hazards or anthropogenic activities in areas where seismic arrays are sparse.

We restrict ourselves to a 2D simulation, because the high-performance computing tools for a realistic 3D simulation are not yet available in the present implementation of `disk++`. This study is thus to be considered as a proof-of-concept to showcase the benefits of using HHO methods through an ease in meshing procedures (polytopal flexibility). First, we illustrate that there is no need to restrict the spatial discretization to a unique cell geometry. If this may not be that relevant in 2D (where a complete discretization with quadrangles is possible), it is clearly a nontrivial issue in 3D realistic situations [63, 43]. Second, we show that HHO allows one to perform straightforwardly simulations using a nonconforming mesh (that is, with hanging nodes).

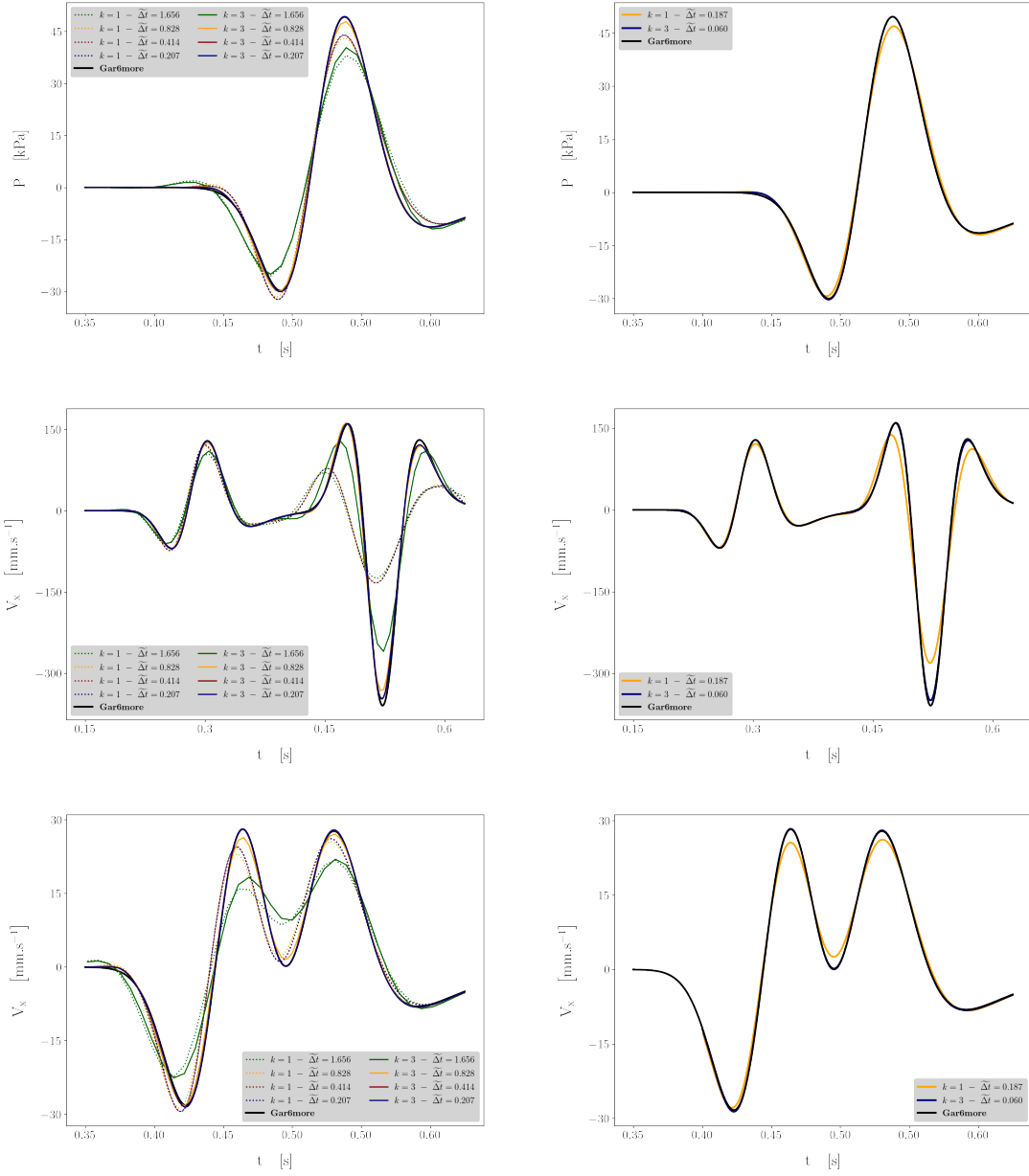


Fig. III.13: Spatial distribution of the acoustic pressure at S^F (top row), x -component of the velocity at S^I (center row) and S^S (bottom row) at times $t \in [0, 0.625]$ [s]. **Left column:** SDIRK(3,4), $k \in \{1, 3\}$, and $\tilde{\Delta t} \in \{0.402, 0.805, 1.609, 3.219\}$. **Right column:** ERK(4), $k \in \{1, 3\}$ and $\tilde{\Delta t} = \{0.117, 0.363\}$ (recall that $CFL^* = 0.087$ for $k = 3$).

III.5.3.1 Test case setting

The geological setting shown in the left panel of Figure III.14 is rather simplistic, especially concerning the spatial dimensions (less than 10 km in each direction, namely the domain extends from -4 [km] to $+4$ [km] laterally, and from -6 [km] to 1.4 [km]

vertically, with a solid-fluid boundary located around a height of +1.1 [km]), whereas interactions of the seismic wavefield with the sedimentary basin-atmosphere can happen several tens of kilometers away from the source [11]. Here, the source term is located under a small mountain (where coupling with the atmosphere is expected, see [46]), and a sedimentary basin is located 1 km away. The seismic motion is introduced as an initial condition in velocity, whose spatial distribution is that of a Ricker wavelet (as in (III.37)) with a central frequency of $f_c = 4$ Hz. The center of the Ricker wavelet is located at (0.563, 0.233) [km] (see Figure III.14). We consider a simulation time $T_f = 1.5$ [s], and material properties are reported in the right panel of Figure III.14.

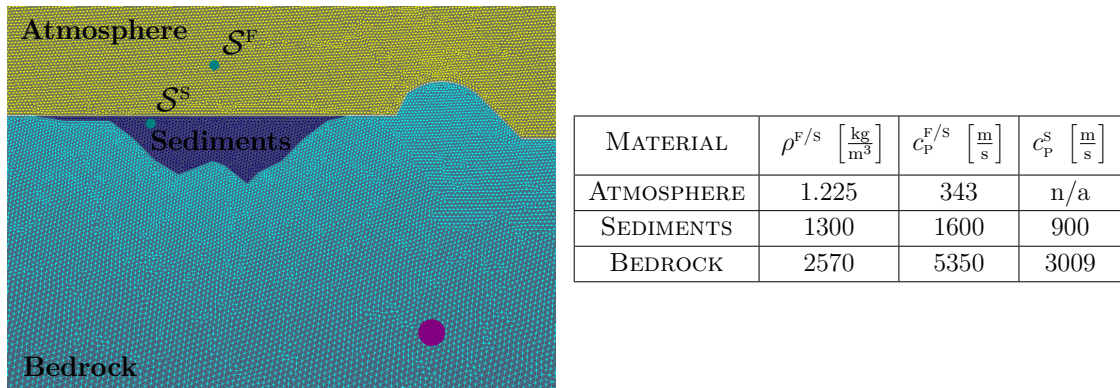


Fig. III.14: **Left panel:** Slightly zoomed-in view of the mesh (with triangles) of the computational domain: a bedrock (such as granite, in turquoise) embeds a sedimentary basin (in dark blue); both are overlaid by a homogeneous atmosphere (in yellow). Sensors (turquoise dots): A barometric sensor S^F is positioned in the atmosphere and a seismometer S^S is positioned in the sedimentary basin. The center of the Ricker wavelet is indicated by a purple point. **Right panel:** Material properties.

Our goal is to discretize the geometry with a classical meshing software (here, `gmsh`), without having to extensively tune the meshing process. Three meshes have therefore been generated: the canonical mesh delivered by *gmsh* with only simplices (Figure III.14, left panel); a second one with quadrangles only; and the last one, a hybrid mesh with both cell geometries (Figure III.15, left panel). This latter hybrid mesh illustrates a common situation where, due to geometric complexity, it becomes difficult for the meshing software to maintain a unique geometrical shape for the mesh cells. As a result, undesired element types—typically simplices—are introduced locally within a mesh that was intended to be uniformly shaped. Dealing with this issue typically requires manually modifying the mesh to make it purely quadrangular, a process that can be cumbersome and that frequently results in elements with poor Jacobian conditioning. Moreover, from a coarse mesh, we also generate a nonconforming mesh with hanging nodes, following a one-step refinement in the atmosphere and in the basin (Figure III.15, right panel). If both mixed and nonconforming meshes have already been used in other contexts [92], we underline that these can be naturally dealt with using HHO by leveraging its polytopal flexibility, without any specific extra procedure.

All the conforming meshes are generated in order for the acoustic waves and the asso-

ciated interface waves to be sufficiently sampled in space, so as to suffer from minimal grid dispersion. This corresponds to a length scale of around 14 [m] along the Earth-atmosphere interface. The nonconforming mesh is generated starting from a characteristic size for the edge length of 28 [m], and then refining in the atmosphere and the sedimentary basin only. The number of cells is 185 923 for the triangular mesh, 94 019 for the quadrangular mesh, 93 490 for the hybrid mesh, and 84 204 for the nonconforming mesh.

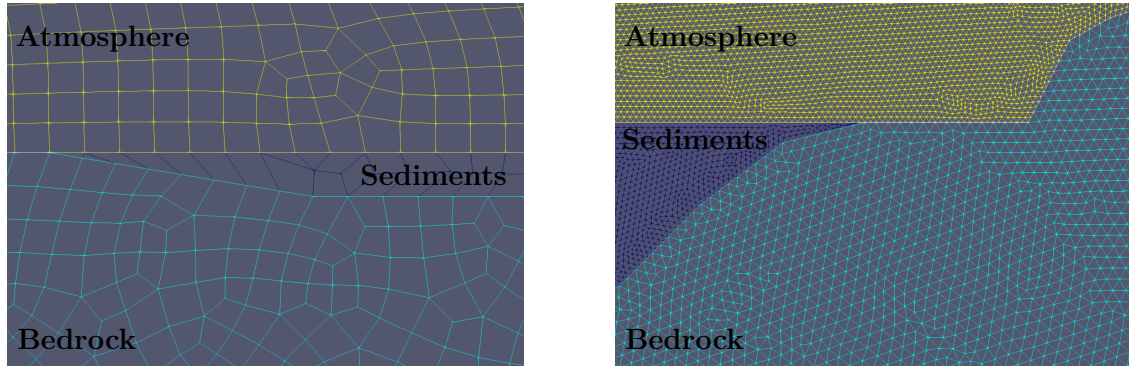


Fig. III.15: **Left panel:** Hybrid mesh generated using gmsh: Most of the cells are quadrangles (more than 99%), but with remaining triangles in some parts of the domain. **Right panel:** Nonconforming mesh with hanging nodes, after a one-pass refinement in the atmosphere and the basin.

III.5.3.2 Numerical results

The results are obtained using SDIRK(3,4) with polynomial degree $k = 3$ and time step $\Delta t = 4.7 \times 10^{-3}$ [s]. A reference solution is computed using the 2D spectral element solver of the SEM3D package (a co-developed and optimized spectral element code, <https://github.com/sem3d/SEM>), which is restricted to quadrangular meshes. This solver relies on a second-order (primal) formulation in time, an explicit Newmark scheme for time integration, with a polynomial degree $k = 4$ (using 5 GLL nodes in each tensorization direction) and a time step $\Delta t = 0.61 \times 10^{-4}$ [s]. In order to underline the significant reduction in dofs associated with static condensation in the case of an implicit time-stepping, these are reported in Table III.5 for the different meshes considered before and after static condensation. The ratio of dofs reduction is about 75% on all the meshes, a value that is consistent with the estimates in Table III.1.

	TYPE OF MESH			
	TRIANGULAR	QUADRANGULAR	HYBRID	NONCONFORMING
DOFS BEFORE STATIC CONDENSATION	8 538 346	4 562 532	4 533 700	3 761 468
DOFS AFTER STATIC CONDENSATION	1 448 120	977 560	971 416	810 344

Tab. III.5: Number of dofs for different meshes, before and after static condensation.

Figure III.16 displays the two-dimensional pressure field in the fluid subdomain and the

Euclidian norm of the velocity field in the solid subdomain at the times $t \in \{0, 0.16, 0.6, 1\}$ [s]. As expected, seismoacoustics coupling happens where the mountain is located (snapshot at $t = 0.16$ [s]): The pressure wave mainly results from the direct transmission of the solid velocity pulse above the mountain, but is also related to inhomogeneous waves that are guided along the interface (lateral head waves). The seismic energy also penetrates the Eastern part of the sedimentary basin. This part of the energy is then trapped in the sedimentary basin (because of differences in impedances with the bedrock), goes back and forth and continuously couples with the atmosphere (snapshots at times $t \in \{0.6, 1\}$ [s]). Long after its initial excitation, the basin still leaks energy into the atmosphere, as reported in [11].

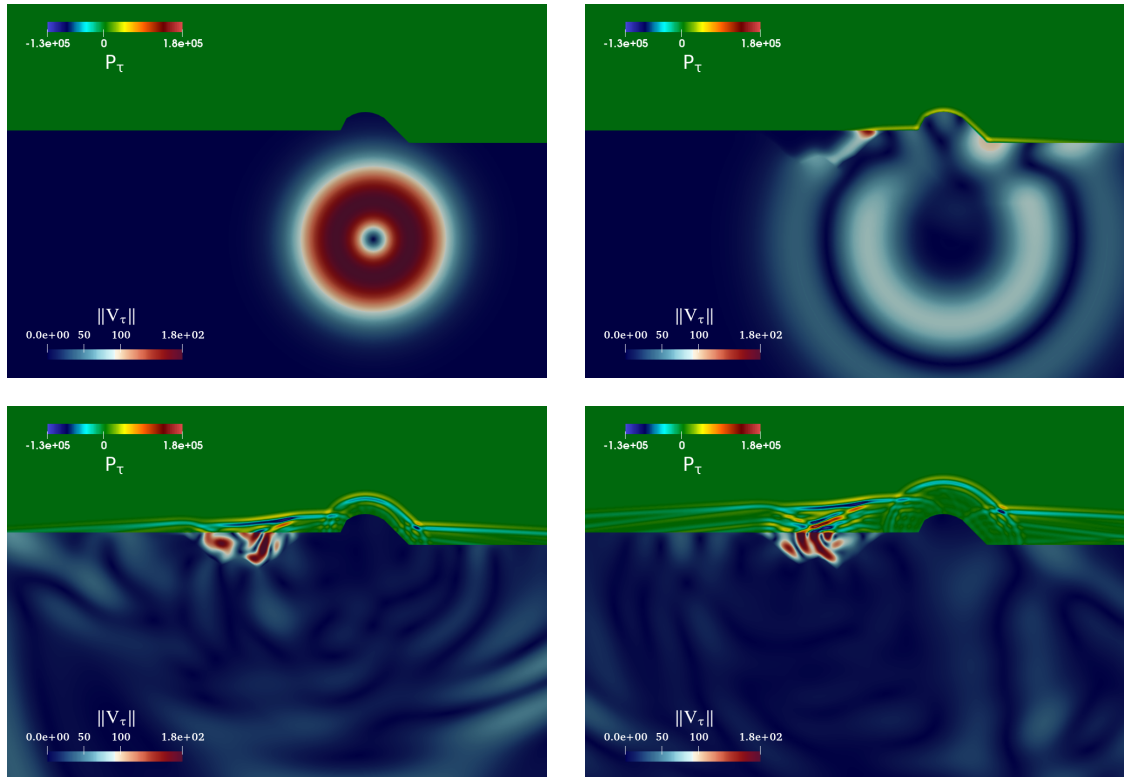


Fig. III.16: Spatial distribution of the acoustic pressure (atmosphere) and the elastic velocity norm (solid subdomain) at $t \in \{0, 0.16, 0.6, 1\}$ [s]. A part of the seismic energy leaks into the atmosphere where the mountain is located; another part is trapped in the sedimentary basin, which continuously emits waves to the atmosphere.

In Figure III.17, we compare the solution obtained using the HHO discretization with the reference solution at the two sensors located at $\mathcal{S}^F := (-0.65, 1.3)$ [km] and $\mathcal{S}^S := (-0.75, 1.08)$ [km]. An important conclusion is that the numerical results obtained using the HHO discretization applied to the different meshes are undistinguishable, thereby confirming the robustness of the proposed method with respect to the mesh. Furthermore, the numerical predictions perfectly match the reference solution for which the mesh is (and can only be) quadrangular. This underlines the accuracy of the developed HHO method for the simulation of wavefield propagation in complex media, and its strong potential for

extension to large-scale simulations. Moreover, it is interesting to notice the oscillations in the atmosphere, that are related to the multiple waves leaking from the sedimentary basin, as seen in Figure III.16.

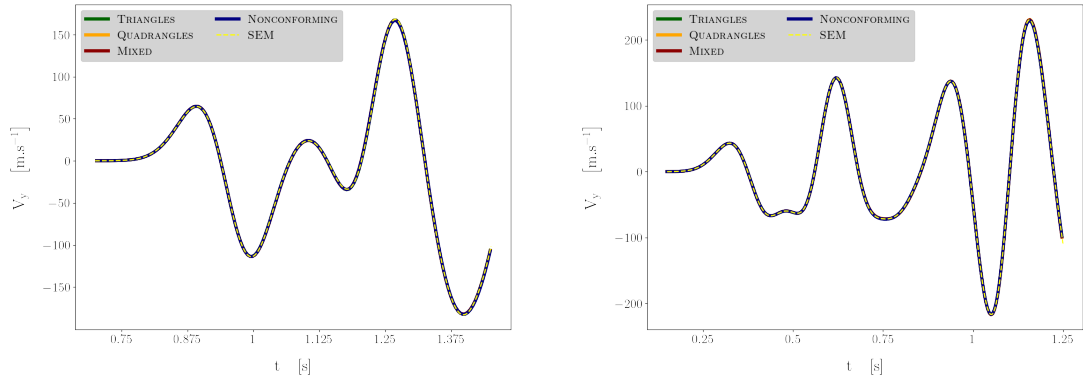


Fig. III.17: Evolution of the vertical component of the velocity as a function of time. **Left:** Record at the S^F sensor, in the atmosphere. **Right:** Record at the S^S sensor, in the sedimentary basin.

III.6 Conclusion

We proposed a HHO method for coupled elasto-acoustic wave propagation, combining first-order formulations in time with explicit and implicit Runge–Kutta schemes. Static condensation significantly reduces computational costs in both cases. A CFL stability condition was derived numerically, and comparisons showed good performances, with implicit schemes favored. Numerical experiments confirmed the accuracy and robustness of the proposed methodology on hybrid and nonconforming meshes, including realistic seismic scenarios.

A natural extension of this work consists in coupling the HHO discretization with SEM, leveraging the geometric flexibility of HHO in complex regions while exploiting the efficiency of the SEM in the bulk where structured meshes can be used. This combined approach would enable realistic, large-scale 3D geophysical simulations to be performed. Transitioning to three dimensions will also require significant numerical and computational developments, including parallelization and possibly GPU acceleration to align with emerging exascale architectures. Such efforts will likely necessitate a renewed performance analysis, in the spirit of [102]. In parallel, further improvements such as structure-preserving time integrators (see [131, 132] for HDG space semi-discretizations) and superconvergent post-processing tailored to HHO can be explored to enhance long-time accuracy. The use of alternative polynomial bases will also be investigated as a possible means to improve accuracy and computational efficiency. Finally, an HHO-based approach combined with adaptive mesh refinement would be particularly well-suited for wave propagation problems. It could leverage the polyhedral flexibility of the method to allow for nonconforming, locally refined meshes, thereby enhancing accuracy in regions with high solution gradients while controlling computational costs.

Unfitted HHO methods stabilized by polynomial extension

Abstract

In this work, we propose the design and the analysis of a novel hybrid high-order (HHO) method on unfitted meshes. HHO methods rely on a pair of unknowns, combining polynomials attached to the mesh faces and the mesh cells. In the unfitted framework, the interface can cut through the mesh cells in a very general fashion, and the polynomial unknowns are doubled in the cut cells and the cut faces. In order to avoid the ill-conditioning issues caused by the presence of small cut cells, the novel approach introduced herein is to use polynomial extensions in the definition of the gradient reconstruction operator. Stability and consistency results are established, leading to optimally decaying error estimates. The theory is illustrated by numerical experiments.

This chapter is based on a paper submitted to *SIAM Journal on Numerical Analysis (SINUM)* entitled “Unfitted HHO methods stabilized by polynomial extension” [37].

Contents

IV.1	Introduction	100
IV.2	Model problem	101
IV.3	Unfitted HHO methods	103
IV.3.1	Unfitted meshes	103
IV.3.2	Unfitted HHO spaces	105
IV.3.3	Local reconstruction operator	106
IV.3.4	Stabilization	108
IV.3.5	Discrete problem	109
IV.4	Stability, consistency, and error estimate	112
IV.4.1	Analysis tools	112
IV.4.2	Stability and well-posedness	113
IV.4.3	Interpolation operator	115
IV.4.4	Consistency	116
IV.4.5	Error estimate	118
IV.5	Numerical results	118
IV.5.1	Implementation aspects	119
IV.5.2	Convergence rates	120

IV.6 Proofs	125
IV.6.1 Proof of Lemma IV.4.1	125
IV.6.2 Proof of Lemma IV.4.2	126

IV.1 Introduction

The meshing of complex domains or of internal interfaces is an important bottleneck in the large-scale computation of solutions to partial differential equations. It is well-known that, for standard finite element methods, the mesh must match the geometry sufficiently well, or accuracy will be lost. This is particularly important for high-order methods. Recently, many methods have been developed aiming at simplifying the meshing procedure by allowing for a larger set of geometric shapes for the computational cells. Examples of discretization methods supporting fairly general polygonal (or polyhedral) cells are the discontinuous Galerkin (dG) method [67, 39], the virtual element method (VEM) [20], and hybrid nonconforming methods in various flavors, such as the hybridizable dG (HDG) method [55], the weak Galerkin (WG) method [141], the nonconforming VEM (ncVEM) method [12] and the hybrid high-order (HHO) method [69]. The tight connections between HDG, WG, and HHO methods are highlighted in [53]. These three methods are formulated by means of degrees of freedom (dofs) both in the bulk of the elements and on the element faces, whereas dG methods only use bulk dofs. Using face dofs leads to advantageous properties, such as the elimination of bulk dofs by static condensation and the absence of minimal threshold to weigh the stabilization.

Nevertheless, difficulties remain when using hybrid nonconforming methods in the presence of curved boundaries or interfaces, whereas the treatment of cells with curved faces in dG methods is more straightforward. One possibility is to enrich (with non-polynomial functions) the set of unknowns on curved faces, as in [146] for HHO and in [21] for ncVEM. Another possibility is to work with mesh cells having flat faces, but to build the geometric representation directly into the discretization, in such a way that solution accuracy is not lost although the mesh does not respect the geometry. This idea has been developed first in the framework of unfitted finite element methods. These methods originate from the penalty method [13, 17] and were further developed for conforming FEM in [16]. Combining the ideas of unfitted FEM with Nitsche's method for interface problems led to a consistent unfitted finite element method for interface problems in [88]. These ideas were then generalized to include much more complex coupling problems including PDEs on surfaces and multiphysics coupling, leading to the cutFEM framework [30]. Unfitted methods have also been considered for dG [19, 97, 113], HDG [56, 129], and HHO [35] methods. A crucial problem for unfitted methods is to handle the instabilities that can occur for certain intersections of the mesh and the interface. In the cutFEM framework using a conforming approximation in each subdomain, this is solved by the addition of certain stabilized terms [28], whereas in dG methods, which are much more flexible with respect to cell geometry, this can be solved by cell agglomeration [133, 97]. This technique can also be used in the context of conforming finite elements [14] (therein called aggregated FEM).

In the present work, we continue the development of unfitted HHO methods. The combination of cell agglomeration and a local weak coupling derived from the HHO framework has been successfully applied to elliptic interface problems [29], incompressible Stokes flows [31], and wave propagation in heterogeneous media [33]. Nevertheless, if these methods have to be integrated in an existing HHO code, the cell-agglomeration procedure becomes a disruptive element since it requires modifying part of the mesh in the interface zone. It is often desirable to keep the underlying mesh fixed and modify instead the algebraic structure of the bulk unknowns. One technique that fits this purpose is the idea of polynomial extension from interior elements to stabilize the method. The idea was first introduced in the context of Lagrange multipliers [89] and then using Nitsche's method for finite element [111, 38], isogeometric [27] and VEM [23, 22, 95] methods. The purpose of this work is to develop and analyze this technique for hybrid nonconforming methods, focusing on HHO methods. Owing to the close links between HDG, WG, ncVEM and HHO methods, the present results are relevant to the development of these other methods as well. Moreover, we focus on elliptic interface problems, but observe that elliptic problems posed on curved domains can be handled by the same techniques.

Let us briefly outline the main idea. Recall that a central ingredient in HHO methods is a local gradient reconstruction from the local cell and face unknowns. The stability and consistency properties of this reconstructed gradient crucially hinge on a discrete trace inequality on the normal derivatives at the cell faces. In the case of ill-cut cells, the constant in this inequality degenerates. One remedy, explored in [35, 29], is to use cell agglomeration around ill-cut cells. This procedure produces an aggregated mesh solely composed of well-cut cells, whose size is close to that of the original mesh. The remedy explored herein is to use the cell and face polynomials of ill-cut cells in the gradient reconstruction of a neighboring well-cut cell. With this approach, the mesh cells remain unmodified, but the stencil associated with the gradient reconstruction operator is slightly extended. The main question is then whether the reconstructed gradient maintains the above stability and optimal approximation properties. The proof of these properties is by no means straightforward and is the main contribution of this work. Interestingly, the main analysis tools (discrete trace inequality and polynomial approximation) are of independent interest.

This work is organized as follows. In Section IV.2, we introduce the model problem. In Section IV.3, we present the unfitted HHO method stabilized using polynomial extensions. The stability and error analysis of the method is covered in Section IV.4. Numerical results are presented in Section IV.5. Finally, the proofs of the analysis tools (discrete trace inequality and polynomial approximation) on unfitted meshes is outlined in Section IV.6.

IV.2 Model problem

Let Ω be a polyhedral domain in \mathbb{R}^d , $d \in \{2, 3\}$ (open, bounded, connected, Lipschitz subset of \mathbb{R}^d), and consider a partition of Ω into two disjoint subdomains $\overline{\Omega} = \overline{\Omega_1} \cup \overline{\Omega_2}$ with interface $\Gamma := \partial\Omega_1 \cap \partial\Omega_2$, as illustrated in Figure IV.1. For all $i \in \{1, 2\}$, we set $\bar{i} := 3 - i$, so that $\Omega \setminus \Omega^i = \Omega^{\bar{i}} \cup \Gamma$. For simplicity, we assume that the interface Γ is of class C^2 and that it does not touch the boundary of Ω . The unit normal vector \mathbf{n}_Γ to Γ

conventionally points from Ω_1 to Ω_2 . For a smooth enough function v defined on $\Omega_1 \cup \Omega_2$, setting $v_i := v|_{\Omega_i}$ for all $i \in \{1, 2\}$, we denote its jump across Γ as $\llbracket v \rrbracket_\Gamma := v_1|_\Gamma - v_2|_\Gamma$.

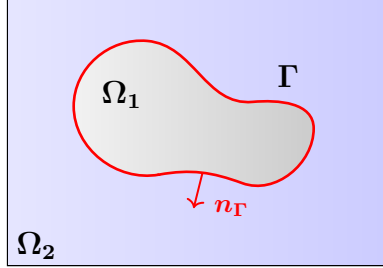


Fig. IV.1: Model problem

Our goal is to approximate the solution $u \in H^1(\Omega_1 \cup \Omega_2)$ of the following elliptic interface problem:

$$-\nabla \cdot (\kappa \nabla u) = f \quad \text{in } \Omega_1 \cup \Omega_2, \tag{IV.1a}$$

$$\llbracket u \rrbracket_\Gamma = g_D \quad \text{on } \Gamma, \tag{IV.1b}$$

$$\llbracket \kappa \nabla u \rrbracket_\Gamma \cdot \mathbf{n}_\Gamma = g_N \quad \text{on } \Gamma, \tag{IV.1c}$$

$$u = 0 \quad \text{on } \partial\Omega, \tag{IV.1d}$$

with $f \in L^2(\Omega)$, $g_D \in H^{\frac{1}{2}}(\Gamma)$ and $g_N \in L^2(\Gamma)$. For simplicity, we consider a homogeneous Dirichlet boundary condition on $\partial\Omega$ (see (IV.1d)). We assume that the diffusion coefficient κ is scalar-valued and that $\kappa_i := \kappa|_{\Omega_i}$ is constant for each $i \in \{1, 2\}$. To fix the ideas, we assume that $\kappa_1 \leq \kappa_2$. Our analysis covers the strongly contrasted case where $\kappa_1 \ll \kappa_2$. We emphasize that it is the property $\kappa_1 \leq \kappa_2$ that fixes the numbering of the subdomains, and not the fact that one of them touches the boundary. Thus, the numbering in Figure IV.1 is only illustrative. We also notice that the above assumptions on Γ and κ can be lifted with additional technicalities.

The weak formulation can be written as

$$\text{Find } u \in V_{g_D}, \quad a(u, w) = \ell(w) \quad \forall w \in V_0, \tag{IV.2}$$

with $V_{g_D} := \{v \in H^1(\Omega_1 \cup \Omega_2) \mid \llbracket v \rrbracket_\Gamma = g_D \text{ on } \Gamma, v = 0 \text{ on } \partial\Omega\}$. Notice that $V_0 = H_0^1(\Omega)$. The symmetric bilinear form a and the linear form ℓ are defined as

$$\left\{ \begin{array}{l} a(v, w) := \sum_{i \in \{1, 2\}} \kappa_i (\nabla v_i, \nabla w_i)_{\Omega_i} \\ \ell(w) := (f, w)_\Omega + (g_N, w)_\Gamma. \end{array} \right. \tag{IV.3a}$$

$$\tag{IV.3b}$$

Here and in what follows, for a measurable subset $S \subset \Omega$, we denote by $(\cdot, \cdot)_S$ the $L^2(S)$ -inner product with appropriate Lebesgue measure and by $\|\cdot\|_S$ the corresponding norm. We notice that, in the weak formulation (IV.2), the jump condition (IV.1b) and the boundary condition (IV.1d) are enforced explicitly in the definition of the functional space V_{g_D} , whereas the jump condition (IV.1c) is enforced weakly (i.e., results from the weak formulation).

IV.3 Unfitted HHO methods

In this section, we present the unfitted HHO method with stabilization of ill-cut cells using polynomial extensions. Let us recall that we use boldface fonts for vectors, as well as for vector-valued fields and spaces composed of such fields.

IV.3.1 Unfitted meshes

Let \mathcal{T}_h be a mesh that covers Ω exactly. A generic mesh cell is denoted $T \in \mathcal{T}_h$, it is considered to be an open set, h_T denotes its diameter, and \boldsymbol{n}_T its unit outward normal. The mesh size is defined as $h := \max_{T \in \mathcal{T}_h} h_T$. For all $T \in \mathcal{T}_h$, its neighboring layers $\Delta_j(T) \subset \mathcal{T}_h$ are defined by induction as $\Delta_0(T) := T$ and $\Delta_j(T) := \left\{ T' \in \mathcal{T}_h \mid \overline{T'} \cap \overline{\Delta_{j-1}(T)} \neq \emptyset \right\}$ for all $j \in \mathcal{N}$. In what follows, we use $j \in \{1, 2\}$. To alleviate the notation, we set $\Delta(T) := \Delta_1(T)$. We make the mild assumption that, for every mesh cell $T \in \mathcal{T}_h$, its convex hull, $\text{conv}(T)$, satisfies

$$\text{conv}(T) \subset \Delta(T). \quad (\text{IV.4})$$

For instance, this assumption trivially holds true if all the mesh cells are convex sets, and it remains a reasonable assumption if the mesh cells are nonconvex. One can also assume more generally that $\text{conv}(T) \subset \Delta_{n_0}(T)$ for some fixed integer n_0 .

The mesh \mathcal{T}_h is typically composed of cells having a simple shape (although this is not a necessary assumption); in our illustrations, we consider a structured mesh composed of squares. Quite importantly, the mesh \mathcal{T}_h is not fitted to the interface Γ , so that Γ can cut arbitrarily across any mesh cell. For all $T \in \mathcal{T}_h$, we set $T^\Gamma := T \cap \Gamma$ and $T^i := T \cap \Omega^i$ for all $i \in \{1, 2\}$ (some of these sets may be empty). The first obvious partition among the mesh cells is between uncut and cut cells. Moreover, among cut cells, we distinguish between well-cut and ill-cut cells. Specifically, we fix a parameter $\vartheta \in (0, 1)$ and say that a cut cell T is a well-cut cell if, for all $i \in \{1, 2\}$, T^i contains a ball of radius ϑh_T , whereas T is an ill-cut cell if this condition fails. It is shown in [35, Lemma 6.2] that, if the mesh size h is small enough (with respect to the curvature of the interface) and the parameter ϑ is small enough (with respect to the shape-regularity parameter of the mesh), then, for every ill-cut cell, the above condition fails on one and only one side of T . In what follows, we assume that this is always the case. The above considerations lead to the following partitions:

$$\mathcal{T}_h := \mathcal{T}_h^{\text{uncut}} \cup \mathcal{T}_h^{\text{cut}}, \quad \mathcal{T}_h^{\text{cut}} := \mathcal{T}_h^{\text{OK}} \cup \mathcal{T}_h^{\text{KO}}, \quad (\text{IV.5})$$

where $\mathcal{T}_h^{\text{uncut}}$ collects the uncut cells, $\mathcal{T}_h^{\text{cut}}$ the cut cells, $\mathcal{T}_h^{\text{OK}}$ the well-cut cells, and $\mathcal{T}_h^{\text{KO}}$ the ill-cut cells. Setting $\mathcal{T}_h^i := \{T \in \mathcal{T}_h \mid T \subset \Omega_i\}$ for all $i \in \{1, 2\}$, we have $\mathcal{T}_h^{\text{uncut}} = \mathcal{T}_h^1 \cup \mathcal{T}_h^2$. For every $T \in \mathcal{T}_h^{\text{uncut}}$, we define $\iota(T) \in \{1, 2\}$ as the index such that $T \in \mathcal{T}_h^{\iota(T)}$. Moreover, for all $T \in \mathcal{T}_h^{\text{KO}}$, we define $\iota(T) \in \{1, 2\}$ as the index for which the above ball condition fails. We then consider the partition $\mathcal{T}_h^{\text{KO}} = \mathcal{T}_h^{\text{KO},1} \cup \mathcal{T}_h^{\text{KO},2}$, where $T \in \mathcal{T}_h^{\text{KO},i}$ if $\iota(T) = i$. In conclusion, a mesh partition that is finer than (IV.5) is

$$\mathcal{T}_h := \underbrace{\mathcal{T}_h^1 \cup \mathcal{T}_h^2}_{\mathcal{T}_h^{\text{uncut}}} \cup \underbrace{\mathcal{T}_h^{\text{OK}} \cup \mathcal{T}_h^{\text{KO},1} \cup \mathcal{T}_h^{\text{KO},2}}_{=\mathcal{T}_h^{\text{cut}}}. \quad (\text{IV.6})$$

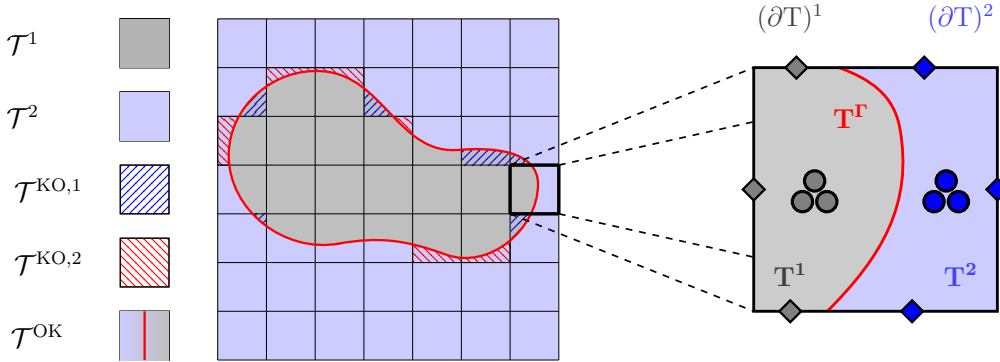


Fig. IV.2: Left: Illustration of the different types of cell in the unfitted mesh. Right: Zoom on the local degrees of freedom in a cut cell $T \in \mathcal{T}_h^{OK}$; here, the approximation is affine in the sub-cells and constant on the sub-faces.

The polynomial extension technique we propose relies on a pairing operator, which maps every ill-cut cell $T \in \mathcal{T}_h^{KO}$ to an uncut or a well-cut cell that belongs to the neighborhood $\Delta(T)$. We denote the pairing operator as $\mathcal{N} : \mathcal{T}_h^{KO} \longrightarrow \mathcal{T}_h$, so that we have

$$\mathcal{N} : \mathcal{T}_h^{KO} \ni S \longmapsto T \in (\mathcal{T}_h^i \cup \mathcal{T}_h^{OK} \cup \mathcal{T}_h^{KO,\bar{i}}) \cap \Delta(S), \quad i := \iota(T). \quad (\text{IV.7})$$

Letting $\mathcal{N}_i := \mathcal{N}|_{\mathcal{T}_h^{KO,i}}$ for all $i \in \{1, 2\}$, we have more specifically

$$\mathcal{N}_i : \mathcal{T}_h^{KO,i} \ni S \longmapsto T \in (\mathcal{T}_h^i \cup \mathcal{T}_h^{OK} \cup \mathcal{T}_h^{KO,\bar{i}}) \cap \Delta(S). \quad (\text{IV.8})$$

We notice that the set $\mathcal{T}_h^{KO,i}$ can be partitioned as follows:

$$\mathcal{T}_h^{KO,i} = \mathcal{N}_i^{-1}(\mathcal{T}_h^i) \cup \mathcal{N}_i^{-1}(\mathcal{T}_h^{OK}) \cup \mathcal{N}_i^{-1}(\mathcal{T}_h^{KO,\bar{i}}), \quad \forall i \in \{1, 2\}. \quad (\text{IV.9})$$

The pairing operator is essentially the one constructed in [29, Algorithm 1]. One difference, however, is that after Step 3 of this algorithm, we need to add an additional Step 4 performing the same operations as in Step 3, but for any mesh cell in $\mathcal{T}_h^{KO,2}$. One way of proceeding is to set $\mathcal{N}_2(T) := S$, whenever $T := \mathcal{N}_1(S) \in \mathcal{T}_h^{KO,2}$ for some cell $S \in \mathcal{T}_h^{KO,1}$. Thus, the well-cut part of S in Ω_2 will be used for T , and the well-cut part of T in Ω_1 will be used for S . The reason why Step 4 is not needed in the context of cell-agglomeration is that by agglomerating T and S in Step 3, T does not require any further stabilization. An illustration of the pairing operators \mathcal{N}_1 and \mathcal{N}_2 is shown in Figure IV.3, and two concrete examples are displayed in the central column of Figure IV.5 below. Notice that it may happen that some cells in \mathcal{T}_h^{OK} are in the image of both \mathcal{N}_1 and \mathcal{N}_2 .

The mesh faces are collected in the set \mathcal{F}_h , and we set $\mathcal{F}_h^i := \{F \in \mathcal{F}_h \mid F \subset \Omega_i\}$ for all $i \in \{1, 2\}$. For every mesh face $F \in \mathcal{F}_h^\Gamma := \mathcal{F}_h \setminus (\mathcal{F}_h^1 \cup \mathcal{F}_h^2)$ cut by the interface Γ , we define its two sub-faces as $F^i := F \cap \Omega_i$ for all $i \in \{1, 2\}$. For all $T \in \mathcal{T}_h$, $\mathcal{F}_{\partial T}$ is the collection of mesh faces composing the boundary ∂T . Moreover, for every cut cell $T \in \mathcal{T}_h^{OK} \cup \mathcal{T}_h^{KO}$, recalling that $T^\Gamma = T \cap \Gamma$, the boundary $\partial(T^i)$ of the sub-cell T^i is decomposed as

$$\partial(T^i) := (\partial T)^i \cup T^\Gamma, \quad (\partial T)^i := \partial T \cap (\overline{\Omega_i} \setminus \Gamma), \quad \forall i \in \{1, 2\}. \quad (\text{IV.10})$$

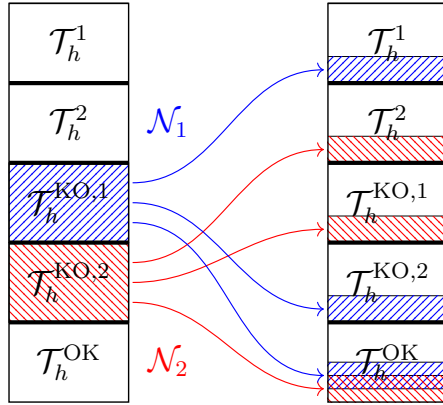


Fig. IV.3: Pairing operators \mathcal{N}_1 and \mathcal{N}_2 acting on the ill-cut cells.

To unify the notation, for every uncut cell $T \in \mathcal{T}_h^i$ with $i := \iota(T) \in \{1, 2\}$, we set (recall that $\bar{i} = 3 - i$)

$$T^i := T, \quad T^{\bar{i}} := \emptyset, \quad (\partial T)^i := \partial T, \quad (\partial T)^{\bar{i}} := \emptyset, \quad T^{\Gamma} := \emptyset. \quad (\text{IV.11})$$

Finally, for all $T \in \mathcal{T}_h$ and all $i \in \{1, 2\}$, the (possibly empty) set

$\mathcal{F}_{(\partial T)^i} := \{F^i = F \cap \Omega_i \mid F \in \mathcal{F}_{\partial T}\}$ is the collection of the (sub-)faces composing $(\partial T)^i$.

IV.3.2 Unfitted HHO spaces

HHO methods utilize polynomial unknowns attached to the mesh cells and to the mesh faces. We consider here the mixed-order HHO method, where the degree of the face unknowns is $k \geq 0$ and that of the cell unknowns is $(k + 1)$. For the motivation of using a mixed-order setting, we refer the reader to [35, Remark 4.1].

For every uncut cell $T \in \mathcal{T}_h^i$, $i \in \{1, 2\}$, the local discrete HHO unknowns are a pair composed of one cell polynomial and a collection of face polynomials (one for each face of T), so that

$$\hat{u}_T := (u_T, u_{\partial T}) \in \hat{\mathcal{U}}_T := P^{k+1}(T) \times P^k(\mathcal{F}_{\partial T}), \quad P^k(\mathcal{F}_{\partial T}) := \bigtimes_{F \in \mathcal{F}_{\partial T}} P^k(F). \quad (\text{IV.12})$$

Here, $P^{k+1}(T)$ (resp., $P^k(F)$) consists of the restriction to T (resp., F) of scalar-valued d variate polynomials of degree at most $(k + 1)$ (resp., $(d - 1)$ -variate polynomials of degree at most k composed with any affine geometric mapping from the hyperplane supporting F to \mathbb{R}^{d-1}). For every cut cell $T \in \mathcal{T}_h^{OK} \cup \mathcal{T}_h^{KO}$, following [35, 29], we double the HHO unknowns so as to have the usual unknowns available in each sub-cell, except on T^{Γ} where there are no unknowns. Thus, the local HHO unknowns in every cut cell are

$$\hat{u}_T := (\hat{u}_{T^1}, \hat{u}_{T^2}) := (u_{T^1}, u_{(\partial T)^1}, u_{T^2}, u_{(\partial T)^2}) \in \hat{\mathcal{U}}_T := \hat{\mathcal{U}}_{T^1} \times \hat{\mathcal{U}}_{T^2}, \quad (\text{IV.13})$$

with $\hat{\mathcal{U}}_{T^i} := P^{k+1}(T^i) \times P^k(\mathcal{F}_{(\partial T)^i})$ and $P^k(\mathcal{F}_{(\partial T)^i}) := \bigtimes_{F^i \in \mathcal{F}_{(\partial T)^i}} P^k(F^i)$, for all $i \in \{1, 2\}$.

To unify the notation between cut and uncut cells, we write \hat{u}_T in the same format as in (IV.13) for every uncut cell as well. Thus, we write $\hat{u}_T := (u_T, u_{\partial T}, 0, 0)$ for all $T \in \mathcal{T}_h^1$ and $\hat{u}_T := (0, 0, u_T, u_{\partial T})$ for all $T \in \mathcal{T}_h^2$.

The global HHO space on the unfitted mesh is

$$\widehat{\mathcal{U}}_h := \mathcal{U}_{\mathcal{T}_h^1} \times \mathcal{U}_{\mathcal{F}_h^1} \times \mathcal{U}_{\mathcal{T}_h^2} \times \mathcal{U}_{\mathcal{F}_h^2}, \quad (\text{IV.14})$$

where

$$\mathcal{U}_{\mathcal{T}_h^i} := \bigtimes_{T \in \mathcal{T}_h} P^{k+1}(T^i), \quad \mathcal{U}_{\mathcal{F}_h^i} := \bigtimes_{F \in \mathcal{F}_h} P^k(F^i), \quad \forall i \in \{1, 2\}. \quad (\text{IV.15})$$

To enforce the homogeneous Dirichlet boundary condition on $\partial\Omega$, we consider the subspace $\widehat{\mathcal{U}}_{h0} := \mathcal{U}_{\mathcal{T}_h^1} \times \mathcal{U}_{\mathcal{F}_h^10} \times \mathcal{U}_{\mathcal{T}_h^2} \times \mathcal{U}_{\mathcal{F}_h^20}$, where $\mathcal{U}_{\mathcal{F}_h^10}$ and $\mathcal{U}_{\mathcal{F}_h^20}$ are the subspaces of $\mathcal{U}_{\mathcal{F}_h^1}$ and $\mathcal{U}_{\mathcal{F}_h^2}$, respectively, where all the unknowns attached to faces located on $\partial\Omega$ are set to zero. Recall that only one of the two subdomains Ω_i touches the boundary, so that, in practice, only one of the two face spaces is modified to account for Dirichlet conditions.

IV.3.3 Local reconstruction operator

The local reconstruction operator is a central tool in the devising of HHO methods. Recall that, in the fitted case, one possibility (see [1, 64]) is to consider, for all $T \in \mathcal{T}_h$, the operator $\mathbf{G}_T^k : \widehat{\mathcal{U}}_T \rightarrow \mathbf{P}^k(T)$ such that, for all $\hat{u}_T = (u_T, u_{\partial T}) \in \widehat{\mathcal{U}}_T$ and all $\mathbf{q} \in \mathbf{P}^k(T)$,

$$(\mathbf{G}_T^k(\hat{u}_T), \mathbf{q})_T := (\nabla u_T, \mathbf{q})_T + (u_{\partial T} - u_T, \mathbf{q} \cdot \mathbf{n}_T)_{\partial T}. \quad (\text{IV.16})$$

In the unfitted case, the idea proposed in [29] is to reconstruct a gradient in each sub-cell T^i . Thus, one defines a pair of local operators $\mathbf{G}_{T^i}^k : \widehat{\mathcal{U}}_T \rightarrow \mathbf{P}^k(T^i)$, $i \in \{1, 2\}$, such that, for all $\hat{u}_T = (u_{T^1}, u_{(\partial T)^1}, u_{T^2}, u_{(\partial T)^2}) \in \widehat{\mathcal{U}}_T$ and all $\mathbf{q} \in \mathbf{P}^k(T^i)$,

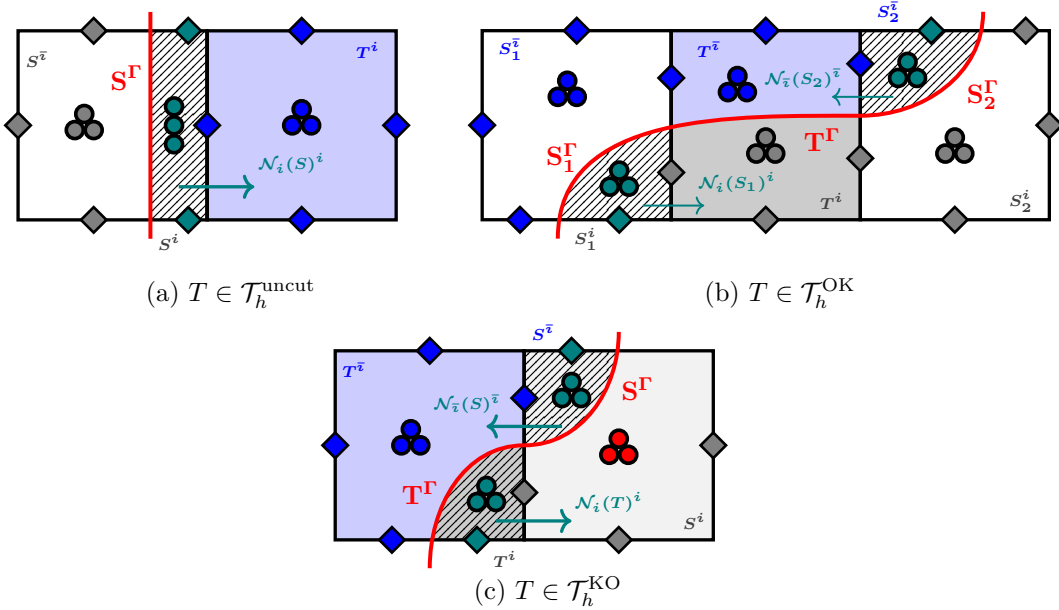
$$(\mathbf{G}_{T^i}^k(\hat{u}_T), \mathbf{q})_{T^i} := (\nabla u_{T^i}, \mathbf{q})_{T^i} + (u_{(\partial T)^i} - u_{T^i}, \mathbf{q} \cdot \mathbf{n}_T)_{(\partial T)^i} - \delta_{i1}([\![u_T]\!]_{\Gamma}, \mathbf{q} \cdot \mathbf{n}_{\Gamma})_{T\Gamma}, \quad (\text{IV.17})$$

with $[\![u_T]\!]_{\Gamma} := u_{T^1}|_{T\Gamma} - u_{T^2}|_{T\Gamma}$ and δ_{i1} denotes the Kronecker delta. Notice that the two gradients are reconstructed independently, but $\mathbf{G}_{T^1}^k$ depends on the cell components on both sides of the interface owing to the last term in (IV.17). This term is only present when $i = 1$ because we assumed $\kappa_1 \leq \kappa_2$ (to fix the ideas, otherwise the term is present only when $i = 2$). As discussed in [29, Section 2.5], this is instrumental to achieve robustness of the error estimate in the highly contrasted case $\kappa_1 \ll \kappa_2$.

Owing to the use of polynomial extensions in the present work, the stencil of the local gradient reconstruction operator needs to be extended. Indeed, on a given mesh cell $T \in \mathcal{T}_h$, this operator now involves the local cell and face unknowns in T (as before), but also the cell and face unknowns of the ill-cut cells $S \in \mathcal{N}^{-1}(T)$ (those are the cells $S \in \mathcal{T}_h$ such that there exists $i \in \{1, 2\}$ so that $\mathcal{N}_i(S) = T$). Therefore, for all $T \in \mathcal{T}_h$, we introduce the notation

$$\hat{u}_T^{\mathcal{N}} := (\hat{u}_T, (\hat{u}_S)_{S \in \mathcal{N}^{-1}(T)}) \in \widehat{\mathcal{U}}_T^{\mathcal{N}} := \widehat{\mathcal{U}}_T \times \bigtimes_{S \in \mathcal{N}^{-1}(T)} \widehat{\mathcal{U}}_S. \quad (\text{IV.18})$$

We can now define, for all $T \in \mathcal{T}_h$, the local gradient reconstruction operators $\mathbf{G}_{T^i}^k : \widehat{\mathcal{U}}_T^{\mathcal{N}} \rightarrow \mathbf{P}^k(T^i)$, for all $i \in \{1, 2\}$. For a polynomial $\mathbf{q} \in \mathbf{P}^k(T^i)$ with $i \in \{1, 2\}$, \mathbf{q}^+ denotes its extension to $T^i \cup \bigcup_{S \in \mathcal{N}_i^{-1}(T)} S^i$. Then, for all $\hat{u}_T^{\mathcal{N}} \in \widehat{\mathcal{U}}_T^{\mathcal{N}}$,

**Fig. IV.4:** Local stencil for gradient reconstruction operator

i) If $T \in \mathcal{T}_h^{\text{uncut}}$, we set, for all $\mathbf{q} \in \mathbf{P}^k(T^i)$ with $i := \iota(T)$,

$$\begin{aligned} (\mathbf{G}_{T^i}^k(\hat{u}_T^N), \mathbf{q})_{T^i} &:= (\nabla u_{T^i}, \mathbf{q})_{T^i} + (u_{(\partial T)^i} - u_{T^i}, \mathbf{q} \cdot \mathbf{n}_T)_{(\partial T)^i} \\ &\quad + \sum_{S \in \mathcal{N}_i^{-1}(T)} \left\{ (u_{(\partial S)^i} - u_{S^i}, \mathbf{q}^+ \cdot \mathbf{n}_S)_{(\partial S)^i} - \delta_{i1} ([u_S]_\Gamma, \mathbf{q}^+ \cdot \mathbf{n}_\Gamma)_{S^R} \right\}, \end{aligned} \quad (\text{IV.19a})$$

$$\mathbf{G}_{T^i}^k(\hat{u}_T^N) := \mathbf{0}, \quad (\text{IV.19b})$$

where the summation over $S \in \mathcal{N}_i^{-1}(T)$ is void if T is not in the image of \mathcal{N}_i ;

ii) If $T \in \mathcal{T}_h^{\text{OK}}$, we set, for all $i \in \{1, 2\}$ and all $\mathbf{q} \in \mathbf{P}^k(T^i)$,

$$\begin{aligned} (\mathbf{G}_{T^i}^k(\hat{u}_T^N), \mathbf{q})_{T^i} &:= (\nabla u_{T^i}, \mathbf{q})_{T^i} + (u_{(\partial T)^i} - u_{T^i}, \mathbf{q} \cdot \mathbf{n}_T)_{(\partial T)^i} - \delta_{i1} ([u_T]_\Gamma, \mathbf{q} \cdot \mathbf{n}_\Gamma)_{T^R} \\ &\quad + \sum_{S \in \mathcal{N}_i^{-1}(T)} \left\{ (u_{(\partial S)^i} - u_{S^i}, \mathbf{q}^+ \cdot \mathbf{n}_S)_{(\partial S)^i} - \delta_{i1} ([u_S]_\Gamma, \mathbf{q}^+ \cdot \mathbf{n}_\Gamma)_{S^R} \right\}; \end{aligned} \quad (\text{IV.20})$$

iii) If $T \in \mathcal{T}_h^{\text{KO}}$, we set, for all $\bar{\mathbf{q}} \in \mathbf{P}^k(T^i)$ with $i := \iota(T)$,

$$\mathbf{G}_{T^i}^k(\hat{u}_T^N) := \nabla u_{T^i}, \quad (\text{IV.21a})$$

$$\begin{aligned} (\mathbf{G}_{T^i}^k(\hat{u}_T^N), \bar{\mathbf{q}})_{T^i} &:= (\nabla u_{T^i}, \bar{\mathbf{q}})_{T^i} + (u_{(\partial T)^i} - u_{T^i}, \bar{\mathbf{q}} \cdot \mathbf{n}_T)_{(\partial T)^i} - \delta_{i1} ([u_T]_\Gamma, \bar{\mathbf{q}} \cdot \mathbf{n}_\Gamma)_{T^R} \\ &\quad + \sum_{S \in \mathcal{N}_i^{-1}(T)} \left\{ (u_{(\partial S)^i} - u_{S^i}, \bar{\mathbf{q}}^+ \cdot \mathbf{n}_S)_{(\partial S)^i} - \delta_{i1} ([u_S]_\Gamma, \bar{\mathbf{q}}^+ \cdot \mathbf{n}_\Gamma)_{S^R} \right\}. \end{aligned} \quad (\text{IV.21b})$$

Since the discretization method is formulated on the mesh sub-cells, we consider the collection thereof, which is conveniently described as a subset of the product set $\mathcal{T}_h \times \{1, 2\}$.

Specifically, we set

$$\begin{aligned}\mathcal{P}_h^{\text{OK}} &:= \{(T, \iota(T)) \mid T \in \mathcal{T}_h^{\text{uncut}}\} \cup \{(T, 1), (T, 2) \mid T \in \mathcal{T}_h^{\text{OK}}\} \\ &\quad \cup \{(T, \bar{i}), \mid T \in \mathcal{T}_h^{\text{KO}}, i := \iota(T)\},\end{aligned}\tag{IV.22a}$$

$$\mathcal{P}_h^{\text{KO}} := \{(T, i) \mid T \in \mathcal{T}_h^{\text{KO}}, i := \iota(T)\}.\tag{IV.22b}$$

Notice that $\mathcal{P}_h := \mathcal{P}_h^{\text{OK}} \cup \mathcal{P}_h^{\text{KO}}$ is the collection of all the mesh sub-cells. As a consequence of (IV.9), the subset $\mathcal{P}_h^{\text{KO}}$ can be enumerated as follows:

$$\mathcal{P}_h^{\text{KO}} = \{(S, i) \in \mathcal{P}_h \mid S \in \mathcal{N}_i^{-1}(T), (T, i) \in \mathcal{P}_h^{\text{OK}}\}.\tag{IV.23}$$

The above notation allows us to rewrite in a synthetic form the formula for the gradient reconstruction while avoiding the proliferation of cases. Indeed, one readily sees that the formulas (IV.19a)-(IV.20)-(IV.21b) are equivalent to setting, for all $(T, i) \in \mathcal{P}_h^{\text{OK}}$, all $\hat{u}_T^{\mathcal{N}} \in \hat{\mathcal{U}}_T^{\mathcal{N}}$ and all $\mathbf{q} \in \mathbf{P}^k(T^i)$,

$$\begin{aligned}(\mathbf{G}_{T^i}^k(\hat{u}_T^{\mathcal{N}}), \mathbf{q})_{T^i} &:= (\nabla u_{T^i}, \mathbf{q})_{T^i} + (u_{(\partial T)^i} - u_{T^i}, \mathbf{q} \cdot \mathbf{n}_T)_{(\partial T)^i} - \delta_{i1}(\llbracket u_T \rrbracket_\Gamma, \mathbf{q} \cdot \mathbf{n}_\Gamma)_{T^\Gamma} \\ &\quad + \sum_{S \in \mathcal{N}_i^{-1}(T)} \left\{ (u_{(\partial S)^i} - u_{S^i}, \mathbf{q}^+ \cdot \mathbf{n}_S)_{(\partial S)^i} - \delta_{i1}(\llbracket u_S \rrbracket_\Gamma, \mathbf{q}^+ \cdot \mathbf{n}_\Gamma)_{S^\Gamma} \right\},\end{aligned}\tag{IV.24}$$

where the summation over $S \in \mathcal{N}_i^{-1}(T)$ is void if T is not in the image of \mathcal{N}_i . Moreover, (IV.21a) means that, for all $(T, i) \in \mathcal{P}_h^{\text{KO}}$, we set

$$\mathbf{G}_{T^i}^k(\hat{u}_T^{\mathcal{N}}) := \nabla u_{T^i}.\tag{IV.25}$$

For all $(T, 1) \in \mathcal{P}_h^{\text{OK}}$, it is convenient to define the discrete lifting operator $\mathbf{L}_{T^1}^k : L^2(\Gamma) \rightarrow \mathbf{P}^k(T^1)$ such that, for all $g \in L^2(\Gamma)$ and all $\mathbf{q} \in \mathbf{P}^k(T^1)$,

$$(\mathbf{L}_{T^1}^k(g), \mathbf{q})_{T^1} := (g, \mathbf{q} \cdot \mathbf{n}_\Gamma)_{T^\Gamma} + \sum_{S \in \mathcal{N}_1^{-1}(T)} (g, \mathbf{q}^+ \cdot \mathbf{n}_S)_{S^\Gamma}.\tag{IV.26}$$

It is also convenient to define on Γ the function given by the jump of the cell components of a discrete HHO variable. Specifically, we define the function $\llbracket u_{\mathcal{T}_h} \rrbracket_\Gamma$ on Γ such that, for all $T \in \mathcal{T}_h^{\text{cut}}$, $\llbracket u_{\mathcal{T}_h} \rrbracket_\Gamma := u_{T^1}|_{T^\Gamma} - u_{T^2}|_{T^\Gamma}$. Then, for all $(T, i) \in \mathcal{P}_h^{\text{OK}}$, we can rewrite (IV.24) as follows:

$$\begin{aligned}(\mathbf{G}_{T^i}^k(\hat{u}_T^{\mathcal{N}}) + \delta_{i1} \mathbf{L}_{T^1}^k(\llbracket u_{\mathcal{T}_h} \rrbracket_\Gamma), \mathbf{q})_{T^i} &:= (\nabla u_{T^i}, \mathbf{q})_{T^i} + (u_{(\partial T)^i} - u_{T^i}, \mathbf{q} \cdot \mathbf{n}_T)_{(\partial T)^i} \\ &\quad + \sum_{S \in \mathcal{N}_i^{-1}(T)} (u_{(\partial S)^i} - u_{S^i}, \mathbf{q}^+ \cdot \mathbf{n}_S)_{(\partial S)^i}.\end{aligned}\tag{IV.27}$$

IV.3.4 Stabilization

We consider three local stabilization bilinear forms. The first one is the usual HHO stabilization bilinear form in the mixed-order setting (in the spirit of the HDG Lehrenfeld–Schöberl stabilization [108]). Its role is to weakly enforce the matching between cell- and

face-based HHO unknowns on the sub-faces of the mesh sub-cells in each sub-domain. For all $\hat{v}_h, \hat{w}_h \in \hat{\mathcal{U}}_{h0}$, we set

$$s_h^\circ(\hat{v}_h, \hat{w}_h) := \sum_{(T,i) \in \mathcal{P}_h} \kappa_i h_T^{-1} (\Pi_{(\partial T)^i}^k(v_{T^i}) - v_{(\partial T)^i}, \Pi_{(\partial T)^i}^k(w_{T^i}) - w_{(\partial T)^i})_{(\partial T)^i}, \quad (\text{IV.28})$$

where $\Pi_{(\partial T)^i}^k$ denotes the L^2 -orthogonal projector onto $P^k(\mathcal{F}_{(\partial T)^i})$.

The second stabilization bilinear form is the same as the one introduced in [35, 29] to control the jumps across the interface Γ . Specifically, we set, for all $\hat{v}_h, \hat{w}_h \in \hat{\mathcal{U}}_{h0}$,

$$s_h^\Gamma(\hat{v}_h, \hat{w}_h) := \sum_{T \in \mathcal{T}_h^{\text{cut}}} \kappa_1 h_T^{-1} ([v_T]_\Gamma, [w_T]_\Gamma)_{T^\Gamma}. \quad (\text{IV.29})$$

The third stabilization bilinear form is specific to the present setting using polynomial extensions. Its aim is to provide some control on the cell components in ill-cut cells. Specifically, we set, for all $\hat{v}_h, \hat{w}_h \in \hat{\mathcal{U}}_{h0}$,

$$s_h^N(\hat{v}_h, \hat{w}_h) := \sum_{(T,i) \in \mathcal{P}_h^{\text{OK}}} \sum_{S \in \mathcal{N}_i^{-1}(T)} \kappa_i h_S^{-1} (v_{S^i} - v_{T^i}^+, w_{S^i} - w_{T^i}^+)_{(\partial S)^i}, \quad (\text{IV.30})$$

where the superscript $+$ denotes the extension of a polynomial originally defined on T^i to $T^i \cup \bigcup_{S \in \mathcal{N}_i^{-1}(T)} S^i$.

Putting everything together, we define, for all $\hat{v}_h, \hat{w}_h \in \hat{\mathcal{U}}_{h0}$,

$$s_h(\hat{v}_h, \hat{w}_h) := s_h^\circ(\hat{v}_h, \hat{w}_h) + s_h^\Gamma(\hat{v}_h, \hat{w}_h) + s_h^N(\hat{v}_h, \hat{w}_h). \quad (\text{IV.31})$$

IV.3.5 Discrete problem

The global discrete problem reads as follows: Find $\hat{u}_h \in \hat{\mathcal{U}}_{h0}$ such that,

$$a_h(\hat{u}_h, \hat{w}_h) = \ell_h(\hat{w}_h) \quad \forall \hat{w}_h \in \hat{\mathcal{U}}_{h0}, \quad (\text{IV.32})$$

where the bilinear a_h is defined as follows: For all $\hat{v}_h, \hat{w}_h \in \hat{\mathcal{U}}_{h0}$,

$$a_h(\hat{v}_h, \hat{w}_h) := b_h(\hat{v}_h, \hat{w}_h) + s_h(\hat{v}_h, \hat{w}_h), \quad (\text{IV.33})$$

with

$$b_h(\hat{v}_h, \hat{w}_h) := \sum_{(T,i) \in \mathcal{P}_h} \kappa_i (\mathbf{G}_{T^i}^k(\hat{v}_T^N), \mathbf{G}_{T^i}^k(\hat{w}_T^N))_{T^i}. \quad (\text{IV.34})$$

Moreover, the linear form ℓ_h is such that, for all $\hat{w}_h \in \hat{\mathcal{U}}_{h0}$,

$$\begin{aligned} \ell_h(\hat{w}_h) &:= \sum_{(T,i) \in \mathcal{P}_h} (f, w_{T^i})_{T^i} + \sum_{T \in \mathcal{T}_h^{\text{cut}}} \left\{ (g_N, w_{T^2})_{T^\Gamma} + \kappa_1 h_T^{-1} (g_D, [w_T]_\Gamma)_{T^\Gamma} \right\} \\ &\quad - \sum_{(T,1) \in \mathcal{P}_h^{\text{OK}}} \kappa_1 (\mathbf{L}_{T^1}^k(g_D), \mathbf{G}_{T^1}^k(\hat{w}_T^N))_{T^1}, \end{aligned} \quad (\text{IV.35})$$

where the lifting operator $\mathbf{L}_{T^1}^k$ is defined in (IV.26). Notice that, in the discrete problem (IV.32), only the Dirichlet boundary condition is enforced explicitly (on the face

unknowns located on the boundary $\partial\Omega$), whereas both jump conditions across the interface, (IV.1b) and (IV.1c), are enforced weakly. We notice that cell unknowns can still be eliminated from (IV.32) by static condensation. Whenever $\mathcal{N}^{-1}(T)$ is nonempty for a mesh cell $T \in \mathcal{T}_h$, all the cell unknowns attached to $T \cup \bigcup_{S \in \mathcal{N}_i^{-1}(T)} S$ are blocked together.

To prepare for the consistency error analysis, we state a useful result on the discrete bilinear and linear forms.

Lemma IV.3.1 (Consistency: preparatory identity). *Let u be the weak solution to (IV.2). Let $\hat{v}_h \in \hat{\mathcal{U}}_{h0}$ be arbitrary and set*

$$\boldsymbol{\delta}_{T,i} := \mathbf{G}_{T^i}^k(\hat{v}_T^{\mathcal{N}}) + \delta_{i1} \mathbf{L}_{T^1}^k([\![u]\!]_{\Gamma}) - \nabla u_i|_{T^i}, \quad \forall (T, i) \in \mathcal{P}_h, \quad (\text{IV.36a})$$

$$\boldsymbol{\delta}_{T,S,i} := \{\mathbf{G}_{T^i}^k(\hat{v}_T^{\mathcal{N}}) + \delta_{i1} \mathbf{L}_{T^1}^k([\![u]\!]_{\Gamma})\}^+|_{S^i} - \nabla u_i|_{S^i}, \quad \forall (T, i) \in \mathcal{P}_h^{\text{OK}}, \forall S \in \mathcal{N}_i^{-1}(T), \quad (\text{IV.36b})$$

where, consistently with the notation introduced above, the superscript $+$ applied to a polynomial in $\mathbf{P}^k(T^i)$ indicates its extension to $T^i \cup \bigcup_{S \in \mathcal{N}_i^{-1}(T)} S^i$. Then, the following holds for all $\hat{w}_h \in \hat{\mathcal{U}}_{h0}$,

$$\begin{aligned} & a_h(\hat{v}_h, \hat{w}_h) - \ell_h(\hat{w}_h) \\ &= \sum_{(T,i) \in \mathcal{P}_h} \kappa_i (\boldsymbol{\delta}_{T,i}, \nabla w_{T^i})_{T^i} \\ &\quad + \sum_{(T,i) \in \mathcal{P}_h^{\text{OK}}} \kappa_i \left\{ (\boldsymbol{\delta}_{T,i} \cdot \mathbf{n}_T, w_{(\partial T)^i} - w_{T^i})_{(\partial T)^i} - \delta_{i1} (\boldsymbol{\delta}_{T,1} \cdot \mathbf{n}_{\Gamma}, [\![w_T]\!]_{\Gamma})_{T^{\Gamma}} \right\} \\ &\quad + \sum_{S \in \mathcal{N}_i^{-1}(T)} \left\{ (\boldsymbol{\delta}_{T,S,i} \cdot \mathbf{n}_S, w_{(\partial S)^i} - w_{S^i})_{(\partial S)^i} - \delta_{i1} (\boldsymbol{\delta}_{T,S,1} \cdot \mathbf{n}_{\Gamma}, [\![w_S]\!]_{\Gamma})_{S^{\Gamma}} \right\} \\ &\quad + s_h^{\circ}(\hat{v}_h, \hat{w}_h) + s_h^{\mathcal{N}}(\hat{v}_h, \hat{w}_h) + \sum_{T \in \mathcal{T}_h^{\text{cut}}} \kappa_1 h_T^{-1} ([\![v_T - u]\!]_{\Gamma}, [\![w_T]\!]_{\Gamma})_{T^{\Gamma}}. \end{aligned} \quad (\text{IV.37})$$

Proof. (1) Recalling the properties (IV.1a)-(IV.1c) satisfied by the exact solution and the definition (IV.35) of the linear form ℓ_h , we infer that, for all $\hat{w}_h \in \hat{\mathcal{U}}_{h0}$, $\ell_h(\hat{w}_h) = L_1 + L_2 + L_3$ with

$$\begin{aligned} L_1 &:= \sum_{(T,i) \in \mathcal{P}_h} -(\nabla \cdot (\kappa_i \nabla u_i), w_{T^i})_{T^i} + \sum_{T \in \mathcal{T}_h^{\text{cut}}} ((\kappa_1 \nabla u_1 - \kappa_2 \nabla u_2) \cdot \mathbf{n}_{\Gamma}, w_{T^2})_{T^{\Gamma}}, \\ L_2 &:= \sum_{T \in \mathcal{T}_h^{\text{cut}}} \kappa_1 h_T^{-1} ([\![u]\!]_{\Gamma}, [\![w_T]\!]_{\Gamma})_{T^{\Gamma}}, \quad L_3 := - \sum_{(T,1) \in \mathcal{P}_h^{\text{OK}}} \kappa_1 (\mathbf{L}_{T^1}^k([\![u]\!]_{\Gamma}), \mathbf{G}_{T^1}^k(\hat{v}_T^{\mathcal{N}}))_{T^1}. \end{aligned}$$

Integrating by parts and re-organizing the boundary term on Γ (recall that $\mathbf{n}_{T^1} = -\mathbf{n}_{T^2} = \mathbf{n}_{\Gamma}$) gives

$$\begin{aligned} \sum_{(T,i) \in \mathcal{P}_h} -(\nabla \cdot (\kappa_i \nabla u_i), w_{T^i})_{T^i} &= \sum_{(T,i) \in \mathcal{P}_h} \kappa_i \{ (\nabla u_i, \nabla w_{T^i})_{T^i} - (\nabla u_i \cdot \mathbf{n}_T, w_{T^i})_{(\partial T)^i} \} \\ &\quad - \sum_{T \in \mathcal{T}_h^{\text{cut}}} \{ (\kappa_1 \nabla u_1 \cdot \mathbf{n}_{\Gamma}, w_{T^1})_{T^{\Gamma}} - (\kappa_2 \nabla u_2 \cdot \mathbf{n}_{\Gamma}, w_{T^2})_{T^{\Gamma}} \}. \end{aligned}$$

Since ∇u_i is single-valued on $(\partial T)^i \cap \Omega_i$ and $w_{(\partial T)^i}$ vanishes on the mesh boundary faces, we obtain

$$\begin{aligned} \sum_{(T,i) \in \mathcal{P}_h} -(\nabla \cdot (\kappa_i \nabla u_i), w_{T^i})_{T^i} &= \sum_{(T,i) \in \mathcal{P}_h} \kappa_i \{ (\nabla u_i, \nabla w_{T^i})_{T^i} + (\nabla u_i \cdot \mathbf{n}_T, w_{(\partial T)^i} - w_{T^i})_{(\partial T)^i} \} \\ &\quad - \sum_{T \in \mathcal{T}_h^{\text{cut}}} \{ (\kappa_1 \nabla u_1 \cdot \mathbf{n}_\Gamma, w_{T^1})_{T^\Gamma} - (\kappa_2 \nabla u_2 \cdot \mathbf{n}_\Gamma, w_{T^2})_{T^\Gamma} \}. \end{aligned}$$

Therefore, we have

$$L_1 = \sum_{(T,i) \in \mathcal{P}_h} \kappa_i \{ (\nabla u_i, \nabla w_{T^i})_{T^i} + (\nabla u_i \cdot \mathbf{n}_T, w_{(\partial T)^i} - w_{T^i})_{(\partial T)^i} \} - \sum_{T \in \mathcal{T}_h^{\text{cut}}} \kappa_1 (\nabla u_1 \cdot \mathbf{n}_\Gamma, [w_T]_\Gamma)_{T^\Gamma}.$$

A rewriting of the last term on the right-hand side gives

$$L_1 = \sum_{(T,i) \in \mathcal{P}_h} \kappa_i \{ (\nabla u_i, \nabla w_{T^i})_{T^i} + (\nabla u_i \cdot \mathbf{n}_T, w_{(\partial T)^i} - w_{T^i})_{(\partial T)^i} - \delta_{i1} (\nabla u_1 \cdot \mathbf{n}_\Gamma, [w_T]_\Gamma)_{T^\Gamma} \}.$$

We now use the enumeration formula (IV.23) for the pairs $(T, i) \in \mathcal{P}_h^{\text{KO}}$. This gives

$$\begin{aligned} L_1 &= \sum_{(T,i) \in \mathcal{P}_h} \kappa_i (\nabla u_i, \nabla w_{T^i})_{T^i} \\ &\quad + \sum_{(T,i) \in \mathcal{P}_h^{\text{OK}}} \kappa_i \left\{ (\nabla u_i \cdot \mathbf{n}_T, w_{(\partial T)^i} - w_{T^i})_{(\partial T)^i} - \delta_{i1} (\nabla u_1 \cdot \mathbf{n}_\Gamma, [w_T]_\Gamma)_{T^\Gamma} \right. \\ &\quad \left. + \sum_{S \in \mathcal{N}_i^{-1}(T)} \{ (\nabla u_i \cdot \mathbf{n}_S, w_{(\partial S)^i} - w_{S^i})_{(\partial S)^i} - \delta_{i1} (\nabla u_1 \cdot \mathbf{n}_\Gamma, [w_S]_\Gamma)_{S^\Gamma} \} \right\}. \end{aligned}$$

(2) For all $\hat{v}_h \in \hat{\mathcal{U}}_{h0}$, setting $\boldsymbol{\gamma}_{T,i} := \mathbf{G}_{T^i}^k(\hat{v}_T^N) + \delta_{i1} \mathbf{L}_{T^1}^k([u]_\Gamma)$ for all $(T, i) \in \mathcal{P}_h^{\text{OK}}$ and $\boldsymbol{\gamma}_{T,i} := \mathbf{G}_{T^i}^k(\hat{v}_T^N)$ for all $(T, i) \in \mathcal{P}_h^{\text{KO}}$, and using the definition (IV.34) of the bilinear form b_h , we infer that

$$\begin{aligned} b_h(\hat{v}_h, \hat{w}_h) - L_3 &= \sum_{(T,i) \in \mathcal{P}_h} \kappa_i (\mathbf{G}_{T^i}^k(\hat{v}_T^N), \mathbf{G}_{T^i}^k(\hat{w}_T^N))_{T^i} + \sum_{(T,1) \in \mathcal{P}_h^{\text{OK}}} \kappa_1 (\mathbf{L}_{T^1}^k([u]_\Gamma), \mathbf{G}_{T^1}^k(\hat{w}_T^N))_{T^1} \\ &= \sum_{(T,i) \in \mathcal{P}_h^{\text{OK}}} \kappa_i (\boldsymbol{\gamma}_{T,i}, \mathbf{G}_{T^i}^k(\hat{w}_T^N))_{T^i} + \sum_{(T,i) \in \mathcal{P}_h^{\text{KO}}} \kappa_i (\boldsymbol{\gamma}_{T,i}, \mathbf{G}_{T^i}^k(\hat{w}_T^N))_{T^i}. \end{aligned}$$

Using the definitions (IV.24)-(IV.25) of the gradient reconstruction operator and since $\boldsymbol{\gamma}_{T,i} \in \mathbf{P}^k(T^i)$ for all $(T, i) \in \mathcal{P}_h$, we obtain

$$\begin{aligned} b_h(\hat{v}_h, \hat{w}_h) &= \sum_{(T,i) \in \mathcal{P}_h} \kappa_i (\boldsymbol{\gamma}_{T,i}, \nabla w_{T^i})_{T^i} \\ &\quad + \sum_{(T,i) \in \mathcal{P}_h^{\text{OK}}} \kappa_i \left\{ (\boldsymbol{\gamma}_{T,i} \cdot \mathbf{n}_T, w_{(\partial T)^i} - w_{T^i})_{(\partial T)^i} - \delta_{i1} (\boldsymbol{\gamma}_{T,1} \cdot \mathbf{n}_\Gamma, [w_T]_\Gamma)_{T^\Gamma} \right. \\ &\quad \left. + \sum_{S \in \mathcal{N}_i^{-1}(T)} \{ (\boldsymbol{\gamma}_{T,i}^+ \cdot \mathbf{n}_S, w_{(\partial S)^i} - w_{S^i})_{(\partial S)^i} - \delta_{i1} (\boldsymbol{\gamma}_{T,1}^+ \cdot \mathbf{n}_\Gamma, [w_S]_\Gamma)_{S^\Gamma} \} \right\}. \end{aligned}$$

(3) Combining the identities from Steps (1) and (2) and recalling that $a_h = b_h + s_h$ completes the proof. \square

IV.4 Stability, consistency, and error estimate

In this section, we perform the stability and error analysis for the unfitted HHO method introduced in the previous section. We use the convention $A \lesssim B$ to abbreviate the inequality $A \leq CB$ for positive real numbers A and B , where the constant C only depends on the polynomial degree, the mesh shape-regularity, the parameter ϑ used in the definition of the pairing operator, and the space dimension.

IV.4.1 Analysis tools

In this section, we present the main tools to perform the error analysis. The proofs are postponed to Section IV.6. For all $(T, i) \in \mathcal{P}_h^{\text{OK}}$, the superscript $+$ is used here to indicate the extension of a polynomial originally defined on T^i to $\Delta(T)$ (recall that $T \cup \bigcup_{S \in \mathcal{N}_i^{-1}(T)} S \subset \Delta(T)$).

Lemma IV.4.1 (Discrete inverse inequalities). *The following holds for all $(T, i) \in \mathcal{P}_h^{\text{OK}}$, all $\phi \in P^\ell(T^i)$, and all $\ell \geq 0$,*

$$\sum_{S \in \{T\} \cup \mathcal{N}_i^{-1}(T)} \left\{ \|\phi^+\|_S + h_S^{\frac{1}{2}} \|\phi^+\|_{(\partial S)^i \cup S^\Gamma} \right\} \lesssim \|\phi\|_{T^i}, \quad (\text{IV.38a})$$

$$\sum_{S \in \{T\} \cup \mathcal{N}_i^{-1}(T)} h_S^{-\frac{1}{2}} \|(I - \Pi_{(\partial S)^i}^k)(\phi^+)\|_{(\partial S)^i} \lesssim \|\nabla \phi\|_{T^i}. \quad (\text{IV.38b})$$

For all $s \geq 0$ and all $i \in \{1, 2\}$, let $E_i^s : H^s(\Omega_i) \rightarrow H^s(\mathbb{R}^d)$ be a stable extension operator. For all $v \in H^s(\Omega_1 \cup \Omega_2)$ with $s > \frac{1}{2}$ and all $(T, i) \in \mathcal{P}_h^{\text{OK}}$, we define

$$I_{T^i}^{k+1}(v_i) := \Pi_T^{k+1}(E_i^s(v_i))|_{T^i} \in P^{k+1}(T^i), \quad (\text{IV.39})$$

where Π_T^{k+1} denotes the L^2 -orthogonal projection onto $P^{k+1}(T)$. (Notice that the operator $I_{T^i}^{k+1}$ depends on the Sobolev index s , but this dependency is not tracked to simplify the notation; notice also that the extension operator is not needed if T is an uncut cell.) Let us set

$$\begin{aligned} \epsilon_{T,i}(v_i) := & \sum_{S \in \{T\} \cup \mathcal{N}_i^{-1}(T)} \left\{ \|v_i - I_{T^i}^{k+1}(v_i)^+\|_{S^i} + h_S^{\frac{1}{2}} \|v_i - I_{T^i}^{k+1}(v_i)^+\|_{(\partial S)^i} \right. \\ & \left. + h_S \|\nabla(v_i - I_{T^i}^{k+1}(v_i)^+)\|_{S^i} + h_S^{\frac{3}{2}} \|\nabla(v_i - I_{T^i}^{k+1}(v_i)^+)\|_{(\partial S)^i} \right\}. \end{aligned} \quad (\text{IV.40})$$

Lemma IV.4.2 (Approximation). *For all $v \in H^s(\Omega_1 \cup \Omega_2)$ with $s \in (\frac{3}{2}, k+2]$ and all $(T, i) \in \mathcal{P}_h^{\text{OK}}$, we have*

$$\epsilon_{T,i}(v_i) \lesssim h_T^s |E_i^s(v_i)|_{H^s(\Delta(T))}, \quad (\text{IV.41a})$$

$$\sum_{S \in \{T\} \cup \mathcal{N}_i^{-1}(T)} h_S^{\frac{1}{2}} \|[v - I_T^{k+1}(v)]^+\|_\Gamma \|_{S^\Gamma} \lesssim h_T^s \sum_{i \in \{1, 2\}} |E_i^s(v_i)|_{H^s(\Delta_2(T))}, \quad (\text{IV.41b})$$

where $\|[v - I_T^{k+1}(v)]^+\|_\Gamma \|_{S^\Gamma} := (v_1 - I_{T^1}^{k+1}(v_1))|_{S^\Gamma} - (v_2 - I_{T^2}^{k+1}(v_2))|_{S^\Gamma}$.

IV.4.2 Stability and well-posedness

We introduce the following norm on $\hat{\mathcal{U}}_{h0}$: For all $\hat{v}_h \in \hat{\mathcal{U}}_{h0}$,

$$\|\hat{v}_h\|_{h0}^2 := \sum_{(T,i) \in \mathcal{P}_h} \kappa_i \|\nabla v_{T^i}\|_{T^i}^2 + |\hat{v}_h|_s^2 + s_h^\Gamma(\hat{v}_h, \hat{v}_h) + s_h^N(\hat{v}_h, \hat{v}_h), \quad (\text{IV.42})$$

where

$$|\hat{v}_h|_s^2 := \sum_{(T,i) \in \mathcal{P}_h} \kappa_i h_T^{-1} \|v_{(\partial T)^i} - v_{T^i}\|_{(\partial T)^i}^2, \quad (\text{IV.43})$$

and the stabilization bilinear forms are defined in Section IV.3.4. We observe that in general $|\hat{v}_h|_s^2 \neq s_h^0(\hat{v}_h, \hat{v}_h)$ since the cell component is projected when evaluating the latter. Furthermore, we notice the following rewriting:

$$\begin{aligned} \|\hat{v}_h\|_{h0}^2 &= \sum_{(T,i) \in \mathcal{P}_h} \kappa_i \left\{ \|\nabla v_{T^i}\|_{T^i}^2 + h_T^{-1} \|v_{(\partial T)^i} - v_{T^i}\|_{(\partial T)^i}^2 + \delta_{i1} h_T^{-1} \|[\![v_T]\!]_\Gamma\|_{T^\Gamma}^2 \right\} \\ &\quad + \sum_{(T,i) \in \mathcal{P}_h^{\text{OK}}} \sum_{S \in \mathcal{N}_i^{-1}(T)} \kappa_i h_S^{-1} \|v_{S^i} - v_{T^i}^+\|_{(\partial S)^i}^2, \end{aligned} \quad (\text{IV.44})$$

where (we recall that) $v_{T^i}^+$ denotes the extension of the polynomial $v_{T^i} \in P^{k+1}(T^i)$ to $T^i \cup \bigcup_{S \in \mathcal{N}_i^{-1}(T)} S^i$. It is straightforward to verify that (IV.42) defines a norm on $\hat{\mathcal{U}}_{h0}$. Indeed, if $\hat{v}_h \in \hat{\mathcal{U}}_{h0}$ satisfies $\|\hat{v}_h\|_{h0} = 0$, then all the cell unknowns and all the face unknowns are constant and take the same value inside each sub-domain Ω_i and globally in the domain Ω . Since the face unknowns on the boundary $\partial\Omega$ vanish, we conclude that all the components of \hat{v}_h are zero.

Lemma IV.4.3 (Stability and boundedness). *We have, for all $\hat{v}_h \in \hat{\mathcal{U}}_{h0}$,*

$$\|\hat{v}_h\|_{h0}^2 \lesssim a_h(\hat{v}_h, \hat{v}_h) \lesssim \|\hat{v}_h\|_{h0}^2. \quad (\text{IV.45})$$

Proof. (1) Bounds on reconstructed gradient. Let $(T, i) \in \mathcal{P}_h^{\text{OK}}$. Then, taking $\mathbf{q} := \nabla v_{T^i} \in \mathbf{P}^k(T^i)$ in (IV.24), we obtain

$$\begin{aligned} \|\nabla v_{T^i}\|_{T^i}^2 &= (\mathbf{G}_{T^i}^k(\hat{v}_T^N), \nabla v_{T^i})_{T^i} - (v_{(\partial T)^i} - v_{T^i}, \nabla v_{T^i} \cdot \mathbf{n}_T)_{(\partial T)^i} + \delta_{i1}([\![v_T]\!]_\Gamma, \nabla v_{T^i} \cdot \mathbf{n}_\Gamma)_{T^\Gamma} \\ &\quad - \sum_{S \in \mathcal{N}_i^{-1}(T)} \left\{ (v_{(\partial S)^i} - v_{S^i}, (\nabla v_{T^i})^+ \cdot \mathbf{n}_S)_{(\partial S)^i} - \delta_{i1}([\![v_S]\!]_\Gamma, (\nabla v_{T^i})^+ \cdot \mathbf{n}_\Gamma)_{S^\Gamma} \right\}. \end{aligned}$$

Since $\nabla v_{T^i} \cdot \mathbf{n}_T \in P^k(\mathcal{F}_{(\partial T)^i})$ and $(\nabla v_{T^i})^+ \cdot \mathbf{n}_S \in P^k(\mathcal{F}_{(\partial S)^i})$, we infer that

$$\begin{aligned} \|\nabla v_{T^i}\|_{T^i}^2 &= (\mathbf{G}_{T^i}^k(\hat{v}_T^N), \nabla v_{T^i})_{T^i} - (v_{(\partial T)^i} - \Pi_{(\partial T)^i}^k(v_{T^i}), \nabla v_{T^i} \cdot \mathbf{n}_T)_{(\partial T)^i} \\ &\quad + \delta_{i1}([\![v_T]\!]_\Gamma, \nabla v_{T^i} \cdot \mathbf{n}_\Gamma)_{T^\Gamma} \\ &\quad - \sum_{S \in \mathcal{N}_i^{-1}(T)} \left\{ (v_{(\partial S)^i} - \Pi_{(\partial S)^i}^k(v_{S^i}), (\nabla v_{T^i})^+ \cdot \mathbf{n}_S)_{(\partial S)^i} - \delta_{i1}([\![v_S]\!]_\Gamma, (\nabla v_{T^i})^+ \cdot \mathbf{n}_\Gamma)_{S^\Gamma} \right\}. \end{aligned}$$

Invoking the Cauchy–Schwarz inequality and the discrete trace inequality (IV.38a), we infer that

$$\|\nabla v_{T^i}\|_{T^i}^2 \lesssim \|\mathbf{G}_{T^i}^k(\hat{v}_T^N)\|_{T^i}^2 + \sum_{S \in \{T\} \cup \mathcal{N}_i^{-1}(T)} \left\{ h_S^{-1} \|v_{(\partial S)^i} - \Pi_{(\partial S)^i}^k(v_{S^i})\|_{(\partial S)^i}^2 + \delta_{i1} h_S^{-1} \|[\![v_S]\!]_\Gamma\|_{S^\Gamma}^2 \right\}.$$

Proceeding similarly proves that

$$\|\mathbf{G}_{T^i}^k(\hat{v}_T^N)\|_{T^i}^2 \lesssim \|\nabla v_{T^i}\|_{T^i}^2 + \sum_{S \in \{T\} \cup \mathcal{N}_i^{-1}(T)} \left\{ h_S^{-1} \|v_{(\partial S)^i} - \Pi_{(\partial S)^i}^k(v_{S^i})\|_{(\partial S)^i}^2 + \delta_{i1} h_S^{-1} \|\llbracket v_S \rrbracket_\Gamma\|_{S^\Gamma}^2 \right\}.$$

Moreover, for all $(T, i) \in \mathcal{P}_h^{\text{KO}}$, we have $\mathbf{G}_{T^i}^k(\hat{v}_T^N) = \nabla v_{T^i}$ in T^i . Therefore, multiplying by κ_i and summing over all $(T, i) \in \mathcal{P}_h$, we infer that

$$\sum_{(T,i) \in \mathcal{P}_h} \kappa_i \|\nabla v_{T^i}\|_{T^i}^2 \lesssim b_h(\hat{v}_h, \hat{v}_h) + s_h^\circ(\hat{v}_h, \hat{v}_h) + s_h^\Gamma(\hat{v}_h, \hat{v}_h), \quad (\text{IV.46a})$$

$$b_h(\hat{v}_h, \hat{v}_h) \lesssim \sum_{(T,i) \in \mathcal{P}_h} \kappa_i \|\nabla v_{T^i}\|_{T^i}^2 + s_h^\circ(\hat{v}_h, \hat{v}_h) + s_h^\Gamma(\hat{v}_h, \hat{v}_h). \quad (\text{IV.46b})$$

Since $s_h^\circ(\hat{v}_h, \hat{v}_h) \leq |\hat{v}_h|_S^2$, the upper bound in (IV.45) readily follows from (IV.46b).

(2) To prove the lower bound in (IV.45), it remains to estimate $|\hat{v}_h|_S^2$. We first observe that

$$|\hat{v}_h|_S^2 = \sum_{(T,i) \in \mathcal{P}_h^{\text{OK}}} \kappa_i \sum_{S \in \{T\} \cup \mathcal{N}_i^{-1}(T)} h_S^{-1} \|v_{(\partial S)^i} - v_{S^i}\|_{(\partial S)^i}^2.$$

Consider first the case $S = T$. The triangle inequality gives

$$\|v_{(\partial T)^i} - v_{T^i}\|_{(\partial T)^i} \leq \|v_{(\partial T)^i} - \Pi_{(\partial T)^i}^k(v_{T^i})\|_{(\partial T)^i} + \|(I - \Pi_{(\partial T)^i}^k)(v_{T^i})\|_{(\partial T)^i},$$

and owing to (IV.38b), we infer that

$$\|v_{(\partial T)^i} - v_{T^i}\|_{(\partial T)^i} \lesssim \|v_{(\partial T)^i} - \Pi_{(\partial T)^i}^k(v_{T^i})\|_{(\partial T)^i} + h_T^{\frac{1}{2}} \|\nabla v_{T^i}\|_{T^i}. \quad (\text{IV.47})$$

Let now $S \in \mathcal{N}_i^{-1}(T)$. The triangle inequality implies that

$$\begin{aligned} \|v_{(\partial S)^i} - v_{S^i}\|_{(\partial S)^i} &\leq \|v_{(\partial S)^i} - \Pi_{(\partial S)^i}^k(v_{S^i})\|_{(\partial S)^i} + \|(I - \Pi_{(\partial S)^i}^k)(v_{S^i} - v_{T^i}^+)\|_{(\partial S)^i} \\ &\quad + \|(I - \Pi_{(\partial S)^i}^k)(v_{T^i}^+)\|_{(\partial S)^i}. \end{aligned}$$

For the second term on the right-hand side, we simply notice that $\|(I - \Pi_{(\partial S)^i}^k)(v_{S^i} - v_{T^i}^+)\|_{(\partial S)^i} \leq \|v_{S^i} - v_{T^i}^+\|_{(\partial S)^i}$, whereas we invoke (IV.38b) to bound the third term. Altogether, this gives

$$\|v_{(\partial S)^i} - v_{S^i}\|_{(\partial S)^i} \lesssim \|v_{(\partial S)^i} - \Pi_{(\partial S)^i}^k(v_{S^i})\|_{(\partial S)^i} + \|v_{S^i} - v_{T^i}^+\|_{(\partial S)^i} + h_S^{\frac{1}{2}} \|\nabla v_{T^i}\|_{T^i}.$$

Squaring this inequality, multiplying by $\kappa_i h_S^{-1}$, summing over $S \in \mathcal{N}_i^{-1}(T)$, combining with (IV.47), and finally summing over $(T, i) \in \mathcal{P}_h^{\text{OK}}$, we infer that

$$|\hat{v}_h|_S^2 \lesssim s_h^\circ(\hat{v}_h, \hat{v}_h) + s_h^N(\hat{v}_h, \hat{v}_h) + \sum_{(T,i) \in \mathcal{P}_h} \kappa_i \|\nabla v_{T^i}\|_{T^i}^2.$$

Combining this bound with (IV.46a) gives

$$\sum_{(T,i) \in \mathcal{P}_h} \kappa_i \|\nabla v_{T^i}\|_{T^i}^2 + |\hat{v}_h|_S^2 \lesssim b_h(\hat{v}_h, \hat{v}_h) + s_h^\circ(\hat{v}_h, \hat{v}_h) + s_h^\Gamma(\hat{v}_h, \hat{v}_h) + s_h^N(\hat{v}_h, \hat{v}_h) = a_h(\hat{v}_h, \hat{v}_h),$$

whence the lower bound in (IV.45) readily follows. \square

IV.4.3 Interpolation operator

For all $T \in \mathcal{T}_h$, the local interpolation operator is defined as follows:

$$\hat{I}_T^k(v) := (\hat{I}_{T^1}^k(v), \hat{I}_{T^2}^k(v)) := (I_{T^1}^{k+1}(v_1), \Pi_{(\partial T)^1}^k(v_1), I_{T^2}^{k+1}(v_2), \Pi_{(\partial T)^2}^k(v_2)) \in \hat{\mathcal{U}}_T, \quad (\text{IV.48})$$

where $I_{T^i}^{k+1}(v_i)$ is defined in (IV.39) for all $(T, i) \in \mathcal{P}_h^{\text{OK}}$, whereas for all $(S, i) \in \mathcal{P}_h^{\text{KO}}$, we set

$$I_S^{k+1}(v_i) := I_{T^i}^{k+1}(v_i)^+|_{S^i}, \quad T := \mathcal{N}_i(S), \quad (\text{IV.49})$$

where we recall that the superscript $+$ is used to indicate the extension of a polynomial originally defined on T^i to $T^i \cup \bigcup_{S \in \mathcal{N}_i^{-1}(T)} S^i$.

The global interpolation operator is denoted by $\hat{I}_h^k : H^s(\Omega_1 \cup \Omega_2) \rightarrow \hat{\mathcal{U}}_h$ and is such that the local components of $\hat{I}_h^k(v)$ on a mesh cell $T \in \mathcal{T}_h$ are those given by $\hat{I}_T^k(v|_T)$. Notice that $\hat{I}_h^k(u) \in \hat{\mathcal{U}}_{h0}$ for the exact solution since $u|_{\partial\Omega} = 0$.

Lemma IV.4.4 (Approximation). *For all $v \in H^s(\Omega_1 \cup \Omega_2)$, $s > \frac{3}{2}$, and all $(T, i) \in \mathcal{P}_h^{\text{OK}}$, set*

$$\boldsymbol{\delta}_{T,i}(v) := \mathbf{G}_{T^i}^k(\hat{I}_T^k(v)^{\mathcal{N}}) + \delta_{i1}\mathbf{L}_{T^1}^k([\![v]\!]_{\Gamma}) - \nabla v_i|_{T^i}, \quad (\text{IV.50a})$$

$$\boldsymbol{\delta}_{T,S,i}(v) := \{\mathbf{G}_{T^i}^k(\hat{I}_T^k(v)^{\mathcal{N}}) + \delta_{i1}\mathbf{L}_{T^1}^k([\![v]\!]_{\Gamma})\}^+|_{S^i} - \nabla v_i|_{S^i}, \quad \forall S \in \mathcal{N}_i^{-1}(T), \quad (\text{IV.50b})$$

and recall the error measure $\epsilon_{T,i}(v)$ defined in (IV.40). Then, the following holds:

$$\|\boldsymbol{\delta}_{T,i}(v)\|_{T^i} + h_T^{\frac{1}{2}}\|\boldsymbol{\delta}_{T,i}(v)\|_{(\partial T)^i \cup T^{\Gamma}} \lesssim h_T^{-1}\{\epsilon_{T,i}(v_i) + \delta_{i1}\epsilon_{T,2}(v_2)\}, \quad (\text{IV.51a})$$

$$\sum_{S \in \mathcal{N}_i^{-1}(T)} \left\{ \|\boldsymbol{\delta}_{T,S,i}(v)\|_{S^i} + h_S^{\frac{1}{2}}\|\boldsymbol{\delta}_{T,S,i}(v)\|_{(\partial S)^i \cup S^{\Gamma}} \right\} \lesssim h_T^{-1}\{\epsilon_{T,i}(v_i) + \delta_{i1}\epsilon_{T,2}(v_2)\}. \quad (\text{IV.51b})$$

Proof. Let $v \in H^s(\Omega_1 \cup \Omega_2)$, $s > \frac{3}{2}$, and let $(T, i) \in \mathcal{P}_h^{\text{OK}}$. Set

$$\boldsymbol{\delta}'_{T,i}(v) := \mathbf{G}_{T^i}^k(\hat{I}_T^k(v)^{\mathcal{N}}) + \delta_{i1}\mathbf{L}_{T^1}^k([\![v]\!]_{\Gamma}) - \nabla I_{T^i}^{k+1}(v_i) \in P^{k+1}(T^i).$$

(1) Let $I_{\mathcal{T}_h}^{k+1}$ be composed of the two cell components of \hat{I}_h^k . We notice that

$$\begin{aligned} \|\boldsymbol{\delta}'_{T,i}(v)\|_{T^i}^2 &= (\mathbf{G}_{T^i}^k(\hat{I}_T^k(v)^{\mathcal{N}}) + \delta_{i1}\mathbf{L}_{T^1}^k([\![v]\!]_{\Gamma}) - \nabla I_{T^i}^{k+1}(v_i), \boldsymbol{\delta}'_{T,i}(v))_{T^i} \\ &= (\mathbf{G}_{T^i}^k(\hat{I}_T^k(v)^{\mathcal{N}}) + \delta_{i1}\mathbf{L}_{T^1}^k([\![I_{T_h}^{k+1}(v)]\!]_{\Gamma}) - \nabla I_{T^i}^{k+1}(v_i), \boldsymbol{\delta}'_{T,i}(v))_{T^i} \\ &\quad + \delta_{i1}(\mathbf{L}_{T^1}^k([\![v - I_{T_h}^{k+1}(v)]\!]_{\Gamma}), \boldsymbol{\delta}'_{T,i}(v))_{T^i}. \end{aligned}$$

Owing to (IV.27) and the definition of the operators \hat{I}_T^k and $\mathbf{L}_{T^1}^k$, we infer that

$$\begin{aligned} \|\boldsymbol{\delta}'_{T,i}(v)\|_{T^i}^2 &= (\Pi_{(\partial T)^i}^k(v_i) - I_{T^i}^{k+1}(v_i), \boldsymbol{\delta}'_{T,i}(v) \cdot \mathbf{n}_T)_{(\partial T)^i} + \delta_{i1}([\![v - I_T^{k+1}(v)]\!]_{\Gamma}, \boldsymbol{\delta}'_{T,1}(v) \cdot \mathbf{n}_{\Gamma})_{T^{\Gamma}} \\ &\quad + \sum_{S \in \mathcal{N}_i^{-1}(T)} \left\{ (\Pi_{(\partial S)^i}^k(v_i) - I_{T^i}^{k+1}(v_i)^+, \boldsymbol{\delta}'_{T,i}(v)^+ \cdot \mathbf{n}_S)_{(\partial S)^i} \right. \\ &\quad \left. + \delta_{i1}([\![v - I_T^{k+1}(v)^+]\!]_{\Gamma}, \boldsymbol{\delta}'_{T,1}(v)^+ \cdot \mathbf{n}_{\Gamma})_{S^{\Gamma}} \right\}. \end{aligned}$$

Invoking the definition of the L^2 -orthogonal projections $\Pi_{(\partial T)^i}^k$ and $\Pi_{(\partial S)^i}^k$ gives

$$\begin{aligned} \|\boldsymbol{\delta}'_{T,i}(v)\|_{T^i}^2 &= (v_i - I_T^{k+1}(v_i), \boldsymbol{\delta}'_{T,i}(v) \cdot \mathbf{n}_T)_{(\partial T)^i} + \delta_{i1}([\![v - I_T^{k+1}(v)]\!]_\Gamma, \boldsymbol{\delta}'_{T,1}(v) \cdot \mathbf{n}_\Gamma)_{T^\Gamma} \\ &+ \sum_{S \in \mathcal{N}_i^{-1}(T)} \left\{ (v_i - I_T^{k+1}(v_i))^+, \boldsymbol{\delta}'_{T,i}(v)^+ \cdot \mathbf{n}_S \right\}_{(\partial S)^i} + \delta_{i1}([\![v - I_T^{k+1}(v)]\!]_\Gamma^+, \boldsymbol{\delta}'_{T,1}(v)^+ \cdot \mathbf{n}_\Gamma)_{S^\Gamma}. \end{aligned}$$

Invoking the Cauchy–Schwarz inequality and the discrete trace inequality (IV.38a), we infer that

$$\begin{aligned} h_T^{\frac{1}{2}} \|\boldsymbol{\delta}'_{T,i}(v)\|_{T^i} &\lesssim \|v_i - I_T^{k+1}(v_i)\|_{(\partial T)^i} + \delta_{i1} \|[\![v - I_T^{k+1}(v)]\!]_\Gamma\|_{T^\Gamma} \\ &+ \sum_{S \in \mathcal{N}_i^{-1}(T)} \left\{ \|v_i - I_T^{k+1}(v_i)^+\|_{(\partial S)^i} + \delta_{i1} \|[\![v - I_T^{k+1}(v)]\!]_\Gamma^+\|_{S^\Gamma} \right\}. \end{aligned}$$

Recalling the definition (IV.40) of $\epsilon_{T,i}(v)$ gives

$$\|\boldsymbol{\delta}'_{T,i}(v)\|_{T^i} \lesssim h_T^{-1} \{ \epsilon_{T,i}(v_i) + \delta_{i1} \epsilon_{T,2}(v_2) \}, \quad (\text{IV.52})$$

and owing to the discrete trace inequality (IV.38a), we obtain

$$\|\boldsymbol{\delta}'_{T,i}(v)\|_{T^i} + h_T^{\frac{1}{2}} \|\boldsymbol{\delta}'_{T,i}(v)\|_{(\partial T)^i \cup T^\Gamma} \lesssim \|\boldsymbol{\delta}'_{T,i}(v)\|_{T^i} \lesssim h_T^{-1} \{ \epsilon_{T,i}(v_i) + \delta_{i1} \epsilon_{T,2}(v_2) \}.$$

Finally, since $\boldsymbol{\delta}_{T,i}(v) = \boldsymbol{\delta}'_{T,i}(v) - \nabla(v_i - I_T^{k+1}(v_i))$ invoking the triangle inequality proves (IV.51a).

(2) Assuming that $\mathcal{N}_i^{-1}(T)$ is nonempty, for all $S \in \mathcal{N}_i^{-1}(T)$, we have

$$\boldsymbol{\delta}_{T,S,i}(v) = \boldsymbol{\delta}'_{T,i}(v)^+|_{S^i} + \nabla(I_T^{k+1}(v_i)^+|_{S^i} - v_i|_{S^i}).$$

The discrete trace inequality (IV.38a) and (IV.52) imply that

$$\|\boldsymbol{\delta}'_{T,i}(v)^+\|_{S^i} + h_S^{\frac{1}{2}} \|\boldsymbol{\delta}'_{T,i}(v)^+\|_{(\partial S)^i \cup S^\Gamma} \lesssim \|\boldsymbol{\delta}'_{T,i}(v)\|_{T^i} \lesssim h_T^{-1} \{ \epsilon_{T,i}(v_i) + \delta_{i1} \epsilon_{T,2}(v_2) \}.$$

Invoking the triangle inequality and recalling (IV.40) proves (IV.51b). \square

IV.4.4 Consistency

Lemma IV.4.5 (Consistency). *Let u be the weak solution to (IV.2). Assume that $u \in H^s(\Omega_1 \cup \Omega_2)$, $s > \frac{3}{2}$. Set $\Phi_h(\hat{w}_h) := a_h(\hat{I}_h^k(u), \hat{w}_h) - \ell_h(\hat{w}_h)$ for all $\hat{w}_h \in \hat{\mathcal{U}}_{h0}$. The following holds:*

$$|\Phi_h(\hat{w}_h)| \lesssim \left\{ \sum_{(T,i) \in \mathcal{P}_h^{\text{OK}}} \kappa_i h_T^{-2} \epsilon_{T,i}(u_i)^2 \right\}^{\frac{1}{2}} \|\hat{w}_h\|_{h0}. \quad (\text{IV.53})$$

Proof. Owing to (IV.37) from Lemma IV.3.1, we have $\Phi_h(\hat{w}_h) = A_1 + A_2 + A_3$ with

$$\begin{aligned} A_1 &= \sum_{(T,i) \in \mathcal{P}_h} \kappa_i (\boldsymbol{\delta}_{T,i}(u), \nabla w_{T^i})_{T^i}, \\ A_2 &= \sum_{(T,i) \in \mathcal{P}_h^{\text{OK}}} \kappa_i \left\{ (\boldsymbol{\delta}_{T,i}(u) \cdot \mathbf{n}_T, w_{(\partial T)^i} - w_{T^i})_{(\partial T)^i} - \delta_{i1} (\boldsymbol{\delta}_{T,1}(u) \cdot \mathbf{n}_\Gamma, [w_T]_\Gamma)_{T^\Gamma} \right. \\ &\quad \left. + \sum_{S \in \mathcal{N}_i^{-1}(T)} \{(\boldsymbol{\delta}_{T,S,i}(u) \cdot \mathbf{n}_S, w_{(\partial S)^i} - w_{S^i})_{(\partial S)^i} - \delta_{i1} (\boldsymbol{\delta}_{T,S,1}(u) \cdot \mathbf{n}_\Gamma, [w_S]_\Gamma)_{S^\Gamma}\} \right\}, \\ A_3 &= s_h^\circ(\hat{I}_h^k(u), \hat{w}_h) + \sum_{T \in \mathcal{T}_h^{\text{cut}}} \kappa_1 h_T^{-1} ([I_T^{k+1}(u) - u]_\Gamma, [w_T]_\Gamma)_{T^\Gamma} + s_h^{\mathcal{N}}(\hat{I}_h^k(u), \hat{w}_h), \end{aligned}$$

where $\boldsymbol{\delta}_{T,i}(u)$ and $\boldsymbol{\delta}_{T,S,i}(u)$ are defined in (IV.50) for all $(T, i) \in \mathcal{P}_h^{\text{OK}}$, whereas we set $\boldsymbol{\delta}_{T,i}(u) := \nabla(I_{T^i}^{k+1}(u_i) - u_i)$ for all $(T, i) \in \mathcal{P}_h^{\text{KO}}$, and where $[I_T^{k+1}(u) - u]_\Gamma$ is defined in Lemma IV.4.2. Owing to (IV.49), we infer that the term A_1 can be rewritten as follows:

$$A_1 = \sum_{(T,i) \in \mathcal{P}_h^{\text{OK}}} \kappa_i \left\{ (\boldsymbol{\delta}_{T,i}(u), \nabla w_{T^i})_{T^i} + \sum_{S \in \mathcal{N}_i^{-1}(T)} (\boldsymbol{\delta}_{T,S,i}(u), \nabla w_{S^i})_{S^i} \right\}.$$

Invoking the Cauchy–Schwarz inequality together with the approximation results from Lemma IV.4.4 gives

$$|A_1| \lesssim \left\{ \sum_{(T,i) \in \mathcal{P}_h^{\text{OK}}} \kappa_i h_T^{-2} \{ \epsilon_{T,i}(u_i) + \delta_{i1} \epsilon_{T,2}(u_2) \}^2 \right\}^{\frac{1}{2}} \left\{ \sum_{(T,i) \in \mathcal{P}_h} \kappa_i \|\nabla w_{T^i}\|_{T^i}^2 \right\}^{\frac{1}{2}}.$$

Since $\kappa_1 \leq \kappa_2$ and recalling the definition (IV.42) of the stability norm $\|\cdot\|_{h0}$, we infer that

$$|A_1| \lesssim \left\{ \sum_{(T,i) \in \mathcal{P}_h^{\text{OK}}} \kappa_i h_T^{-2} \epsilon_{T,i}(u_i)^2 \right\}^{\frac{1}{2}} \|\hat{w}_h\|_{h0}.$$

The same arguments prove that

$$|A_2| \lesssim \left\{ \sum_{(T,i) \in \mathcal{P}_h^{\text{OK}}} \kappa_i h_T^{-2} \epsilon_{T,i}(u_i)^2 \right\}^{\frac{1}{2}} \|\hat{w}_h\|_{h0}.$$

Finally, let us write $A_3 = A_{31} + A_{32} + A_{33}$ with obvious notation. First, observing that $s_h^\circ(\hat{w}_h, \hat{w}_h) \leq |\hat{w}_h|_s^2$, we obtain

$$\begin{aligned} |A_{31}| &\leq \left\{ \sum_{(T,i) \in \mathcal{P}_h} \kappa_i h_T^{-1} \|\Pi_{(\partial T)^i}^k(u_i - I_{T^i}^{k+1}(u_i))\|_{(\partial T)^i}^2 \right\}^{\frac{1}{2}} |\hat{w}_h|_s \\ &\leq \left\{ \sum_{(T,i) \in \mathcal{P}_h} \kappa_i h_T^{-1} \|u_i - I_{T^i}^{k+1}(u_i)\|_{(\partial T)^i}^2 \right\}^{\frac{1}{2}} |\hat{w}_h|_s, \end{aligned}$$

where the second bound follows from the L^2 -stability of $\Pi_{(\partial T)^i}^k$. Owing to (IV.49), the summation on the right-hand side can be rewritten as

$$|A_{31}| \leq \left\{ \sum_{(T,i) \in \mathcal{P}_h^{\text{OK}}} \sum_{S \in \{T\} \cup \mathcal{N}_i^{-1}(T)} \kappa_i h_S^{-1} \|u_i - I_{T^i}^{k+1}(u_i)^+\|_{(\partial S)^i}^2 \right\}^{\frac{1}{2}} |\hat{w}_h|_s.$$

Therefore, we conclude that

$$|A_{31}| \leq \left\{ \sum_{(T,i) \in \mathcal{P}_h^{\text{OK}}} \kappa_i h_T^{-2} \epsilon_{T,i}(u_i)^2 \right\}^{\frac{1}{2}} |\hat{w}_h|_s.$$

Concerning A_{32} , the Cauchy–Schwarz inequality and the same arguments as above give

$$|A_{32}| \leq \left\{ \sum_{(T,i) \in \mathcal{P}_h^{\text{OK}}} \kappa_i h_T^{-2} \epsilon_{T,i}(u_i)^2 \right\}^{\frac{1}{2}} s_h^{\Gamma}(\hat{w}_h, \hat{w}_h)^{\frac{1}{2}}.$$

Finally, $s_h^{\mathcal{N}}(\hat{I}_h^k(u), \hat{w}_h) = 0$ owing to (IV.49). Putting everything together proves the claim. \square

IV.4.5 Error estimate

We are now ready to establish the main result of our error analysis.

Theorem IV.4.6 (Error estimate). *Let u be the weak solution to (IV.2). Assume that $u \in H^s(\Omega_1 \cup \Omega_2)$ with $s \in (\frac{3}{2}, k+2]$. The following holds:*

$$\begin{aligned} \left\{ \sum_{(T,i) \in \mathcal{P}_h} \kappa_i \|\nabla(u_i - u_{T^i})\|_{T^i}^2 \right\}^{\frac{1}{2}} &\lesssim \left\{ \sum_{(T,i) \in \mathcal{P}_h^{\text{OK}}} \kappa_i h_T^{2(s-1)} |E_i^s(u_i)|_{H^s(\Delta_2(T))}^2 \right\}^{\frac{1}{2}} \\ &\lesssim h^{s-1} \sum_{i \in \{1,2\}} \kappa_i^{\frac{1}{2}} |u_i|_{H^s(\Omega_i)}. \end{aligned} \quad (\text{IV.54})$$

Proof. Define the discrete error as $\hat{e}_h := \hat{I}_h^k(u) - \hat{u}_h \in \hat{\mathcal{U}}_{h0}$. Since $a_h(\hat{e}_h, \hat{e}_h) = \Phi_h(\hat{e}_h)$, invoking the stability result from Lemma IV.4.3 and the bound on the consistency error from Lemma IV.4.5 gives

$$\|\hat{e}_h\|_{h0}^2 \lesssim \sum_{(T,i) \in \mathcal{P}_h^{\text{OK}}} \kappa_i h_T^{-2} \epsilon_{T,i}(u_i)^2.$$

Invoking the triangle inequality and the approximation result from Lemma IV.4.2 establishes the first bound in (IV.54). The second bound follows from the shape-regularity of the mesh, and the H^s -stability of the extension operators E_i^s . \square

IV.5 Numerical results

In this section, we present numerical results to illustrate the convergence rates established in Theorem IV.4.6. We also compare the present method to the one from [29] stabilized by a cell-agglomeration procedure, and we briefly investigate some aspects related to the implementation (quadrature, local polynomial bases, pairing criterion).

In all cases, we consider the unit square domain $\Omega := (0, 1)^2$ discretized with uniform Cartesian meshes of size $h := \sqrt{2} \times 0.1 \times 2^{-\ell}$ with $\ell \in \{0, \dots, 4\}$. The polynomial degree is taken such that $k \in \{0, \dots, 3\}$. The interface is defined using a level-set function Φ ,

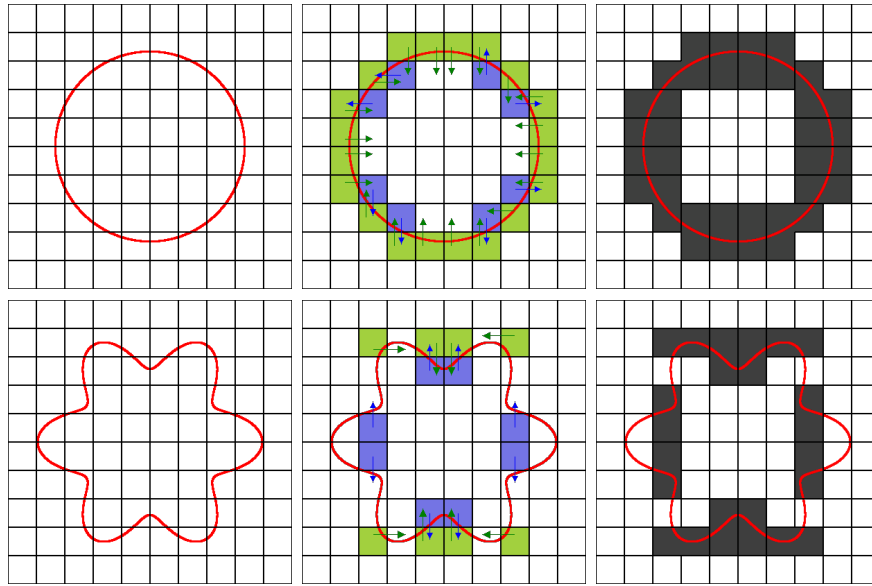


Fig. IV.5: Circular (top row) and flower-like (bottom row) interfaces. Left column: Coarsest mesh. Central column: Outcome of pairing procedure for polynomial extension stabilization, cells in $\mathcal{T}_h^{\text{KO},1}$ are colored in green, and cells in $\mathcal{T}_h^{\text{KO},2}$ are colored in blue, arrows indicate the pairing cell. Right column: Outcome of pairing procedure for cell-agglomeration stabilization, agglomerated cells are colored in dark.

with $\Gamma := \{(x, y) \in \Omega \mid \Phi(x, y) = 0\}$ and $\Omega_i = \{(x, y) \in \Omega \mid (-1)^i \Phi(x, y) > 0\}$ for all $i \in \{1, 2\}$. We always take $\kappa_1 := 1$, and modify the diffusivity contrast by taking $\kappa_2 = 10^m$, $m \in \{1, \dots, 4\}$, where $m = 1$ correspond to no contrast and $m = 4$ to a highly contrasted setting. We consider two shapes for the interface: a circular shape and a flower-like shape, defined by the following level-set functions:

$$\Phi_C(x, y) := (x - a)^2 + (y - b)^2 - R^2, \quad (\text{IV.55a})$$

$$\Phi_F(x, y) := (x - a)^2 + (y - b)^2 - R^2 + c \cos(n\theta), \quad (\text{IV.55b})$$

with $\theta := \arctan\left(\frac{y-b}{x-a}\right)$ if $x \geq a$, and $\theta := \pi + \arctan\left(\frac{y-b}{x-a}\right)$ if $x < a$, $a := b := 0.5$, $R = \frac{1}{3}$, $c := 0.03$, and $n = 8$. Figure IV.5 illustrates on the coarsest mesh ($\ell = 0$) the two interfaces (left column), and the outcome of the pairing procedure for polynomial extension stabilization (central column) and for cell-agglomeration stabilization (right column).

IV.5.1 Implementation aspects

Quadratures along the interface and in the cut sub-cells are realized by dividing the interface into 2^r segments, $r \in \mathbb{N}$, and creating a sub-triangulation of the two cut sub-cells. The construction of the sub-triangulation is performed as discussed in [29]; see, in particular, Figure IV.5 therein for an illustration. Unless explicitly stated otherwise, we set $r := 8$.

Another important aspect is the choice of the polynomial bases in the sub-cells and the sub-faces. Both bases are realized by considering centered and scaled monomials. In

particular, the barycenter of each sub-cell is used for the centering of the corresponding basis. The barycenter is computed using the above sub-triangulation. Unless explicitly stated otherwise, the scaling of the monomials is isotropic and uses half of the diameter of the original cell.

IV.5.2 Convergence rates

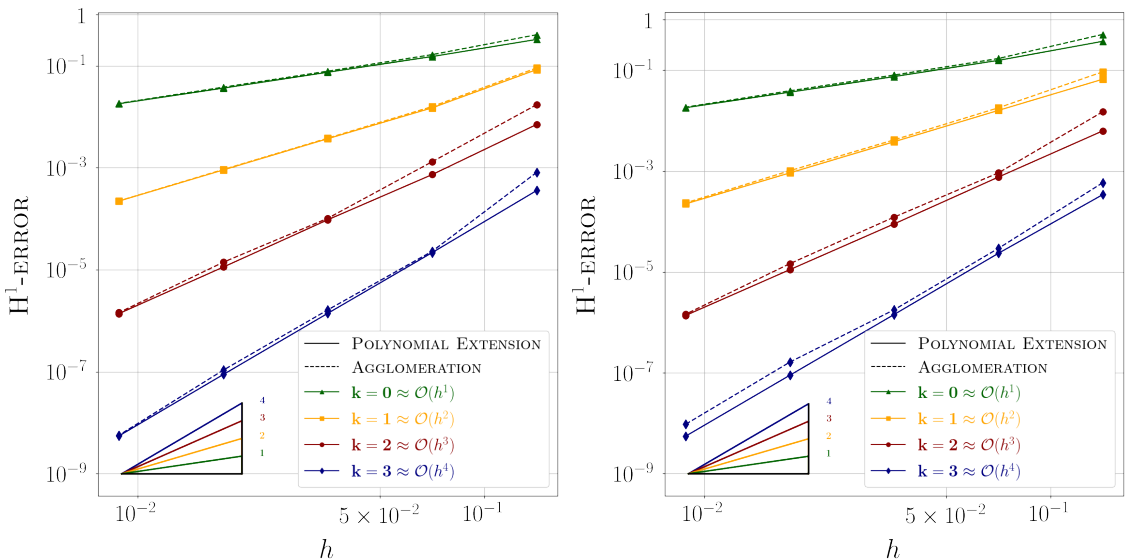


Fig. IV.6: Errors as a function of the mesh-size for the exact solution (IV.56). Comparison between stabilization by polynomial extension (solid lines) and by cell agglomeration (dashed lines). Left: Circular interface. Right: Flower-like interface.

We consider first a test case with no contrast and no jumps ($g_D = g_N = 0$). The exact solution is taken to be (in Cartesian coordinates (x, y))

$$u(x, y) := \sin(\pi x) \sin(\pi y). \quad (\text{IV.56})$$

Errors are reported in Figure IV.6 for the circular interface (left panel) and the flower-like interface (right panel). Here and below, errors are evaluated using the energy norm considered in Theorem IV.4.6. In both panels, we compare the results obtained using stabilization by polynomial extension (solid lines) and by cell agglomeration (dashed lines). Both approaches yield similar results, with slightly better errors when using polynomial extension, especially on coarse meshes.

We next study the sensitivity of the errors with respect to the value of the pairing parameter ϑ used for flagging ill-cut cells. We consider again the exact solution (IV.56). Errors are reported in Figure IV.7 for $k = 3$ and $\vartheta \in \{0, 0.1, 0.2, 0.3\}$ ($\vartheta = 0$ corresponds to no pairing, irrespective of the ill cut). The left (resp., right) panel corresponds to polynomial extension (resp., cell agglomeration). Solid lines correspond to polynomial bases centered at the barycenter of each sub-cell (the default choice in our implementation), whereas dashed lines correspond to centering at the barycenter of the original cell for both sides of the cut. We observe that this second choice yields poor results owing to poor

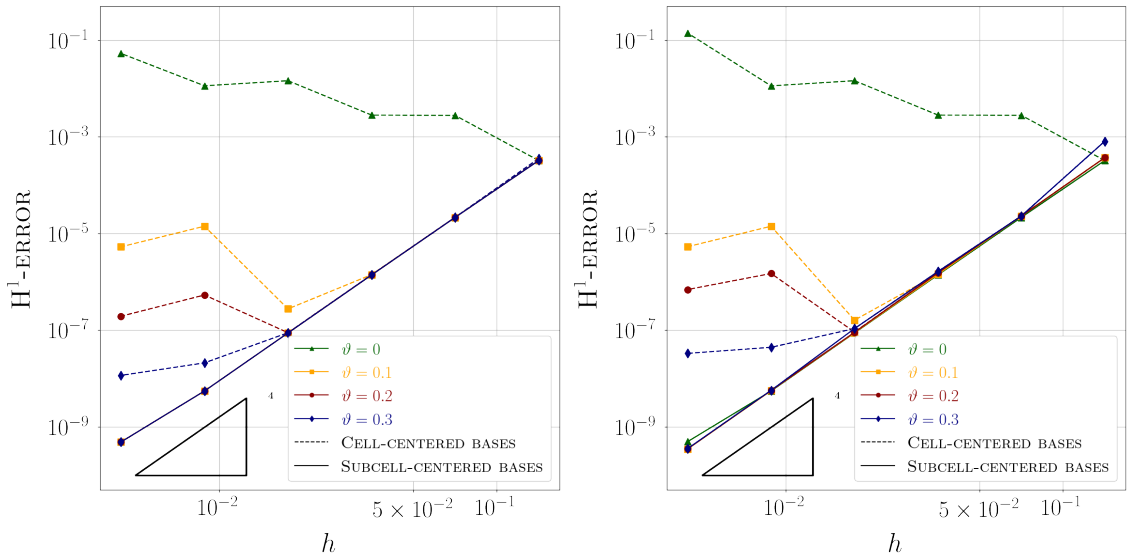


Fig. IV.7: Errors as a function of the mesh size for the exact solution (IV.56) for $k = 3$ and various values of the pairing parameter ϑ used for flagging ill-cut cells. Left: polynomial extension. Right: cell agglomeration.

conditioning of the local matrices, whereas the first choice is robust to the presence of ill cuts. Somewhat surprisingly, the robustness is such that it allows to flag cells with a very loose criterion ($\vartheta = 0.1$) or even to flag no cells at all ($\vartheta = 0$), and still obtain close-to-optimal errors.

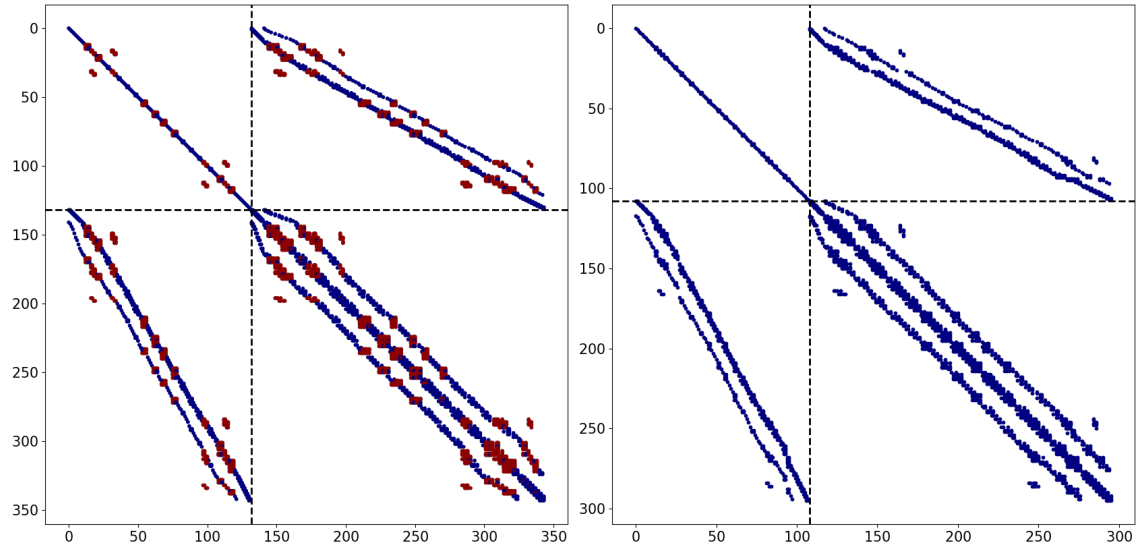


Fig. IV.8: Sparsity profiles of the stiffness matrices obtained using polynomial extension (left) and cell agglomeration (right). In the left panel, the red dots indicate the coupling blocks resulting from polynomial extension. In both panels, the global block-decomposition into cell and face unknowns is indicated by black dashed lines. Coarsest mesh ($\ell = 0$).

A further comparison between polynomial extension and cell agglomeration is provided in Figure IV.8 which compares the sparsity profiles of the stiffness matrices obtained with both procedures. We observe that both approaches lead to a similar sparsity profile, and that the stiffness matrix corresponding to cell agglomeration is slightly smaller (as expected). The sparsity pattern of the matrix corresponding to cell agglomeration directly results from the data structure of the agglomerated mesh, whereas the sparsity pattern of the matrix corresponding to polynomial extension is derived at the assembly stage by means of the pairing operator.

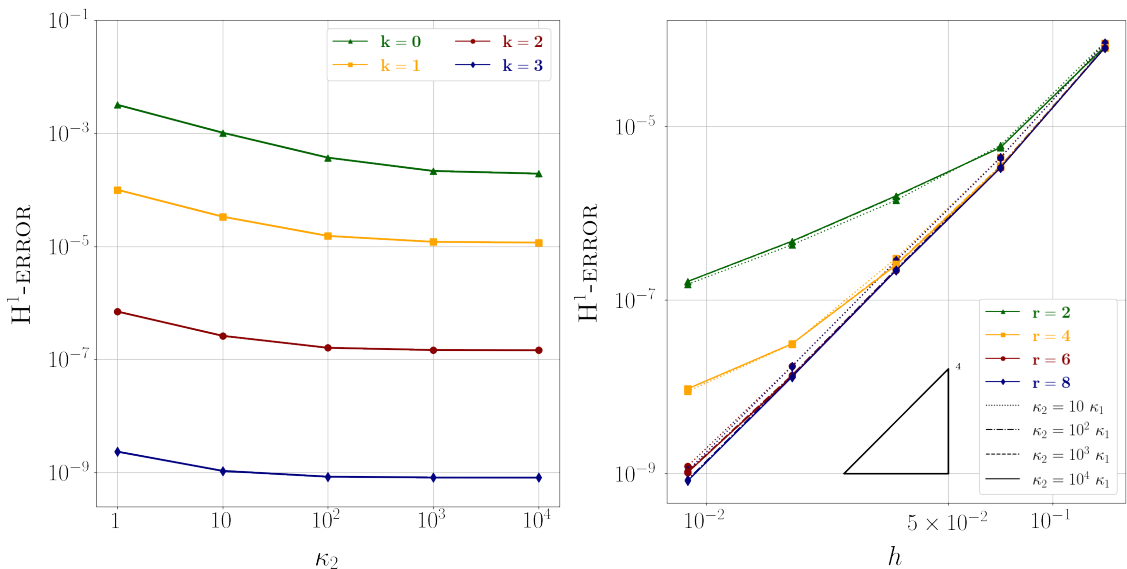


Fig. IV.9: Left: Errors for the exact solution (IV.57) as a function of the diffusivity contrast on the finest mesh ($\ell = 4$) and for various polynomial degrees ($k \in \{0, \dots, 3\}$). Right: Errors as a function of the mesh size for various values of the sub-triangulation parameter, $k = 3$, $r \in \{2, 4, 6, 8\}$, and various diffusivity contrasts, $m \in \{1, \dots, 4\}$.

We now turn our attention to a test case with diffusivity contrast and jumps across the interface. We first consider the exact solution for the circular interface such that (in radial coordinates (ρ, θ))

$$u_1(\rho) := \frac{\rho^6}{\kappa_1}, \quad u_2(\rho) := \frac{\rho^6}{\kappa_2} + R^6 \left(\frac{1}{\kappa_1} - \frac{1}{\kappa_2} \right). \quad (\text{IV.57})$$

Notice that this solution does not exhibit jumps across the interface ($g_D = g_N = 0$). The errors in the highly contrasted case where $\kappa_2 = 10^4 \kappa_1$ exhibit the same optimal convergence rates as those reported in Figure IV.6 (not shown for brevity). To highlight the robustness of the approach with respect to the diffusivity contrast, we report in the left panel of Figure IV.9 the errors as a function of $\kappa_2 = 10^m \kappa_1$, $m \in \{0, \dots, 4\}$, obtained on the finest mesh ($\ell = 4$) and for various polynomial degrees ($k \in \{0, \dots, 3\}$). The right panel of Figure IV.9 underlines the importance of ensuring sufficient geometric resolution when performing quadratures in the cut sub-cells. Therein, we report the error as a function of the mesh size for the sub-triangulation parameter $r \in \{2, 4, 6, 8\}$ and various

diffusivity contrasts. We observe that in all cases, taking $r \geq 6$ is required to avoid that the geometric errors pollute the optimal decay of the discretization errors.

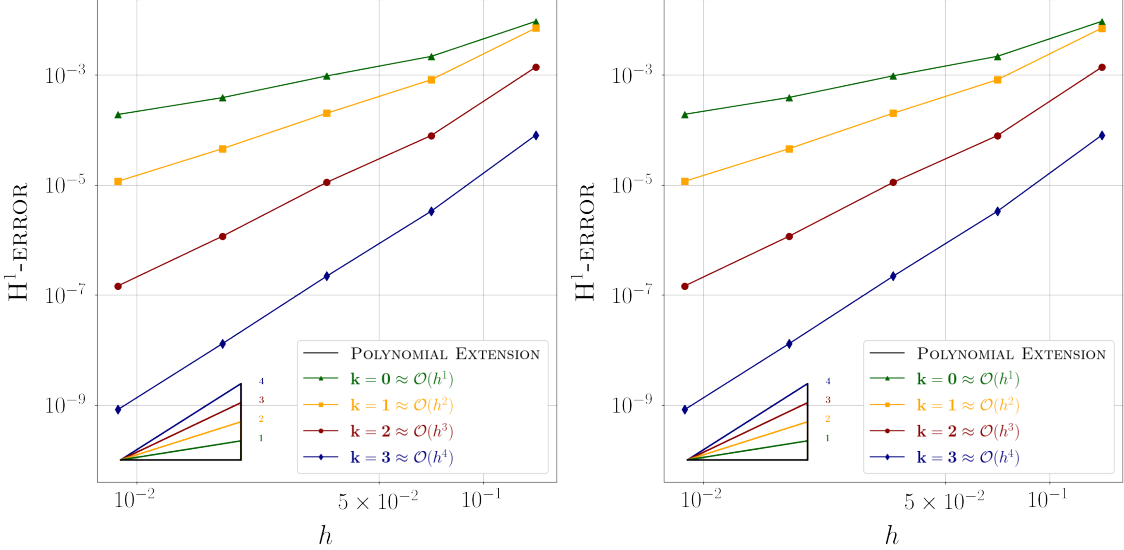


Fig. IV.10: Errors as a function of the mesh size for the exact solution (IV.58a) (left) and the exact solution (IV.58b) (right) for various polynomial degrees $k \in \{0, \dots, 3\}$; diffusivity contrast set to $\kappa_2 = 10^4 \kappa_1$.

We now include jumps across the interface while considering the highly contrasted setting where $\kappa_2 = 10^4 \kappa_1$. For this purpose, we modify the exact solution in (IV.57) and set

$$u_1(\rho) := \frac{\rho^6}{\kappa_1}, \quad u_2(\rho) := \frac{\rho^8 - R^8}{\kappa_2} + \frac{R^6}{\kappa_1}, \quad (\text{IV.58a})$$

$$u_1(\rho) := \frac{\rho^6}{\kappa_1}, \quad u_2(\rho) := \frac{\rho^6}{\kappa_2}. \quad (\text{IV.58b})$$

Notice that, for the exact solution (IV.58a), we have $g_N = 2R^5(3 - 4R^2)$ and $g_D = 0$, whereas, for the exact solution (IV.58b), we have $g_N = 0$ and $g_D = R^6(\frac{1}{\kappa_1} - \frac{1}{\kappa_2})$. Errors as a function of the mesh size are reported in Figure IV.10 for polynomial degrees $k \in \{0, \dots, 3\}$. Optimal convergence rates are observed in all cases. Actually, the errors for both exact solutions are very similar.

A more challenging setting is obtained when considering for the exact solution

$$u_1(x, y) := \cos(y)e^x, \quad u_2(x, y) := \sin(\pi x)\sin(\pi y), \quad (\text{IV.59})$$

leading to variable jump data g_D and g_N . Here, we do not consider a diffusivity contrast ($\kappa_1 = \kappa_2 = 1$). Errors as a function of the mesh size are reported in the left panel of Figure IV.11 for various polynomial degrees $k \in \{0, \dots, 3\}$ and sub-triangulation parameter set to $r = 10$. Optimal convergence rates are observed in all cases. To motivate the choice for r , we report in the right panel of Figure IV.11 the errors as a function of the mesh size for $k = 3$ and $r \in \{2, 4, 6, 8, 10\}$. We observe that the geometric error does not pollute the

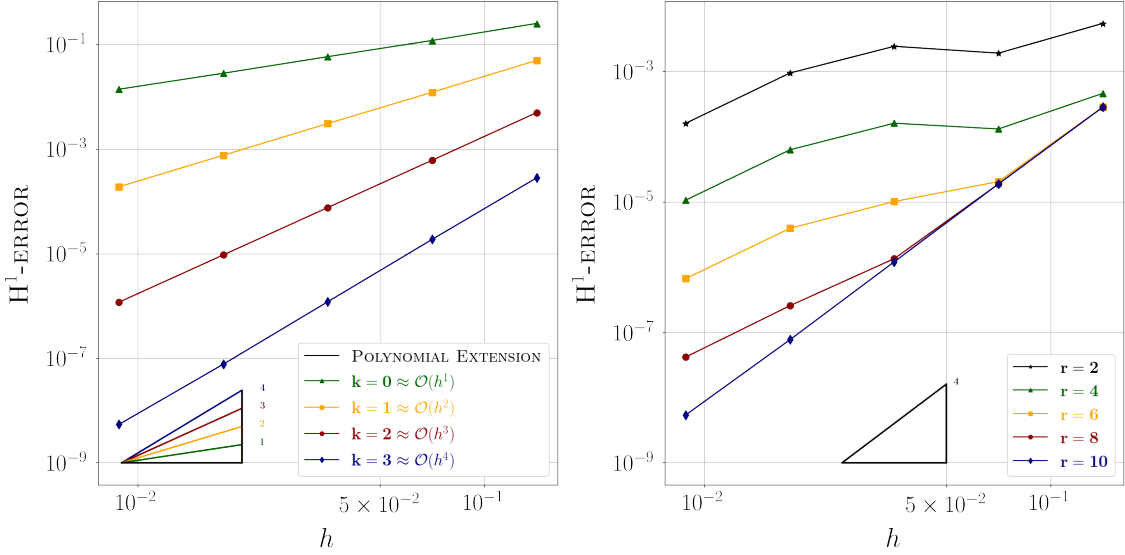


Fig. IV.11: Left: Errors as a function of the mesh size for the exact solution (IV.59) for various polynomial degrees $k \in \{0, \dots, 3\}$ (with sub-triangulation parameter set to $r = 10$). Right: Errors as a function of the mesh size for $k = 3$ and $r \in \{2, 4, 6, 8, 10\}$. No diffusivity contrast.

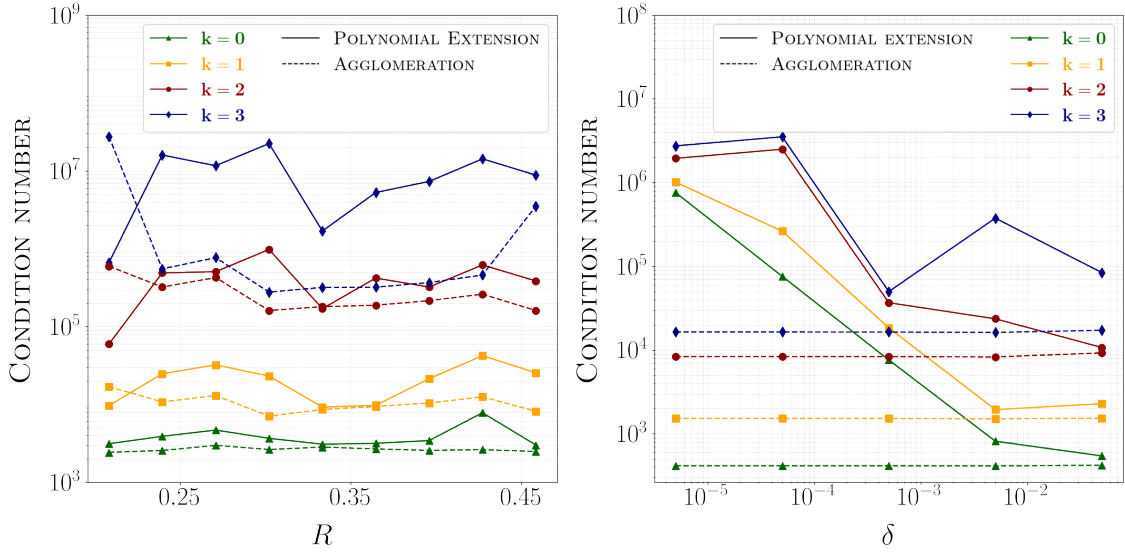


Fig. IV.12: Euclidean condition number of the stiffness matrix on the coarsest mesh ($\ell = 0$) as a function of the radius of the circular interface (left) and as a function of the position parameter δ for the square interface, using polynomial extension (solid lines) and cell agglomeration (dashed lines).

discretization error only for $r = 10$ (notice in passing the very low values attained by the error).

Finally, we perform a brief study of the conditioning of the stiffness matrix. In the left panel of Figure IV.12, we consider a circular interface with radius $R = \frac{1}{3} + \frac{i}{32}$, $i \in$

$\{-4, \dots, 4\}$, and we report the Euclidean condition number as a function of the radius, using either polynomial extension (solid lines) or cell agglomeration (dashed lines). We consider the coarsest mesh ($\ell = 0$) and polynomial degrees $k \in \{0, \dots, 3\}$. We observe that, for each polynomial degree, the conditioning remains fairly insensitive to the stabilization method of the ill-cut cells. To exacerbate the effect of ill-cut cells, we now consider a square interface with level-set function $\Phi_S(x, y) := \max(x - a, y - b) - (0.25 + \delta)$ and position parameter $\delta = 0.5 \times 10^{-p}$, $p \in \{1, \dots, 5\}$. Since cut cells can become very anisotropic, we use here an anisotropic scaling of the polynomial bases in each sub-cell, whereby the variable x (resp., y) is scaled by $\frac{1}{2}h_x$ (resp., $\frac{1}{2}h_y$), where (h_x, h_y) are the lengths of the sides of the bounding box of the sub-cell. The right panel of Figure IV.12 reports the Euclidean condition number as a function of the position parameter of the square interface. We observe that the use of polynomial extension leads to some sensitivity of the conditioning for severe ill cuts, with a linear growth in δ^{-1} . Similar observations are reported in [27] in the context of isogeometric methods. Somewhat surprisingly, the cell agglomeration approach appears to deliver robust condition numbers. We emphasize that the errors still behave optimally when using polynomial extension (figure omitted for brevity), in agreement with the above convergence analysis.

IV.6 Proofs

This section collects the proofs of the two results stated in Section IV.4.1.

IV.6.1 Proof of Lemma IV.4.1

Proof. (1) Proof of (IV.38a). Let $(T, i) \in \mathcal{P}_h^{\text{OK}}$ and $\phi \in P^\ell(T^i)$. Invoking the discrete trace inequality from [35, Lemma 3.4] shows that

$$\sum_{S \in \{T\} \cup \mathcal{N}_i^{-1}(T)} \left\{ \|\phi^+\|_S + h_S^{\frac{1}{2}} \|\phi^+\|_{(\partial S)^i \cup S^F} \right\} \lesssim \sum_{S \in \{T\} \cup \mathcal{N}_i^{-1}(T)} \|\phi^+\|_S \lesssim \|\phi^+\|_{\Delta(T)},$$

where the last bound follows from the construction of the pairing operator. We next observe that there is a ball $\mathcal{B}(\Delta(T))$ of diameter γh_T such that $\Delta(T) \subset \mathcal{B}(\Delta(T))$, where γ only depends on the mesh shape-regularity parameter. We also recall that, since $(T, i) \in \mathcal{P}_h^{\text{OK}}$, there is a ball $\mathcal{B}(T, i)$ of diameter ϑh_T , so that $\mathcal{B}(T, i) \subset T^i$. We then infer that

$$\|\phi^+\|_{\Delta(T)} \leq \|\phi^+\|_{\mathcal{B}(\Delta(T))} \lesssim \|\phi\|_{\mathcal{B}(T, i)} \leq \|\phi\|_{T^i},$$

where the inverse inequality invoked in the second inequality follows by the arguments given in the proof of [29, Lemma 3.4]. This completes the proof of (IV.38a).

(2) Proof of (IV.38b). Let $(T, i) \in \mathcal{P}_h^{\text{OK}}$ and $\phi \in P^\ell(T^i)$. Let $\langle \phi \rangle_{\mathcal{B}(T, i)}$ denote the mean-value of ϕ in $\mathcal{B}(T, i)$. Since $(I - \Pi_{(\partial S)^i}^k)(\phi^+) = (I - \Pi_{(\partial S)^i}^k)((\phi - \langle \phi \rangle_{\mathcal{B}(T, i)})^+)$, invoking the L^2 -stability of $\Pi_{(\partial S)^i}^k$ followed by (IV.38a) gives

$$\begin{aligned} \sum_{S \in \{T\} \cup \mathcal{N}_i^{-1}(T)} h_S^{-\frac{1}{2}} \|(I - \Pi_{(\partial S)^i}^k)(\phi^+)\|_{(\partial S)^i} &\leq \sum_{S \in \{T\} \cup \mathcal{N}_i^{-1}(T)} h_S^{-\frac{1}{2}} \|(\phi - \langle \phi \rangle_{\mathcal{B}(T, i)})^+\|_{(\partial S)^i} \\ &\lesssim h_T^{-1} \|\phi - \langle \phi \rangle_{\mathcal{B}(T, i)}\|_{T^i}, \end{aligned}$$

where we also used the mesh shape-regularity which implies that $h_T \lesssim h_S \lesssim h_T$ for all $S \in \Delta(T)$. The bound (IV.38b) now follows from the discrete Poincaré inequality established in [29, Lemma 3.4]. \square

IV.6.2 Proof of Lemma IV.4.2

Proof. Let $v \in H^s(\Omega_1 \cup \Omega_2)$ with $s \in (\frac{3}{2}, k+2]$ and let $(T, i) \in \mathcal{P}_h^{\text{OK}}$. Set $\tilde{v}_i := E_i^s(v_i)$.

(1) Recall that the ball $\mathcal{B}(T, i)$ of diameter ϑh_T is a subset of T^i since $(T, i) \in \mathcal{P}_h^{\text{OK}}$. Let $\langle v_i \rangle_{\mathcal{B}(T, i)}$ denote the mean-value of v_i in $\mathcal{B}(T, i)$. In this step, we prove that, for all $S \in \{T\} \cup \mathcal{N}_i^{-1}(T)$,

$$\|\tilde{v}_i - \langle v_i \rangle_{\mathcal{B}(T, i)}\|_S \lesssim h_T \|\nabla \tilde{v}_i\|_{\Delta(T)}. \quad (\text{IV.60})$$

We have $\|\tilde{v}_i - \langle v_i \rangle_{\mathcal{B}(T, i)}\|_S \leq \|\tilde{v}_i - \langle v_i \rangle_{\mathcal{B}(T, i)}\|_{\Delta(T)}$ since, by construction, $S \subset \Delta(T)$. Let $\langle \tilde{v}_i \rangle_{\Delta(T)}$ denote the mean-value of \tilde{v}_i on $\Delta(T)$. Invoking [76, Lemma 5.7] gives

$$\|\tilde{v}_i - \langle \tilde{v}_i \rangle_{\Delta(T)}\|_{\Delta(T)} \lesssim h_T \|\nabla \tilde{v}_i\|_{\Delta(T)}.$$

Moreover, letting $\partial\mathcal{B}(T, i)$ denote the boundary of the ball $\mathcal{B}(T, i)$ and since $\mathcal{B}(T, i) \subset \Delta(T)$, we have

$$\begin{aligned} \|\langle v_i \rangle_{\mathcal{B}(T, i)} - \langle \tilde{v}_i \rangle_{\Delta(T)}\|_{\Delta(T)} &= |\Delta(T)|^{\frac{1}{2}} |\partial\mathcal{B}(T, i)|^{-\frac{1}{2}} \|\langle v_i \rangle_{\mathcal{B}(T, i)} - \langle \tilde{v}_i \rangle_{\Delta(T)}\|_{\partial\mathcal{B}(T, i)} \\ &\leq |\Delta(T)|^{\frac{1}{2}} |\partial\mathcal{B}(T, i)|^{-\frac{1}{2}} (\|v_i - \langle v_i \rangle_{\mathcal{B}(T, i)}\|_{\partial\mathcal{B}(T, i)} + \|\tilde{v}_i - \langle \tilde{v}_i \rangle_{\Delta(T)}\|_{\partial\mathcal{B}(T, i)}), \end{aligned}$$

since $\tilde{v}_i|_{\partial\mathcal{B}(T, i)} = v_i|_{\partial\mathcal{B}(T, i)}$. Invoking a multiplicative trace inequality from $\partial\mathcal{B}(T, i)$ to $\mathcal{B}(T, i)$ gives

$$\|v_i - \langle v_i \rangle_{\mathcal{B}(T, i)}\|_{\partial\mathcal{B}(T, i)} \lesssim h_T^{-\frac{1}{2}} \|v_i - \langle v_i \rangle_{\mathcal{B}(T, i)}\|_{\mathcal{B}(T, i)} + h_T^{\frac{1}{2}} \|\nabla v_i\|_{\mathcal{B}(T, i)},$$

and the Poincaré inequality in $\mathcal{B}(T, i)$ then gives

$$\|v_i - \langle v_i \rangle_{\mathcal{B}(T, i)}\|_{\partial\mathcal{B}(T, i)} \lesssim h_T^{\frac{1}{2}} \|\nabla v_i\|_{\mathcal{B}(T, i)}.$$

The same arguments, together with $\mathcal{B}(T, i) \subset \Delta(T)$ and the mesh shape-regularity, lead to

$$\|\tilde{v}_i - \langle \tilde{v}_i \rangle_{\Delta(T)}\|_{\partial\mathcal{B}(T, i)} \lesssim h_T^{\frac{1}{2}} \|\nabla \tilde{v}_i\|_{\Delta(T)}.$$

Combining the above bounds and since $|\Delta(T)|^{\frac{1}{2}} |\partial\mathcal{B}(T, i)|^{-\frac{1}{2}} \lesssim h_T^{\frac{1}{2}}$ proves (IV.60).

(2) The higher-order version of (IV.60) is established by invoking the Morrey polynomial of v_i based on mean-values of higher-order derivatives of v_i (see, e.g., the proof of [76, Lemma 5.6]). Omitting the details for brevity, this gives, for all $0 \leq m < s$, a polynomial $q_m(v_i) \in P^{k+1}(T^i)$ such that, for all $S \in \{T\} \cup \mathcal{N}_i^{-1}(T)$,

$$|\tilde{v}_i - q_m(v_i)|_{H^m(S)} \lesssim h_T^{s-m} |\tilde{v}_i|_{H^s(\Delta(T))}. \quad (\text{IV.61})$$

(3) Since $I_{T^i}^{k+1}(q_0(v_i)) = q_0(v_i)$, the triangle inequality gives

$$\|\tilde{v}_i - I_{T^i}^{k+1}(v_i)^+\|_S \leq \|\tilde{v}_i - q_0(v_i)\|_S + \|I_{T^i}^{k+1}(v_i - q_0(v_i))^+\|_S.$$

The first term on the right-hand side is estimated by using (IV.61) with $m = 0$. For the second term, the discrete inverse inequality (IV.38a) gives

$$\|I_{T^i}^{k+1}(v_i - q_0(v_i))^+\|_S \lesssim \|I_{T^i}^{k+1}(v_i - q_0(v_i))\|_{T^i} \leq \|I_{T^i}^{k+1}(v_i - q_0(v_i))\|_T \leq \|\tilde{v}_i - q_0(v_i)\|_T,$$

where we used the L^2 -orthogonality of $I_{T^i}^{k+1}$ in T . Invoking again (IV.61) with $m = 0$ and combining the above two bounds proves that

$$\sum_{S \in \{T\} \cup \mathcal{N}_i^{-1}(T)} \|\tilde{v}_i - I_{T^i}^{k+1}(v_i)^+\|_S \lesssim h_T^s |\tilde{v}_i|_{H^s(\Delta(T))}.$$

A similar reasoning with $q_1(v_i)$ in (IV.61) also gives

$$\sum_{S \in \{T\} \cup \mathcal{N}_i^{-1}(T)} h_S \|\nabla(\tilde{v}_i - I_{T^i}^{k+1}(v_i)^+)\|_S \lesssim h_T^s |\tilde{v}_i|_{H^s(\Delta(T))}.$$

Altogether, this proves that

$$\begin{aligned} & \sum_{S \in \{T\} \cup \mathcal{N}_i^{-1}(T)} \left\{ \|v_i - I_{T^i}^{k+1}(v_i)^+\|_{S^i} + h_S \|\nabla(v_i - I_{T^i}^{k+1}(v_i)^+)\|_{S^i} \right\} \\ & \leq \sum_{S \in \{T\} \cup \mathcal{N}_i^{-1}(T)} \left\{ \|\tilde{v}_i - I_{T^i}^{k+1}(v_i)^+\|_S + h_S \|\nabla(\tilde{v}_i - I_{T^i}^{k+1}(v_i)^+)\|_S \right\} \lesssim h_T^s |\tilde{v}_i|_{H^s(\Delta(T))}. \end{aligned}$$

(4) Invoking a multiplicative trace inequality on all the faces composing $(\partial S)^i$ for all $S \in \{T\} \cup \mathcal{N}_i^{-1}(T)$, and since $s > \frac{3}{2}$ by assumption, we infer from the above bounds that

$$\sum_{S \in \{T\} \cup \mathcal{N}_i^{-1}(T)} \left\{ h_S^{\frac{1}{2}} \|v_i - I_{T^i}^{k+1}(v_i)^+\|_{(\partial S)^i} + h_S^{\frac{3}{2}} \|\nabla(v_i - I_{T^i}^{k+1}(v_i)^+)\|_{(\partial S)^i} \right\} \lesssim h_T^s |\tilde{v}_i|_{H^s(\Delta(T))}.$$

This completes the proof of (IV.41a).

(5) To prove (IV.41b), we bound the jump across S^Γ by the triangle inequality, so that we need to estimate the traces on S^Γ from both sides of S^Γ , for all $S \in \{T\} \cup \mathcal{N}_i^{-1}(T)$. On each side, we invoke a multiplicative trace inequality on S^Γ . This inequality is established with a slight adaptation of the arguments in the proof of [35, Lemma 3.3], whereby we make a specific choice for the apex of the cone, say $C(S^\Gamma)$, considered in that proof.

(5a) Assume first that $S = T$. The triangle inequality gives

$$h_T^{\frac{1}{2}} \|\llbracket v - I_T^{k+1}(v) \rrbracket_\Gamma\|_{T^\Gamma} \leq h_T^{\frac{1}{2}} \|v_i - I_{T^i}^{k+1}(v_i)\|_{T^\Gamma} + h_T^{\frac{1}{2}} \|v_{\bar{i}} - I_{T^{\bar{i}}}^{k+1}(v_{\bar{i}})\|_{T^\Gamma}.$$

For the first term on the right-hand side, the apex of the cone $C(T^\Gamma)$ is taken to be the center of the ball $B(T, i)$. Since $C(T^\Gamma) \subset \text{conv}(T) \subset \Delta(T)$ by the assumption (IV.4), we infer that

$$h_T^{\frac{1}{2}} \|v_i - I_{T^i}^{k+1}(v_i)\|_{T^\Gamma} \lesssim \|\tilde{v}_i - I_{T^i}^{k+1}(v_i)^+\|_{\Delta(T)} + h_T \|\nabla(\tilde{v}_i - I_{T^i}^{k+1}(v_i)^+)\|_{\Delta(T)},$$

and adapting the above arguments gives

$$h_T^{\frac{1}{2}} \|v_i - I_{T^i}^{k+1}(v_i)\|_{T^\Gamma} \lesssim h_T^s |\tilde{v}_i|_{H^s(\Delta(T))}.$$

To bound $h_T^{\frac{1}{2}}\|v_{\bar{i}} - I_{T^{\bar{i}}}^{k+1}(v_{\bar{i}})\|_{T^\Gamma}$, we can consider the same cone to derive the multiplicative trace inequality, so that

$$h_T^{\frac{1}{2}}\|v_{\bar{i}} - I_{T^{\bar{i}}}^{k+1}(v_{\bar{i}})\|_{T^\Gamma} \lesssim h_T^s |\tilde{v}_{\bar{i}}|_{H^s(\Delta(T))},$$

where $\tilde{v}_{\bar{i}} := E_{\bar{i}}^s(v_{\bar{i}})$. Altogether, this proves that

$$h_T^{\frac{1}{2}}\|\llbracket v - I_T^{k+1}(v) \rrbracket_\Gamma\|_{T^\Gamma} \lesssim \sum_{i \in \{1, 2\}} h_T^s |\tilde{v}_i|_{H^s(\Delta(T))}.$$

(5b) Assume now that $S \in \mathcal{N}_i^{-1}(T)$. Then, the apex of the cone, $C(S^\Gamma)$, to establish the multiplicative trace inequality is taken to be the center of the ball $B(S, \bar{i})$ (indeed, if $(S, i) \in \mathcal{P}_h^{\text{KO}}$, then $(S, \bar{i}) \in \mathcal{P}_h^{\text{OK}}$). This yields $C(S^\Gamma) \subset \text{conv}(S) \subset \Delta(S) \subset \Delta_2(T)$. Invoking the same arguments as above then yields

$$h_S^{\frac{1}{2}}\|\llbracket I_T^{k+1}(v)^+ - v \rrbracket_\Gamma\|_{S^\Gamma} \lesssim \sum_{i \in \{1, 2\}} h_T^s |\tilde{v}_i|_{H^s(\Delta_2(T))}.$$

This completes the proof. \square

Conclusion and perspectives

In this concluding chapter, we briefly summarize the main contributions of this Thesis, and outline possible directions for future research building upon the present work.

V.1 Summary

The main contributions of this Thesis are as follows:

Chapter II: HHO methods for elasto-acoustic wave propagation in the time domain. This chapter addressed the development of HHO methods for wave propagation in heterogeneous media (solids and fluids). We first established an optimal space semi-discrete error estimate in the energy norm. Then, we presented various numerical results reaching the following conclusions:

- A spectral analysis showing the need for $\mathcal{O}(1)$ -stabilization when using explicit time discretization schemes, in order to avoid overly restrictive CFL conditions;
- Optimal convergence rates of order $(k+1)$ for both equal-order ($k' = k$) and mixed-order ($k' = k + 1$) discretizations with $\mathcal{O}(1)$ -stabilization, and rates reaching order $(k+2)$ when using mixed-order schemes and $\mathcal{O}(1/h)$ -stabilization in an implicit time discretization setting;
- Numerical experiments based on Ricker wavelets as initial condition, highlighted the accuracy and robustness of the proposed method in media exhibiting strong material contrasts.

Chapter III: Wave propagation in geophysical media using HHO methods on general meshes. This chapter extended the numerical study initiated in Chapter 2 by exploring the benefits of locally eliminating face unknowns in the explicit case and cell unknowns in the implicit case. It also included a realistic geophysical benchmark. The main results are as follows:

- The possibility of static condensation in both implicit and explicit settings;
- The derivation of an empirical CFL condition for explicit time schemes for various polynomial degrees and mesh shapes;
- A comparison of the efficiency of explicit and implicit schemes in the case of a Ricker wavelet, showing the benefits of an implicit time scheme in several situations;
- The possibility to perform two-dimensional simulations in realistic geophysical settings, showing the geometric flexibility of the HHO method. In particular, hybrid and nonconforming meshes (with hanging nodes) were handled without loss of accuracy.

Chapter IV: Unfitted HHO methods stabilized by polynomial extension.

This chapter presented a novel contribution to the design of unfitted HHO methods, proposing and analyzing a stabilization strategy based on polynomial extension. We provided a stability and error analysis, followed by numerical results that illustrated the method behavior. The most salient numerical results included:

- A comparison between agglomeration-based and polynomial extension-based approaches, with an analysis of the sparsity patterns of the resulting stiffness matrices;
- Convergence rates for different choices of polynomial bases and various values of the ball criterion parameter ϑ , assessing the sensitivity to poor cut configurations;
- A robustness study with respect to material contrast and imposed jumps at the interface;
- A conditioning study of the stiffness matrix.

Software developments. All the computational and numerical developments presented in Chapters 2 and 3 have been implemented in the open-source code `disk++`, developed at CERMICS [48]. Owing to the specific data structures required by unfitted methods, the related developments have been carried out within the `ProtoN` prototyping platform, also an open-source code from CERMICS. These software developments have led to the creation of dedicated branches in both computational codes, involving substantial modifications at various levels, including data structures, discrete operators, assembly processes, solver interfaces and postprocessing of the data.

V.2 Perspectives

Several research directions could be pursued to further extend and enhance the work presented in this Thesis. These directions can be broadly categorized into two groups: those with an applicative focus, and those aiming to advance the design of hybrid discontinuous methods for geophysical applications.

Numerical perspectives:

- **Integration of unfitted tools into `disk++`.** While the developments related to unfitted methods were carried out in the `ProtoN` prototyping platform, a full integration of these tools into the main `disk++` infrastructure remains to be completed. This would provide a unified computational code for fitted and unfitted HHO simulations.
- **Unfitted elasto-acoustic coupling.** The coupling strategy developed in Chapters II and III assumed a fitted setting. A promising research direction would be to extend this formulation to unfitted interfaces, enabling the simulation of coupled elasto-acoustic waves in curved complex domains.

- **Structure-preserving time integration.** Exploring symplectic or energy-preserving time integrators could be beneficial for long-time wave simulations, leveraging previous work on dG and HDG methods for wave equations [128, 131, 132].
- **Reduction of CFL constraints.** To alleviate the restrictive CFL conditions associated with explicit time integration, two complementary strategies could be explored:
 - the use of local time-stepping, whereby each element is advanced with a time step adapted to its characteristic size. This strategy has already been explored using other numerical methods [128, 70, 18, 86, 41];
 - the design of IMEX (implicit-explicit) integrators, in which small elements are treated implicitly while larger ones are handled explicitly, providing a compromise between stability and computational efficiency.
- **Superconvergent post-processing for explicit time integration.** Building on the post-processing strategies introduced in [57] in the context of HDG methods, it would be worth investigating similar approaches for HHO methods. The goal would be to reconstruct enhanced approximations of the primal unknowns and assess whether superconvergence phenomena can be observed in this framework.

Applicative perspectives:

- **SEM-HHO coupling.** It would be interesting to design a numerical scheme that couples the spectral element method (SEM) with the HHO method. Such a SEM–HHO coupling would retain the geometric flexibility of HHO methods where it is needed, while exploiting the tensorized structure of SEM in regions where the mesh is regular and does not pose difficulties. This hybrid approach could lead to highly efficient and accurate solvers.
- **Three-dimensional geophysical applications.** A natural continuation of the numerical studies presented in Chapter III consists in performing three-dimensional simulations in realistic geophysical settings. Such studies would allow to fully leverage the geometric flexibility of the HHO method in complex environments and to assess its performance and scalability in large-scale applications.
- **Robust 3D unfitted HHO platform.** In three dimensions, the large variety of cut configurations poses a significant challenge for performing unfitted methods. It would be an interesting challenge to extend our approach to 3D.

Bibliography

- [1] M. Abbas, A. Ern, and N. Pignet. Hybrid high-order methods for finite deformations of hyperelastic materials. *Comput. Mech.*, 62(4):909–928, 2018.
- [2] M. Abbas, A. Ern, and N. Pignet. A hybrid high-order method for incremental associative plasticity with small deformations. *Comput. Methods Appl. Mech. Engrg.*, 346:891–912, 2019.
- [3] K. Aki and P. Richards. *Quantitative seismology*. University Science Books, Melville, NY, 2002.
- [4] G. Allaire. *Numerical analysis and optimization: an introduction to mathematical modelling and numerical simulation*. OUP Oxford, 2007.
- [5] P. F. Antonietti, F. Bonaldi, and I. Mazzieri. A high-order discontinuous Galerkin approach to the elasto-acoustic problem. *Comput. Methods Appl. Mech. Engrg.*, 358:112634, 29, 2020.
- [6] P. F. Antonietti, F. Bonaldi, and I. Mazzieri. Simulation of three-dimensional elastoacoustic wave propagation based on a discontinuous Galerkin spectral element method. *Internat. J. Numer. Methods Engrg.*, 121(10):2206–2226, 2020.
- [7] P. F. Antonietti, L. B. da Veiga, and G. Manzini. *The virtual element method and its applications*, volume 31. Springer, Cham, 2022.
- [8] D. Appelö and N. A. Petersson. A stable finite difference method for the elastic wave equation on complex geometries with free surfaces. *Commun. Comput. Phys.*, 5(1):84–107, 2009.
- [9] D. N. Arnold, F. Brezzi, B. Cockburn, and L. D. Marini. Unified analysis of discontinuous Galerkin methods for elliptic problems. *SIAM J. Numer. Anal.*, 39(5):1749–1779, 2001.
- [10] S. Arrowsmith, J. Johnson, D. Drob, and M. Hedlin. The seismoacoustic wavefield: A new paradigm in studying geophysical phenomena. *Rev Geophys.*, 48:RG4003, 2010.
- [11] J. Assink, G. Averbach, S. Shani-Kadmiel, P. Smets, and L. Evers. A seismo-acoustic analysis of the 2017 North Korean nuclear test. *Seismol. Res. Lett.*, 89(6):2025–2033, 2018.
- [12] B. Ayuso de Dios, K. Lipnikov, and G. Manzini. The nonconforming virtual element method. *ESAIM Math. Model. Numer. Anal.*, 50(3):879–904, 2016.
- [13] I. Babuška. The finite element method with penalty. *Math. Comp.*, 27:221–228, 1973.
- [14] S. Badia, F. Verdugo, and A. F. Martín. The aggregated unfitted finite element method for elliptic problems. *Comput. Methods Appl. Mech. Engrg.*, 336:533–553, 2018.

- [15] G. A. Baker. Error estimates for finite element methods for second order hyperbolic equations. *SIAM J. Numer. Anal.*, 13(4):564–576, 1976.
- [16] J. W. Barrett and C. M. Elliott. A finite-element method for solving elliptic equations with Neumann data on a curved boundary using unfitted meshes. *IMA J. Numer. Anal.*, 4(3):309–325, 1984.
- [17] J. W. Barrett and C. M. Elliott. Finite element approximation of the Dirichlet problem using the boundary penalty method. *Numer. Math.*, 49(4):343–366, 1986.
- [18] H. Barucq, M. Duruflé, and M. N’diaye. High-order locally A-stable implicit schemes for linear ODEs. *J. Sci. Comput.*, 85(2):Paper No. 31, 33, 2020.
- [19] P. Bastian and C. Engwer. An unfitted finite element method using discontinuous Galerkin. *Internat. J. Numer. Methods Engrg.*, 79(12):1557–1576, 2009.
- [20] L. Beirão da Veiga, F. Brezzi, A. Cangiani, G. Manzini, L. D. Marini, and A. Russo. Basic principles of virtual element methods. *Math. Models Methods Appl. Sci.*, 23(1):199–214, 2013.
- [21] L. Beirão da Veiga, Y. Liu, L. Mascotto, and A. Russo. The nonconforming virtual element method with curved edges. *J. Sci. Comput.*, 99(1):Paper No. 23, 35, 2024.
- [22] S. Bertoluzza, M. Montardini, M. Pennacchio, and D. Prada. The virtual element method on polygonal pixel-based tessellations. *J. Comput. Phys.*, 518:Paper No. 113334, 22, 2024.
- [23] S. Bertoluzza, M. Pennacchio, and D. Prada. Weakly imposed Dirichlet boundary conditions for 2D and 3D virtual elements. *Comput. Methods Appl. Mech. Engrg.*, 400:Paper No. 115454, 27, 2022.
- [24] A. Bertrand-Grenier. Technologie - l’élastographie : cartographier le corps humain. *Dire*, 24, 2015.
- [25] F. Brezzi, A. Buffa, and K. Lipnikov. Mimetic finite differences for elliptic problems. *M2AN Math. Model. Numer. Anal.*, 43(2):277–295, 2009.
- [26] F. Brezzi, K. Lipnikov, and V. Simoncini. A family of mimetic finite difference methods on polygonal and polyhedral meshes. *Math. Models Methods Appl. Sci.*, 15(10):1533–1551, 2005.
- [27] A. Buffa, R. Puppi, and R. Vázquez. A minimal stabilization procedure for isogeometric methods on trimmed geometries. *SIAM J. Numer. Anal.*, 58(5):2711–2735, 2020.
- [28] E. Burman. Ghost penalty. *C. R. Math. Acad. Sci. Paris*, 348(21-22):1217–1220, 2010.
- [29] E. Burman, M. Cicuttin, G. Delay, and A. Ern. An unfitted hybrid high-order method with cell agglomeration for elliptic interface problems. *SIAM J. Sci. Comput.*, 43(2):A859–A882, 2021.

- [30] E. Burman, S. Claus, P. Hansbo, M. G. Larson, and A. Massing. CutFEM: discretizing geometry and partial differential equations. *Internat. J. Numer. Methods Engrg.*, 104(7):472–501, 2015.
- [31] E. Burman, G. Delay, and A. Ern. An unfitted hybrid high-order method for the Stokes interface problem. *IMA J. Numer. Anal.*, 41(4):2362–2387, 2021.
- [32] E. Burman, O. Duran, and A. Ern. Hybrid high-order methods for the acoustic wave equation in the time domain. *Commun. Appl. Math. Comput.*, 4(2):597–633, 2022.
- [33] E. Burman, O. Duran, and A. Ern. Unfitted hybrid high-order methods for the wave equation. *Comput. Methods Appl. Mech. Engrg.*, 389:Paper No. 114366, 23, 2022.
- [34] E. Burman, O. Duran, A. Ern, and M. Steins. Convergence analysis of hybrid high-order methods for the wave equation. *J. Sci. Comput.*, 87(3):30, 2021.
- [35] E. Burman and A. Ern. An unfitted hybrid high-order method for elliptic interface problems. *SIAM J. Numer. Anal.*, 56(3):1525–1546, 2018.
- [36] E. Burman, A. Ern, and M. A. Fernández. Explicit runge–kutta schemes and finite elements with symmetric stabilization for first-order linear pde systems. *SIAM J. Numer. Anal.*, 48(6):2019–2042, 2010.
- [37] E. Burman, A. Ern, and R. Mottier. Unfitted hybrid high-order methods stabilized by polynomial extension for elliptic interface problems. 2025. <https://arxiv.org/abs/2503.11397>.
- [38] E. Burman, P. Hansbo, and M. G. Larson. A cut finite element method with boundary value correction. *Math. Comp.*, 87(310):633–657, 2018.
- [39] A. Cangiani, Z. Dong, E. H. Georgoulis, and P. Houston. *hp-version discontinuous Galerkin methods on polygonal and polyhedral meshes*. SpringerBriefs in Mathematics. Springer, Cham, 2017.
- [40] A. Cangiani, G. Manzini, and O. J. Sutton. Conforming and nonconforming virtual element methods for elliptic problems. *IMA J. Numer. Anal.*, 37(3):1317–1354, 2017.
- [41] C. Carle and M. Hochbruck. Error analysis of second-order local time integration methods for discontinuous Galerkin discretizations of linear wave equations. *Math. Comp.*, 93(350):2611–2641, 2024.
- [42] E. Chaljub, Y. Capdeville, and J.-P. Vilotte. Solving elastodynamics in a fluid-solid heterogeneous sphere: a parallel spectral element approximation on non-conforming grids. *J. Comput. Phys.*, 187(2):457–491, 2003.
- [43] E. Chaljub, P. Moczo, S. Tsuno, P.-Y. Bard, J. Kristek, M. Käser, M. Stupazzini, and M. Kristekova. Quantitative comparison of four numerical predictions of 3d ground motion in the Grenoble valley, France. *Bull. Seismol. Soc. Am.*, 100(4):1427–1455, 2010.

- [44] E. Chaljub and B. Valette. Spectral element modelling of three-dimensional wave propagation in a self-gravitating Earth with an arbitrarily stratified outer core. *Geophys. J. Int.*, 158(1):131–141, 2004.
- [45] T. Chaumont-Frelet, A. Ern, S. Lemaire, and F. Valentin. Bridging the multiscale hybrid-mixed and multiscale hybrid high-order methods. *ESAIM Math. Model. Numer. Anal.*, 56(1):261–285, 2022.
- [46] I.-Y. Che, K. Kim, A. Le Pichon, J. Park, S. Arrowsmith, and B. Stump. Illuminating the North Korean nuclear explosion test in 2017 using remote infrasound observations. *Geophys. J. Int.*, 228(1):308–315, 2021.
- [47] E. T. Chung and B. Engquist. Optimal discontinuous Galerkin methods for wave propagation. *SIAM J. Numer. Anal.*, 44(5):2131–2158, 2006.
- [48] M. Cicuttin, D. A. Di Pietro, and A. Ern. Implementation of discontinuous skeletal methods on arbitrary-dimensional, polytopal meshes using generic programming. *J. Comput. Appl. Math.*, 344:852–874, 2018.
- [49] M. Cicuttin, A. Ern, and S. Lemaire. A hybrid high-order method for highly oscillatory elliptic problems. *Comput. Methods Appl. Math.*, 19(4):723–748, 2019.
- [50] M. Cicuttin, A. Ern, and N. Pignet. *Hybrid high-order methods—a primer with applications to solid mechanics*. SpringerBriefs in Mathematics. Springer, Cham, 2021.
- [51] J. F. Claerbout. *Fundamentals of geophysical data processing: with applications to petroleum prospecting*. McGraw-Hill, NY, 1976.
- [52] B. Cockburn. *Static condensation, hybridization, and the devising of the HDG methods*, volume 114 of *Lect. Notes Comput. Sci. Eng.* Springer, Cham, 2016.
- [53] B. Cockburn, D. A. Di Pietro, and A. Ern. Bridging the hybrid high-order and hybridizable discontinuous Galerkin methods. *ESAIM Math. Model. Numer. Anal.*, 50(3):635–650, 2016.
- [54] B. Cockburn, Z. Fu, A. Hungria, L. Ji, M. A. Sánchez, and F.-J. Sayas. Stormer-Numerov HDG methods for acoustic waves. *J. Sci. Comput.*, 75(2):597–624, 2018.
- [55] B. Cockburn, J. Gopalakrishnan, and R. Lazarov. Unified hybridization of discontinuous Galerkin, mixed, and continuous Galerkin methods for second order elliptic problems. *SIAM J. Numer. Anal.*, 47(2):1319–1365, 2009.
- [56] B. Cockburn, W. Qiu, and M. Solano. A priori error analysis for HDG methods using extensions from subdomains to achieve boundary conformity. *Math. Comp.*, 83(286):665–699, 2014.
- [57] B. Cockburn and V. Quenneville-Bélair. Uniform-in-time superconvergence of the HDG methods for the acoustic wave equation. *Math. Comp.*, 83(285):65–85, 2014.

- [58] B. Cockburn and C.-W. Shu. TVB Runge-Kutta local projection discontinuous Galerkin finite element method for conservation laws. II. General framework. *Math. Comp.*, 52(186):411–435, 1989.
- [59] G. C. Cohen. *Higher-order numerical methods for transient wave equations*. Scientific Computation. Springer-Verlag, Berlin, 2002.
- [60] G. C. Cohen, P. Joly, J. E. Roberts, and N. Tordjman. Higher order triangular finite elements with mass lumping for the wave equation. *SIAM J. Numer. Anal.*, 38(6):2047–2078, 2001.
- [61] F. Dassi, A. Fumagalli, I. Mazzieri, A. Scotti, and G. Vacca. A virtual element method for the wave equation on curved edges in two dimensions. *J. Sci. Comput.*, 90(1), 2022.
- [62] J. de Basabe, J. Sen, and M. Wheeler. The interior penalty discontinuous Galerkin method for elastic wave propagation: grid dispersion. *Geophys. J. Int.*, 175(1):83–93, 2008.
- [63] E. Delavaud. Simulation numérique de la propagation d'ondes en milieu géologique complexe : application à l'évaluation de la réponse sismique du bassin de Caracas (Venezuela). *Univ. Paris VII Denis Diderot*, 2007.
- [64] D. A. Di Pietro and J. Droniou. A hybrid high-order method for Leray-Lions elliptic equations on general meshes. *Math. Comp.*, 86(307):2159–2191, 2017.
- [65] D. A. Di Pietro and J. Droniou. *The hybrid high-order method for polytopal meshes*, volume 19 of *MS&A. Modeling, Simulation and Applications*. Springer, Cham, 2020.
- [66] D. A. Di Pietro, J. Droniou, and G. Manzini. Discontinuous skeletal gradient discretisation methods on polytopal meshes. *J. Comput. Phys.*, 355:397–425, 2018.
- [67] D. A. Di Pietro and A. Ern. *Mathematical aspects of discontinuous Galerkin methods*, volume 69 of *Mathématiques & Applications*. Springer, Heidelberg, 2012.
- [68] D. A. Di Pietro and A. Ern. A hybrid high-order locking-free method for linear elasticity on general meshes. *Comput. Methods Appl. Mech. Engrg.*, 283:1–21, 2015.
- [69] D. A. Di Pietro, A. Ern, and S. Lemaire. An arbitrary-order and compact-stencil discretization of diffusion on general meshes based on local reconstruction operators. *Comput. Methods Appl. Math.*, 14(4):461–472, 2014.
- [70] J. Diaz and M. J. Grote. Multi-level explicit local time-stepping methods for second-order wave equations. *Comput. Methods Appl. Mech. Engrg.*, 291:240–265, 2015.
- [71] J. Diaz and P. Joly. Robust high order non-conforming finite element formulation for time domain fluid-structure interaction. *J. Comput. Acoust.*, 13(3):403–431, 2005.
- [72] S. Du and F.-J. Sayas. A note on devising HDG+ projections on polyhedral elements. *Math. Comp.*, 90(327):65–79, 2021.

- [73] M. Dumbser and M. Käser. An arbitrary high-order discontinuous Galerkin method for elastic waves on unstructured meshes - II. The three-dimensional isotropic case. *Geophys. J. Int.*, 167(1):319–336, 2006.
- [74] R. Dunlop, W. L. Gannon, M. Kiley-Worthington, P. S. M. Hill, A. Wessel, and J. A. Thomas. *Exploring animal behavior through sound: Volume 1: Methods*. Springer, Cham, 2022.
- [75] T. Dupont. L^2 -estimates for Galerkin methods for second order hyperbolic equations. *SIAM J. Numer. Anal.*, 10:880–889, 1973.
- [76] A. Ern and J.-L. Guermond. Finite element quasi-interpolation and best approximation. *ESAIM Math. Model. Numer. Anal.*, 51(4):1367–1385, 2017.
- [77] A. Ern and J.-L. Guermond. *Finite elements I—Approximation and interpolation*, volume 72 of *Texts in Applied Mathematics*. Springer, Cham, 2021.
- [78] A. Ern and J.-L. Guermond. *Finite elements II—Galerkin approximation, elliptic and mixed PDEs*, volume 73 of *Texts in Applied Mathematics*. Springer, Cham, 2021.
- [79] A. Ern and J.-L. Guermond. *Finite elements III—first-order and time-dependent PDEs*, volume 74 of *Texts in Applied Mathematics*. Springer, Cham, 2021.
- [80] A. Ern and R. Khot. Explicit runge-kutta schemes with hybrid high-order methods for the wave equation in first order form. *HAL-04763478*, 2024.
- [81] A. Ern and M. Steins. Convergence analysis for the wave equation discretized with hybrid methods in space (HHO, HDG and WG) and the leapfrog scheme in time. *J. Sci. Comput.*, 101(1):28, 2024.
- [82] R. S. Falk and G. R. Richter. Explicit finite element methods for symmetric hyperbolic equations. *SIAM J. Numer. Anal.*, 36(3):935–952, 1999.
- [83] A. Fichtner, B. L. N. Kennett, V. C. Tsai, C. H. Thurber, A. J. Rodgers, C. Tape, N. Rawlinson, R. D. Borcherdt, S. Lebedev, K. Priestley, C. Morency, E. Bozdağ, J. Tromp, J. Ritsema, B. Romanowicz, Q. Liu, E. Golos, and F. Lin. Seismic tomography 2024. *B SEISMOL SOC AM*, 114(3):1185–1213, 2024.
- [84] A. Fichtner, B. L. N. Kennett, V. C. Tsai, C. H. Thurber, A. J. Rodgers, C. Tape, N. Rawlinson, R. D. Borcherdt, S. Lebedev, K. Priestley, C. Morency, E. Bozdağ, J. Tromp, J. Ritsema, B. Romanowicz, Q. Liu, E. Golos, and F. Lin. Seismic tomography 2024. *Bull. Seismol. Soc. Am.*, 114(3):1185–1213, 2024.
- [85] G. N. Gatica, A. Márquez, and S. Meddahi. Analysis of the coupling of primal and dual-mixed finite element methods for a two-dimensional fluid-solid interaction problem. *SIAM J. Numer. Anal.*, 45(5):2072–2097, 2007.
- [86] M. J. Grote, S. Michel, and S. A. Sauter. Stabilized leapfrog based local time-stepping method for the wave equation. *Math. Comp.*, 90(332):2603–2643, 2021.

- [87] M. J. Grote, A. Schneebeli, and D. Schötzau. Discontinuous Galerkin finite element method for the wave equation. *SIAM J. Numer. Anal.*, 44(6):2408–2431, 2006.
- [88] A. Hansbo and P. Hansbo. An unfitted finite element method, based on Nitsche’s method, for elliptic interface problems. *Comput. Methods Appl. Mech. Engrg.*, 191(47-48):5537–5552, 2002.
- [89] J. Haslinger and Y. Renard. A new fictitious domain approach inspired by the extended finite element method. *SIAM J. Numer. Anal.*, 47(2):1474–1499, 2009.
- [90] M. Hedlin, K. Walker, D. Drob, and C. de Groot-Hedlin. Infrasound: Connecting the solid earth, oceans, and atmosphere. *Ann Rev Earth Planet Sci*, 40:327–354, 2012.
- [91] F. Heimann, C. Lehrenfeld, P. Stocker, and H. von Wahl. Unfitted Trefftz discontinuous Galerkin methods for elliptic boundary value problems. *ESAIM Math. Model. Numer. Anal.*, 57(5):2803–2833, 2023.
- [92] V. Hermann, M. Käser, and C. E. Castro. Non-conforming hybrid meshes for efficient 2-d wave propagation using the discontinuous galerkin method. *Geophysical Journal International*, 184(2):746–758, 2011.
- [93] B. Hernandez, A. Le Pichon, J. Vergoz, P. Herry, L. Ceranna, C. Pilger, E. Marchetti, M. Ripepe, and R. Bossu. Estimating the ground-motion distribution of the 2016 mw 6.2 Amatrice, Italy, Earthquake using remote infrasound observations. *Seismol. Res. Lett.*, 89(6):2227–2236, 09 2018.
- [94] J. S. Hesthaven and T. Warburton. *Nodal discontinuous Galerkin methods*, volume 54 of *Texts in Applied Mathematics*. Springer, NY, 2008.
- [95] Y. Hou, Y. Liu, and Y. Wang. A high-order shifted boundary virtual element method for Poisson equations on 2D curved domains. *J. Sci. Comput.*, 99(3):27, 2024.
- [96] Y. Huang, J. Li, and D. Li. Developing weak Galerkin finite element methods for the wave equation. *Numer. Methods Partial Differential Equations*, 33(3):868–884, 2017.
- [97] A. Johansson and M. G. Larson. A high order discontinuous Galerkin Nitsche method for elliptic problems with fictitious boundary. *Numer. Math.*, 123(4):607–628, 2013.
- [98] C. Johnson and J. Pitkäranta. An analysis of the discontinuous Galerkin method for a scalar hyperbolic equation. *Math. Comp.*, 46(173):1–26, 1986.
- [99] P. Joly. Variational methods for time-dependent wave propagation problems. In *Topics in computational wave propagation*, volume 31 of *Lect. Notes Comput. Sci. Eng.*, pages 201–264. Springer, Berlin, 2003.
- [100] D. Komatitsch, C. Barnes, and J. Tromp. Wave propagation near a fluid-solid interface: A spectral-element approach. *Geophys.*, 65(2):623–631, 2000.

- [101] D. Komatitsch and J.-P. Vilotte. The Spectral Element Method: an effective tool to simulate the seismic response of 2D and 3D geological structures. *Bull. Seism. Soc. Am.*, 88:368–392, 1998.
- [102] M. Kronbichler, S. Schoeder, C. Müller, and W. A. Wall. Comparison of implicit and explicit hybridizable discontinuous Galerkin methods for the acoustic wave equation. *Internat. J. Numer. Methods Engrg.*, 106(9):712–739, 2016.
- [103] T. Lay and T. C. Wallace. *Modern global seismology*, volume 58. Academic Press, San Diego-London, 1995.
- [104] A. Léger and M. Deschamps. *Ultrasonic Wave Propagation in non homogeneous media*. Springer Berlin, Heidelberg, 2009.
- [105] C. Lehrenfeld. *Hybrid discontinuous Galerkin methods for incompressible flow problems*. Diploma thesis, CCESMath/IGPM RWTH, Aachen, 2010.
- [106] C. Lehrenfeld. High order unfitted finite element methods on level set domains using isoparametric mappings. *Comput. Methods Appl. Mech. Engrg.*, 300:716–733, 2016.
- [107] C. Lehrenfeld and A. Reusken. Analysis of a high-order unfitted finite element method for elliptic interface problems. *IMA J. Numer. Anal.*, 38(3):1351–1387, 2018.
- [108] C. Lehrenfeld and J. Schöberl. High order exactly divergence-free hybrid discontinuous Galerkin methods for unsteady incompressible flows. *Comput. Methods Appl. Mech. Engrg.*, 307:339–361, 2016.
- [109] S. Lemaire. Bridging the hybrid high-order and virtual element methods. *IMA J. Numer. Anal.*, 41(1):549–593, 2021.
- [110] P. Lesaint and P.-A. Raviart. On a finite element method for solving the neutron transport equation. In *Mathematical aspects of finite elements in partial differential equations (Proc. Sympos., Math. Res. Center, Univ. Wisconsin, Madison, Wis., 1974)*, pages 89–123. Academic Press, New York-London, 1974.
- [111] A. Main and G. Scovazzi. The shifted boundary method for embedded domain computations. Part I: Poisson and Stokes problems. *J. Comput. Phys.*, 372:972–995, 2018.
- [112] K. J. Marfurt. Accuracy of finite-difference and finite-element modelling of the scalar and elastic wave equations. *Geophys.*, 49:533–549, 1984.
- [113] R. Massjung. An unfitted discontinuous Galerkin method applied to elliptic interface problems. *SIAM J. Numer. Anal.*, 50(6):3134–3162, 2012.
- [114] Y. Masson. Distributional finite-difference modelling of seismic waves. *Geophys. J. Int.*, 233(1):264–296, 2022.

- [115] I. Mazzieri and F. Rapetti. Dispersion analysis of triangle-based spectral element methods for elastic wave propagation. *Numer. Algorithms*, 60(4):631–650, 2012.
- [116] E. Mercerat, J.-P. Vilotte, and F. Sánchez-Sesma. Triangular spectral element simulation of 2d elastic wave propagation using unstructured triangular grids. *Geophys. J. Int.*, 166(2):679–698, 2006.
- [117] E. D. Mercerat and N. Glinsky. A nodal high-order discontinuous Galerkin method for elastic wave propagation in arbitrary heterogeneous media. *Geophys. J. Int.*, 201(2):1101–1118, 2015.
- [118] P. Moczo, J. Kristek, and M. Galis. *The finite-difference modelling of earthquake motions: waves and ruptures*. Cambridge University Press, 2014.
- [119] P. Monk and G. R. Richter. A discontinuous Galerkin method for linear symmetric hyperbolic systems in inhomogeneous media. *J. Sci. Comput.*, 22/23:443–477, 2005.
- [120] R. Mottier, A. Ern, and L. Guillot. Elasto-acoustic wave propagation in geophysical media using hybrid high-order methods on general meshes. 2025. <https://hal.science/hal-05076055>.
- [121] R. Mottier, A. Ern, R. Khot, and L. Guillot. Hybrid high-order methods for elasto-acoustic wave propagation in the time domain. 2025. <http://arxiv.org/abs/2502.10870>.
- [122] N. C. Nguyen, J. Peraire, and B. Cockburn. High-order implicit hybridizable discontinuous Galerkin methods for acoustics and elastodynamics. *J. Comput. Phys.*, 230(10):3695–3718, 2011.
- [123] J. Nitsche. Über ein Variationsprinzip zur Lösung von Dirichlet-Problemen bei Verwendung von Teilräumen, die keinen Randbedingungen unterworfen sind. *Abh. Math. Sem. Univ. Hamburg*, 36:9–15, 1971.
- [124] J. Ophir, I. Céspedes, H. Ponnekanti, Y. Yazdi, and X. Li. Elastography: A quantitative method for imaging the elasticity of biological tissues. *Ultrason. Imaging*, 13(2):111–134, 1991.
- [125] A. Patera. A spectral element method for fluid dynamics: laminar flow in a channel expansion. *J. Comput. Phys.*, 54:468–488, 1984.
- [126] I. Perugia, P. Pietra, and A. Russo. A plane wave virtual element method for the Helmholtz problem. *ESAIM Math. Model. Numer. Anal.*, 50(3):783–808, 2016.
- [127] N. A. Petersson and B. Sjögreen. High order accurate finite difference modeling of seismo-acoustic wave propagation in a moving atmosphere and a heterogeneous Earth model coupled across a realistic topography. *J. Sci. Comput.*, 74(1):290–323, 2018.

- [128] S. Piperno. Symplectic local time-stepping in non-dissipative DGTD methods applied to wave propagation problems. *M2AN Math. Model. Numer. Anal.*, 40(5):815–841, 2006.
- [129] W. Qiu, M. Solano, and P. Vega. A high order HDG method for curved-interface problems via approximations from straight triangulations. *J. Sci. Comput.*, 69(3):1384–1407, 2016.
- [130] W. H. Reed and T. R. Hill. Triangular mesh methods for the neutron transport equation. Technical report, Los Alamos Scientific Lab., NM (USA), 1973.
- [131] M. A. Sánchez, C. Ciuca, N. C. Nguyen, J. Peraire, and B. Cockburn. Symplectic Hamiltonian HDG methods for wave propagation phenomena. *J. Comput. Phys.*, 350:951–973, 2017.
- [132] M. A. Sánchez, B. Cockburn, N.-C. Nguyen, and J. Peraire. Symplectic Hamiltonian finite element methods for linear elastodynamics. *Comput. Methods Appl. Mech. Engrg.*, 381:Paper No. 113843, 23, 2021.
- [133] W. E. H. Sollie, O. Bokhove, and J. J. W. van der Vegt. Space-time discontinuous Galerkin finite element method for two-fluid flows. *J. Comput. Phys.*, 230(3):789–817, 2011.
- [134] M. Stanglmeier, N. C. Nguyen, J. Peraire, and B. Cockburn. An explicit hybridizable discontinuous Galerkin method for the acoustic wave equation. *Comput. Methods Appl. Mech. Engrg.*, 300:748–769, 2016.
- [135] M. Steins, A. Ern, O. Jamond, and F. Drui. Time-explicit hybrid high-order method for the nonlinear acoustic wave equation. *ESAIM Math. Model. Numer. Anal.*, 57(5):2977–3006, 2023.
- [136] T. L. Szabo. *Diagnostic ultrasound imaging: inside out*. Elsevier, Oxford, 2014.
- [137] C. Talischi, G. H. Paulino, A. Pereira, and I. F. M. Menezes. PolyMesher: a general-purpose mesh generator for polygonal elements written in Matlab. *Struct. Multidiscip. Optim.*, 45(3):309–328, 2012.
- [138] S. Terrana, J. P. Villette, and L. Guillot. A spectral hybridizable discontinuous Galerkin method for elastic-acoustic wave propagation. *Geophys. J. Int.*, 213(1):574–602, 2017.
- [139] R. van Vossen, J. O. A. Robertsson, and C. H. Chapman. Finite-difference modeling of wave propagation in a fluid-solid configuration. *Geophys.*, 67(2):618–624, 2002.
- [140] J. Virieux. P-SV wave propagation in heterogeneous media: Velocity-stress finite-difference method. *Geophys.*, 51(4):889–901, 1986.
- [141] J. Wang and X. Ye. A weak Galerkin finite element method for second-order elliptic problems. *J. Comput. Appl. Math.*, 241:103–115, 2013.

- [142] J. Wang and X. Ye. A weak Galerkin mixed finite element method for second order elliptic problems. *Math. Comp.*, 83(289):2101–2126, 2014.
- [143] L. C. Wilcox, G. Stadler, C. Burstedde, and O. Ghattas. A high-order discontinuous Galerkin method for wave propagation through coupled elastic-acoustic media. *J. Comput. Phys.*, 229(24):9373–9396, 2010.
- [144] P. Wriggers and P. Junker. On a space-time implementation of the wave equation using virtual elements. *Computational Mechanics*, pages 1–15, 2024.
- [145] R. Ye, M. V. de Hoop, C. L. Petrovitch, L. J. Pyrak-Nolte, and L. C. Wilcox. A discontinuous Galerkin method with a modified penalty flux for the propagation and scattering of acousto-elastic waves. *Geophys. J. Int.*, 205(2):1267–1289, 2016.
- [146] L. Yemm. A new approach to handle curved meshes in the hybrid high-order method. *Found. Comput. Math.*, 24(3):1049–1076, 2024.
- [147] X. Zhang and M. Feng. A weak Galerkin mixed finite element method for acoustic wave equation. *Adv. Appl. Math. Mech.*, 14(4):936–959, 2022.